APPLIED COMPUTATIONAL ELECTROMAGNETICS SOCIETY JOURNAL

June 2015
Vol. 30 No. 6
ISSN 1054-4887

The ACES Journal is abstracted in INSPEC, in Engineering Index, DTIC, Science Citation Index Expanded, the Research Alert, and to Current Contents/Engineering, Computing & Technology.

The illustrations on the front cover have been obtained from the research groups at the Department of Electrical Engineering, The University of Mississippi.

EMERITUS EDITORIAL ASSISTANTS

JUNE 2015 REVIEWERS

THE APPLIED COMPUTATIONAL ELECTROMAGNETICS SOCIETY

JOURNAL

Vol. 30 No. 6 June 2015

TABLE OF CONTENTS

Design and Evaluation of the Multilevel Mesh Generation Mode for Computational Electromagnetics

Javier Moreno, María J. Algar, Iván González, and Felipe Cátedra

Electromagnetic Computing Group, Department of Computer Sciences
University of Alcalá, Alcalá de Henares, E-28871, Spain
javi.moreno@uah.es, chus.algar@uah.es, ivan.gonzalez@uah.es, felipe.catedra@uah.es

Abstract ─ This work presents a multilevel technique developed for speeding-up efficiently the mesh generation process of large and complex bodies for electromagnetic analysis. The targets are meshed by generating intermediate meshes with elements of decreasing size edge until the desired size is reached. The technique minimizes the time of meshing any given geometry and ensures a high quality mesh, as the input geometry at any level is composed of simple surfaces that can be meshed easily. The times of meshing on several geometries with and without the proposed method are compared as well as the quality statistics of the meshes obtained. The Method-of-Moments is used to evaluate the accuracy of the resulting meshes.

Index Terms ─ Applied classical electromagnetism, meshers, Method-of-Moments, Radar Cross Section.

I. INTRODUCTION

The analysis of a wide set of problems in many technological areas such as electromagnetics, fluid dynamics, and heat transfer problems requires a good geometrical description of the objects to be analyzed. In most of these cases, the geometrical model must be discretized into elements with simple shapes and suitable sizes in the mesh generation process. Many algorithms of mesh generation have been developed to solve this problem, and most of them work with triangular or quadrilateral elements for surfaces and tetrahedra or hexahedra for volumes.

Optimizing a mesh generator designed for electromagnetic analysis is the main aim of this work. The Method-of-Moments [1-2] is the technique used for verifying with simulations the resulting meshes, so body-fitted quadrilateral or hexahedral elements are generated to reduce the number of unknowns to be analyzed.

In this paper, a method developed to accelerate the mesh generation by using a multilevel strategy is described. In particular, this work has been focused on a hybrid version of the paving algorithm [3-4], which generates meshes composed of quadrangular elements, and introduces some triangular elements in particular cases [5-6]. Anyway, the proposed technique may be applied on any mesh generation algorithm, both superficial and volumetric methods.

In the second section of the paper, the initial state of the considered mesh generator is evaluated as well as the already included optimization techniques and the lacks found for developing the multilevel mode instead of another method. The multilevel meshing mode is detailed in the third section. The fourth section is focused in the time reductions and mesh quality achieved when the multilevel mode is used or not. After evaluating the influence of the technique in the generated meshes, a set of simulations with the Method-of-Moments is included to verify that the results obtained are equivalent with and without using the multilevel mode in the fifth section. The main conclusions are summarized in last section.

II. ANALYSIS OF THE PROBLEM

Because of the strong influence of the geometrical models on the accuracy of results on EM simulations, an own mesh generator that works on NURBS surfaces [7] has been developed. It provides a high level detail with simple mathematical models, and allows to use less dense meshes than plane facets models.

The mesh generator is a hybrid version of the paving algorithm [3-4] optimized for electromagnetic simulation purposes that generates meshes of quadrilateral and triangular body-fitted elements. The use of hybrid meshes instead of only triangular or quadrilateral elements [8] provides an additional degree of freedom to electromagnetic solvers, as fewer unknowns are considered for quadrilateral elements but better features are achieved when some triangular elements are inserted in particular cases. Anyway, most of the elements of the generated meshes are quads, and the triangular elements are only inserted when they provide better quality (in terms of size homogeneity and angles quadrature of the elements) than the generation of quadrilateral irregular elements [5].

The mesh generator has been parallelized by using

Submitted On: May 27, 2014
Accepted On: March 29, 2015

the MPI paradigm. To avoid using complex geometry rasterization algorithms [9], the domain decomposition [10] is simply done by distributing the surfaces among the available processors to obtain a fair sharing out of the area to be meshed in each processor. The combination of a pre-processing stage that automatically detects the topologies between the surfaces to be distributed and the insertion of the common nodes between neighbouring surfaces before starting the mesh generation ensure the electrical continuity in the final meshes [5].

To optimize the combination of the mesh generator and the simulation kernels, several pre-processing and post-processing stages have been included and validated in different benchmark experiments [11-14].

To evaluate the dependence of the time of meshing on the number of elements generated, a square plate with an area of 1 m^2 has been meshed with different size edge. Every mesh has been generated with the same CPU, an Intel Core i7 – 740QM at 1.73 GHz with 8 GB of RAM and by using only one processor. The number of elements and the times of meshing are depicted in Fig. 1 with logarithmic axes. It should be noted that the times of meshing may be greater for more complex geometries due to the extreme simplicity of the square plate; as every generated element is a perfect quadrangle, less intersections need to be solved during the mesh generation, and then most of elements are generated by perfect rows in continuous steps. However, in more complex geometries, the time of meshing may be slightly greater due to the increasing number of intersections for which boundaries must be resolved. According to the Fig. 1, the time of meshing of the plate is almost quadratically increased with the number of elements.

Although a relatively low-power computer has been used for meshing the plate, such a machine is good enough for understanding the behavior of the algorithm in any computer. The same effects appear when more powerful machines are used.

In spite of parallelizing the mesh generator, the selected method for the load distribution may cause some bottleneck in particular cases such as in the square plate example; as the geometry has an only surface, the same time of meshing is required regardless of the number of processors used, as only a processor is really working. To solve this problem, additional techniques are required to accelerate the mesh generation process.

The slowness of the mesh generation method is solved by adopting a hierarchical strategy that provides two different benefits: the bottlenecks of the parallelization are dispelled; and the mesh generation is simplified in every step.

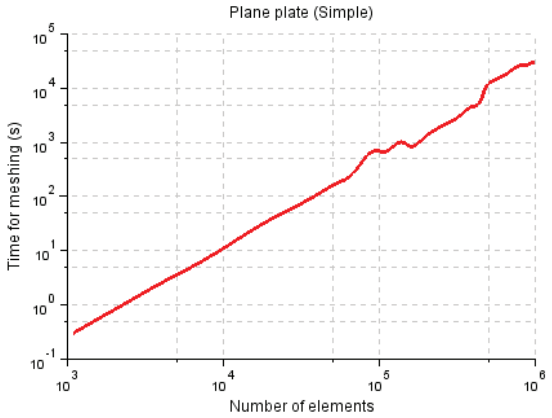

Fig. 1. Time of meshing of a square plate without the multilevel mode.

Consider a very simplified meshing algorithm as presented in Fig. 2, where the input parameters are the number of surfaces to be meshed `S`, the geometrical description in the `surfaces` array, and the total number of elements that should be generated in the whole geometry `N`. The main tasks of the mesh generation are the insertion of new elements on every `surfaces`, `InsertNewElement`, and the evaluation and resolution (if necessary) of intersections between the new element and the existing ones, `CheckIntersection`. To simplify the complexity analysis, the cost of both operations is considered as constant `K`, and the area of every surface is identical, so the same number of elements per surface is expected. With these assumptions, the overall cost associated to the meshing algorithm may be written as:

$$C = \sum_{i=0}^{S-1} \sum_{j=0}^{N/S-1} K \sum_{k=0}^{j-1} K = S \cdot \frac{\frac{N}{S} \cdot \left(\frac{N}{S} - 1 \right)}{2} K^2 , \qquad (1)$$

that can be simplified for very electrically large cases (`N>>S`), as:

$$C \approx \frac{N^2}{2 \cdot S} K^2 . \qquad (2)$$

However, reducing the computational order of the algorithm is possible by setting a good relation between `N` and `S`, so we need to change the S according to the magnitude of the problem that depends on `N`. This is the goal of the multilevel meshing mode, as the number of surfaces of the second and next levels is given by the number of elements generated in the previous levels. In particular, if the number of input surfaces of a given level is computed as:

$$S = \frac{N}{1 + 2 \cdot \log_2 N} , \qquad (3)$$

the complexity of the meshing algorithm is reduced from N^2 to $N \cdot \log_2(N)$, and the size of the new input surfaces also tends to be homogenous, which may not happen in the original geometries.

```
SimplestMeshAlgorithm(S, surfaces, N)
{
   for (i=0; i<S; i++)
   {
      for (j = 0; j < N/S; j++)
      {
         InsertNewElement(surfaces[i],j)
         for (k = 0; k < j; k++)
         {
            CheckIntersection(j, k)
         }
      }
   }
}
```

Fig. 2. Pseudo-code of a simple mesh algorithm.

More detailed information about the multilevel mode is presented in the next section.

III. MULTILEVEL TECHNIQUE

The multilevel mode consists on dividing the geometry to be meshed into as many intermediate meshes as necessary. The process is simple, and the time of meshing is widely reduced in comparison with the conventional technique whenever the intermediate meshes are generated efficiently and the number of levels is optimal.

According to the scheme of the multilevel mode shown in Fig. 3, the complete process of meshing is described as follows:

1. First, the geometry is loaded and the size edges of the mesh elements are computed for every surface.
2. Thereafter, the geometry is evaluated. The shapes of the surfaces are analyzed and those that do not meet certain criteria of simplicity are split in more simple surfaces. For example, the meshing process for a cylinder built with four cylindrical surfaces connected together is easier than the one for the built with only a closed surface; therefore, at the preprocessing stage, the closed cylinder is divided into several simpler surfaces.
3. Sometimes, especially in electromagnetic applications such as the Method-of-Moments, the electrical continuity in the meshes is one of the most essential requirements; therefore, this stage must be included. Before starting the meshing, all the neighborhood relationships between the surfaces in electrical contact are established (topologies detection). This stage may be time-consuming, because it is based on the search of common points between near surfaces.
4. An estimation of the final number of elements in the mesh is performed taking into account the size edge of the elements, the area surfaces and the topologies between them.
   The number of levels required to generate the final mesh is evaluated by considering several parameters, such as the estimated number of elements, the number of surfaces to be meshed, the difference in size between the biggest surface and the smallest one, or the shapes of the most complex surfaces. For example, when a single surface is meshed with millions of elements, several levels are recommended; however, if there are hundreds of surfaces and all of them have similar dimensions, generating the mesh in a single level is faster.
5. If the estimation of the direct meshing mode is better than the multilevel one, the meshing algorithm is applied without any additional restriction.
6. Otherwise, the optimum size edge is calculated for each level to ensure that the same number of elements per surface is achieved in every level. The ratio between the size edge in a given level to the previous one should be neither too high, as too many levels with near densities of elements would waste time; nor too low, as if the number of elements to generate per surface in some level is too large, it would be the bottleneck of the algorithm. In the first level, the original meshing algorithm is applied with the biggest size edge. In the following levels, several preprocessing steps similar to the initial ones are applied just before meshing.
   6.1. In the first step, the input mesh is preprocessed. Because of the corresponding input geometry is a mesh, all the new surfaces generated are simple, and the quality evaluation is not required. To optimize the memory resources when there are too many input elements, the complete set of information about the original geometry (defined by its NURBS parameters) is deleted after the first level, and then the global description of the input mesh is only stored (indexed coordinates for the points and group of points indexes for the elements).
   6.2. The topology detection of continuous meshes is obtained with a simpler and faster method than of NURBS geometries. The search of common points between near surfaces is not necessary for finding the neighboring relations between the input elements. To identify all the relationships between the elements in the mesh, a simple search of shared points (in terms of indexes) is performed, as the input mesh has been generated with the criterion of sharing indexes of points when there is

electrical continuity between elements. The topologies of millions of elements may be computed in a few seconds with this method.

6.3. After preprocessing the input mesh, the desired meshing algorithm is applied to every surface until the mesh of the level is finished. As the meshing method works with NURBS surfaces, only the input element that is being meshed is parametrized as a NURBS entity, and after meshing it, its description is erased.

6.4. This process is repeated until the last level is reached, as indicated in the scheme in Fig. 3 by ellipsis.

7. When the whole geometry has been meshed, the information of final mesh is gathered, and the output files are generated.

This technique together with the parallelization of the mesh algorithm minimize the time of meshing, as shown in the efficiency results section.

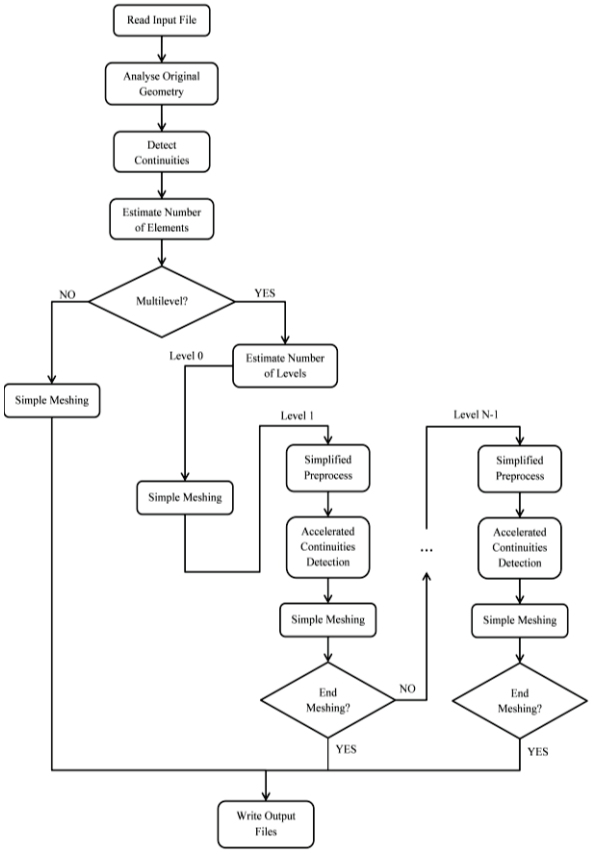

Fig. 3. Scheme for meshing with the multilevel mode.

IV. EFFICIENCY RESULTS

The results for the time of meshing of a simple and a complex geometry are presented in this section. The quality of the mesh obtained for the complex example is studied in detail.

The first example is the square plate of Section II to contrast the results obtained with and without the multilevel mode. Although this is one of the simplest cases to be analyzed, the conclusions obtained from it can be applied to any problem, as all the steps of the meshing algorithm represented in Fig. 3 are always applied. The variation on the time of each step may cause slight differences in performance on different problems. For example, the more surfaces in contact are found in a given geometry, the slower is the continuity detection step. On the other hand, another example such as a plane plate with tens of near holes may require more time for solving the intersections of confronted elements than the rest of the steps.

The times of meshing of the case of the square plate by using the multilevel mode are shown in Fig. 4.

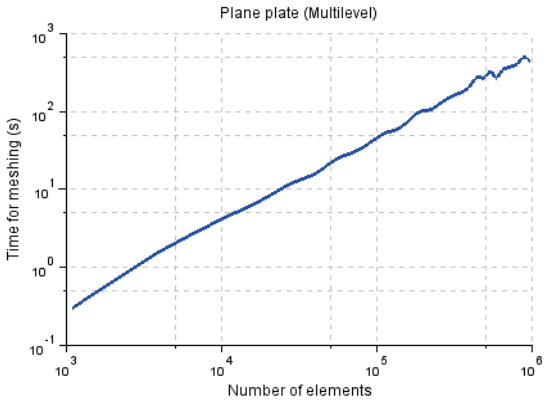

Fig. 4. Time of meshing of a square plate with the multilevel mode.

The number of elements for a given size edge by using the multilevel mode is not exactly equal to that used in the analysis without the multilevel mode, because this number depends on the input geometry of that particular level. If the size edge at a given level is not a multiple of the size edge at the next level, the size of the elements may vary slightly from the desired one, and the number of elements in the mesh may be different in consequence.

The shape of the curve with the multilevel mode in Fig. 4 is similar to the curve without the multilevel mode in Fig. 1, but the times have been minimized. Some oscillations may appear when intersections are computed, as also seen in the case of the simple meshing mode. To compare the times of meshing with and without the multilevel mode, the ratio between the times of meshing with the multilevel technique to the simple mode is represented in Fig. 5. This ratio, which we call the time relation, has a decreasing linear form, with the ratio reducing to a value of approximately 1 percent (less than 6 minutes) when we have more than half a million elements. According to the curve, the

more elements are generated, the bigger is the time reduction provided by the multilevel method.

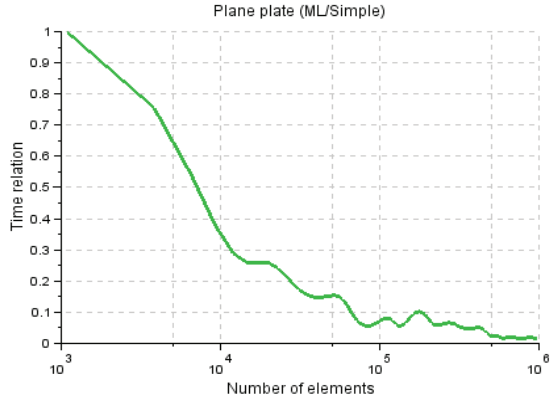

Fig. 5. Time of meshing relation of a square plate.

The proposed method for meshing is equally efficient for higher frequencies whenever a good relation between the number of levels employed and the density of elements per level is correctly distributed, as the number of elements generated per surface in each level must be large enough.

To evaluate the effect of the multilevel mode in a real geometry, the model of a vehicle has been meshed with a high density of elements by using several processors. It is composed of 363 curved surfaces with different shapes and sizes, and thus, the relative efficiency of the multilevel mode is enhanced. The original geometry and a mesh with a low density of elements are represented in Fig. 6.

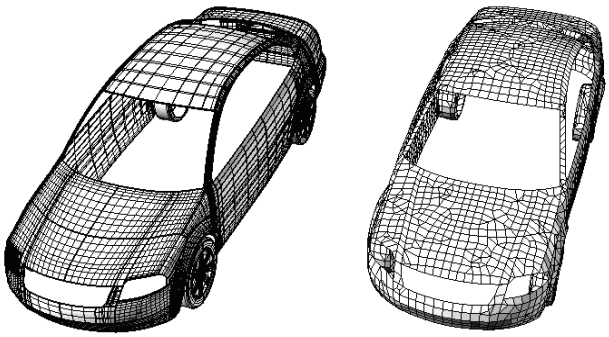

Fig. 6. Original (left) and meshed (right) vehicle.

The desired size edge for the elements is 1.5 mm, which leads to a high density mesh for the vehicle with six and a half million of elements. This case may be too large to be meshed on a personal computer; therefore, it has been meshed on a SUN X4000 Quad Opteron workstation with 32 cores at 2.4 GHz and 256 GB of RAM.

The vehicle has been meshed with the same size edge while varying the number of processors both with the simple meshing algorithm and with the multilevel mode by considering two levels.

The times of meshing in parallel of the vehicle without the multilevel mode are shown in Fig. 7 with linear axes. The more processors are used, the time of meshing is reduced. The expected shape of the curve is a decreasing logarithm. However, although the processing time is ideally decreased with the number of processors, the data distribution and synchronization between the processors require additional computation time. When multiple processors are used, the same number of surfaces per processor is distributed by trying to mesh the same area in each processor. The inconvenient of this type of load distribution may be observed when multiple large or complex surfaces are assigned to the same processor. The simplest example to explain this case is a geometry made with four identical surfaces to be meshed with thousands of elements: if four processors are used, only a quarter of the total time than with a processor is required; however, if two or three processors are used, the half of the total time is required because the processors with two surfaces assigned are the bottleneck. A similar problem may appear when several complex surfaces are assigned to the same processor. This effect is also depicted in Fig. 7, in particular when 13 and 17 processors are used.

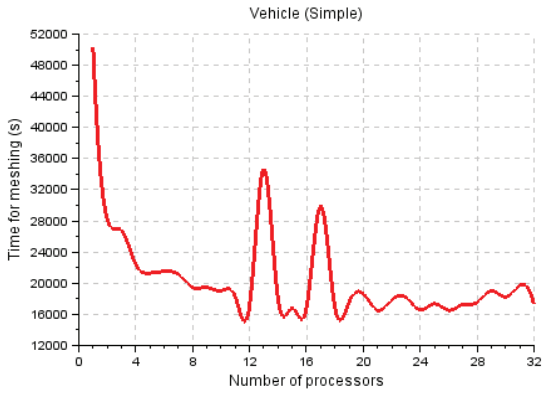

Fig. 7. Time of meshing of a vehicle without the multilevel mode and multiple processors.

If the multilevel mode is applied, the surfaces area of the input geometry is more homogeneous at every level, so these surfaces are meshed easily and the time of meshing of the whole geometry is reduced, as shown in Fig. 8. The curve of time of meshing versus the number of processors with the multilevel mode is reverted to the expected exponentially decreasing shape.

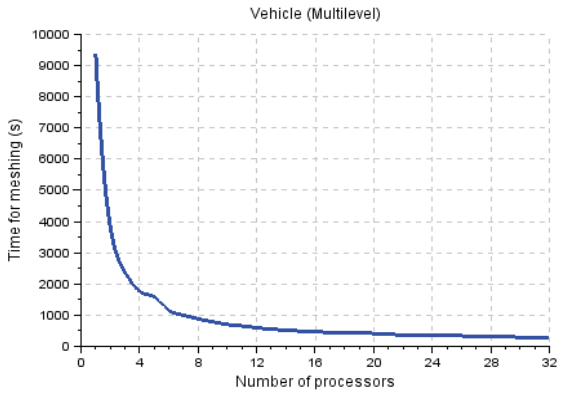

Fig. 8. Time of meshing of a vehicle with the multilevel mode and multiple processors.

The time relation between the times of meshing by using the multilevel mode to the simple mode with the number of processors (as defined previously) is shown in Fig. 9. At the beginning, the time relation decreases quickly; as the number of processors is increased, the curve tends to be stabilized around one percent.

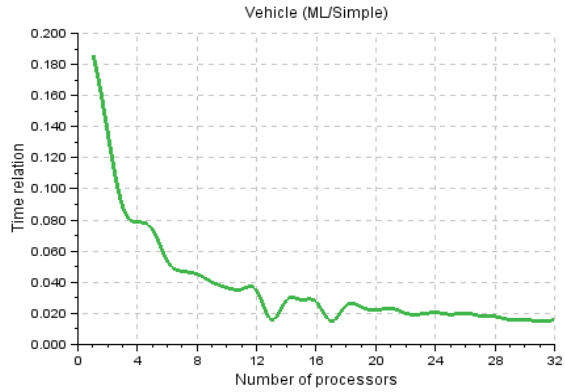

Fig. 9. Time of meshing relation of a vehicle with multiple processors.

The improvement in computation times when the multilevel mode is enabled can be explained clearly with an analysis of the areas in the input geometries.

The original geometry of the vehicle is composed of 363 surfaces with many small surfaces and a few large ones, as represented in the histogram in Fig. 10. As the histogram distribution is irregular, the mesh generation is limited by the time of meshing of the largest and the most complex surfaces, which have an area of 1.7 m^2 and require approximately 750,000 elements to be meshed.

When the first level is completely meshed, the areas of most of its elements are concentrated into the desired range of values for that level, as shown in Fig. 11. The histogram shape is not a perfect delta because of the existence of some surfaces in the original geometry smaller than the desired area elements for the first level and because of the appearance of triangular elements and imperfect quadrangles resulting from the intersections or unions performed during the mesh generation. The mean area of the elements is 7.5 cm^2 in this distribution; so 350 new elements will be generated approximately in the next level for each element in the current level.

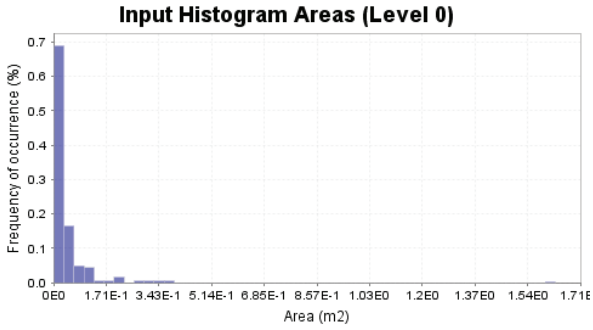

Fig. 10. Histogram of areas of the input surfaces of the vehicle.

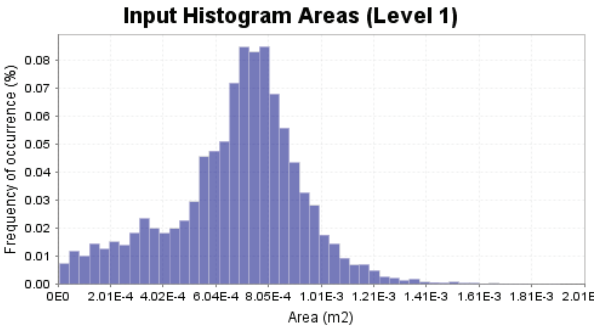

Fig. 11. Histogram of areas of the input elements of a vehicle at the second level.

After finishing the meshing process, the area of most of the elements is very close to the desired value (size edge of 1.5 mm, area of 2.25 mm^2), and the output histograms tend to be a delta function both with and without the multilevel mode, as shown in Fig. 12.

To verify that the final mesh corresponding to the multilevel mode is correct, the histograms of some statistics are studied in the following.

As the main objective of the implemented mesh generator is the generation of quadrilateral elements, verifying the quality by considering the size edge and the inner angles of these elements is required. In Fig. 13, the histogram of size edges of the elements generated is represented while comparing the results from the mesh obtained with the simple meshing algorithm to the obtained with the multilevel mode. The

distribution of lengths of the elements is better in the multilevel mesh, as it is more concentrated at the desired length of 1.5 mm.

The histogram of inner angles has a similar distribution both for the simple and the multilevel meshes, with most of the angles clustered near 90 degrees, as represented in Fig. 14.

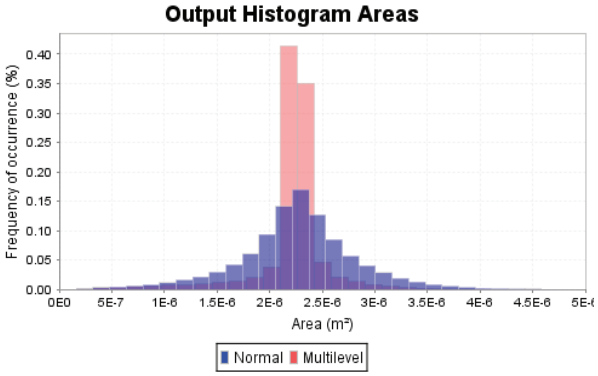

Fig. 12. Histogram of areas of the final output elements of a vehicle.

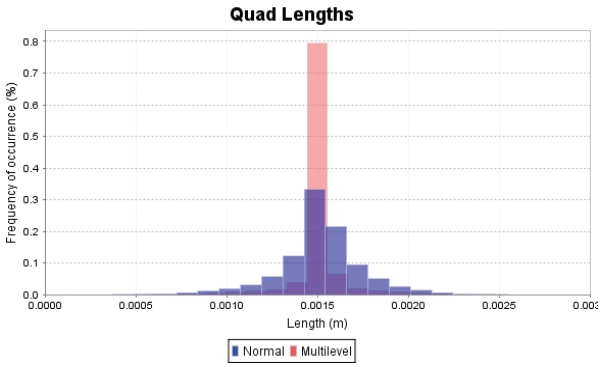

Fig. 13. Histogram of lengths of the final output quads of a vehicle.

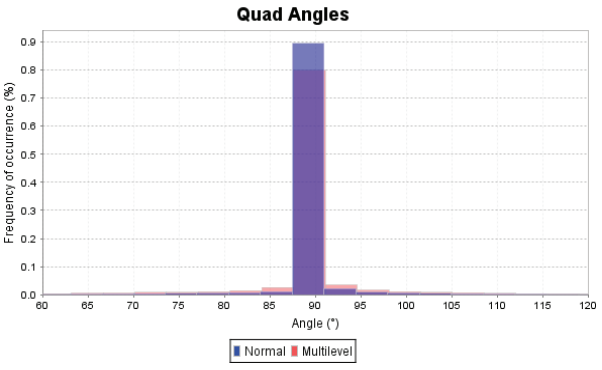

Fig. 14. Histogram of inner angles of the final output quads of a vehicle.

With these results, it is verified that most of the elements in the mesh are perfect quads.

The modified version of the paving algorithm developed inserts triangular elements only when it is the best solution or when the size of the rows is adjusted during the mesh generation. Therefore, the triangles do not satisfy the criterion of having all the borders with the same size edge or the same angle. It is likely that the triangles have two borders with the same length when they are generated for a perfect quad, and a third one that may be different because it is the union between the other two borders. This explanation is verified with the histogram shown in Fig. 15, where the size edge of the triangles is represented, and the histogram of the inner angles shown in the Fig. 16. The angles are concentrated between 30 and 90 degrees, and the size edges are clustered near 1.5 mm for the two meshing modes. The distribution is wider than of the quads histograms because of the uncontrolled generation of the triangles.

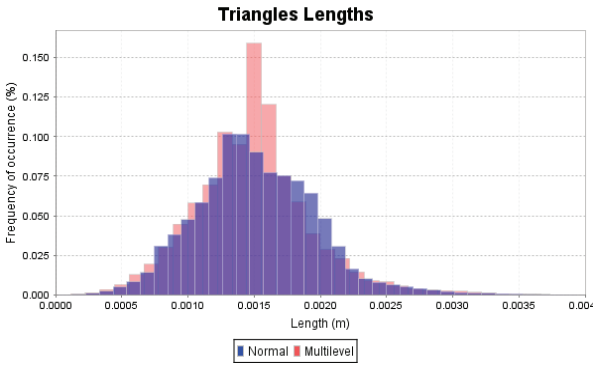

Fig. 15. Histogram of lengths of the final output triangles of a vehicle.

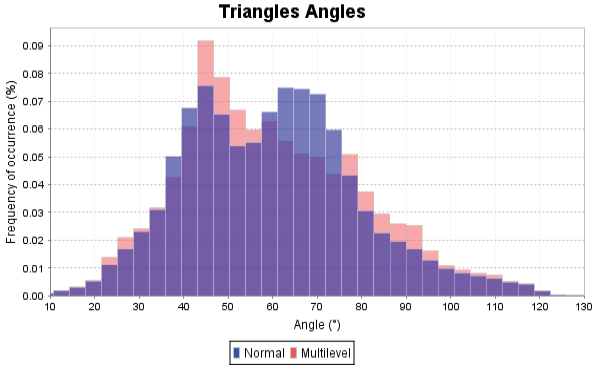

Fig. 16. Histogram of inner angles of the final output triangles of a vehicle.

The mesh of a ship with a very high density (150 million of elements) has been generated in only three

hours by using 16 processors and the multilevel mode. The ship has dimensions of 160x30x30 m (length x width x height) and an area of 9,885.52 m^2, but with an irregular distribution of surfaces. A resume of some parameters of interest for meshing that ship by using two levels with a size edge of 8.3 mm is represented in Table 1.

Table 1: Statistics of areas by levels for a ship

Level	Number of Surfaces	Mean Area (m^2)	Max. Area (m^2)	Min. Area (m^2)
0	162	64.41	934.3	0.43
1	19,482	0.51	1.41	0.00482

The parameters of the level 0 in Table 1 correspond to the original geometry of the ship, which is composed of 162 surfaces and has a factor of 2,000 between the largest and the smallest area surfaces. The area of the largest surface in the ship exceeds 900 m^2, so it requires approximately 13 million elements.

However, in the second level, the factor between the largest and the smallest area surface is reduced to 300, the surfaces are smaller and more homogeneous, and the largest surface is meshed with only 20.000 elements approximately, so the meshing is easier and faster at this level.

V. ACCURACY RESULTS

Several electromagnetic problems are solved in order to show that the new features of the mesher keep the accuracy of results. All analyses are performed with 8 processors in a SUN 2 QUAD Core Intel Xeon 2.27 GHz machine, with 12 GB of RAM, by applying the Method-of-Moments.

In every case there is a slightly difference between the meshes obtained with the traditional single level mesh algorithm and with the new one. Even though the original geometry to be meshed is the same, in the multilevel approach the input geometry at the next levels to the first one are simplified models after meshing the original one, so the mesh generation process is simpler and the final mesh is different.

The first case of the study is the parabolic reflector fed with a pyramidal horn located at its focus shown in Fig. 17. The diameter of the aperture is 5 m and the focal length is 2.5 m. When this geometry is meshed with a single level 233,692 elements are generated, whereas 212,920 elements are generated by considering two meshing levels. For both meshes, the radiation pattern is obtained at the frequency 3 GHz.

Figure 18 presents the comparison of the results by considering both meshes for the cut ϕ=0°. As the final mesh in both cases come from the same input geometry with the same size edge for elements, the gain of them are almost identical and the minimum differences are due to the fact that the simulated meshes with the Method-of-Moments are slightly different.

The geometrical model of the second case of study is the *Tabarca* ship shown in Fig. 19. The number of elements that compose the mesh when it is obtained by applying the multilevel mode is 268,943, and 267,645 when this technique is not considered.

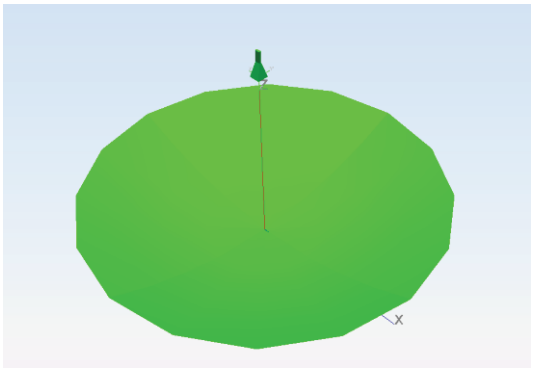

Fig. 17. Geometrical model of a reflector.

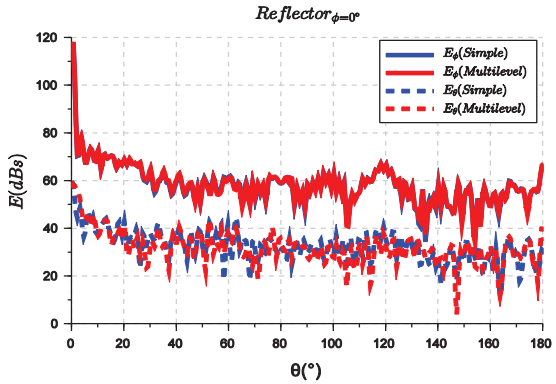

Fig. 18. Comparison between gain results of a reflector for both meshes, cut ϕ=0°.

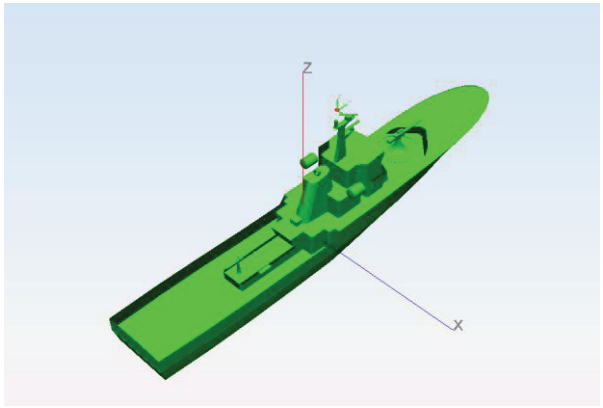

Fig. 19. Geometrical model of a ship.

A electric dipole is located at (0.0 m, 4.0 m, 11.0 m), represented in Fig. 19 with a secondary reference system on top of the ship, in order to obtain the far field at the cut ϕ=0° and a sweep from θ=0° to θ=180°at 1 GHz. Figure 20 shows the comparison of the radiation pattern by considering both meshes, and the results are almost identical again.

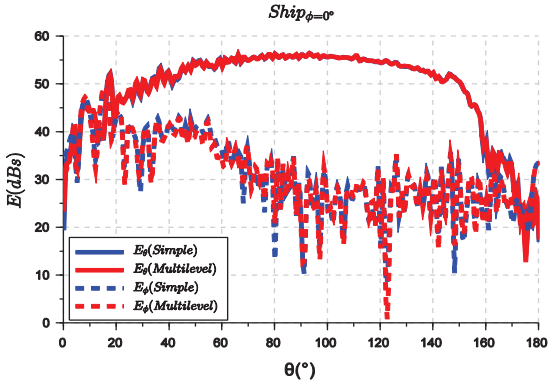

Fig. 20. Comparison between the far field results of a ship for both meshes, ϕ=0°.

Finally, the Radar Cross Section (RCS) of the airplane shown in Fig. 21 has been calculated at 2 GHz. The number of elements of the two meshes is slightly different as in the previous cases: 252,537 elements when this geometry is meshed by applying the multilevel approach are obtained, and 231,420 elements are generated without this technique.

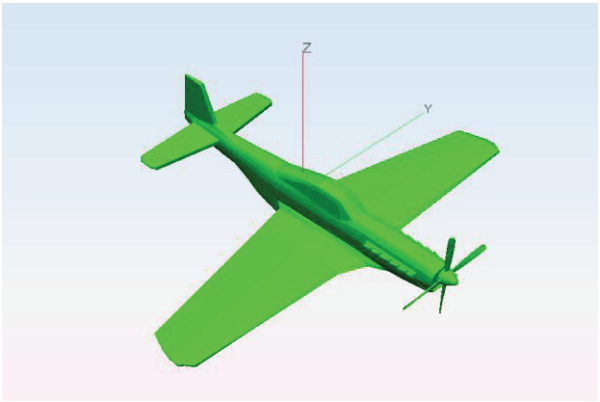

Fig. 21. Geometrical model of an airplane.

The results of the bistatic RCS for the cut ϕ=0° and a sweep from θ=0° to θ=180° are plotted in Fig. 22. Although the meshes are different, the theta-component of the electrical field, that is the strongest (co-polar) component, is almost equal. The differences between the two curves of the phi-component are not very significant because it is the weakest (cross-polar) component and therefore the dependency on the mesh is stronger, so both results are valid.

Table 2 shows the consumed time using the normal and the multilevel procedure for the test cases analyzed before.

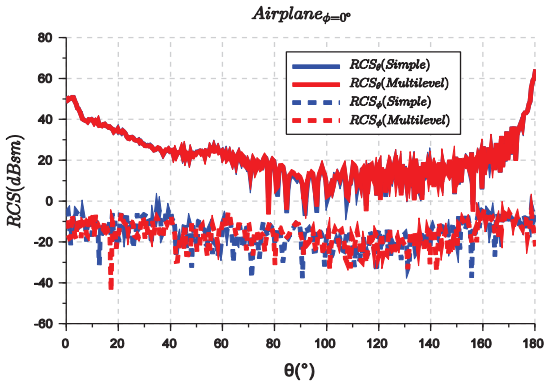

Fig. 22. Comparison between the RCS components of an airplane for both meshes, ϕ = 0°.

Table 2: Time of meshing of different cases

Case 1: Reflector	Time (s)	Number of Elements
Multilevel	66	211,616
Normal	431	233,866
Case 2: Ship	Time (s)	Number of Elements
Multilevel	58	268,889
Normal	148	267,433
Case 3: Airplane	Time (s)	Number of Elements
Multilevel	36	252,568
Normal	124	231,415

VI. CONCLUSIONS

Mesh generation is crucial for the convergence and quality of results in many numerical methods, and therefore, the meshes must be accurate and homogeneous.

There are many algorithms for mesh generation available in the literature, each one with its advantages and disadvantages. Although triangulation is one of the fastest methods, the number of unknowns to be analyzed may be excessive. Thus, in electromagnetic studies, meshes of quadrilateral elements are preferred, but the generation of these elements may be very complex.

One of the best methods of generating quadrilateral meshes is the paving algorithm, which consists of generating elements in an advancing front and ensuring that most of the elements in the mesh are perfect

quadrilaterals. However, this algorithm may be very slow for cases in which the input surfaces are extremely complex or when the number of elements to be generated is too high.

In addition to the parallelization of the meshing algorithms, the generation of meshes in progressive steps is a good solution for minimizing the times of meshing, especially in cases with a very large number of elements in the same surface, when this technique is clearly advantageous.

The computation time reduction with the multilevel mode is demonstrated in the simple case of a square plate as well as in real geometries, such as a vehicle or a ship. Furthermore, when the multilevel mode is used, the quality of the meshes is equal to or better than the ones obtained by using the conventional technique because most of the elements are close to perfect quads.

Despite of designing and validating the proposed algorithm with a superficial mesh generator, the technique may be extended to volumetric mesh generators. Due to the computational complexity of the most of volumetric mesh algorithms, especially the advancing front methods, the efficiency of this technique should be widely enhanced.

ACKNOWLEDGMENT

This work has been supported in part by the Spanish Department of Science and Technology Project TEC 2013-46587-R and by University of Alcalá Project CCG2014/EXP-089.

REFERENCES

[1] R. F. Harrington and J. L. Harrington, *Field Computation by Moment Methods*, Oxford University Press, 1996.

[2] W. C. Chew, J. Jin, E. Michielssen, and J. Song, Editors, *Fast and Efficient Algorithms in Computational Electromagnetics*, Artech House, Inc., Norwood, MA, USA, 2001.

[3] T. D. Blacker and M. B. Stephenson, "Paving: a new approach to automated quadrilateral mesh generation," *International Journal for Numerical Methods in Engineering*, vol. 32, 811-847, 1991.

[4] R. J. Cass, S. E. Benzley, R. J. Meyers, and T. D. Blacker, "Generalized 3D paving: an automated quadrilateral surface mesh generation algorithm," *International Journal for Numerical Methods in Engineering*, vol. 39, no. 9, pp. 1475-1490, May 1996.

[5] J. Moreno, M. J. Algar, I. González-Diego, and M. F. Cátedra, "Redesign and optimization of the paving algorithm applied to electromagnetic tools," *Progress In Electromagnetics Research B*, vol. 29, 409-429, 2011.

[6] J. Moreno, M. J. Algar, I. González, and F. Cátedra, "A new mesh generator optimized for electromagnetic analysis," *Proceedings of the 5th European Conference on Antennas and Propagation (EUCAP)*, vol., no., pp. 1734-1738, Rome, Italy, Apr. 2011.

[7] G. Farin, *Curves and Surfaces for Computer Aided Geometric Design*, San Diego, CA: Academic, 1988.

[8] J. F. Thompson, B. K. Soni, and N. P. Weatherill, Editors, *Handbook of Grid Generation*, Chapter 23, CRC Press, Boca Raton, Fl, 1999.

[9] U. Tremel, F. Deister, O. Hassan, and N. P. Weatherill, "Parallel generation of unstructured surface grids," *Engineering with Computers*, 2005.

[10] J. F. Thompson, B. K. Soni, and N. P. Weatherill, Editors, *Handbook of Grid Generation*, Chapter 24, CRC Press, Boca Raton, Fl, 1999.

[11] F. Cátedra, L. Lozano, I. González, E. García, and M. J. Algar, "Efficient techniques for accelerating the ray-tracing for computing the multiple bounce scattering of complex bodies modeled by flat facets," *Applied Computational Electromagnetics Society Journal*, vol. 25, pp. 395-409, May 2010.

[12] I. González, A. Tayebi, J. Gómez, C. Delgado, and F. Cátedra, "Fast analysis of a dual-band reflectarray using two different numerical approaches based on the moment method," *IEEE Trans. Antennas Propag*., vol. 61, no. 4, pp. 2333-2336, 2013.

[13] M. J. Algar, L. Lozano, J. Moreno, I. González, and F. Cátedra, "Application of asymptotic and rigorous techniques for the characterization of interferences caused by a wind turbine in its neighborhood," *International Journal of Antennas and Propagation*, vol. 2013, Article ID 173286, 10 pages, 2013.

[14] J. Moreno, I. Gonzalez, and M. F. Catedra, "Conversion of open objects to volumes to be analyzed with MoM-CFIE," *Proceedings of the 7th European Conference on Antennas and Propagation (EUCAP)*, vol., no., pp. 819-822, Gothenburg, Sweden, Apr. 2013.

Javier Moreno-Garrido received the Telecommunication Engineering degree from the Technical University of Cartagena (Spain) in 2009. He joined the Computer Sciences Department, University of Alcalá (Spain) in 2009. In 2011, he received the Master Degree in Computer Management from the University of Alcalá. In 2012, he was at the Centre National d'Études

Spatiales, in Toulouse (France), to collaborate on the analysis of antennas mounted on spatial launchers. He obtained his Ph.D. in 2013, researching and developing algorithms for the mesh generation applied to electromagnetic analysis.

María Jesús Algar-Díaz was born in Madrid, Spain in 1984. She received a M.S. (2007) in Telecommunications Engineering from Alfonso X El Sabio University, Madrid, Spain, and a Ph.D. (2011) in Telecommunications from the University of Alcalá, Madrid, Spain. She worked as an Assistant Research and Assistant Professor at the University of Alcalá in the Computer Science Department. In 2014 she has joined NEWFASANT S.L. where she is involved in research projects developing algorithms for high frequency techniques. Her current research interests include analysis of on-board antennas, radio propagation on mobile communications, ray-tracing techniques and high frequency techniques.

Iván González-Diego was born in Torrelavega, Spain, in 1971. He received the B.S. and M.S. in Telecommunications Engineering from the University of Cantabria, Spain, in 1994 and 1997, respectively, and the Ph.D. in Telecommunications Engineering from the University of Alcalá, Madrid, Spain, in 2004. He worked in the Detectability Laboratory of the National Institute of Technical Aerospace (INTA), Madrid, Spain, in RCS prediction and measurements, and as Assistant Researcher at the University of Alcalá. Since 2004, he has worked as an Assistant Professor at the University of Alcalá in the Computation Science Department, teaching concepts of database systems. He has participated in several research projects with Spanish and European companies, related to analysis of onboard antennas, radio propagation in mobile communications, and RCS computation. His research interests are in numerical methods applied to electromagnetic problems; rigorous and asymptotic techniques such as the Method-of-Moments, GTD/UTD, and PO. Investigations of numerical methods to represent complex bodies for electromagnetic techniques and computer graphics are some of his research areas.

Manuel F. Cátedra-Pérez received his M.S. and Ph.D. degrees in Telecommunications Engineering from the Polytechnic University of Madrid in 1977 and 1982 respectively. From 1976 to 1989 he was with the Radio communication and Signal Processing Department of the UPM. He has been a Professor at the University of Cantabria from 1989 to 1998. He is currently a Professor at the University of Alcalá, in Madrid, Spain. He has worked on ninety research projects, solving problems of electromagnetic compatibility in radio and telecommunication equipment, antennas, microwave components, and radar cross section and mobile communications. He has directed eighteen Ph.D. dissertations, has published seventy papers, and three books. He has given short courses and a hundred and thirty presentations in international symposia.

On an Antenna Design for 2D Scalar Near-Field Microwave Tomography

Nozhan Bayat and Puyan Mojabi

Department of Electrical and Computer Engineering
University of Manitoba, Winnipeg, MB, R3T 5V6, Canada
Bayatn@myumanitoba.ca, Puyan.Mojabi@UManitoba.ca

Abstract ― Some desired antenna specifications for performing two-dimensional (2D) transverse magnetic (TM) microwave tomography imaging are presented and discussed. These desired specifications are governed by the need to reduce the discrepancy between the 3D measurement configuration and the utilized 2D TM inversion algorithm, as well as the desire to enhance the achievable image accuracy and resolution. Driven by these specifications, an existing compact ultrawideband antenna element is modified. These modifications attempt to make the near-field distribution of this antenna more focused in the two orthogonal planes in the forward near-field zone of the antenna, while keeping its physical size relatively small and maintaining multiple frequencies of operation for this antenna. The final antenna has a physical size of 26×29×38.5 mm^3 and can operate at two different frequency bands (2.34-5.04 GHz and 8.06-13 GHz based on the $|S_{11}| \leq$ -8 dB impedance bandwidth definition). The measured near-field distribution of this antenna is presented in the imaging plane and the plane perpendicular to the imaging plane.

Index Terms ― Antenna design and measurements, microwave tomography, near-field zone.

I. INTRODUCTION

Microwave tomography (MWT) is a non-ionizing imaging technique that uses microwave scattering measurements collected outside the object of interest (OI) to create quantitative images from the relative permittivity and conductivity profiles of the OI. These two quantitative images can then be used for several applications including industrial non-destructive evaluation and biomedical diagnosis [1-3]. Creating MWT images requires performing at least two steps. In the first step, the data collection step, the OI is successively irradiated by some antennas. The resulting scattered fields emanating from the OI are then collected at some receiving antennas. The second step, usually referred to as the inversion step, attempts to reconstruct the dielectric profile of the OI from this measured scattered data by solving the associated electromagnetic inverse scattering problem. These two steps are interlinked; the antenna and hardware design need to be performed in such a way to support the assumptions made in the development of the utilized inversion algorithm. Any discrepancies between the actual measurement and computational model configurations result in the so-called modeling error [4]; thus, degrading the achievable image resolution and accuracy. The link between the inversion algorithm and the required antenna specifications for the so-called 2D TM near-field MWT systems will be discussed in Section II.

2D TM near-field MWT systems, e.g., see [5-7], are the most common form of MWT systems. In such systems, the inversion algorithm assumes a 2D imaging domain, located in the *x-y* plane, which is irradiated by an electric field perpendicular to the imaging domain, E_z. 2D TM near-field systems offer ease of system and algorithm implementation, and can also provide a reasonable balance between the number of unknowns to be reconstructed and the number of measured data points [8, Section 1.4.1]. However, the main disadvantage of these MWT systems lies in performing 2D TM inversion on microwave scattering data collected in a 3D scattering environment, thus, suffering from the modeling error. One way to mitigate these 3D effects in the 2D inversion using an appropriate antenna near-field distribution is discussed in Section II.

This paper starts with attempting to establish a relation between the assumptions made in 2D TM inversion algorithms and preferable antenna specifications for such systems. We then consider some other preferable antenna specifications that can result in further enhancement of the achievable resolution and accuracy. Based on these specifications, an existing antenna element is modified and fabricated. The measurement results and a final discussion will then be presented. Finally, we note that the materials of this paper have been taken from the M.Sc. thesis of the first author [8]. A one-page abstract of this work was also presented by the authors in [9].

II. FROM 2D TM NUMERICAL MODEL TO ANTENNA DESIGN SPECIFICATIONS

Let's consider the full-wave MWT formulation as

Submitted On: October 1, 2014
Accepted On: April 20, 2015

presented in [10]:

$$\nabla^2 \boldsymbol{E} + \omega^2 \varepsilon\mu \boldsymbol{E} + \nabla(\boldsymbol{E}.\nabla\varepsilon/\varepsilon) = -\mathrm{j}\omega\mu \boldsymbol{J}, \quad (1)$$

where ∇^2 is the Laplacian operator and ∇ represents the gradient operator. The vector $\boldsymbol{E}$ represents the vectorial electric field having three components in the Cartesian coordinate. The current source term is denoted by $\boldsymbol{J}$, and the inhomogeneous complex permittivity profile is denoted by ε. As noted in [10], the third term on the left side of (1) couples the three components of the electric field vector together. On the other hand, a 2D TM inversion algorithm assumes that the wave propagation is represented by the following scalar equation:

$$\nabla^2 E_z + \omega^2 \varepsilon\mu E_z = -\mathrm{j}\omega\mu J_z, \quad (2)$$

where E_z and J_z are the $\hat{z}$ components of $\boldsymbol{E}$ and $\boldsymbol{J}$ respectively. Any discrepancies between the full-wave formulation of (1), and the scalar wave equation of (2) can be regarded as the modelling error in the 2D TM MWT problem. To minimize this discrepancy, the $\hat{z}$ contribution of the third term on the left side of (1) needs to be as small as possible. That is,

$$\frac{\partial}{\partial z}\left(\frac{\frac{\partial\varepsilon}{\partial x}E_x+\frac{\partial\varepsilon}{\partial y}E_y+\frac{\partial\varepsilon}{\partial z}E_z}{\varepsilon}\right) \to 0. \quad (3)$$

Note that the variations of the complex permittivity profile with respect to x and y are to be imaged; thus, it cannot be assumed that $\frac{\partial\varepsilon}{\partial x}$ and $\frac{\partial\varepsilon}{\partial y}$ are very small. Also, E_z is the electric field vector used in 2D TM inversion; thus, this component cannot be assumed to be small either. Therefore, we may enforce (3) by making E_x, E_y, and $\frac{\partial\varepsilon}{\partial z}$ very small.

In practical applications, we have no control over $\frac{\partial\varepsilon}{\partial z}$. Therefore, to reduce the effect of this quantity, we speculate that if the antenna has a focused near-field distribution in a plane perpendicular to the imaging domain, the antenna will have limited solid angle view along the z direction. As a result, the variation of the permittivity profile along the z direction will be less "seen" by the antenna, thus, effectively reducing the contribution of $\frac{\partial\varepsilon}{\partial z}$. Therefore, the near-field focusing on a plane perpendicular to the imaging domain will serve as our first requirement to mitigate the 3D effects. Also, as noted earlier, we need to ensure that E_x and E_y of the antenna are sufficiently small. This will serve as our second requirement to alleviate the 3D effects.

Using numerical studies, we have recently shown that the MWT quantitative accuracy and resolution can be enhanced by using appropriate antenna incident field distributions [8,11,12]. In particular, in [8,11,12], we have shown that the use of an antenna with a focused near-field distribution can enhance the achievable resolution and accuracy from MWT. To this end, we are interested in designing an antenna whose near-field distribution is sufficiently focused within the imaging plane. Note that our first requirement was concerned with focusing in a plane perpendicular to the imaging domain; however, this new third requirement is concerned with focusing within the imaging domain. Also, note that the studies in [8,11,12] assume that we have sufficient number of antennas around the OI; otherwise, having few wide angle illuminations can be more useful than few focused illuminations.

It has also been shown that enhanced MWT reconstruction can be obtained by the use of multiple-frequency data sets [13]. To this end, we have another requirement: the antenna element should operate at multiple frequencies. Also, the bandwidth around each frequency should not be too narrow as the resonance frequencies might shift due to mutual coupling and fabrication inaccuracy [14]. In addition, in MWT, the number of required measured data points to reconstruct an OI is dependent on the OI itself. Since the OI is the unknown of the problem, the general strategy is to collect as much data as possible. Therefore, another requirement will be for the size of the antenna to be sufficiently small so as to accommodate several co-resident antennas in the data collection system. Finally, from a numerical point of view, it is desired that the antenna can be modeled in the inversion algorithm [15]. Satisfying all these criteria simultaneously may not be possible; thus, a trade-off between these different criteria is often sought.

III. DESIGN PROCEDURE

We consider an existing antenna as reported in [16]. This monopole-like slot antenna already satisfies two of the criteria: it is ultrawideband (UWB), and is reasonably small (26×29 mm^2). To accommodate the other criteria, we start by attempting to increase its near-field focusing in two orthogonal planes, one of which is the imaging plane. We then discuss how these modifications affect the other required criteria. As noted earlier, we consider near-field MWT in which the imaging domain resides in the radiating near-field zone of the antenna. Thus, we avoid using far-field terms such as "pattern", "polarization", etc. Instead, we use "field distribution", "E_x and E_y compared to E_z", etc.

The initial antenna, which is a monopole-like slot antenna as reported in [16], was modeled in the ANSYS HFSS software as shown in Fig. 1 (a). (This figure shows the initial antenna after performing some geometrical optimizations; thus, some of its dimensions differ from that reported in [16].) As can be seen in this figure, we have chosen a Cartesian coordinate system in such a way that the top surface of the antenna lies within the y-z plane. This antenna is fed by a fork-shaped coplanar waveguide structure, which is itself fed by a 50 Ω coaxial cable. Also, this antenna is linearly polarized. Although polarization of an antenna is a far-field quantity, and we are concerned with near-field MWT, it was speculated that starting with a linearly polarized antenna may correspond to a more dominant E_z as compared to E_x and

E_y, thus, helping satisfy (3).

We then considered the fact that the final antenna eventually needs to be used in an actual MWT system. Therefore, the backward radiation of the antenna needs to be minimized so as to reduce non-desired reflections from the feeding cables and the MWT enclosure. To this end, we employed the idea of using a metallic cavity that was presented in [17]. This metallic cavity, which is an open box below the monopole-like slot antenna, can be best seen in Fig. 4 [left], which shows the fabricated antenna. Having seen the fabricated cavity, Fig. 1 (b), which shows this cavity in the HFSS software, can now be better understood. However, as opposed to [17], we do not use radio frequency absorbers to fill the space between the metallic cavity and the antenna. Initially, we chose to not do that so as to increase the efficiency of the final antenna element. However, we later speculated that we might be able to use the reflection of the metallic cavity to strengthen the near-field focusing in the forward direction of the antenna. (This will be explained later in more details.) Therefore, we chose to not include any absorbers between the metallic cavity and the slot antenna. This resulted in two different issues. First, the resulting antenna lost its UWB properties. At this point, we optimized the antenna using the HFSS software so as to improve its bandwidth. This improved bandwidth did not make the antenna UWB, but resulted in an antenna supporting multiple frequencies of operation. Styrofoam was then used to hold the cavity and antenna together. This can be best seen by looking at the space below the fabricated antenna in Fig. 4 [left].

Based on a recent work on a Vivaldi antenna for radar-based microwave imaging applications [18], we then added a dielectric superstrate to the antenna so as to make its near-field distribution more focused. To this end, we chose a piece of RT/duroid 6010 that has a relative permittivity of $\varepsilon_r = 10.2$, and a loss tangent of $tan\,\delta = 0.0023$. (The standard thickness of this dielectric material is 1.9 mm. This thickness was thus chosen.) It was speculated that this dielectric material is appropriate since it has a larger permittivity as compared to the antenna FR4 substrate; thus, tending to keep the electric field distribution around itself, and helping toward near-field focusing. We also decided to choose the surface area of this superstrate to be a rectangle covering the slot of the antenna, as shown in Fig. 1 (b). To find an appropriate separation between this superstrate and the antenna, the impedance bandwidth was optimized over several slot and feeding parameters as well as the separation between the superstrate and the slot.

At this point, we noticed that the near-field distribution of the antenna toward the $\hat{x}$ direction becomes more focused due to the presence of this superstrate. Based on this observation, we decided to focus the near-field distribution of the antenna in the negative $\hat{x}$ direction using the same technique with the hope that this focused near-field distribution might be reflected back by the metallic cavity toward the forward direction of the antenna, thus, strengthening the effect of the focused near-field distribution in the $\hat{x}$ direction. To this end, we placed the same RT/duroid 6010 dielectric material between the slot and the cavity; see Fig. 4 [right] and Fig. 2. This dielectric was placed below the antenna, and directly beneath the superstrate. To find an appropriate separation between this dielectric and the slot, the impedance bandwidth of the antenna was optimized over several parameters including the separation the superstrate from the slot.

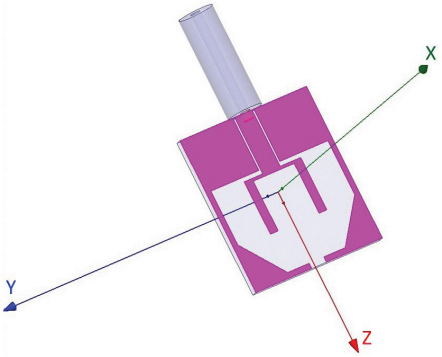

(a) Monopole-like slot antenna (see [16])

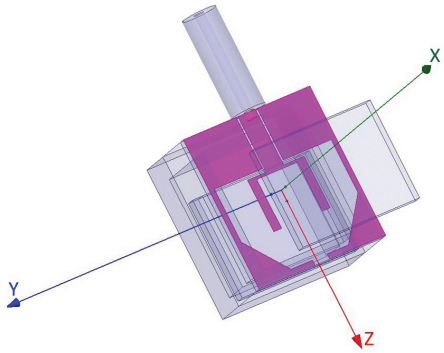

(b) Covered monopole-like slot antenna

Fig. 1. (a) Monopole-like slot antenna on a FR4 PCB with a thickness of h=1.55 mm (see [16]), and (b) covered monopole-like slot antenna. The covered monopole-like slot antenna uses a metallic cavity and a superstrate as well as a dielectric material between the slot and the metallic cavity.

This concludes our design procedure. The final antenna is shown in Fig. 4 [right]. As can be seen, the whole antenna is covered in a styrofoam box with three openings, the middle one to fit the monopole-like slot antenna, and the other two to fit the RT/duroid 6010 dielectric material. The final dimensions of the antenna are listed in Table 1. The variables in this Table refer to the notation used in Figs. 2 and 3.

Table 1: The dimensions of the final antenna element

Parameter	Value [mm]	Parameter	Value [mm]
Ws	24	Wfh	0.5
Ls	18	Wfv	1.6
L2	10.5	Wf	3.6
L3	7.7	G	0.8
L4	6.1	S	0.35
Wg	1	Ds	6.5
Lf	9.5	Hc	7.9
Sf	8.4	Hs	16.5
H	1.55	d	18.5
Thickness of superstrate	1.90	Width of superstrate	24
Length of superstrate	19		

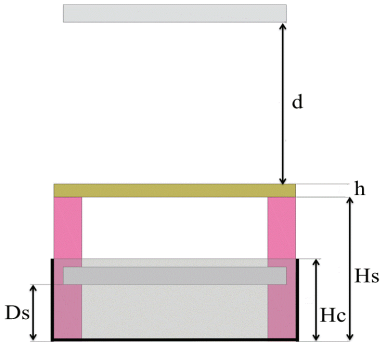

Fig. 2. Side view: brown horizontal rectangle represents the slot, two gray horizontal rectangles represent RT/duroid 6010 dielectric materials, two vertical purple rectangles represent styrofoam used for holding the cavity and the slot antenna together, and the black line represents the metallic cavity.

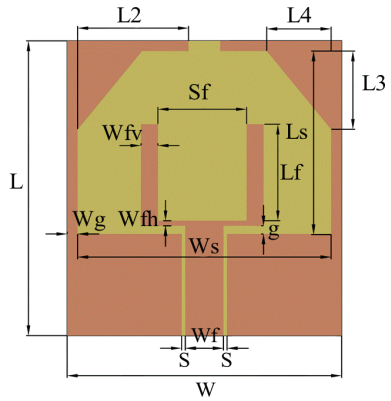

Fig. 3. Slot and feeding structure. (Note that after applying some modifications to this antenna, some of the geometrical parameters shown above are different than the original antenna presented in [16].)

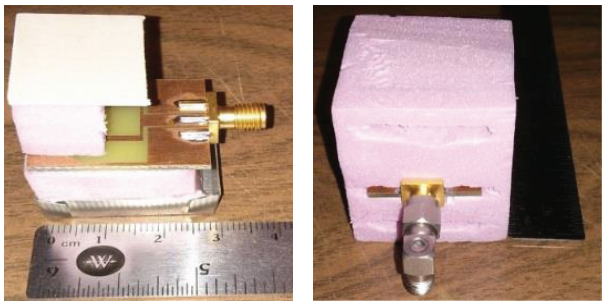

Fig. 4. [left] This demonstration model shows the superstrate on top of the slot antenna held with a piece of styrofoam, and the open metallic cavity placed beneath the antenna using a piece of styrofoam. The dielectric material placed between the cavity and the slot is not visible. [right] The final fabricated antenna is covered with the styrofoam box with three openings for the superstrate, slot antenna, and the dielectric between the slot and the cavity.

IV. SIMULATION AND MEASUREMENT RESULTS

Throughout this section, we refer to the monopole-like slot antenna with the metallic cavity and the two pieces of RT/duroid 6010 dielectric material as the "covered monopole-like slot antenna". We then refer to the same monopole-like slot antenna without the metallic cavity and without the two RT/duroid 6010 dielectric materials as the "monopole-like slot antenna". In both of these two antennas, the geometrical parameters of the slot and the fork-shaped feed are the same, and correspond to the modifications described in Section III, which has been listed in Table 1.

A. $|S_{11}|$ measurements

The simulated and measured $|S_{11}|$ of the covered monopole-like slot antenna are shown in Fig. 5. As can be seen in this figure, some of the impedance bandwidth of the original UWB monopole-like slot antenna, as reported in [16], has been sacrificed toward its evolution into the covered antenna. For MWT applications, we note that the impedance bandwidth requirement of $|S_{11}| \leq$ -10 dB might be too strict. Relaxing the definition of the impedance bandwidth to $|S_{11}| \leq$ -8 dB, the covered monopole-like slot antenna has the following impedance bandwidth of operation: 2.34 GHz to 5.04 GHz and 8.06 GHz to 13 GHz. Therefore, this covered monopole-like slot antenna can support multiple-frequency inversion. It should also be noted that these frequencies span a very wide range. Therefore, we speculate that it is more likely for this antenna to provide more independent information regarding the OI compared to another antenna that provides multiple frequencies of operation but within a limited range.

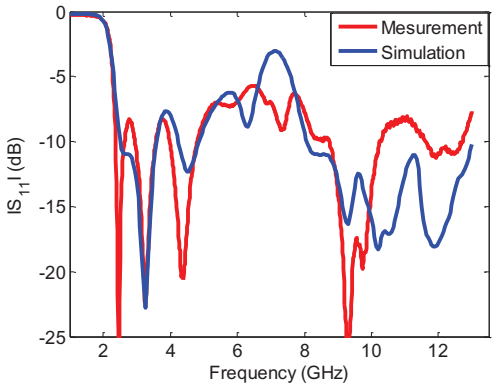

Fig. 5. Simulated and measured $|S_{11}|$ for the covered monopole-like slot antenna.

B. Near-field measurements

The near-field distributions of these two antennas were measured with a planar near-field range (PFNR). This PNFR, shown in Fig. 6, was manufactured by the Nearfield Systems Inc. (NSI). In this PNFR, the antenna under test (AUT) is stationary, and the measurement probe moves in front of the AUT to collect its near fields. The measurement probe is a WR90 open-ended waveguide probe with tapered ends. We had only access to an X-band (8.2 GHz- 12.4 GHz) probe. Thus, the near-field measurements are all performed in the X-band. In this PNFR, the probe is capable of sweeping a scan area with the size of 0.9×0.9 m^2 with a rectilinear data collection grid.

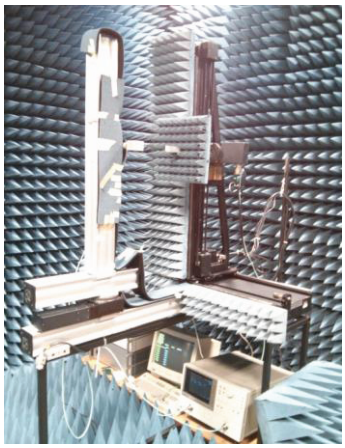

Fig. 6. Planar near-field range: the antenna backed with pyramidal absorbers is the open-ended waveguide probe. The other antenna is the covered monopole-like slot antenna under test. Absorbers have been taped on the tower that holds the antenna under test.

Based on the coordinate system shown in Fig. 1, the measurement plane will be in the *y*-*z* plane. Herein, for each of these two antennas we only show three sets of measurements, each of which corresponds to a specific distance (based on the coordinate system shown in Fig. 1, these distances are in the positive x direction from the AUT) from the slot to the measurement plane. These distances are 5 cm, 10 cm, and 14 cm. The size of the measurement plane for each of these distances is chosen in such a way that all these measurement planes will be within the same solid angle from the center of the antenna. (This solid angle represents a cone with the apex angle of 60º.) Therefore, the farther the measurement plane is from the antenna, the larger the measurement plane will be. For each of these measurement planes, we show the near-field data at three different frequencies within the X-band; namely, 8.6 GHz, 9 GHz, and 10 GHz.

For each set of measurements, the PNFR collects two components of the electric field at each point on the rectilinear grid of the measurement plane. Based on the coordinate system shown in Fig. 1, these two components of the electric fields are E_z and E_y, which are the tangential components of the electric fields on the measurement plane. It should be noted that, the PNFR is capable of performing these two electric field measurements due to its ability to rotate the probe 90º. Since the scope of this paper is 2D TM_z MWT, we only show the E_z measurements here. Also, to be able to compare different near-field measurement plots better, all the plots are normalized and the lower magnitude has been truncated to -10 dB.

As can be seen in Figs. 7 to 9, the covered monopole-like slot antenna creates a more focused beam in the measurement plane as compared to the monopole-like slot antenna. Also, a general trend that can be seen for both of these antennas is that the illumination area will become larger and larger as the distance of the probe from the antenna increases. Note that the number of near-field data points in the measurement planes corresponding to different distances are different due to the required sampling resolution in the PNFR.

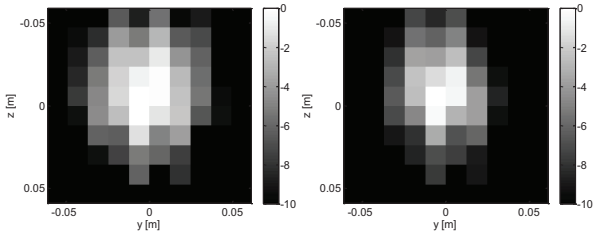

(a) 8.6 GHz (b) 8.6 GHz

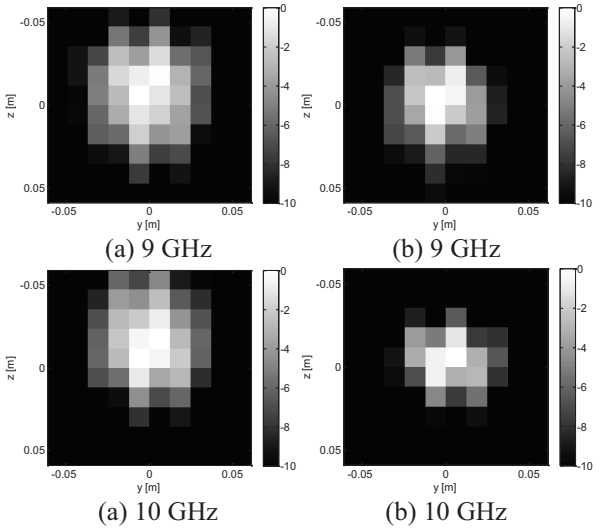

(a) 9 GHz (b) 9 GHz

(a) 10 GHz (b) 10 GHz

Fig. 7. [left] Monopole-like slot antenna, and [right] covered monopole-like slot antenna. The measured near-field E_z distribution of the antenna when the measurement plane is 5 cm away from the antenna at three different frequencies.

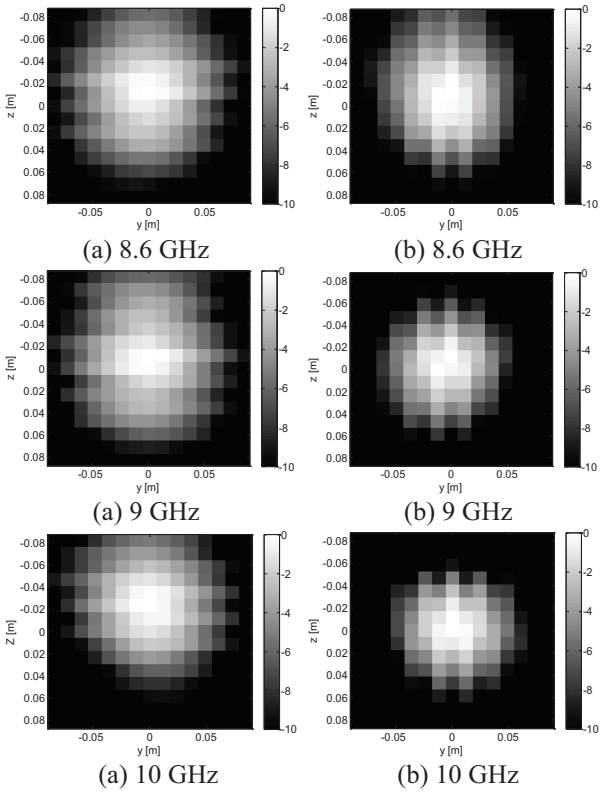

(a) 8.6 GHz (b) 8.6 GHz

(a) 9 GHz (b) 9 GHz

(a) 10 GHz (b) 10 GHz

Fig. 8. [left] Monopole-like slot antenna, and [right] covered monopole-like slot antenna. The measured near-field E_z distribution of the antenna when the measurement plane is 10 cm away from the antenna at three different frequencies.

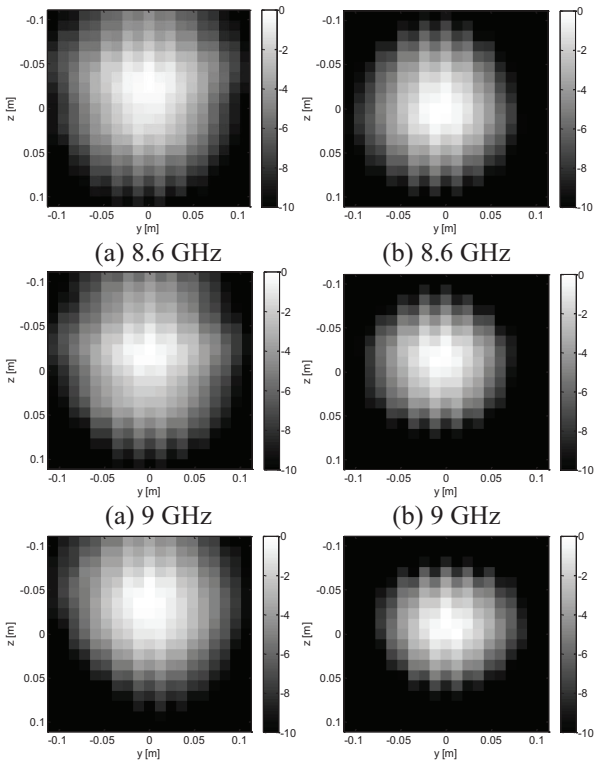

(a) 8.6 GHz (b) 8.6 GHz

(a) 9 GHz (b) 9 GHz

(a) 10 GHz (b) 10 GHz

Fig. 9. [left] Monopole-like slot antenna, and [right] covered monopole-like slot antenna. The measured near-field E_z distribution of the antenna when the measurement plane is 14 cm away from the antenna at three different frequencies.

Based on Fig. 7 to Fig. 9, we have shown that the covered monopole-like slot antenna has a more focused near-field distribution in the *y-z* plane as compared to the monopole-like slot antenna. This is important to satisfy our first requirement as noted in Section II. Now what remains is the measurement of the near-field of these two antennas in the imaging plane (*x-y* plane) for our third requirement as noted in Section II. However, this is not directly possible with the PNFR, as the PNFR is capable of performing measurements only in the *y-z* plane. Therefore, to this end, we measured the near-field data of each antenna at 23 different *y-z* planes starting from 5 cm away from the antenna to 16 cm with the step of 5 mm within the solid angle which has an apex of 60°. Having these 23 different sets of measurements, we can then extract the measurements that correspond to the points located on the *x-y* plane. However, since the spatial position of near-field data points can be different on each measurement plane, we used the *interpn* MATLAB function to interpolate these measurements into an identical sampling grid. Based on this approach, we were able to find the near-field data on the *x-y* plane. This measured near-field data at 9 GHz has been shown

in Fig. 10. As can be seen, the covered monopole-like slot antenna seems to have slightly more focused near-field beam in the *x-y* plane as compared to the monopole-like slot antenna. We note that the enhanced focusing is more clear in the measurement planes parallel to the *y-z* plane as compared to the plot in the *x-y* plane. This might be due to the fact that the chosen *x-y* plane has a smaller width (11 cm). This is in contrast to the *y-z* measurement planes whose width varies from about 11 cm to 20 cm. Note that, to obtain the near-field data over the *x-y* plane, we had to combine all these *y-z* near-field data. Therefore, the width of the resulting *x-y* near-field data will be the same as the smallest width in the *y-z* measurement planes. Also, it should be noted that the interpolation used to obtain the near-field data over the *x-y* plane might have some smoothing effects on the data, thus, not showing the focusing of the antenna sufficiently well.

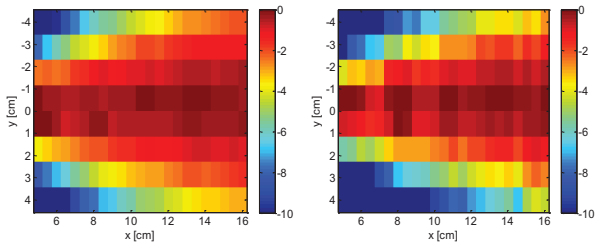

Fig. 10. Extracted measured near-field data over the *x-y* plane at 9 GHz for the two antennas: [left] monopole-like slot antenna, [right] covered monopole-like slot antenna

We also note that this extracted measured near-field data, as shown in Fig. 10, can be useful for the inversion algorithm. This can be understood by noting that inversion algorithms require the knowledge of the incident field data within the imaging domain. However, this incident field data is often not available; thus, inversion algorithms often assume some numerical model for the incident field distribution within the imaging domain, *e.g.*, a cylindrical Hankel function. Therefore, the use of such extracted near-field distributions can be helpful in reducing the modeling error. It should be noted that the fabricated antenna is a 3D structure, and therefore, cannot be entirely modeled within a 2D TM inversion algorithm.

We also investigated the near-field data over a larger *x-y* plane using the HFSS simulation. The *x-y* domain over which we chose to show this simulation is $x \in [0\ 20]$ cm and $y \in [-10\ 10]$ cm. Figures 11 and 12 show this simulation for two different frequencies: 4 GHz and 9 GHz. As expected, the covered monopole-like slot antenna creates a more focused near-field distribution in this domain. In summary, in this section, we have shown that the covered monopole-like slot antenna provides enhanced near-field focusing as compared to the monopole-like slot antenna in both the imaging plane and the plane perpendicular to the imaging plane.

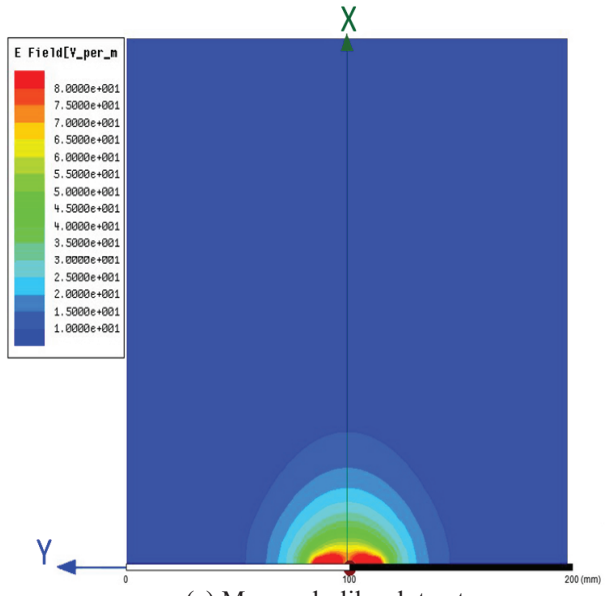

(a) Monopole-like slot antenna

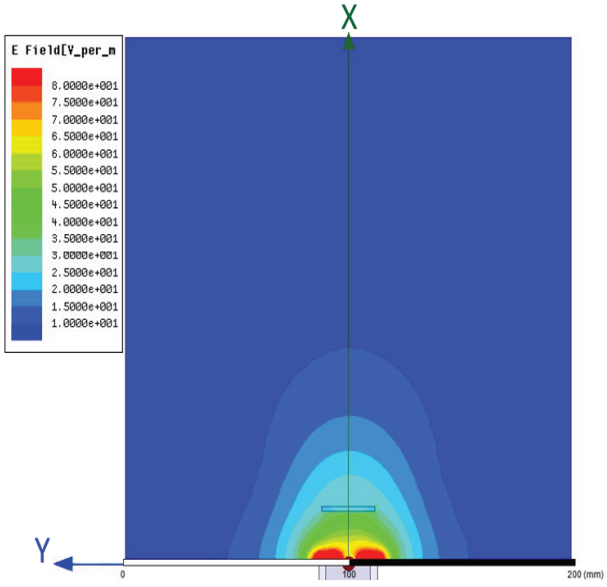

(b) Covered monopole-like slot antenna

Fig. 11. Simulated near-field data over the *x-y* plane at 4 GHz for the two antennas.

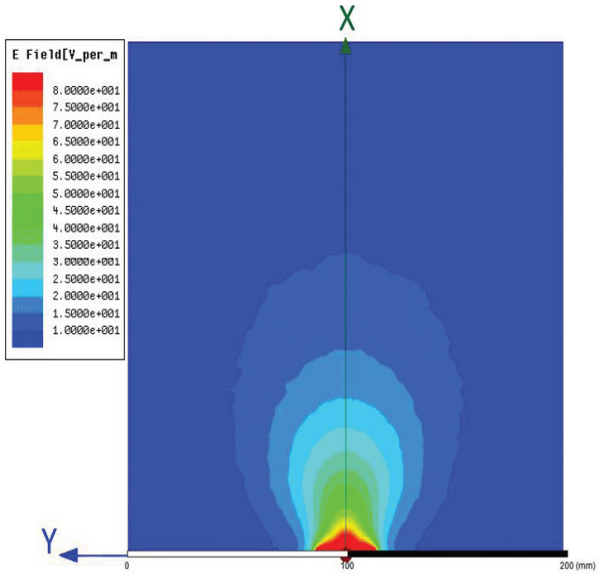

(a) Monopole-like slot antenna

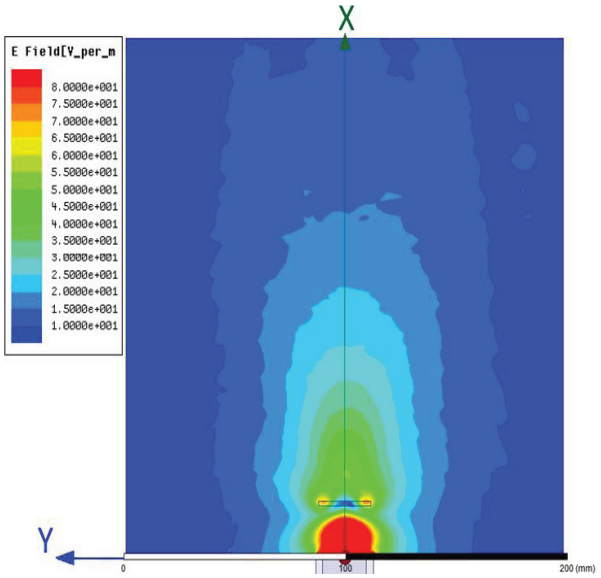

(b) Covered monopole-like slot antenna

Fig. 12. Simulated near-field data over the *x-y* plane at 9 GHz for the two antennas.

C. Electric field's vector components

The above results considered that component of the electric field that will be used for 2D TM$_z$ MWT; namely E_z component. As noted in Section II, it is desired to have E_x and E_y components of the vector electric field as small as possible in the imaging domain so as to reduce the modelling error associated with 2D TM inversion. Herein, using the HFSS simulations, we show the three components of the vector electric field on a semi-circle in front of the antenna in the *x-y* plane (imaging plane). This will be shown for two different radii, namely 7 cm and 10 cm, at two different frequencies, namely 9 GHz and 10 GHz. As can be seen in Figs. 13 and 14, the covered monopole-like slot antenna did not increase the magnitudes of E_x and E_y with respect to the desired component E_z as compared to the monopole-like slot antenna (maybe, except Fig. 14 (b)). In fact, as can be seen in these two figures, the covered antenna somehow improved the relative magnitude of E_z with respect to E_x and E_y.

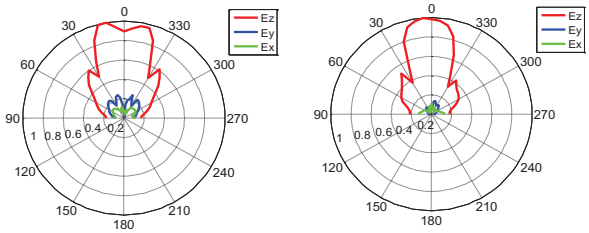

(a) Monopole-like slot (b) Covered monopole-like slot

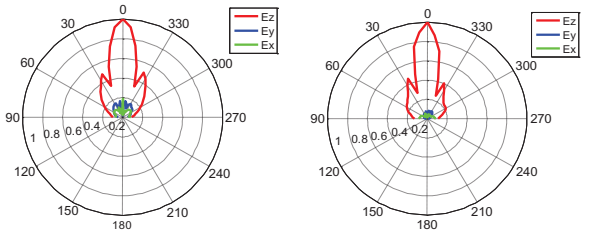

(c) Monopole-like slot (d) Covered monopole-like slot

Fig. 13. Simulation of the normalized magnitudes of the vector electric field components in the *x-y* plane at 9 GHz: (a)-(b) on a semi-circle of radius 7 cm, and (c)-(d) on a semi-circle of radius 10 cm.

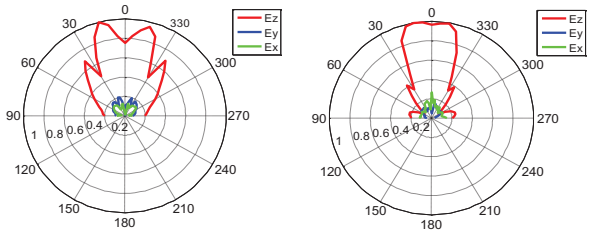

(a) Monopole-like slot (b) Covered monopole-like slot

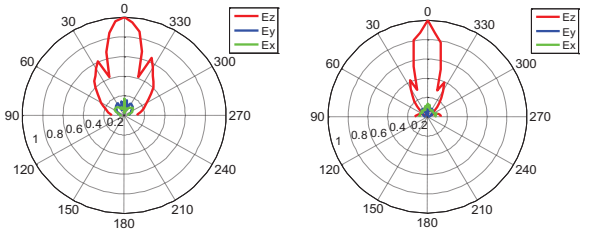

(c) Monopole-like slot (d) Covered monopole-like slot

Fig. 14. Simulation of the normalized magnitudes of the vector electric field components in the *x-y* plane (imaging plane) at 10 GHz: (a)-(b) on a semi-circle of radius 7 cm, and (c)-(d) on a semi-circle of radius 10 cm.

V. CONCLUSION

We presented and discussed some desired antenna specifications for performing 2D TM MWT so as to reduce the modeling error and enhance the achievable image accuracy. These desired specifications are near-field focusing in two orthogonal planes in the forward hemisphere of the antenna, reducing the backward radiation, making tangential electric field components on the imaging plane as small as possible, having multiple frequencies of operation and small size for the antenna, and the ability to model the antenna in the inversion algorithm. To this end, we have modified an existing antenna element. The modified antenna has been fabricated and tested in a PNFR. Through different experiments and simulations, it was shown that the modifications performed on this antenna were able to make its near-field distribution more focused, while maintaining multiple frequencies of operation, and keeping the antenna's physical size relatively small.

ACKNOWLEDGMENT

The financial support of the Natural Sciences and Engineering Research Council of Canada and the University of Manitoba's GETS is appreciated.

REFERENCES

[1] P. M. Meaney, M. W. Fanning, T. Raynolds, C. J. Fox, Q. Fang, C. A. Kogel, S. P. Poplack, and K. D. Paulsen, "Initial clinical experience with microwave breast imaging in women with normal mammography," *Acad Radiol*., 2007.

[2] S. Y. Semenov, R. H. Svenson, V. G. Posukh, A. G. Nazarov, Y. E. Sizov, A. E. Bulyshev, A. E. Souvorov, W. Chen, J. Kasell, and G. P. Tatsis, "Dielectrical spectroscopy of canine myocardium during acute ischemia and hypoxia at frequency spectrum from 100 KHz to 6 GHz," *IEEE Trans. Med. Imag*., vol. 21, no. 6, pp. 703-707, Jun. 2002.

[3] W. H. Weedon, W. C. Chew, and P. E. Mayes, "A step-frequency radar imaging system for microwave nondestructive evaluation," *Progress in Electromagnetic Research*, vol. 28, pp. 121-146, 2000.

[4] P. M. Meaney, K. D. Paulsen, J. T. Chang, M. W. Fanning, and A. Hartov, "Nonactive antenna compensation for fixed-array microwave imaging: part II-imaging results," *IEEE Trans. Med. Imag*., vol. 18, no. 6, pp. 508-518, 1999.

[5] T. Rubaek, P. M. Meaney, P. Meincke, and K. D. Paulsen, "Nonlinear microwave imaging for breast-cancer screening using Gauss-Newton's method and the CGLS inversion algorithm," *IEEE Trans. Antennas Propag.*, vol. 55, no. 8, pp. 2320-2331, Aug. 2007.

[6] S. Semenov, J. Kellam, Y. Sizov, A. Nazarov, T. Williams, B. Nair, A. Pavlovsky, V. Posukh, and M. Quinn, "Microwave tomography of extremities: 1. dedicated 2D system and physiological signatures," *Phys. Med. Biol*., vol. 56, pp. 2005-2017, 2011.

[7] C. Gilmore, P. Mojabi, A. Zakaria, M. Ostadrahimi, C. Kaye, S. Noghanian, L. Shafai, S. Pistorious, and J. LoVetri, "A wideband microwave tomography system with a novel frequency selection procedure," *IEEE Trans. Biomed. Eng*., vol. 57, no. 4, pp. 894-904, 2010.

[8] N. Bayat, *On the Role of Antennas in the Achievable Resolution and Accuracy from Near-Field Microwave Tomography*, M.Sc. thesis, University of Manitoba, Canada, 2014.

[9] N. Bayat and P. Mojabi, "An antenna element with improved near-field focusing for multiple-frequency microwave tomography applications," *IEEE APS and USNC-URSI Meeting*, Memephis, Tennessee, USA, Jul. 2014.

[10] C. Gilmore, *Towards an Improved Microwave Tomography System*, Ph.D. thesis, University of Manitoba, Canada, 2010.

[11] N. Bayat and P. Mojabi, "The effect of antenna incident field distribution on microwave tomography reconstruction," *Progress In Electromagnetics Research*, vol. 145, pp. 153-161, Mar. 2014.

[12] N. Bayat and P. Mojabi, "A mathematical framework to analyze the achievable resolution from microwave tomography," submitted, 2014.

[13] J. D. Shea, P. Kosmas, S. C. Hagness, and B. D. Van Veen "Three-dimensional microwave imaging of realistic numerical breast phantoms via a multiple-frequency inverse scattering technique," *Medical Physics*, vol. 37, no. 8, pp. 4210-4226, 2010.

[14] J. P. Stang, *A 3D Active Microwave Imaging System for Breast Cancer Screening*, Ph.D. dissertation, Duke University, Durham, USA, 2008.

[15] P. Mojabi and J. LoVetri, "A novel microwave tomography system using a rotatable conductive enclosure," *IEEE Trans. Antennas Propag*., vol. 59, no. 5, pp. 1597-1605, 2011.

[16] X. Qing and Z. N. Chen, "Compact coplanar waveguide-fed ultra-wideband monopole-like slot antenna," *Microwaves, Antennas Propagation, IET*, vol. 3, pp. 889-898, 2009.

[17] X. Qing and Z. N. Chen, "A miniaturized directional UWB antenna," *IEEE APS*, pp. 1470-147, Spokane, Washington, USA, Jul. 2011.

[18] J. Bourqui, M. Okoniewski, and E. Fear, "Balanced antipodal Vivaldi antenna with dielectric director for near-field microwave imaging," *IEEE Trans. Antennas Propag*., vol. 58, no. 7, pp. 2318-2326. Jul. 2010.

Nozhan Bayat received his M.Sc. degree in Electrical Engineering from the University of Manitoba, Canada, in 2014, where he is currently working towards the Ph.D. degree in Electrical Engineering. Bayat is a recipient of two international awards; namely, 2014 IEEE Antennas and Propagation Society (AP-S) Pre-Doctoral Research Award (awarded up to six students worldwide), and 2014 Antenna Measurement Techniques Association (AMTA) Student Travel Scholarship (awarded to one student worldwide). Bayat also received the Edward R. Toporek Graduate Fellowship in Engineering from Faculty of Engineering at the University of Manitoba in 2015. He is also a 2015 recipient of the University of Manitoba Graduate Fellowship for his doctoral studies. Bayat has also received an Outstanding Achievement Recognition Award in the Graduate Student Conference (GradCon) of the University of Manitoba's Department of Electrical and Computer Engineering in 2013.

Puyan Mojabi received his B.Sc. degree in Electrical Engineering from the University of Tehran, Iran, in 2002, M.Sc. degree in Electrical Engineering from Iran University of Science and Technology, Iran, in 2004 and Ph.D. degree in Electrical Engineering from the University of Manitoba, Canada, in 2010. He is currently an Assistant Professor with the Electrical and Computer Engineering Department at the University of Manitoba. Mojabi is a recipient of two Young Scientist Awards from the International Union of Radio Science (URSI) in 2014 (GASS) and 2015 (AT-RASC), and two student conference paper awards from the Applied Computational Electromagnetic Society (ACES) in 2007 and the Canadian National Committee of the URSI in 2008. He is also a recipient of the 2014 Excellence in Teaching Award from the Faculty of Engineering at the University of Manitoba. Mojabi is the elected Early Career Representative of URSI's Commission K. He also serves as the national representative of Commission E of the Canadian National Committee of URSI, and is also the current chair of the IEEE Winnipeg Section.

Ultra-Compact Polarization Splitter Based on Silica Liquid Crystal Photonic Crystal Fiber Coupler

Rasha A. Hussein [1,2], Mohamed F. O. Hameed [3,4], and Salah S. Obayya [3]

[1] Department of Engineering Applications of Lasers
National Institute of Laser Enhanced Sciences, Cairo University, Giza, Egypt

[2] Department of Physics, Faculty of Science
Al-Muthana University, Muthana, Iraq
rasha.lasereng@gmail.com

[3] Centre of Photonics and Smart Materials
Zewail City of Science and Technology, Sheikh Zayed District, 6th of October City, Giza, Egypt
mfarahat@zewailcity.edu.eg, sobayya@zewailcity.edu.eg

[4] Department of Mathematics and Engineering Physics, Faculty of Engineering
Mansoura University, Mansoura, 35516, Egypt

Abstract ─ An ultra-compact polarization splitter based on dual core nematic liquid crystal silica photonic crystal fiber (NLC-PCF) is proposed and analyzed. The refractive index difference between the NLC and silica material guaranties the index guiding through the reported splitter. The dual core NLC-PCF has strong polarization dependence due to the birefringence between the two polarized modes. The coupling characteristics of the proposed design are studied thoroughly using full vectorial fine difference method (FV-FDM) and the propagation analysis is performed by full vectorial finite difference beam propagation method (FVFD-BPM). The numerical results reveal that the reported splitter has short device length of 482 μm with low crosstalk better than -20 dB with wide bandwidths of 31.5 nm and 19 nm for the quasi TE and quasi TM modes, respectively. The compact coupling lengths as well as the low crosstalks over reasonable bandwidths are the main advantages of the reported dual core NLC-PCF.

Index Terms ─ Beam propagation method, finite difference method, photonic crystal fibers, polarization splitter.

I. INTRODUCTION

The high-level integration of fiber functionalities into photonic devices is the latest trend in the development of all-fiber devices. Photonic devices based on photonic crystal fibers (PCFs) have attracted a great attention recently [1]. This is due to unique design flexibilities and optical properties of PCFs that cannot be achieved by conventional optical fiber. In this regard, PCFs possess numerous unusual properties, such as, single-mode operation [2], high birefringence [3], controllable dispersion [4], and large mode area [5]. Moreover, the polarization properties of PCFs can be manipulated by thermo-optical responsive infiltration such as nematic liquid crystal (NLC) [6,7] into the air holes or hollow core. The NLC material is a thermotropic LC which undergoes phase transitions with temperature variation. The phase of the NLC material is changed from solid to LC state at the melting temperature T_M, and from LC to isotropic liquid state at the clearing temperature T_C. The nematic–isotropic transition of the E7 NLC material occurs at clearing temperature of 60°C. The LCs are anisotropic materials due to the tendency of the LC molecules to orient themselves along a preferred direction known as the director n. The optical anisotropy of the LC material is defined as $\Delta n = n_e - n_o$, where n_e, and n_o are the extraordinary, and ordinary refractive indices of the LC material, respectively. In addition, the refractive indices of the NLC material are temperature dependent [8]. Hence, the material anisotropy of the NLC can be tuned by changing the temperature. Moreover, the optical anisotropy is related to the polarization that occurs when an electric field is applied to the LC. For n_e the vibration vector of the plane polarized light is parallel to the director, while for n_o the vibration vector is perpendicular to the director. Hence, the optical properties of the NLC material can be changed by applying external fields [9].

Although PCFs are usually composed of central

Submitted On: January 20, 2015
Accepted On: May 10, 2015

defect surrounded by air holes arranged in regular lattice, the development of manufacturing technologies provides the ability to realize multicore PCFs as well [8,10,11]. In addition, the employment of dual core PCFs as wavelength division multiplexing (WDM) components [12], and polarization splitter [13] has been investigated. Polarization splitter can be used to separate a light signal into two orthogonal polarizations. Therefore, various PCF polarization splitters have been investigated [14-16]. In 2006, Florous*, et al.* [14] reported a polarization independent splitter which allows wavelength multiplexing at 1.3 μm, and 1.55 μm. Moreover, Hameed, *et al*. [15] proposed polarization splitter based on index guiding soft glass nematic liquid crystal PCF with device length of 8.227 mm. Furthermore, a polarization dependent coupling in dual core PCF selectively filled with gold wires has been investigated in [16].

In this paper, the polarization dependent coupling in dual core silica based PCF filled with NLC of type E7 is presented and investigated. The simulation results are obtained using full vectorial finite difference method (FV-FDM) [17] with absorbing perfectly matched layer (PML) boundary conditions [18,19] using stretched complex coordinates [20]. The beam propagation method (BPM) [21,22] can be utilized to study the field propagation along the axial direction. The propagation analysis of the suggested coupler is investigated by using full-vectorial finite difference beam propagation method (FVFD-BPM) [22]. The reported nematic liquid crystal PCF (NLC-PCF) polarization splitter guides light by modified total internal reflection (MTIR) technique, since the ordinary n_o and extraordinary n_e refractive indices of the E7 NLC are greater than that of silica background glass n_s. Further, the NLC-PCF polarization splitter has high tunability with the temperature or the applied electric field. The effect of structure parameters and temperature on the coupling characteristics of the suggested design is studied. The proposed design has short coupling length of 482 μm with crosstalk better than -20 dB. The reported splitter has bandwidths (BWs) of 19 nm, and 31.5 nm for the quasi transverse magnetic (TM) and quasi transverse electric (TE) modes, respectively. The suggested splitter is different than the LC soft glass PCF coupler (LC-SGPCF) [8]. The LC-SGPCF coupler of device length 6.232 mm has a soft glass background material with a small hole of radius 0.5 μm filled with LC material. Therefore, the propagation through the region occurs around the LC central hole. However, the proposed PCF splitter in this paper has a silica background with compact device length of 482 μm with low crosstalk.

Many fabrication techniques have been implemented to realize PCF such as, stack and draw method [23], drilling [24], and sol-gel casting method [25]. The most commonly used method is the stack and draw introduced by Knight, *et al*. [23]. Besides that, in [26] the authors have presented rapid preform connecting method using furnace of the fiber drawing tower. Additionally, various selective filling techniques are reported including UV glue sealing [27], arc fusion deformation [28], and capillary forces [29]. Moreover, Wang, *et al*. [30], presented flexible and reliable method for selective infiltration of PCF with the assistance of femtosecond (fs) laser micromachining. In this method, all cladding air holes are blocked with a section of conventional single mode fiber (SMF). Then a fs laser direct drilling is used to open the air holes selected to be filled. After that, materials such as the NLC can be infiltrated in these holes from the micro-machined fiber end by capillary action. Therefore, the authors believe that the suggested design can be fulfilled experimentally.

II. DESIGN CONSDIRATION AND NUMERICAL APPROACHES

Figure 1 depicts the proposed polarization splitter. The air holes are arranged in a triangular array in silica background with refractive index of 1.45. Dual identical cores are formed by filling two large central air holes with NLC material of type E7. The structure is basically an index guiding directional coupler since the ordinary n_o and extraordinary n_e refractive indices of the E7 NLC are greater than the refractive index of silica background. In addition, the suggested PCF can be placed between two electrodes [31] to control the orientation of the NLC director. All the cladding air holes have the same diameter and are arranged with hole pitch spacing of Λ = 1.25 μm. The separation between the centers of the two infiltrated cores is $\sqrt{3}\,\Lambda$. Moreover, the rotation angle of the E7 NLC director is taken as 0º, while the temperature is fixed at 25ºC. On the other hand, n_o and n_e refractive indices of the E7 material are taken as 1.5024, and 1.6970, respectively at the operating wavelength λ = 1.55 μm. The relative permittivity tensor of the E7 NLC is taken as [32]:

$$\varepsilon_r = \begin{pmatrix} n_o^2\sin^2\varphi + n_e^2\cos^2\varphi & (n_e^2 - n_o^2)\cos\phi\sin\varphi & 0 \\ (n_e^2 - n_o^2)\cos\varphi\sin\varphi & n_o^2\cos^2\varphi + n_e^2\sin^2\varphi & 0 \\ 0 & 0 & n_o^2 \end{pmatrix}, \quad (1)$$

where φ is the rotation angle of the director n of the liquid crystal molecules as shown in the inset of Fig. 1. In this case, the director n can be expressed as $\mathrm{n} = \cos\varphi\,\hat{x} + \sin\varphi\,\hat{y}$.

The suggested design supports even and odd modes for each of the two orthogonal polarization states. The coupling length (L_C) is one of the important parameters that is used to determine the minimum distance at which the power is transferred from one core to the other core. At a given wavelength, the L_C of the

directional coupler is given by:

$$L_C^{x,y} = \frac{\lambda}{2(n_{even}^{x,y} - n_{odd}^{x,y})}, \quad (2)$$

where $n_{even}^{x,y}$ and $n_{odd}^{x,y}$ are the effective indices of the even and odd modes, for x and y polarization, respectively, and λ is the operating wavelength.

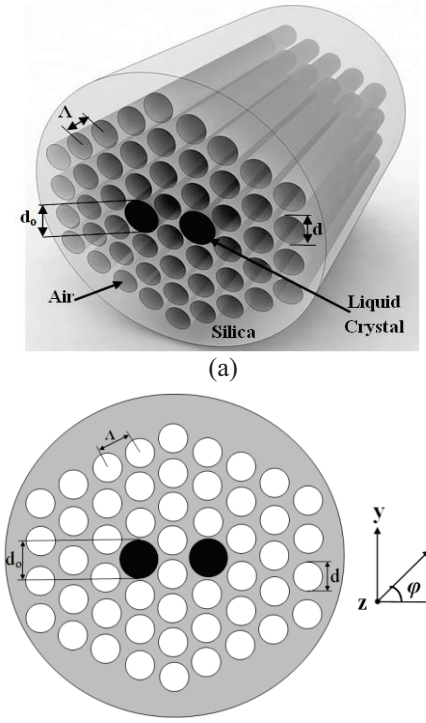

Fig. 1. The suggested dual core NLC-PCF. (a) 3D structure, (b) 2D-cross section. The director n of the NLC with rotation angle φ is shown in the right.

The effective indices of the two polarized modes are calculated as follows:

First, the vector wave equation for the magnetic field vector ***H*** can be derived from Maxwell's equation as follows:

$$\nabla \times \left(\varepsilon^{-1} \nabla \times H\right) - \omega^2 \mu_o H = 0, \quad (3)$$

where ω is the angular frequency, μ_o is the free space permeability and ε is the permittivity tensor of the waveguide material which is given by:

$$\varepsilon = \varepsilon_o \varepsilon_r = \varepsilon_o \begin{pmatrix} \varepsilon_{xx} & \varepsilon_{xy} & 0 \\ \varepsilon_{yx} & \varepsilon_{yy} & 0 \\ 0 & 0 & \varepsilon_{zz} \end{pmatrix}, \quad (4)$$

where ε_o is the free space permittivity, and ε_r is the relative permittivity tensor of the waveguide material. Using the divergence relation $\nabla \cdot H = 0$, and the vector wave equation, one can obtain the following full vector eigenvalue equation after some algebraic manipulations:

$$\begin{bmatrix} A_{xx} & A_{xy} \\ A_{yx} & A_{yy} \end{bmatrix} \begin{bmatrix} H_x \\ H_y \end{bmatrix} = \beta^2 \begin{bmatrix} H_x \\ H_y \end{bmatrix}, \quad (5)$$

where β is the propagation constant, and the differential operators A_{xx}, A_{xy}, A_{yx}, and A_{yy} can be found in [17]. Equation (5) is the full vector eigenvalue equation which describes the propagated modes for anisotropic optical waveguides. The eigenvectors are the two transverse field components H_x and H_y, and β^2 is the corresponding eigenvalue. The effective index of the propagated mode can be calculated from β such that $n_{eff} = \beta/k$, where k is the free space wave number. The differential operators can be approximated by using FDM [17] and the robust PML boundary condition [18,19] is employed at the edges of the computational window to account for the leakage property of the modes. In this investigation, the grid sizes Δx and Δy in x and y directions, respectively are taken as 0.02 μm through all simulations.

To analyze the propagation along the suggested polarization splitter, the use of full vectorial beam propagation method [19,22,33] is mandatory. In this investigation, the FVFDM-BPM [22] is used to study the propagation of the light along the propagation direction z of the suggested splitter with slowly varying envelope approximation such that $H_t = \hat{H}_t e^{-jkn_0 z}$. The following two equations can then be obtained after some algebraic manipulation:

$$\left[1 + j\Delta z \alpha B_{xx}\right] \hat{H}_x^{L+1} = \left[1 - j\Delta z (1-\alpha) B_{xx}\right] \hat{H}_x^{L} - j\Delta z B_{xy} \hat{H}_y^{L}, \quad (6)$$

$$\left[1 + j\Delta z \alpha B_{yy}\right] \hat{H}_y^{L+1} = \left[1 - j\Delta z (1-\alpha) B_{yy}\right] \hat{H}_y^{L} - j\Delta z B_{yx} \hat{H}_x^{L}, \quad (7)$$

where n_0 is the reference index required to satisfy the slowly varying envelope approach, α is a weighting factor introduced to control the stability of the finite difference scheme. Further, B_{xx}, B_{xy}, B_{yx}, and B_{yy} are the new differential operators which are approximated using the FDM [17,22]. The required magnetic fields can be calculated by solving equations (6) and (7) for the transverse magnetic fields by an iterative procedure. The magnetic fields $\hat{H}_x^{L+1}$ and $\hat{H}_y^{L+1}$ at a distance L+1 in the z-direction can be obtained from the previous magnetic fields, $\hat{H}_x^{L}$ and $\hat{H}_y^{L}$, respectively at a distance L in the z-direction. In this study, the step sizes Δx and Δy are fixed to 0.02 μm while the longitudinal step size Δz is taken as 1.0 μm. In this regard, Obayya, *et al.* [33] proves that the beam propagation analysis is unconditionally stable when the longitudinal step size $\Delta z \leq 1.0$ μm. Additionally, the reference index n_0 is taken as the effective index of the fundamental mode launched at the input waveguide. Also, α is chosen within the range, $0.5 \leq \alpha \leq 1.0$, to have unconditionally stable FVFD-BPM [22].

III. NUMERICAL RESULTS

Figure 2 shows the wavelength dependence of the coupling length of the two polarized modes at different core radii r_o, 0.625 µm, 0.65 µm, and 0.675 µm, respectively. In this study, the hole pitch Λ, cladding air hole radius r, and rotation angle are fixed to 1.25 µm, 0.525 µm, and 0º, respectively. As the wavelength increases, the modal fields will be less confined inside the NLC infiltrated cores. As a result, the distance taken by the two guided modes and hence, the coupling lengths decrease with increasing the wavelength as shown in Fig. 2. In addition, the distance between the two cores and hence, the coupling lengths decrease by increasing the core radius.

It is also noticed from Fig. 2 that the coupling length of the quasi TE mode is longer than that of the quasi TM mode at φ = 0º. At φ = 0º the permittivity tensor of the E7 material is a diagonal of $\varepsilon_r = [n_e^2, n_o^2, n_o^2]$ so $\varepsilon_{xx} = n_e^2$, and $\varepsilon_{yy} = n_o^2$. Therefore, the index contrast seen by the quasi TE modes is greater than that seen by the quasi TM modes. Hence, the quasi TE modes are more confined in the core region than the quasi TM modes. Thus, the quasi TM modes take shorter distance than the quasi TE modes to transfer from one core to the other. As a result, the coupling length of the quasi TM mode is shorter than that of the quasi TE mode. The coupling length of the quasi TE mode and quasi TM modes at the operating wavelength λ = 1.55 µm with core radius r_o = 0.675 µm are equal to 482 µm, and 241 µm, respectively.

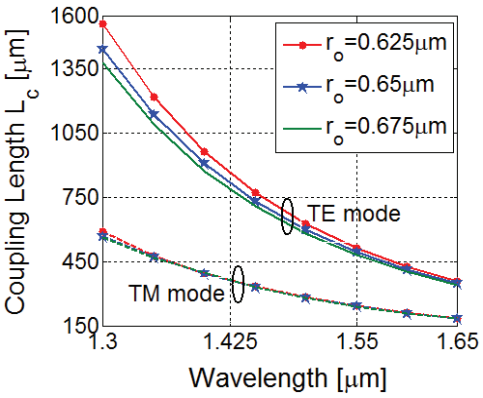

Fig. 2. Variation of the coupling length of the two polarized modes of the dual core NLC-PCF coupler with the wavelength at different core radii r_o, 0.625 µm, 0.65 µm, and 0.675 µm.

The form birefringence is defined as the ratio of the difference ($L_{CTE} - L_{CTM}$) between the coupling lengths of the quasi TE mode L_{CTE} and quasi TM modes L_{CTM} to the coupling length of the quasi TE mode L_{CTE}. The variation of the form birefringence with the wavelength at different core radii r_o, 0.625 µm, 0.65 µm, and 0.675 µm, respectively is depicted in Fig. 3. It is noted that the form birefringence decreases with increasing the core radius. As the core radius increases from 0.625 µm to 0.675 µm, the form birefringence decreases from 52.72% to 50%, respectively at the operating wavelength λ = 1.55 µm.

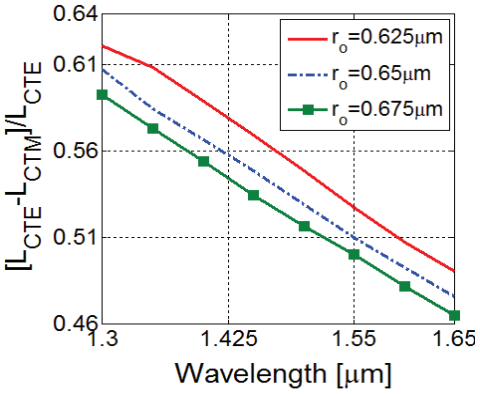

Fig. 3. Variation of the form birefringence of the dual core NLC-PCF coupler with the wavelength at different core radii r_o, 0.625 µm, 0.65 µm, and 0.675 µm.

As the ordinary n_o and extraordinary n_e refractive indices of the E7 material are temperature dependent, the effect of temperature on the coupling length of the proposed coupler is investigated. Figure 4 presents the variation of the coupling length of the two polarized modes with the temperature. In this investigation, the hole pitch Λ, core radius r_o, clad air hole radius r, rotation angle, and operating wavelength are fixed to 1.25 µm, 0.675 µm, 0.525 µm, 0º, and 1.55 µm, respectively. It is clear from this figure that the coupling length of the quasi TE mode decreases with increasing temperature while the coupling length of the quasi TM is almost constant. As the temperature increase from 15ºC to 45ºC, the n_e of the E7 material decreases from 1.7096 to 1.6604 at the operating wavelength λ = 1.55 µm. On the other hand, there is a slight change in the n_o of this material. At φ = 0º, ε_{xx} of the permittivity tensor is equal to n_e^2, and hence, it decreases with increasing temperature. As the temperature increases, the index contrast seen by the quasi TE modes decreases, while that seen by the quasi TM modes is almost constant. Thus, the quasi TE modes will be less confined inside the core regions and accordingly the distance required by the quasi TE modes to move from one core to the other decreases with increasing the temperature. As a result, the coupling length of the quasi TE modes decreases with increasing temperature while that of the quasi TM modes is almost invariant.

The influence of the cladding air hole radius on the coupling length of the two polarized modes is examined

as shown in Fig. 5. In this study, the hole pitch Λ, core radius r_o, rotation angle, and operating wavelength are taken as 1.25 µm, 0.675 µm, 0º, and 1.55 µm, respectively. As the cladding air hole radius increases, the coupling lengths of the two guided modes also increase. Since the index contrast between the core and cladding regions increases, the two modes will be more confined in the core region. In addition, the silica bridge between the two cores decreases, and hence, the coupling lengths of the two guided modes increase. As the cladding air hole radius increases from the 0.5 µm to 0.575 µm, the coupling lengths of the quasi TE modes arises from 433 µm to 653 µm while the coupling length of the quasi TM mode varies from 218 µm to 318 µm at the operating wavelength λ = 1.55 µm. It is also obvious from Fig. 5 that the suggested coupler has high birefringence, which is defined as the difference between the effective indices of the two polarized modes.

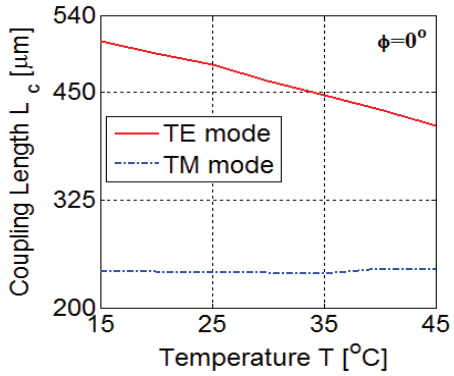

Fig. 4. Variation of the coupling length of the two polarized modes of the dual core NLC-PCF coupler with the temperature.

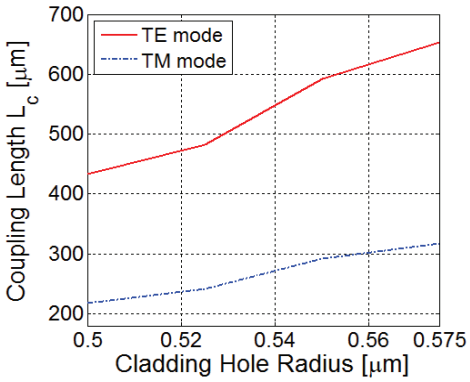

Fig. 5. Variation of the coupling length of the two polarized modes of the dual core NLC-PCF coupler with the cladding air hole radius.

The effect of the deformation of the dual infiltrated holes into elliptical cores on the performance of the proposed coupler is investigated. In this study, a_o and b_o are the elliptical hole radii in x- and y-directions, respectively as shown in the inset of Fig. 6. Figure 6 presents the wavelength dependence of the coupling length of the two polarized modes at different b_o values, 0.5 µm, 0.6 µm, 0.675 µm. In this investigation, the hole pitch Λ, cladding air hole radius r, rotation angle, and temperature are fixed to 1.25 µm, 0.525 µm, 0º, and 25ºC, respectively. However, the radius in the x-direction a_o is fixed to 0.675 µm. It is evident from this figure that the coupling length of the two guided modes increases with increasing the b_o value. Furthermore, the coupling length of the quasi TE mode is more affected by the variation of the b_o value, while the coupling length of the quasi TM mode is slightly affected. Consequently, the form birefringence increases with increasing the b_o value at constant value of a_o as shown in Fig.7. As b_o increases from 0.5 µm to 0.675 µm, the form birefringence increases from 45.41% to 50%. At φ = 0º, the index contrast seen by the quasi TE mode is greater than that seen by the quasi TM mode. Therefore, the quasi TE polarized mode will be more confined through the NLC infiltrated core. In addition, the quasi TE mode will be more affected by core deformation than the quasi TM mode. It is found that the suggested design offers short coupling lengths for the two polarized modes of 482 µm, and 241 µm for the quasi TE and quasi TM modes, respectively at the operating wavelength λ = 1.55 µm with b_o = 0.675 µm. The effect of the radius a_o in the x-direction is also studied. It is found that it has the same effect of the b_o value on the performance of the suggested coupler.

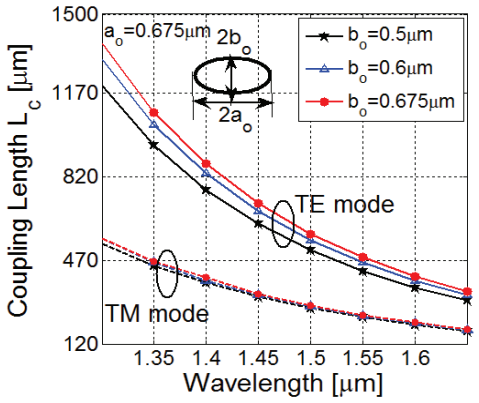

Fig. 6. Variation of the coupling length of the two polarized modes of the dual core NLC-PCF coupler with the wavelength at different b_o values while a_o is taken as 0.675 µm.

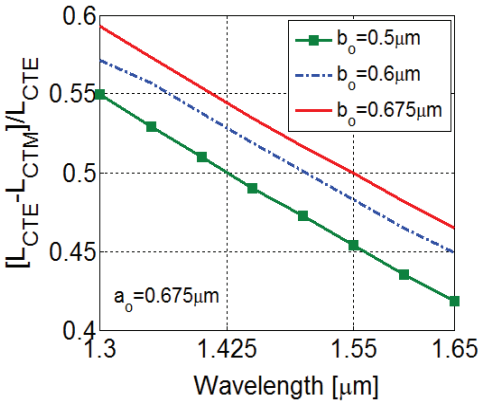

Fig. 7. Variation of the form birefringence of the dual core NLC-PCF coupler with the wavelength at different b_o values while a_o is taken as 0.675 μm.

Figure 5 also reveals that the proposed coupler is polarization dependant due to the infiltration of NLC material that increases the birefringence between the two guided modes. Thus, the reported coupler can be used as polarization splitter. The fiber coupler can split up the two polarized states if the coupling lengths of the quasi TE and quasi TM modes satisfy the coupling ratio R [34] at a given wavelength:

$$R = L_{CTE} : L_{CTM} = i : j, \tag{8}$$

where L_{CTE} and L_{CTM} are the coupling lengths of the quasi TE and TM modes, respectively. In addition, i and j are two integers of different parities. The coupler length in this case is equal to $L_f = L_{CTM} \times i/j$. Consequently, to achieve the shortest splitter, the optimal value of R should be 2. Figure 8 presents the coupling length ratio between the L_{CTE} and L_{CTM} as a function of cladding hole radius at two different hole pitches 1.21 μm and 1.25 μm, respectively. It is evident from this figure that the coupling ratio increases with increasing the cladding hole radius at specific hole pitch value. It is also shown from Fig. 8 that the coupling ratio is equal to 2 at cladding hole radius and hole pitch of 0.525 μm and 1.25 μm, respectively. The L_{CTE} and L_{CTM} calculated by the FV-FDM [17] are equal to 482 μm and 241 μm, respectively at the operating wavelength λ = 1.55 μm.

The FVFD-BPM [22] is used to confirm the polarization splitter based on the proposed coupler and to study the propagation along its axial direction. At z = 0, the fundamental components H_y and H_x of the quasi TE and quasi TM modes, respectively of silica PCF with one hole infiltrated with NLC obtained using FV-FDM [17] at λ = 1.55 μm are launched into the left core of the reported coupler. These input fields start to transfer to the right core of the coupler and the fields are completely transferred to the right core at the corresponding coupling lengths. The coupling lengths calculated by the FVFD-BPM are equal to 482 μm and 241 μm for the quasi TE and TM modes, respectively, which are the same values obtained by the FV-FDM. As the coupling ratio is equal to 2, therefore the length of the reported coupler is L_f = (482+2*241)/2 = 482 μm at which the two polarization states are separated well.

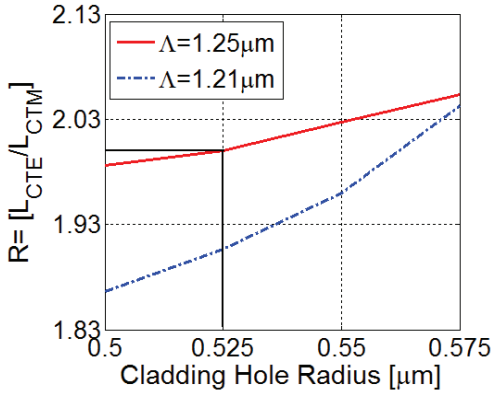

Fig. 8. Variation of the coupling length ratio for the quasi TE and quasi TM modes with the cladding hole radius at two different hole pitches 1.21 μm and 1.25 μm.

Figure 9 shows the normalized power of the two polarized modes at the operating wavelength λ = 1.55 μm in the left core of the suggested coupler. It is clear from this figure that the two polarized modes are separated well after a propagation distance equals to L_f = 482 μm. In addition, at z = 482 μm, the normalized power of the quasi TE mode in the right and left core of the proposed coupler are equal to 0.002056, and 0.9979, respectively. However, the normalized powers of the quasi TM mode in the right and left cores of the reported coupler are equal to 0.9986, and 0.001447, respectively.

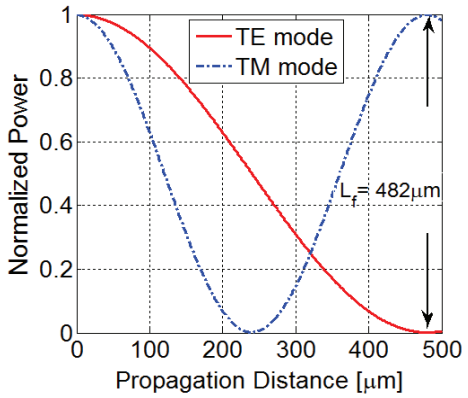

Fig. 9. Evolution of the normalized powers on the left core for the quasi TE and quasi TM modes at the operating wavelength λ=1.55 μm along the propagation direction.

The field distributions of the dominant field component H_y and H_x of the quasi TE and TM modes, respectively at the operating wavelength λ = 1.55 μm are shown in Fig. 10 at different propagation distances z, 0, 241 μm, and 482 μm. At z = 0, the input fields are launched into the left core, and as the propagation distance increases, the normalized power in the right core increases, while that in the left core decreases. When the propagation distance is equal to the coupling length of the quasi TM mode, the normalized power of the quasi TM mode is transferred to the right core. Finally, when the propagation distance is equal to the device length L_f, the two polarized modes are separated.

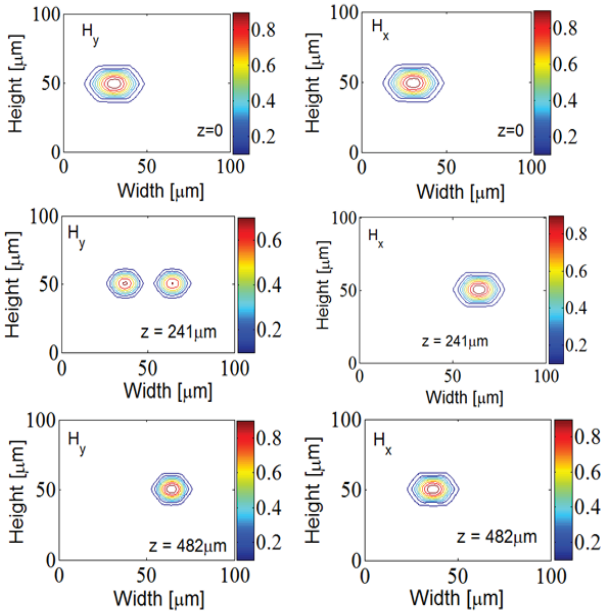

Fig. 10. Field contour patterns for H_y and H_x of the quasi TE and quasi TM modes, respectively, at z, 0, 241 μm, and 482 μm at λ=1.55 μm.

One of the important parameters in designing the fiber coupler is the crosstalk, which is defined as the amount of undesirable power remaining at the end of the suggested coupler. Figure 11 shows the crosstalk (CT) for the quasi TE and quasi TM modes around the operating wavelength λ = 1.55 μm. The crosstalk in decibel of the wanted quasi TE mode at the right core of the reported coupler is given by:

$$CT_{TE} = 10\log_{10}\left(\frac{P_{uTM}}{P_{dTE}}\right), \quad (9)$$

where P_{dTE} and P_{uTM} are the normalized powers of the desired quasi TE and undesired quasi TM modes, respectively. However, the crosstalk of the desired quasi TM mode at the left core of the proposed coupler is defined as:

$$CT_{TM} = 10\log_{10}\left(\frac{P_{uTE}}{P_{dTM}}\right), \quad (10)$$

where P_{dTE} and P_{uTM} are the normalized powers of the desired quasi TE and undesired quasi TM modes, respectively at the left core.

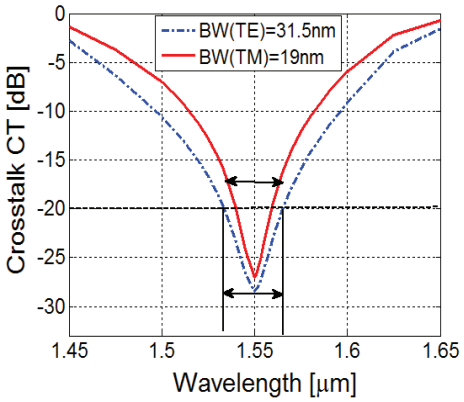

Fig. 11. Variation of crosstalk of the quasi TE and quasi TM modes of the dual core NLC-PCF coupler around the operating wavelength λ=1.55 μm.

It is clear from Fig. 11 that the reported splitter has bandwidths of 31.5 nm, and 19 nm for the quasi TE and quasi TM modes, respectively at which the crosstalks are better than -20 dB. Consequently, the reported polarization splitter is less affected by the perturbation introduced during the manufacturing process due to the low level crosstalks with wide ranges of wavelength. The suggested splitter has BWs much greater than those reported in [14] and [35]. In [14], the BW is 2.0 nm around the operating wavelength λ = 1.55 μm, while in [35], the BW is 2.7 nm. Moreover, the proposed splitter is much shorter than those reported in [14] and [35] of lengths 15.4 mm and 9.08 mm, respectively. In addition, the dual core NLC-PCF splitter has wavelength range wider than the splitter suggested by Chen, *et al.* [34] of BW = 25.4 nm for the quasi TE mode around λ = 1.55 μm. On the other hand, the splitter reported in [34] has longer length of 10.69 mm than the suggested splitter. This is due to our proposed design is based on NLC core which is a birefringent material so the birefringence between the quasi TE and quasi TM modes is large as shown in Fig. 2. Hence, the quasi TE and quasi TM modes can be easily separated in a compact length. However, the reported design in the literature [34] is based on small birefringent PCF. Therefore, the coupling length [34] is greater than our design since the coupling length is inversely proportional to the birefringence as revealed from equation (2). Further, the proposed splitter is shorter than the soft glass NLC-PCF splitter reported by

Hameed, *et al.* [15] with 8.227 mm device length. Also, in [8], the authors reported soft glass PCF with dual NLC core with 6.232 mm length which is longer than the suggested splitter. Hence, the dual core NLC-PCF splitter has shorter coupling length than those reported in [8,14,15,34,35]. The proposed structure is compact in size and easy to fabricate, making it promising for miniaturized communication devices.

It should be noted that Hu and Whinnery [36] have measured the scattering losses of the bulk NLC of around 15 to 40 dB/cm. However, the scattering losses through the NLC can be decreased to 1-3 dB/cm by filling the LC into small capillaries with inner diameters less than 8 μm as reported by Green and Madden [37]. Scattering losses of 1.5 to 2.4 dB/cm [37] have been calculated along silica fiber length of 30 cm. However, the suggested NLC-PCF of device length 482 μm has two large central holes of diameter 1.35 μm filled with NLC. Therefore, low scattering losses can be obtained for our compact design.

IV. CONCLUSION

A polarization splitter based on dual core NLC-PCF coupler has been introduced and analyzed. The polarization dependent coupling is enhanced by introducing high birefringent NLC material in the two cores. The advantages of the reported splitter are the compact coupling lengths, as well as the low crosstalks over reasonable bandwidths. The suggested design has short device length of 482 μm with a crosstalk better than – 25 dB with bandwidths of 31.5 nm and 19 nm for the quasi TE and quasi TM modes, respectively.

REFERENCES

[1] K. J. Lee, K. S. Hong, H. C. Park, and B. Y. Kim, "Polarization coupling in a highly birefringent photonic crystal fiber by torsional acoustic wave," *Opt. Express*, vol. 16, no. 7, pp. 4631-4638, 2008.

[2] T. A. Birks, J. C. Knight, and P. St. J. Russell, "Endlessly single-mode photonic crystal fiber," *Opt. Lett*, vol. 22, no. 13, pp. 961-963, 1997.

[3] T. P. Hansen, J. Broeng, S. E. B. Libori, E. Knudsen, A. Bjarklev, J. R. Jensen, and H. Simonsen, "Highly birefringent index-guiding photonic crystal fibers," *IEEE Photon. Technol. Lett*., vol. 13, no. 6, 2001.

[4] F. Shi, Y. Wu, M. Li, Y. Zhao, and L. Zhao, "Highly birefringent two-mode photonic crystal fibers with near-zero flattened dispersion," *IEEE Photonics Journal*, vol. 3, no. 6, 2011.

[5] M. Napierała, T. Nasiłowski, E. Pawlik, F. Berghmans, J. Wójcik, and H. Thienpont, "Extremely large-mode-area photonic crystal fiber with low bending loss," *Opt. Express*, vol. 18, no. 15, pp. 15408-15418, 2010.

[6] G. Ren, P. Shum, J. Hu, X. Yu, and Y. Gong, "Study of polarization-dependent bandgap formation in liquid crystal filled photonic crystal fibers," *IEEE Photonics Technology Letters*, vol. 20, no. 8, 2008.

[7] M. F. O. Hameed, S. S. A. Obayya, and H. A. El-Mikati, "Highly nonlinear birefringent soft glass photonic crystal fiber with liquid crystal core," *IEEE Photonics Technology Letters*, vol. 23 no. 20, pp. 1478-1480, 2011.

[8] M. F. O. Hameed and S. S. A. Obayya, "Coupling characteristics of dual liquid crystal core soft glass photonic crystal fiber," *IEEE J. Quantum Electron*., vol. 47, no. 10, pp. 1283-1290, 2011.

[9] V. A. Tolmachev, T. S. Perova, S. A. Grudinkin, V. A. Melnikov, and E. V. Astrova, "Electrotunable in-plane one-dimensional photonic structure based on silicon and liquid crystal," *Appl. Phys. Lett*., vol. 90, 011908, 2007.

[10] Z. Zhang, Y. Shi, B. Bian, and J. Lu, "Resonance-related coupling of symmetric dual-core hybrid photonic crystal fibers," *IEEE Photon. Technol. Lett*., vol. 21, no. 8, pp. 525-527, 2009.

[11] M. F. O. Hameed, S. S. A. Obayya, K. Al Begain, A. M. Nasr, and M. I. Abo ElMaaty, "Coupling characteristics of a soft glass nematic liquid crystal photonic crystal fiber coupler," *IET Optoelectronics*, vol. 3, no. 6, pp. 264-273, 2009.

[12] M. F. O. Hameed, S. S. A. Obayya, and R. J. Wiltshire, "Multiplexer–demultiplexer based on nematic liquid crystal photonic crystal fiber coupler," *J. Opt. Quantum Electron.*, vol. 41, no. 4, pp. 315-326, 2009.

[13] L. Zhang and C. Yang, "Polarization splitter based on photonic crystal fibers," *Opt. Express*, vol. 11, no. 9, pp. 1015-1020, 2003.

[14] N. J. Florous, K. Saitoh, and M. Koshiba, "Synthesis of polarization independent splitters based on highly birefringent dual-core photonic crystal fiber platforms," *IEEE Photon. Technol. Lett*., vol. 18, no. 11, pp. 1231-1233, 2006.

[15] M. F. O. Hameed and S. S. A. Obayya, "Polarization splitter based on soft glass nematic liquid crystal photonic crystal fiber," *IEEE Photon. J*., vol. 1, no. 6, pp. 265-276, 2009.

[16] P. Li and J. Zhao, "Polarization-dependent coupling in gold-filled dual-core photonic crystal fibers," *Opt. Express*, vol. 21, no. 5, pp. 5232-5238, 2013.

[17] A. B. Fallahkhair, K. S. Li, and T. E. Murphy, "Vector finite difference mode solver for anisotropic dielectric waveguides," *J. Lightwave Technol*., vol. 26, no. 11, pp. 1423-1431, 2008.

[18] W. C. Chew and W. H. Weedon, "A 3D perfectly matched medium from modified Maxwell's

equations with stretched coordinates," *Microwave Optical Tech. Letters*, vol. 7, pp. 590-604, 1994.

[19] S. Obayya, *Computational Photonics*, John Wiley & Sons, 2011.

[20] W. C. Chew, J. M. Jin, and E. Michielssen, "Complex coordinate stretching as a generalized absorbing boundary condition," *Microwave and Opt. Technol. Lett*., vol. 15, no. 6, pp. 363-369, 1997.

[21] M. Rajarajan, S. S. A. Obayya, B. M. A. Rahman, K. T. V. Grattan, and H. A. El-Mikali, "Characterization of low-loss waveguide bends with offset-optimization for compact photonic integrated circuits," *Optoelectronics, IEE Proceedings*, vol. 147, no. 6, pp. 382-388, 2000.

[22] W. P. Huang and C. L. Xu, "Simulation of three-dimensional optical waveguides by a full-vector beam propagation method," *IEEE J. Quantum Electron.*, vol. 29, no. 10, pp. 2639-2649, 1993.

[23] J. C. Knight, T. A. Birks, P. St. J. Russell, and D. M. Atkin, "All-silica single-mode optical fiber with photonic crystal cladding," *Optics Letters*, vol. 21, pp. 1547-1549, 1996.

[24] A. Mori, K. Shikano, K. Enbutsu, K. Oikawa, K. Naganuma, M. Kato, and S. Aozasa, "1.5μm band zero-dispersion shifted tellurite photonic crystal fibre with a nonlinear coefficient of 675 $W^{-1}km^{-1}$," *The 30th Eur. Conf. Optical Commun*. *Conf*., th. 3.3.6, 2004.

[25] H. El Hamzaoui, L. Bigot, G. Bouwmans, I. Razdobreev, M. Bouazaoui, and B. Capoen, "From molecular precursors in solution to microstructured optical fiber: a sol-gel polymeric route," *Optical Materials Express*, vol. 1, pp. 234-242, 2011.

[26] D. M. Chow, S. R. Sandoghchi, and F. R. M. Adikan, "Fabrication of photonic crystal fibers," *IEEE 3rd International Conference on Photonics*, 227-230, 2012.

[27] B. T. Kuhlmey, B. J. Eggleton, and D. K. C. Wu, "Fluid-filled solid-core photonic bandgap fibers," *J. Lightwave Technol*., vol. 27, no. 11, pp. 1617-1630, 2009.

[28] L. Xiao, W. Jin, M. S. Demokan, H. L. Ho, Y. L. Hoo, and C. L. Zhao, "Fabrication of selective injection microstructured optical fibers with a conventional fusion splicer," *Opt. Express*, vol. 13, no. 22, pp. 9014-9022, 2005.

[29] Y. Y. Huang, Y. Xu, and A. Yariv, "Fabrication of functional microstructured optical fibers through a selective filling technique," *Appl. Phys. Lett*., vol. 85, no. 22, pp. 5182-5184, 2004.

[30] Y. Wang, C. R. Liao, and D. N. Wang, "Femtosecond laser-assisted selective infiltration of microstructured optical fibers," *Opt. Express*, vol. 18, no. 17, pp. 18056-18060, 2010.

[31] M. W. Haakestad, T. T. Alkeskjold, M. D. Nielsen, L. Scolari, J. Riishede, H. E. Engan, and A. Bjarklev, "Electrically tunable photonic bandgap guidance in a liquid-crystal-filled photonic crystal fiber," *IEEE Photon. Technol. Lett*., vol. 17, no. 4, 2005.

[32] G. Ren, P. Shum, X. Yu, J. Hu, G. Wang, and Y. Gong, "Polarization dependent guiding in liquid crystal filled photonic crystal fibers," *Opt. Commun.*, vol. 281, no. 6, pp. 1598-1606, 2008.

[33] S. S. A. Obayya, B. M. A. Rahman, and H. A. El-Mikati, "New full-vectorial numerically efficient propagation algorithm based on the finite element method," *J. Lightwave Technol.*, vol. 18, no. 3, 2000.

[34] M. Y. Chen and J. Zhou, "Polarization-independent splitter based on all-solid silica-based photonic-crystal fibers," *J. Lightwave Technol*., vol. 24, no. 12, pp. 5082-5086, 2006.

[35] N. Florous, K. Saitoh, and M. Koshiba, "A novel approach for designing photonic crystal fiber splitters with polarization-independent propagation characteristics," *Opt. Express*, vol. 13, no. 19, pp. 7365-7373, 2005.

[36] C. Hu and J. R. Whinnery, "Losses of a nematic liquid-crystal optical waveguide," *J. Opt. Soc. Am.*, vol. 64, pp. 1424-1432, 1974.

[37] M. Green and S. J. Madden, "Low loss nematic liquid crystal cored fiber waveguides," *Appl. Opt.*, vol. 28, pp. 5202-5203, 1989.

Fast and Accurate Electric Field Estimation from a Single Ray Tracing Simulation

Juan Pascual-García, José-María Molina-Garcia-Pardo, María-Teresa Martínez-Inglés, José-Víctor Rodríguez, and Leandro Juan-Llácer

Universidad Politécnica de Cartagena (UPCT)
Departamento de Tecnologías de la Información y las Comunicaciones
Antiguo Cuartel de Antigones, Plaza del Hospital, 1, 30202 Cartagena (Murcia), Spain
{juan.pascual, josemaria.molina, mteresa.martinez, jvictor.rodriguez, leandro.juan}@upct.es

Abstract ─ In this work, an efficient field estimation technique is developed. This technique uses a single simulation of a ray tracing tool, at one spatial point at one frequency, to compute the field in the vicinity of the simulated point throughout a complete frequency range. The developed technique is a two-step procedure. Firstly, it operates over the images and field contributions generated by the ray tracing tool at the simulated receiver point to obtain an appropriate set of field contributions for each new receiver point. Secondly, once the new set of images and contributions at one frequency is obtained, a very simple extrapolation procedure is applied to obtain the electric field throughout a frequency range. The whole technique is computationally very efficient and it is also accurate, as the measurements comparison shows.

Index Terms ─ mm-W band, radio channel characterization, ray tracing, wave propagation prediction.

I. INTRODUCTION

Present and future wireless communication systems require accurate and fast radio channel characterization techniques to achieve a successful design and deployment. Ray-optical propagation techniques are one of the most precise approaches to estimate the received electric field in a known environment [1-3]. These techniques include "brute force" ray tracing, also called ray launching, and ray tracing based on image theory.

The main drawback of these techniques is the high computational cost which, consequently, implies a slow channel prediction. Therefore, several efforts have been made to reduce the simulation time. Most of these methods are based on the analysis of the topological relations between the transmitter position, the objects in the environment, and the receiver position. The relations analysis can be used to establish those objects that yield significant propagation paths, reducing in that way the complexity of the field prediction problem. This idea was exploited in [4], where the visibility tree concept was introduced. Subsequently, this concept was improved in other works. In [5], a sweep line algorithm was developed in order to efficiently obtain the visibility tree. In [6], the visibility tree mechanism was improved in order to construct the tree and find the paths at the same time. The main disadvantage of the visibility tree is the dependence on the transmitter and receiver positions. If the receiver changes its position the tree must be recalculated.

Other works used the topological information without applying the visibility tree concept. In [7], the topological information of the environment, which is independent of the transmitter and receiver, was analyzed to compute the relation between walls only once; this information can be used to estimate the wave propagation at different receiver points. A different approach consists of dividing the coverage area into sectors where the visibility conditions are evaluated. This approach was used in [8], where for each source and each receiver a list of visible objects was obtained from the sectors information. Recently, virtual sources (images) were used to define the so-called ray entities in a "brute force" ray tracing tool [9]; one ray entity defines a path where a propagation mechanism is present. The generation of ray entities was used to reduce the memory usage and the computational burden of new ray tracing simulations.

In [10], a spherical wave model was used to obtain the multiple-input and multiple-output (MIMO) channel from a single-input and single-output (SISO) channel. By considering the previous model, a new electric field estimation technique based on 3D ray tracing has been developed in the presented work. Firstly, all images are calculated for one receiver point. Each image represents one ray that reaches the receiver point. The developed technique modifies the module and phase of each ray in order to obtain an appropriate set of rays at a new

Submitted On: February 13, 2014
Accepted On: November 2, 2014

receiver point. Thus, the new technique is able to predict the field at several receivers, whereas the above mentioned works, except [7] and [9], depend on the receiver position. After the calculation of the new rays for each new receiver point, a simple frequency extrapolation technique is applied. Therefore, the whole technique is able to predict the field at a set of points throughout a certain bandwidth from only one simulation at one point at one frequency.

The presented technique has been validated through a comparison with data obtained from measurements in the 60 GHz band. This band has been selected because it is a very promising option for the deployment of future Gbps wireless systems [11]. The design and deployment of these systems needs fast and reliable field prediction techniques and channel estimator tools like the one developed in this work. Moreover, this band represents a difficult test due to the structural complexity of the channel in the mm-W band.

The paper is organized as follows. In Section II the field prediction technique, based on the calculation of a new set of images, is presented. In Section III the frequency extrapolation procedure is shown. Section IV presents the validation of the proposed technique by means of measurements, and finally Section V shows the conclusions.

II. FIELD PREDICTION TECHNIQUE

A. Technique explanation

Ray tracing tools evaluate the total received field considering different field contributions at the receiver point. Specifically, ray tracing based on image theory considers each contribution as a spherical wave that departs from one image and reaches directly the receiver point. Different types of contributions can be considered:

- Line-of-sight ray from the transmitter: in this case the image is the transmitter itself.
- Single reflections: each single reflection is evaluated from the images of the transmitter with respect to the elements of the environment. These images are named first order images.
- Multiple reflections: images of each first order image can be calculated; these second order images represent double reflection contributions. The process of creating new images can be applied successively in order to evaluate the contribution of multiple reflections (M-order reflections).
- Diffracted rays: in this case, the impact point of the wedge where the diffraction takes place must be determined. Uniform theory of diffraction (UTD) is used to evaluate the diffracted field.
- Reflections of a diffracted ray: the above mentioned diffraction point can be considered as a new transmitter. First and higher order images of this point can be calculated to evaluate the field corresponding to these contributions.
- Diffracted rays of a reflected ray: a reflected ray can be diffracted in one wedge. In this case, the diffraction point must be determined taking into account the reflection image position.

In the presented technique, a ray tracing tool is used to obtain the images and field contributions at one point. The ray tracing tool was developed by our research group and considers all previous contributions; in [12], the main characteristics of this tool are briefly explained. The developed ray tracing tool was validated by comparing simulations and measurements of different scenarios found in [13] and [14] with simulations performed using our tool. We call the simulated point the original receiver point. After this first ray tracing calculation, the original images and contributions are transformed in order to evaluate the contributions at a new receiver point placed near the original receiver point. The transformation is based on a module and phase change, as explained below.

Each type of contribution needs a suitable transformation. The original line-of-sight field, assuming spherical wave propagation, is shown in Eq. 1:

$$H_{LOS,O} = \frac{1}{R_{Tx-O}} \cdot e^{-j\vec{k}\cdot\vec{R}_{Tx-O}}, \qquad (1)$$

where k is the wave number and $R_{Tx\text{-}O}$ is the distance between the transmitter and the original receiver point (O), as seen in Fig. 1.

The line-of-sight field at the new receiver point can be straightforwardly evaluated from the original field by applying the transformation shown in Eq. 2:

$$H_{LOS,N} = H_{LOS,O} \cdot e^{-j\vec{k}\cdot(\vec{R}_{Tx-N}-\vec{R}_{Tx-O})} \cdot \frac{R_{Tx-O}}{R_{Tx-N}}, \qquad (2)$$

where $R_{Tx\text{-}N}$ is the distance between the transmitter and the new receiver point (N).

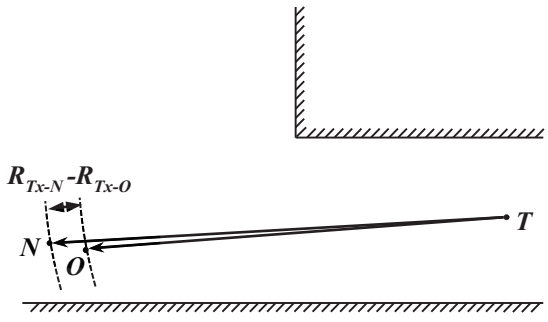

Fig. 1. Line-of-sight scheme. Original receiver point (O), new receiver point (N), and transmitter (Tx) positions are shown. The difference between distances, $R_{Tx\text{-}N}$-$R_{Tx\text{-}O}$, is used to calculate the field at the new receiver point.

The field corresponding to an M-order reflection is

calculated using the M-order image:

$$H_{REFL,O} = \frac{1}{R_{I-O}} \cdot \Gamma \cdot e^{-j\vec{k}\cdot\vec{R}_{I-O}}, \quad (3)$$

where k is the wave number, Γ is the reflection coefficient for single reflections and the accumulated reflection coefficient for multiple reflections [13], and $R_{I\text{-}O}$ is the distance between the M-order image and the original receiver point.

Once the original field is evaluated at the original receiver point, the reflection field at the new receiver point can be estimated by applying the next transformation:

$$H_{REFL,N} = H_{REFL,O} \cdot e^{-j\vec{k}\cdot(\vec{R}_{I-N}-\vec{R}_{I-O})} \cdot \frac{R_{I-O}}{R_{I-N}}, \quad (4)$$

where $R_{I\text{-}N}$ is the distance between the M-order image and the new receiver point. In Fig. 2, the particular situation of M=1, which corresponds to a single reflection ray, is shown; in this case the image is the transmitter image. For M=2, which corresponds to a two-reflection ray, the image used in Eq. 4 to compute the desired field is the image of a first-order image. In this way, Eq. 4 can be applied for any M-order reflection using the appropriate M-order image.

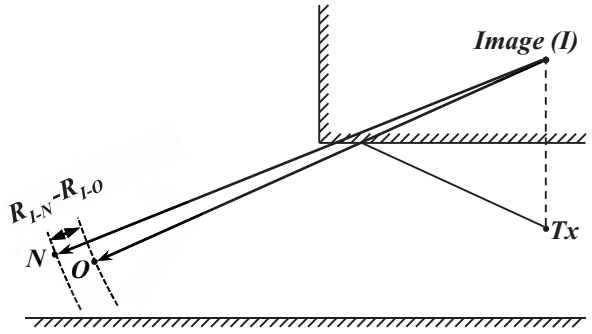

Fig. 2. Single reflection scheme. The difference between distances, $R_{I\text{-}N}$-$R_{I\text{-}O}$, is used to calculate the field at the new receiver point.

It is assumed that the reflection coefficient does not change in a significant way in the vicinity of the original receiver point, this way Γ in Eq. 3 is used in Eq. 4. The area where this approximation is acceptable depends on the diversity of the environment. If the diversity of the environment is high the area will be small; however, even in high diversity scenarios, as the one used in this work to test the developed method, the reflection coefficient remains constant inside an area wide enough to characterize the channel with accuracy.

The field corresponding to a diffracted wave is evaluated using the uniform theory of diffraction (UTD) as seen in Eq. 5:

$$H_{DIF,O} = D\left(\phi_O, \phi_O', L_O, k, \beta_0', n\right) \cdot A\left(s_O, s_O'\right) \cdot \frac{1}{s_O'} \cdot e^{-j\vec{k}\cdot\left(\vec{s}_O+\vec{s}_O'\right)}, \quad (5)$$

where k is the wave number, D is the diffraction coefficient introduced by Luebbers in [15], ϕ_O' is the angle between the transmitter and the "0" face, ϕ_O is the angle between the original receiver point and the "0" face, β_0' is the angle between the transmitter and the edge where the diffraction point is placed, s_O' is the distance between the transmitter and the diffraction point, s_O is the distance between the original receiver point and the diffraction point, and n depends on the angle between the "n" face and the "0" face [14]. All these parameters are depicted in Fig. 3.

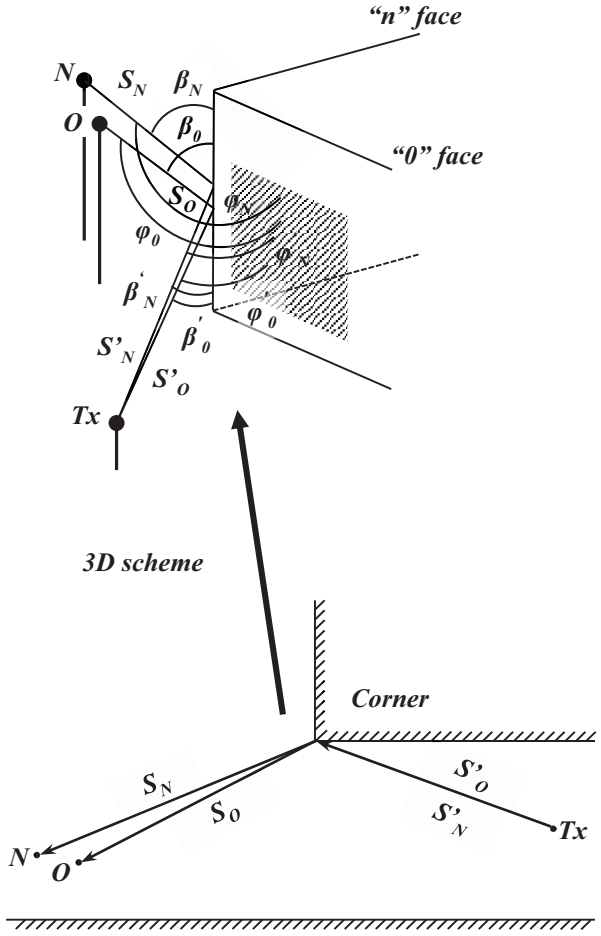

Fig. 3. Diffraction scheme. The diffraction parameters for the original receiver point and for the new receiver point are shown. The new receiver point has its own diffraction impact point in the wedge.

The parameter L_o in Eq. 5 is:

$$L_O = \frac{s_O^{'} s_O \sin^2 \beta_0}{s_O^{'} + s_O}, \tag{6}$$

and the parameter A in Eq. 5 is:

$$A\left(s_O^{'}, s_O\right) = \sqrt{\frac{s_O^{'}}{s_O \cdot \left(s_O^{'} + s_O\right)}}, \tag{7}$$

since the wave is considered to be spherical.

The diffraction field depends on the impact point position as seen in Fig. 3. This impact point depends on the receiver position. Therefore, the modification of the diffracted wave at the new receiver point implies the calculation of a new impact point in the diffraction wedge, as depicted in Fig. 3. New angles ($\phi_N^{'}, \phi_N$) and distances ($s_N^{'}, s_N$) must be calculated for the field estimation at the new receiver point. Distance $s_O^{'}$ (s_O) cannot be used in the new field estimation because this distance could be very different to $s_N^{'}$ (s_N) in terms of wavelengths. Thus, the use of $s_O^{'}$ and s_O may yield a large difference in the field phase, which affects the whole field evaluation.

The field at the new receiver point corresponding to the diffracted wave can be expressed as:

$$H_{DIF,N} = D\left(\phi_N, \phi_N^{'}, L_N, k, \beta_N^{'}, n\right) \cdot A\left(s_N, s_N^{'}\right) \cdot \frac{1}{s_N^{'}} \cdot e^{-j\vec{k}\cdot\left(\vec{s}_N + \vec{s}_N^{'}\right)}, \tag{8}$$

where the parameters $(\phi^{'}, \phi, \beta^{'}, s^{'}, s, L)$ have been recalculated for the new receiver point, as seen in Fig. 3.

Single reflections of a diffracted wave are also considered as contributions to the total received field. The field of such contributions can be evaluated as:

$$H_{DIF\_REFL,O} = D\left(\phi_O, \phi_O^{'}, L_O, k, \beta_0^{'}, n\right) \cdot A\left(s_O, s_O^{'}\right) \cdot \frac{1}{s_O^{'}} \cdot \Gamma \cdot e^{-j\vec{k}\cdot\left(\vec{s}_O + \vec{s}_O^{'}\right)}, \tag{9}$$

where the Γ is the reflection coefficient and s_O is now the total distance between the diffraction point and the original receiver point.

As in the previous case, it is necessary to calculate a new diffraction point for each new receiver point. The new diffraction point implies new diffraction parameters as well as a new image, as shown in Fig. 4. Once all the new parameters are recalculated, the field at the new receiver point due to this type of contribution is expressed as follows:

$$H_{DIF\_REFL,N} = D\left(\phi_N, \phi_N^{'}, L_N, k, \beta_N^{'}, n\right) \cdot A\left(s_N, s_N^{'}\right) \cdot \frac{1}{s_N^{'}} \cdot \Gamma \cdot e^{-j\vec{k}\cdot\left(\vec{s}_N + \vec{s}_N^{'}\right)}, \tag{10}$$

where s_N is the total distance between the new diffraction point and the new receiver point, as seen in Fig. 4. It is assumed that the reflection coefficient does not change in a significant way, so Γ in Eq. 10 is the reflection coefficient used in Eq. 9. All the new diffraction parameters are recalculated as in the single diffraction case.

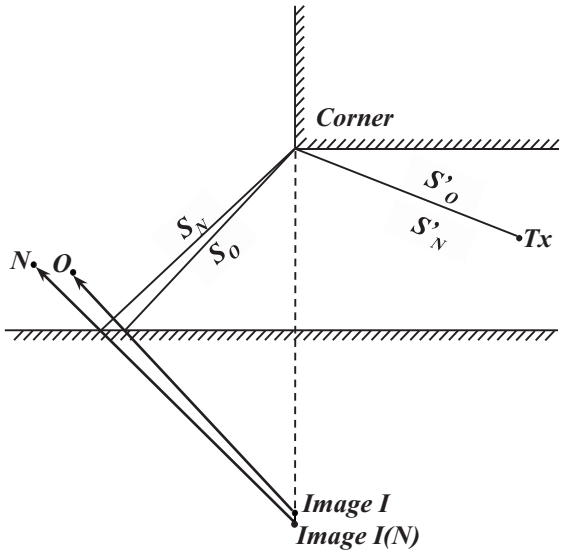

Fig. 4. Diffraction plus reflection scheme. The new receiver point has its own diffraction impact point, which implies a new image called I(N). The image of the original impact point is called image I.

Finally, diffracted rays of reflected rays are considered. In these contributions a single reflection wave impinges in a wedge and suffers a diffraction process before reaching the receiver point. The field corresponding to this type of contributions is:

$$H_{REFL\_DIF,O} = D\left(\phi_O, \phi_O^{'}, L_O, k, \beta_0^{'}, n\right) \cdot A\left(s_O, s_O^{'}\right) \cdot \frac{1}{s_O^{'}} \cdot \Gamma \cdot e^{-j\vec{k}\cdot\left(\vec{s}_O + \vec{s}_O^{'}\right)}, \tag{11}$$

where $s_O^{'}$ is the total distance between the transmitter and the diffraction point. This distance is the distance from the transmitter image I to the diffraction point, as seen in Fig. 5.

In this case, the new field evaluation does not imply a new image calculation as in the diffraction plus reflection case shown in Fig. 5. Nevertheless, it is necessary again to calculate a new impact point of the diffraction wedge. Therefore, new diffraction parameters are evaluated as seen in Eq. 12:

$$H_{REFL\_DIF,N} = D\left(\phi_N, \phi_N^{'}, L_N, k, \beta_N^{'}, n\right) \cdot A\left(s_N, s_N^{'}\right) \cdot \frac{1}{s_N^{'}} \cdot \Gamma \cdot e^{-j\vec{k}\cdot\left(\vec{s}_N + \vec{s}_N^{'}\right)}, \tag{12}$$

where $s_N^{'}$ is the total distance between the transmitter and the new diffraction point as seen in Fig. 5.

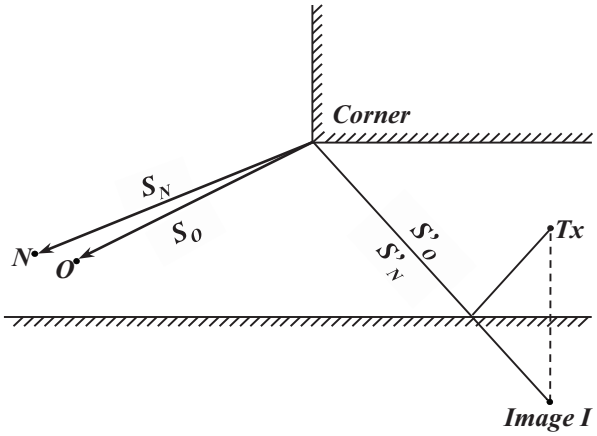

Fig. 5. Reflection plus diffraction scheme. The new receiver point has its own diffraction impact point.

B. Technique validation through simulations

The precision of the described field prediction technique has been checked in two ways. Firstly, the technique results have been compared with simulation results obtained from the ray tracing tool. Secondly, the usefulness of the technique has been tested by means of a comparison with results extracted from measurements. In this section we show the comparison with ray tracing simulations, and in Section IV we show the measurements comparison.

The measurement (and simulated) scenario, which is shown in Fig. 6, is a laboratory located on the first floor of the Universidad Politécnica de Cartagena research building (Spain). The 4.5 × 7 × 2.5 m laboratory is furnished with several cupboards, shelves, desktops, and chairs as seen in Fig. 6. A numerical model of the scenario has been generated in order to estimate the field with the ray tracing tool and with the developed field prediction technique. As seen in Fig. 7, the mentioned numerical model is a satisfactory representation of the measured scenario as it includes the main scenario elements.

Fig. 6. Photo of the measured scenario.

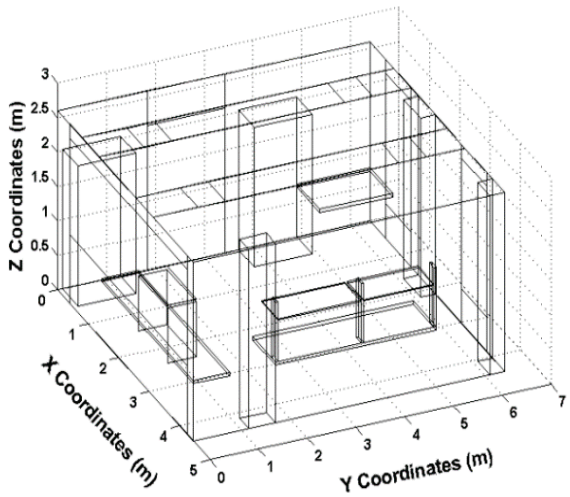

Fig. 7. Modeled scenario of Fig. 6.

Two sets of receiver positions (Rx_1 and Rx_2) and one set of transmitter positions (Tx) have been used to test the prediction technique. Each receiver set is composed of 36 positions distributed in a regular grid, as depicted in Fig. 8. The separation between two consecutive positions is 2 mm; this distance is lower than λ/2, with λ=5 mm at the central frequency of the band. Thus, the total coverage of the regular grid is 1 cm × 1 cm. As seen in Fig. 8, the transmitter set is composed of 5 positions; the separation between two consecutive transmitter positions is also 2 mm. The height of the transmitter positions is 1.44 m and the height of the receiver positions is 1.54 m.

Thus, the field was simulated with the ray tracing tool in the 36 regular grid distributed positions of Rx_1 and Rx_2. The developed technique was also used to evaluate the field at the mentioned positions from a single simulation; in each set, the single simulation was performed at a point placed in the central position of the corresponding regular grid; this point is the original receiver point of Eq. 1-12. In this section, the Tx point is the third position of the linear array scheme shown in Fig. 8.

Different contributions were considered in the field simulation: single and second order reflections, diffracted waves, reflected waves from diffracted waves, and diffracted waves from the single reflected waves. Furthermore, real omnidirectional antenna patterns were included in the simulation in order to represent faithfully the performed measurements shown in Section IV. In Fig. 9 (a) and Fig. 10 (a), the channel attenuation at 61.5 GHz estimated with the ray tracing tool is shown for Rx_1 and Rx_2, respectively. The difference between the attenuation computed with the ray tracing tool and the field prediction technique is depicted in Fig. 9 (b) and Fig. 10 (b). Both figures show the high accuracy reached by the field prediction technique; the maximum error in

the Rx_1 set is below 0.03 dB and in the Rx_2 case is also very small (0.43 dB).

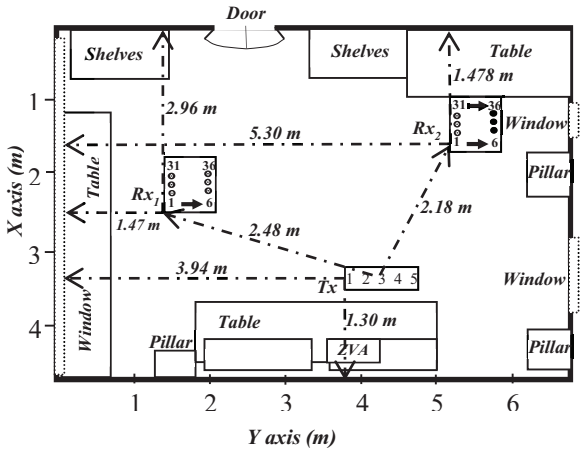

Fig. 8. Scheme of the measured and simulated positions.

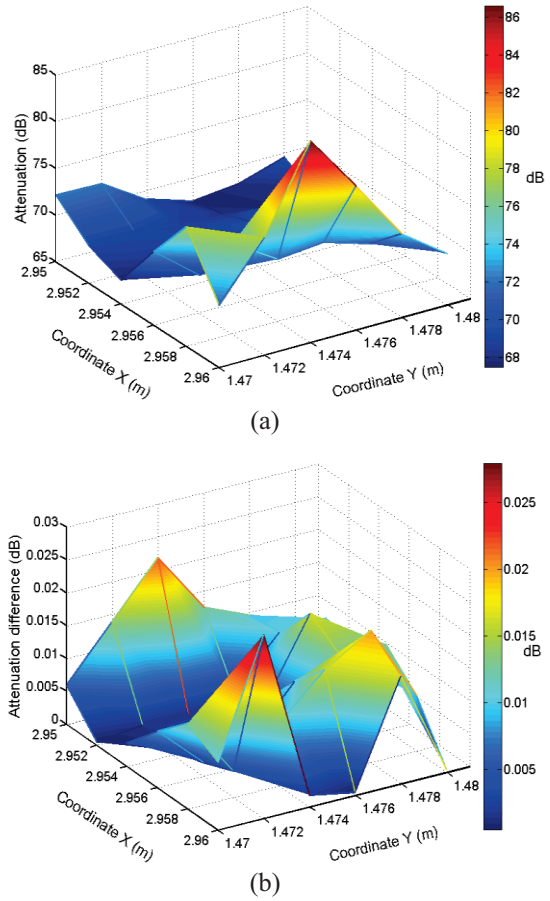

Fig. 9. (a) Attenuation at 61.5 GHz for Rx_1 positions, and (b) attenuation difference between the ray tracing tool and the presented field prediction technique.

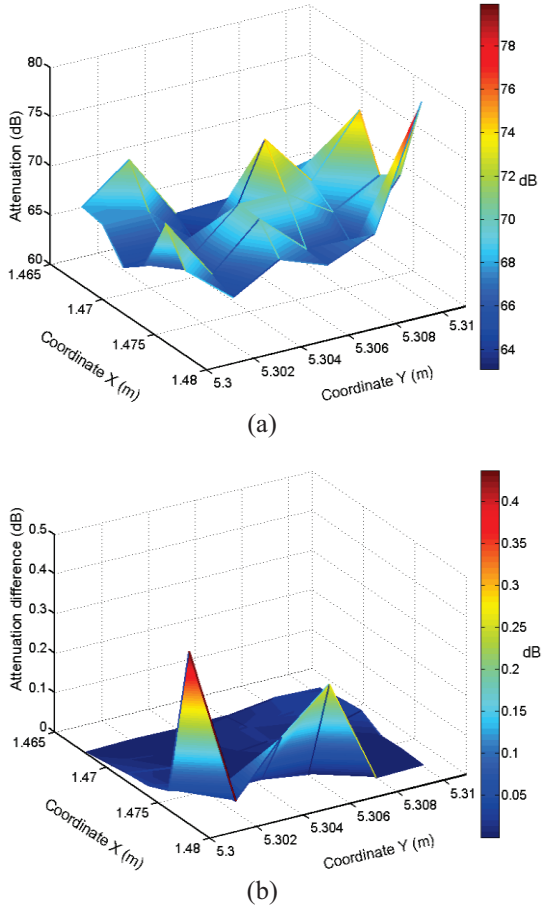

Fig. 10. (a) Attenuation at 61.5 GHz for Rx_2 positions, and (b) attenuation difference between the ray tracing tool and the presented field prediction technique.

The presented technique is very accurate in the field evaluation of all contributions. The normalized mean square error (NMSE) between the simulated and predicted field values has been used to compare the precision of the new technique in all propagation mechanisms considered. The NMSE of a given propagation mechanism is defined as:

$$NMSE = \sqrt{\frac{\sum_{i=1}^{P}\left|H_{sim,i} - H_{pred,i}\right|^2}{\sum_{i=1}^{P}\left|H_{sim,i} - \bar{H}_{sim}\right|^2}}, \qquad (13)$$

where P is the number of points in the receiver set (P=36), $H_{sim,i}$ is the total electric field corresponding to a propagation mechanism simulated with the ray tracing technique in the *i-th* spatial point, $\bar{H}_{sim}$ is the mean of the P values, and $H_{pred,i}$ is the total electric field corresponding to the same propagation mechanism predicted with the developed technique at the *i-th* spatial

point.

In Table 1, the NMSE of the propagation mechanisms corresponding to positions sets Rx_1 and Rx_2 is shown. The wavelength at 60 GHz is very small; thus, any error in the phase transformation or any incorrect new image calculation would yield large NMSE levels. Nevertheless, the computed NMSE is very low for all types of propagation mechanisms, even for the Diffr_Refl mechanism in Rx_2. Therefore, the presented technique will be accurate regardless of the predominant propagation mechanism, provided that the original and the new receiver points have the same contributions.

The main advantage of the field prediction technique is the time saved in the computation of the desired channel response. The simulation of 36 positions takes 1000 seconds; the new technique needs only one simulation (less than 30 seconds) and 75 seconds for the computation of the field at the P=36 receiver points. Thus, in this example, the field prediction technique is approximately 10 times faster than the ray tracing tool. Moreover, as the number of simulated positions increases, the new technique becomes more profitable. All simulations were performed with a computer based on a 64 bits Intel CPU at 3.20 GHz with 8 GB RAM.

Table 1: NMSE for all considered propagation mechanisms. Refl corresponds to reflected waves, Diffr corresponds to diffracted waves, Diffr_Refl corresponds to waves reflected after diffraction, and Refl_Diffr corresponds to waves diffracted after a reflection

Set	Refl	Diffr	Diffr_Refl	Refl_Diffr
Rx_1	0.00630	0.00100	0.00730	0.00020
Rx_2	0.00030	0.00020	0.06480	0.00002

III. FREQUENCY EXTRAPOLATION PROCEDURE

A. Frequency extrapolation procedure explanation

The field prediction technique explained above is able to evaluate the field in the vicinity of a given point at one frequency. Therefore, the prediction technique is limited to one frequency evaluation, which could make the technique impractical, especially if the frequency channel response evaluation is desired. For this reason, we have applied a very simple extrapolation procedure to evaluate the field in a given frequency range from the contributions at one frequency. The mentioned procedure consists of the phase correction in every contribution. The field of one contribution can be expressed as:

$$H_1 = |H_1| \cdot e^{j\phi_1} \cdot e^{-j\vec{k}_1 \cdot \vec{R}}, \quad (14)$$

where R is the total distance traveled by the wave, k_1 is the wave number at frequency f_1, and ϕ_1 is a term which depends on the reflection coefficients, diffraction coefficients, and the antenna pattern.

We assume that, for all frequencies in the frequency range, the reflection and diffraction coefficients remain constant. This assumption is feasible even for large bandwidths because the electromagnetic properties of the materials remain constant in large bandwidths [13]. Thus, the extrapolation procedure performs a phase correction only in the term which depends on the distance:

$$H_2 = H_1 \cdot \frac{e^{-j\vec{k}_2 \cdot \vec{R}}}{e^{-j\vec{k}_1 \cdot \vec{R}}} \cdot \quad (15)$$

The above equation yields the extrapolated field in frequency f_2 from the known field in frequency f_1.

The complete technique follows the next steps:

1. Obtain the contributions and images at one point (original receiver point) with the ray tracing tool at one frequency.
2. Apply the field prediction technique explained in Section II at a new receiver point at the mentioned frequency. This step gives a suitable set of contributions for the new receiver point.
3. Apply the frequency extrapolation procedure to every contribution calculated in the previous step. This procedure yields a set of contributions at a new frequency for the new receiver point.

B. Frequency extrapolation procedure validation through simulations

In order to test the frequency extrapolation procedure, the frequency response in the 60 GHz band was calculated with the ray tracing tool and with the prediction technique. The number of frequency points was set to 4096 and the bandwidth ranges from 57 GHz to 66 GHz. The prediction technique uses the 61.5 GHz frequency to evaluate the original received field. In Fig. 11 (a), the difference between both frequency responses is shown for one point selected from the Rx_1 set; the selected point corresponds to the one where the error performed with the prediction technique was largest at 61.5 GHz. In Fig. 11 (b), the same comparison is depicted for the worst point of the Rx_2 set. Both figures show the high accuracy of the complete technique, which involves the prediction of the field at a new spatial point and the frequency extrapolation. In both cases, the transmitter point is the third position of the linear set shown in Fig. 8.

The precision of the new technique is clearly shown when the complex impulse response h(τ) (CIR) is calculated. The channel is static; therefore the CIR can be evaluated from the frequency response by applying an inverse Fourier transform:

$$h(\tau) = FT^{-1}\{H(f)\}. \quad (16)$$

In Fig. 12 (a) and Fig. 12 (b) the absolute value, expressed in logarithmic units, of the CIR evaluated with the two techniques is depicted. In Table 2, the root mean square delay spread (RMS DS) and the path loss (PL) are

shown for the studied CIR. A 30 dB threshold was used in the RMS delay spread calculation to keep the most energetic paths. The agreement between the original ray tracing and the complete technique is excellent, as seen in Fig. 12 and in Table 2.

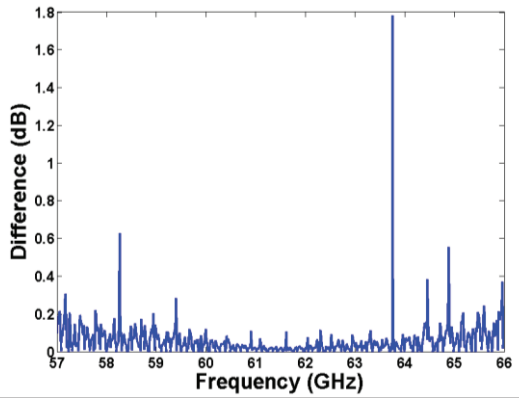

(a)

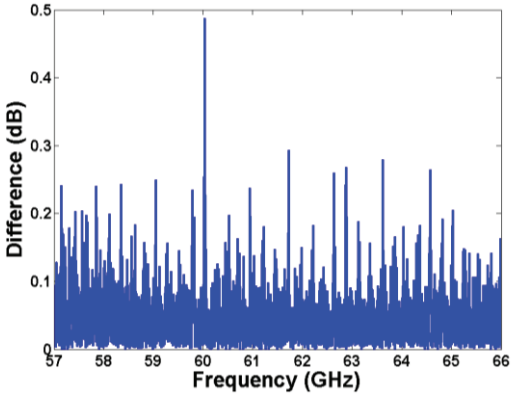

(b)

Fig. 11. Difference in dB between the frequency responses calculated with the ray tracing tool and the developed technique. In (a), the difference corresponding to the worst point of Rx_1 is shown; in (b), the difference corresponding to the worst point of Rx_2 is shown.

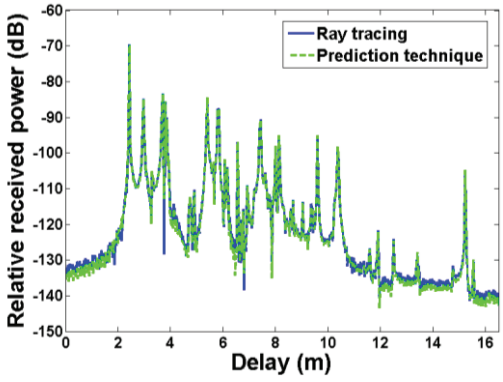

(a)

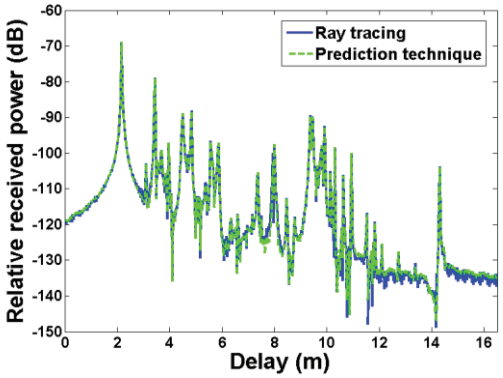

(b)

Fig. 12. CIR calculated with the ray tracing tool and the developed technique. In (a), the CIR of the worst point of Rx_1 is depicted; in (b), the CIR of the worst point of Rx_2 is depicted.

Table 2: RMS delay spread and path loss of the CIR shown in Fig. 12, which correspond to the worst points of the studied sets. These parameters have been evaluated for the new prediction technique data and for the original ray tracing tool (RT) data

Position	RMS DS (ns)		PL (dB)	
	RT	Prediction	RT	Prediction
Rx_1	3.52	3.52	68.62	68.62
Rx_2	4.22	4.17	67.75	67.74

IV. VALIDATION BASED ON MEASUREMENTS

The complete technique explained in Sections II and III was tested through measurements performed in the laboratory shown in Fig. 6. In particular, the frequency response was measured for every pair of transmitter and receiver positions depicted in Fig. 8. The channel sounder is based on a Rohde & Schwartz ZVA67 Vector Network Analyzer (VNA). As in the simulations of Section III, the measured frequency range was 57–66 GHz using 4096 frequency points. A 10 Hz intermediate frequency was selected and a dynamic range of more than 100 dB was obtained. Two amplifiers were used in the transmission to compensate for the attenuation of the used cables (HXI HLNA-465). The system is through calibrated to eliminate the effect of cables and amplifiers. The VNA Tx power was set to -10 dBm.

Both Tx and Rx antennas are vertically-polarized omnidirectional antennas (Q-par QOM55-65 VRA) with 4.5 dBi gain. As in the simulations of the previous section, the height of the transmitting antenna was 1.44 m and 1.54 m for the receiving antenna. Nobody was inside the room during the measurements campaign, so the channel can be considered as static.

Once all frequency responses were collected, the CIR for every pair of points was calculated by applying the inverse Fourier transform operation shown in Eq. 16.

The power delay profile (PDP) of each one of the two Tx-Rx sets is the ensemble of the corresponding complex impulse responses [13]:

$$PDP(\tau) = \left\langle |h(\tau)|^2 \right\rangle . \quad (17)$$

The PDP of the Tx-Rx sets was also evaluated with the field prediction technique. For each one of the five Tx positions a single simulation with the ray tracing tool was performed. This simulation allowed the calculation of the field corresponding to all propagation mechanisms, at all Rx set points at the central frequency 61.5 GHz. The frequency extrapolation procedure was then applied in order to obtain the frequency response at all points. Therefore, the PDP evaluation with the new technique needed:

1. The calculation of five simulations with the ray tracing tool (see Table 3).
2. Five executions of the spatial field prediction technique explained in Section II. This technique is at least one order of magnitude faster than the ray tracing simulations.
3. The execution of the frequency extrapolation at each one of the Rx points for each one of the Tx positions. A total of 36•5=180 executions of this procedure are needed. Each execution is very fast as it needs only 0.85 seconds to evaluate the frequency response for one spatial point.

The time taken by the new technique is very small in comparison with the time needed by the ray tracing tool as seen in Table 3. The new technique takes only 668 seconds to evaluate the PDP for each Rx set, whereas the ray tracing tool would have needed a huge amount of time (the time shown in Table 3 for the ray tracing tool is an estimation based on the time needed to compute one CIR). The measurements also needed several days to be completed, as seen in Table 3. Thus, the new technique is a very useful tool to characterize the wireless channel.

Table 3: Time taken to calculate the PDP with the new technique, time theoretically needed to compute the PDP with the original ray tracing tool, and time spent to measure the channel. All simulations were performed with a computer based on a 64 bits Intel CPU at 3.20 GHz with 8 GB RAM

New Technique			
5 Simulations with the RT	5 Executions of Spatial Field Prediction	5x36 = 180 Executions of Frequency Extrapolation	Total Time
140 s.	375 s.	153 s.	668 s.
Ray Tracing Tool			
5x36x4096 = 737280 simulations with the RT			
>238 days			
Measurement Time			
3 days			

The precision of the new technique can be perceived in Fig. 13. The new technique is able to properly grasp the main propagation mechanisms. For the sake of comparison, noise was added to the simulated CIR.

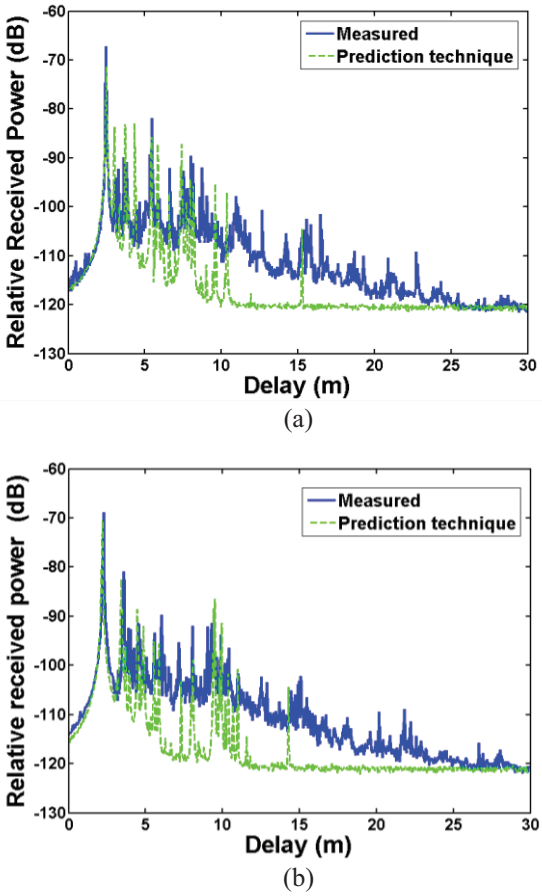

Fig. 13. (a) PDP of the Rx_1 set, and (b) PDP of the Rx_2 set. The measured PDP and the PDP obtained through the prediction technique are compared.

The accuracy of the new technique has also been quantitatively tested. Table 4 summarizes the RMS delay spread and path loss of the PDPs. As in Section III, a 30 dB threshold was used in the RMS delay spread calculation. As seen in Table 4, the new technique is a reliable tool to characterize the wireless channel, even in the complex 60 GHz band. Some differences are found in Table 4, i.e., in the PL of Rx_2; however, such differences are, in part, attributable to the imperfect representation of both the antenna patterns and the modeling of the scenario.

The PDP in this work was evaluated in an area of 1 cm × 1 cm. As the frequency decreases the area needed to evaluate the PDP increases. Therefore, one original receiver point might not be enough to obtain accurate results. In this case, new original receiver points can be simulated increasing the accuracy; the proposed

technique would be still profitable since the time saved is very large as seen in Table 3.

Table 4: RMS delay spread and Path Loss of the PDP shown in Fig. 13. These parameters have been evaluated for the new prediction technique data (Pred.) and for the measured data (Meas.)

Position Set	RMS DS (ns)		PL (dB)	
	Meas.	Pred.	Meas.	Pred.
Rx_1	3.17	3.98	67.64	68.69
Rx_2	4.35	4.49	64.50	67.98

V. CONCLUSION

A very efficient field prediction technique has been presented. The new technique firstly evaluates the field contributions in the vicinity of one point and secondly performs a frequency extrapolation to yield the frequency response at all new spatial points. The validation results have shown that the precision of the new technique is similar to that obtained with the ray tracing tool, even at high frequencies where the wavelength is very small. Such precision is only reached in the vicinity of the simulated point. Nevertheless, this spatial limitation is enough to calculate channel functions such as the power delay profile. The spatial and frequency limits where the proposed method is accurate will be studied in future works. The presented technique is very fast in comparison with both measurements and ray tracing simulations. Therefore, for all the above reasons, the new technique permits a fast and reliable characterization of the channel. The mentioned ability makes the developed technique a useful tool in the design of wireless communications systems, especially in those that use MIMO techniques and those based on ultrawideband technology.

ACKNOWLEDGMENT

This work was supported by the Ministerio de Economía y Competitividad (MINECO), Spain (TEC2013-47360-C3-2) and by the European FEDER funds.

REFERENCES

[1] G. de la Roche, A. Alayón-Glazunov, and B. Allen, "*Simulation and Performance*," in *LTE-Advanced and Next Generation Wireless Networks: Channel Modelling and Propagation*, John Wiley and Sons, Chichester, UK, pp. 271-292, 2013.

[2] R. A. Valenzuela, "A ray tracing approach to predicting indoor wireless transmission," in *Proc. of IEEE 43rd Vehicular Technology Conference*, pp. 214-218, 1993.

[3] D. Dardari, L. Minelli, V. Tralli, and O. Andrisano, "Fast ray-tracing characterisation of indoor propagation channels at 60 GHz," in *Proc. of IEEE 47th Vehicular Technology Conference*, vol. 2, pp. 989-993, 1997.

[4] M. G. Sánchez, L. de Haro, A. G. Pino, and M. Calvo, "Exhaustive ray tracing algorithm for microcellular propagation prediction models," *Electronics Letters*, vol. 32, no. 7, pp. 624-625, Feb. 1996.

[5] F. Aguado-Agelet, F. Pérez-Fontán, and A. Formella, "Fast ray tracing for microcellular and indoor environments," *IEEE Trans. on Magnetics*, vol. 33, no. 2, pp. 1484-1487, Mar. 1997.

[6] P. Wang, L. X. Guo, and Y. S. Feng, "A fast ray-tracing algorithm for microcellular propagation prediction models," in *Proc. of 10th International Symposium on Antennas, Propagation & EM Theory (ISAPE)*, pp. 436-339, 2012.

[7] A. Toscano, F. Bilotti, and L. Vegni, "Fast ray-tracing technique for electromagnetic field prediction in mobile communications," *IEEE Trans. on Magnetics*, vol. 39, no. 3, pp. 1238-1241, May 2003.

[8] W. M. O'Brien, E. M. Kenny, and P. J. Cullen, "An efficient implementation of a three-dimensional microcell propagation tool for indoor and outdoor urban environments," *IEEE Trans. on Vehicular Technology*, vol. 49, no. 2, pp. 622-630, Mar. 2000.

[9] N. Magata, R. Zentner, and A. Katalanic-Mucalo, "Ray entity based post processing of ray tracing data for continuous modeling of radio channel," in *Proc. of Euro-COST Conference*, 2013.

[10] J. M. Molina-García-Pardo, J. V. Rodriguez, and Leandro Juan-Llacer, "Parametric spherical-wave MIMO model for ray-based simulations," *Radio Science*, Jan. 2007.

[11] P. Smulders, "Exploiting the 60 GHz band for local wireless multimedia access: prospects and future directions," *IEEE Communications Magazine*, vol. 40, no. 1, pp. 140-147, Jan. 2002.

[12] M. T. Martínez-Inglés, J. Pascual-García, J. V. Rodriguez, J. M. Molina-García-Pardo, Leandro Juan-Llacer, D. P. Gaillot, M. Lienard, and P. Degauque, "Indoor radio channel characterization at 60 GHz," in *Proc. of 7th European Conference on Antennas and Propagation (EuCAP)*, pp. 2796-2799, 2013.

[13] T. S. Rappaport, *Wireless Communications: Principles and Practice*, Prentice-Hall, New Jersey, 1996.

[14] A. S. Balanis, *Geometrical Theory of Diffraction, in Advanced Engineering Electromagnetics*, John Wiley and Sons, New York, 1989.

[15] R. Luebbers, "Finite conductivity uniform GTD versus knife edge diffraction in prediction of propagation path loss," *IEEE Trans. on Antennas and Propagation*, vol. 32, no. 1, pp. 70-76, Jan. 1984.

Juan Pascual García was born in Castellón, Spain, in 1975. He received the Telecommunications Engineer degree from the Technical University of Valencia (UPV), Valencia, Spain, in 2001 and the Ph.D. in Communications Engineering from the Universidad Politécnica de Cartagena (UPCT), Cartagena, Spain, in 2010. In 2003, he joined the Communications and Information Technologies Department, UPCT as a Research Assistant and then as an Associated Professor. In 2009 he joined the SiCoMo Research Group of the UPCT where he is currently developing his research tasks.

His research interests include radio wave propagation, ray tracing techniques and radio channel propagation models

José-María Molina-García-Pardo received the Engineer of Telecommunications degree from the Universidad Politécnica de Valencia (Spain, 2000), and the M.Sc. in "Communication and Signal Processing" in Newcastle Upon Tyne (United Kingdom) in September 2001 and the Ph.D. degree in Telecommunications from the Universidad Politécnica de Cartagena (UPCT, Spain) in 2004. In 2001, he joined the Information Technologies and Communications Department of the Universidad Politécnica de Cartagena, where he has been an Associate Professor since 2007, and recently accredited as a Full Professor.

His research activities are centered on radio-communications, propagation, channel modelling and experimental channel sounding in different frequency band (400 MHz to 60 GHz) and technologies (GSM, UMTS, LTE, WiFi, WSN, TETRA, mmW, OFDM, MIMO, cognitive radio). He currently leads the SICOMO research group. He is the Lead Researcher in some national projects, and participates actively in the European COST action IC-1004 (Radio Communications for Green Smart Environments). He is author of more than 50 journals indexed in the JCR, more than 100 international conferences and author of three book chapters.

María-Teresa Martínez-Inglés was born in Sucina, Murcia, Spain, in 1983. She received the Telecommunications Engineering degree in 2009, and the Ph.D. degree in Telecommunications in 2014 from the Universidad Politécnica de Cartagena (UPCT), Cartagena, Spain.

Her research line aims to study the modelling and characterization of the millimeter wave frequency band.

José-Víctor Rodríguez was born in Murcia, Spain, in 1975. He received the Telecommunications Engineering degree from the Universidad Politécnica de Valencia (UPV), Spain, in 2001 - after doing his graduate thesis at the Lund Institute of Technology, Lund University, Sweden, in collaboration with Ericsson Mobile Communications AB - and the Ph.D. in Communications Engineering from the Universidad Politécnica de Cartagena (UPCT), Spain, in 2006. In 2002, he joined the Department of Information Technologies and Communications, at the Universidad Politécnica de Cartagena (UPCT), Spain, where he is currently an Associated Professor.

His research interests include the modeling of radio wave propagation in the mobile environment, with an emphasis on multiple-building diffraction.

Leandro Juan-Llácer was born in Albatera, Alicante, Spain, in 1967. He received the Telecommunications Engineering degree from the Universitat Politècnica de Catalunya (UPC), Barcelona, Spain, in 1993, and the Ph.D. in Communications Engineering from the Universidad Politécnica de Valencia (UPV), Valencia, Spain, in 1998. In 1994, he joined the UPV's Department of Signal Theory and Communications, where he was an Associate Professor (AP) of Electromagnetics from 1995 to 2000. He is currently Professor at the Universidad Politécnica de Cartagena (UPCT)'s Department of Information Technologies and Communications.

He has also been participating in COST actions 256, 259 and 273 and in IC1004 action. His research activities have focused on the characterization and modelling of radio wave propagation in mobile communication systems.

Dual Band-Notched Small Monopole Antenna with Bandwidth Enhancement by Means of Defected Ground Structure (DGS) for UWB Application

Z. Esmati and M. Moosazadeh

Institute for Infrastructure Engineering
University of Western Sydney, Penrith NSW 2751, Australia
Z.esmati@uws.edu.au, m.moosazadeh@uws.edu.au

Abstract ─ In this study, a small and compact dual band-notched microstrip-fed printed monopole antenna for ultra-wideband applications has been presented. This antenna consists of a square patch as radiator and a defected ground structure (DGS). In order to generate dual band-notched function, we use four slots in the ground plane. A parametric study of the proposed antenna is provided to achieve the dual band-notched by adjusting the lengths of the rectangular-shaped slots. The proposed antenna can easily adjust its stop-band functions by half-wavelength. Mainly, desired stop-bands are obtained without any variation on the patch. Using of this structure on the ground plane, the impedance bandwidth is effectively improved at the higher band, which results in a wide usable fractional bandwidth of more than 134% (2.7-13.7 GHz), defined by VSWR<2, with two notched bands, covering all the 5.2/5.8-GHz WLAN, 3.5/5.5-GHz WiMAX, and 4-GHz C-bands. The constructed antenna is small (15×15 mm^2) when compared with previously proposed single- and double-filtering monopole antennas with DGS in terms of slots on the ground only. The antenna has a desirable voltage standing wave ratio (VSWR) level and acceptable antenna gain for ultra-wideband frequency band range.

Index Terms ─ Defective ground structure, frequency band notched function, monopole antenna, ultra-wideband (UWB) antenna.

I. INTRODUCTION

There is a tremendous increase in the applications that use the ultra-wideband (UWB) technology. After the allocation of the frequency band between 3.1–10.6 GHz by the Federal Communication Commission (FCC) in 2002, the ultra-wideband (UWB) technology has become one of the most promising technologies for future high-data-rate wireless communication and imaging systems. One of the key elements in successful UWB system is the design of a compact UWB antenna with compact dimensions and proper characteristics providing wideband characteristic over the whole operating band. Different methods such as the truncated slot on the antenna patch have been proposed for increasing impedance bandwidth [1]. Since there are several existing systems operating within the UWB frequency spectrum, such as the IEEE802.11a WLAN (5.15-5.825 GHz) and the IEEE802.16 WiMAX (3.3-3.6 GHz), and C-band system (3.7-4.2 GHz), the UWB antenna is required to have the capability to notch those bands and thus to cancel any interference between those systems and the UWB system [2]. A number of printed microstrip antennas by combination of different types of slots in both patch and ground to generate more resonant modes for a wider impedance bandwidth have been introduced [3-12]. Many reports have appeared about the development of the band-notched characteristics which includes the capacitively-loaded loop (CLL) resonators [13], an open loop notch band resonator [14], a modified H-shaped resonator [15], a complementary split-ring resonator (CSRR) [16], and M-shaped parasitic element [17]. In [18], band-notch functions are obtained by T-shaped strip inside the slotted radiator and a pair of mirror inverted L-shaped slots at the two sides of the radiator. Moreover, band-

Submitted On: September 4, 2014
Accepted On: January 9, 2015

rejection characteristics are generated by using a resonator at the center of a fork-shaped antenna [19] and with employing a U-slot defected ground structure in the ground plane on the back side and etching a split ring slot in the radiation patch on the front side [20]. In [21], by slitting an open-ended quarter-wavelength split slot on the back of the feed and a short-ended half-wavelength split-ring slot near the stepped slot, a second-order notched band is achieved. To obtain dual band-notched function, defected ground structure (DGS) has been used based on without any slots in radiating patch in this study. The ground plane is located at the bottom layer that is slotted with four rectangular-shaped slots. Dual band-notched of proposed antenna is achieved by adjusting the dimensions of the slots. Regarding defective ground structure (DGS), the creating slot in the ground plane provides an additional current path which it changes the inductance and capacitance of the input impedance, resulting in a change in the bandwidth. As a result, additional resonance is excited and bandwidth is improved, which obtains a fractional bandwidth of more than 134% (2.7-13.7 GHz). Compared with other reported antennas with DGS, this design has relatively small size which it is suitable to be integrated in portable devices. Good agreement between the measurement and simulation is obtained. Radiation patterns of the antenna are approximately omnidirectional. Detail of the antenna design and comparison between the measurement and simulation results are presented.

II. ANTENNA DESIGN

The schematic configuration of the proposed microstrip-fed planar monopole antenna for band-notched function is shown in Fig. 1. The design of proposed antenna is based on a microstrip patch antenna that is low profile and simple but it has relatively large dimensions ($\sim\lambda_g/2$, λ_g is a guided wavelength at the center frequency of the UWB) and does not satisfy dual-notched bands. To design a small and compact antenna with desired performance with the following design procedure has been used. The dimensions of the patch antenna were significantly reduced and the four rectangular-shaped slots were made within the ground plane. The design of the four slots was based on the expectation that they can be on the other side of substrate when they provide the desired notched frequencies. For this purpose, the initial lengths of each part of the slots was selected in such a way that the total length are about a half of the guided wavelength at the desired notched frequency ($L_{slot\_1}+L_{slot\_2}\sim\lambda_g/2$) using the approximate effective permittivity approach. Based on the DGS, the proposed structure is designed to minimize the space utilized around patch. It is also expected that far-field radiation patterns of the antenna will be omnidirectional since the patch is electric small. In this design, the antenna is printed on FR4 substrate with permittivity of 4.4, thickness of (t_{sub}) of 1.6 mm, and loss tangent of 0.02. The impedance of 50-Ω is obtained by width of the feed-line microstrip (W_f). In order to show the impact of using the defected ground plane, the antenna's performance is simulated for different cases as indicated in Fig. 2. If the proposed antenna be used without slot_2 (Fig. 2 (a)) and without slot_3 (Fig. 2 (b)), the impedance matching will be poor at the frequency band over 5 GHz as shown in Fig. 3. However, this frequency band does not notched the desired frequency bands in particular at 5.2/5.8 GHz WLAN. As shown in Fig. 3 (Fig. 2 (c)), in order to generate single band-notched characteristics (5.2/5.8-GHz WLAN), we use slot_1 and slot_2. By adding slot_3 and slot_4, a dual band-notched function is obtained that covers all the 5.2/5.8-GHz WLAN, 3.5/5.5-GHz WiMAX, and 4-GHz C-bands. It is worth mentioning that the DGS structure improves the performance at the upper frequency band. Also, by DGS, additional resonances are excited, and hence the bandwidth is increased; especially at the frequency band over 10 GHz.

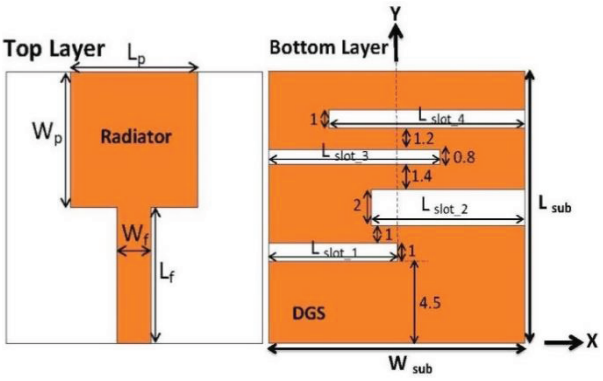

Fig. 1. Geometry of the proposed antenna with DGS structure. *(Units: mm)*

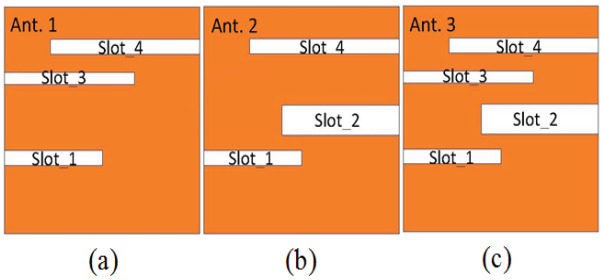

Fig. 2 Structure of various antennas used for simulation studies: (a) the antenna without slot_2, (b) the antenna without slot_3, and (c) the antenna with final design.

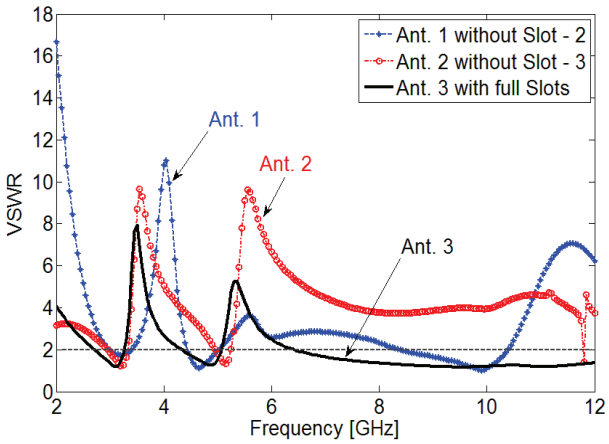

Fig. 3. Simulated VSWR characteristics for various antenna structures shown in Fig. 2.

For displaying the effect of the parameters slot_1, slot_2, slot_3, and slot_4, the simulated performance of the antenna is computed for various lengths of the proposed antenna. The length of slot_1 and slot_2 defines the upper notched band (5.07-6.4 GHz), whereas the length of slot_3 and slot_4 defines the lower notched band (3.27-4.4 GHz). The relation between the center of the notched bands (f_{c1} and f_{c2}) and length of notches is approximately by:

$$L_{slot_1} + L_{slot_2} = \frac{c}{2(f_{c1})\sqrt{\varepsilon_{eff}}}, \quad (1)$$

$$L_{slot_3} + L_{slot_4} = \frac{c}{2(f_{c2})\sqrt{\varepsilon_{eff}}}, \quad (2)$$

$$\varepsilon_{eff} = \frac{\varepsilon_r + 1}{2} + \frac{\varepsilon_r - 1}{2\sqrt{1 + \frac{12h}{W_f}}}, \quad (3)$$

where c, ε_{eff}, ε_r, h, and W_f are the speed of light in free space, effective dielectric constant, dielectric constant, thickness of substrate, and the width of the feed line, respectively. As a result, the values of the designed parameters L_{slot_1} and L_{slot_2} that are centered at the frequencies 5.5 and L_{slot_3} and L_{slot_4} at the 3.5 GHz can be calculated from (1) and (2). The effect of the value of the L_{slot_1} and L_{slot_2} on VSWR is shown in Fig. 4. It can be seen in Fig. 4 that the center of the band-notch for WLAN is determined by the length of the slot_1 and slot_2 indicated in Fig. 2 (c). The length of slot_1 and slot_2 is equal to half guided wavelength at the center of the rejected sub-band. The effect of the value of the L_{slot_3} and L_{slot_4} on VSWR is shown in Fig. 5. The increase in the values cause the lower rejected sub-band to shift down in the frequency without almost any impact on the upper rejected sub-band. It can be seen in Fig. 5 that the center of the band-notch for WiMAX is determined by the length of the slot_3 and slot_4 indicated in Fig. 2 (c). The length of slot_3 and slot_4 is equal to half guided wavelength at the center of the lower rejected sub-band.

The optimization of the structure is obtained using the Ansoft simulator (HFSS) [22]. Optimal parameters for the proposed antenna are as follows: W_{sub} = 15 mm, L_{sub} = 15 mm, W_f = 2 mm, L_f = 7.5 mm, W_p = 7.5 mm, L_p = 7.5 mm, L_{slot_1} = 7.5 mm, L_{slot_2} = 9 mm, L_{slot_3} = 10 mm, L_{slot_4} = 11.5 mm. For further examining of the whole designed antenna, the excited surface current distributions on the DGS approach are provided by the simulation tool HFSS. As shown in Fig. 6, current concentrates mainly in opposite directions around slot_1 and slot_2 at 5.5 GHz, whereas it concentrates in opposite directions around slot_3 and slot_4 at 3.5 GHz. Thus, the total effective radiation from the antenna becomes almost zero. Therefore, the antenna impedance changes at these frequencies due to the band-notched properties of the DGS structure. Figure 7 shows the simulated input impedance of the proposed antenna with defected

ground structure. As observed, the impedance changes nearby the notched resonant frequencies. The real part of impedance is close to zero, resulting in the mismatch of the antenna at the first and second notched frequency bands.

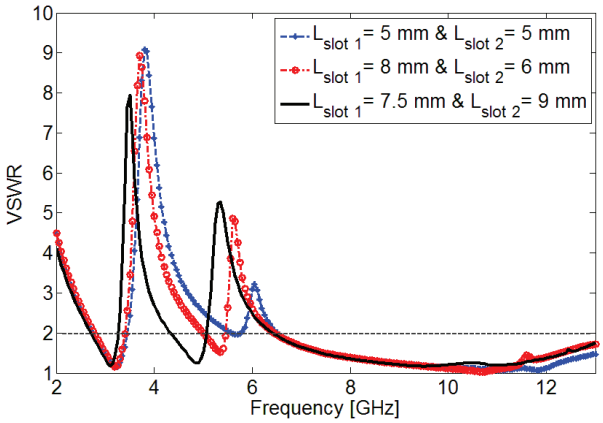

Fig. 4. Simulated VSWR of the antenna for various Lslot_1 and Lslot_2.

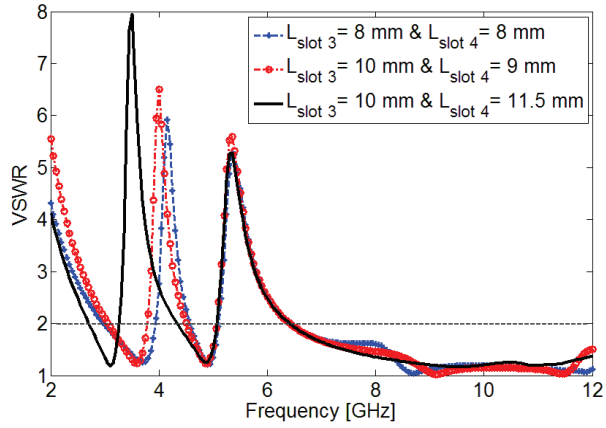

Fig. 5. Simulated VSWR of the antenna with various for Lslot_3 and Lslot_4.

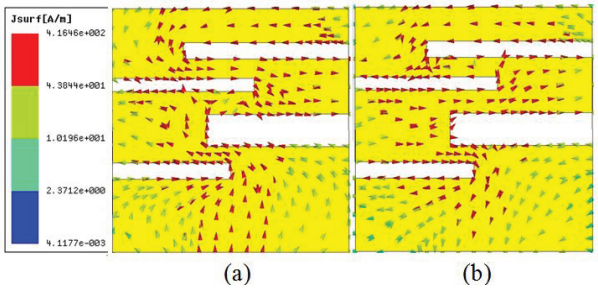

Fig. 6. Simulated current distribution of the dual-notched monopole antenna at: (a) 3.5 GHz and (b) 5.5 GHz.

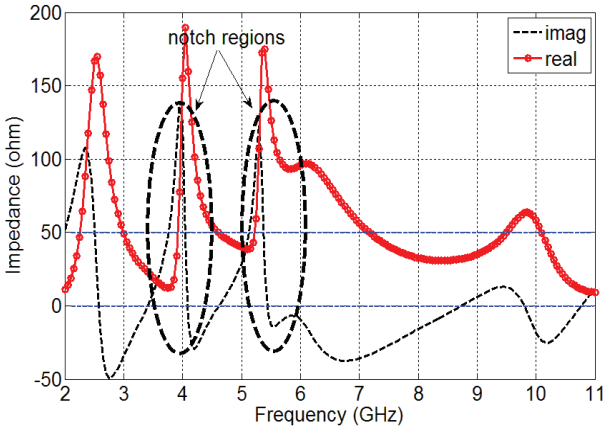

Fig. 7. Simulated real and imaginary part of impedance of the proposed antenna with notch regions.

III. RESULTS AND DISCUSSIONS

The designed antenna is fabricated (Fig. 8) and tested by using an Agilent 8722ES Vector Network Analyzer. The effect of the coaxial cable connecting the antenna with the VNA becomes a main problem in process of measurement. The cable distorts the far-field radiation pattern of the antenna. Several techniques were introduced to decouple the cable, such as using different types of baluns, ferrite beads or optic links [23-25]. In order to minimize the effect of the cable on the antenna, high impedance ferrite beads approach are applied along the measurement cable close to its connection with the antenna to reflect and/or absorb the induced power on the cable. The simulated and measured VSWR of the antenna with DGS method is shown in Fig. 8. The presented antenna can cover the frequency band between 2.7 GHz and 13.7 GHz with band-notch characteristics around 3.27-4.4 GHz and 5.07-6.4 GHz for specified criteria VSWR less than 2. There is generally good agreement between the simulation and measurement results. Figure 9 shows the simulated and measured maximum antenna gain of the proposed antenna which is used to propose notched bands. The values in Fig. 9 depict that the obtained dual band-notched antenna has relatively good gain. It also clearly shows that the gain values at notch band frequencies are significantly lower than at the whole frequency band. Figure 10 shows the simulated radiation efficiency of the proposed antenna. Results of the calculations show that the designed antenna features a good efficiency, being

greater than 88% across the entire radiating band except in two notched bands. The simulated radiation efficiencies at 3.5 and 5.5 GHz are only about 40 and 50%, respectively. The radiation pattern of the antenna is also tested to confirm its omnidirectional performance as mainly required by the short range indoor UWB communication systems. Figure 11 shows the measured radiation pattern at 3, 4.5, 7.5 and 10 GHz, in the H-plane (xz-plane) and E-plane (yz-plane) knowing that the antenna is assumed to be located in the xy-plane. It can be seen that radiation patterns in the xz-plane are nearly omnidirectional for four frequencies.

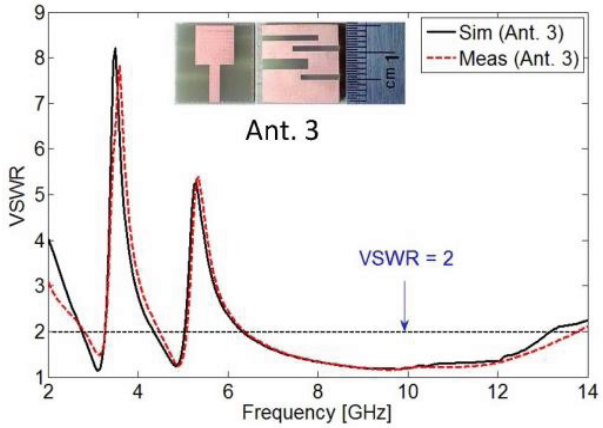

Fig. 8. Measured and simulated VSWR of the proposed dual band-notched monopole antenna (inset).

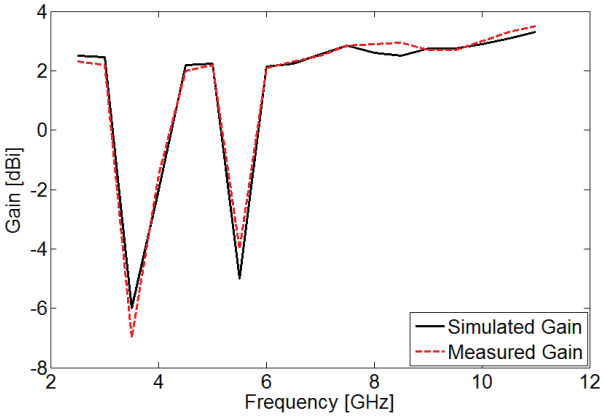

Fig. 9. Measured and simulated maximum gain of the proposed antenna.

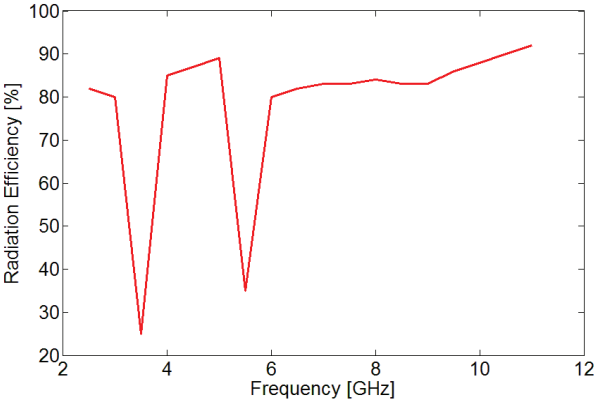

Fig. 10. Simulated radiation efficiency of the proposed antenna.

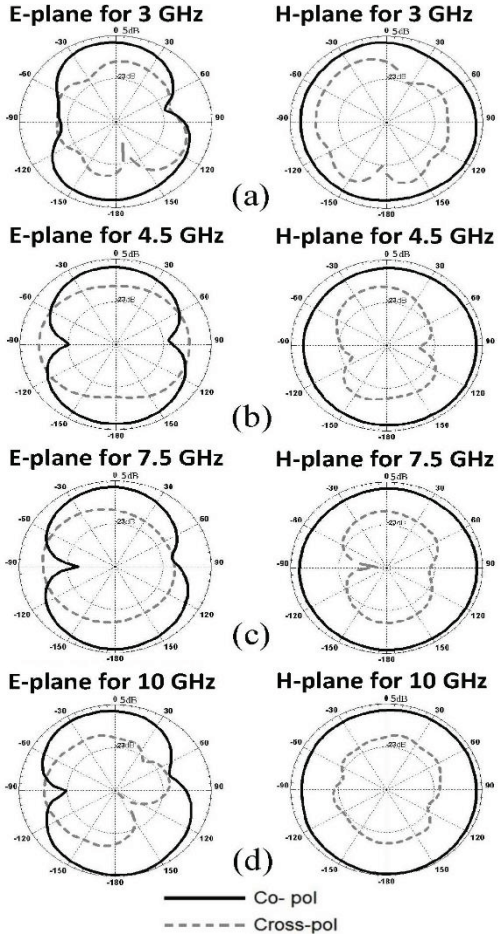

Fig. 11. The Measured radiation patterns of the proposed antenna at: (a) 3 GHz, (b) 4.5 GHz, (c) 7.5 GHz, and (d) 10 GHz.

IV. CONCLUSION

In this paper, a compact planar antenna with a new method to create dual band-notched characteristics and wide band-width capability for UWB applications has been presented. The antenna consists of a square patch as the main radiator and defected ground structure (DGS). Implementing the DGS, the dual band-notched characteristics are achieved by means of four rectangular-shaped slots at the ground plane. Also by introducing this structure, additional resonance is excited and the bandwidth is improved, resulting in a fractional bandwidth of more than 134%. Simulation and measured results are in good agreement and they show that the desired band-notch for WLAN/WiMAX/C-bands, gain and radiation pattern for UWB application can be obtained. The designed antenna can be a suitable choice for dual band-notched characteristics due to its small size, simple configuration, and omnidirectional radiation pattern.

REFERENCES

[1] M. Moosazadeh, C. Ghobadi, and M. Dousti, "Small monopole antenna with checkered-shaped patch for UWB application," *IEEE Antennas Wireless Propa. Lett*., vol. 9, pp. 1014-1017, 2010.

[2] M. Moosazadeh and Z. Esmati, "Simple and compact dual band-notched monopole antenna using U-shaped forms on the conductor-backed plane for UWB applications," *Appl. Comp. Electro. Society (ACES) Journal*, vol. 28, no. 11, pp. 1074-1079, 2013.

[3] A. Nouri and G. R. Dadashzadeh, "A compact UWB band-notched printed monopole antenna with defected ground structure," *IEEE Antennas Wireless Propa. Lett*., vol. 10, pp. 1178-1181, 2011.

[4] S.-J. Wu and J.-H. Tarng, "Planar band-notched ultra-wideband antenna with square-looped and end-coupled resonator," *IET Microw. Antennas Propag*., vol. 5, pp. 1227-1233, 2011.

[5] M. Moosazadeh and Z. Esmati, "Design of compact CPW-fed planar antenna with dual notched bands using slotted conductor-backed plane for UWB application," *Appl. Comp. Electro. Society (ACES) Journal*, vol. 29, no. 3, pp. 243-247, 2014.

[6] J. Wang, Y. Yin, X. Liu, and T. Wang, "Trapezoid UWB antenna with dual band-notched characteristics for WiMAX/WLAN bands," *Electron. Lett*., vol. 49, pp. 685-686, 2013.

[7] H. K. Yoon, Y. J. Yoon, H. Kim, and C.-H. Lee, "Flexible ultra-wideband polarisation diversity antenna with band-notch function," *IET Microwave Antennas Propag*., vol. 5, pp. 1463-1470, 2011.

[8] Y. S. Seo, J. W. Jung, H. J. Lee, and Y. S. Lim, "Design of trapezoid monopole antenna with band-notched performance for UWB," *Electron. Lett*., vol. 48, pp. 673-674, 2012.

[9] M. N. Jahromi, A. Falahati, and R. M. Edwards, "Application of fractal binary tree slot to design and construct a dual band-notch CPW-ground-fed ultra-wide band antenna," *IET Microwave Antennas Propag*., vol. 5, pp. 1424-1430, 2011.

[10] P. Gao, L. Xiong, J. Dai, S. He, and Y. Zheng, "Compact printed wide-slot UWB antenna with 3.5/5.5 dual band-notched characteristics," *IEEE Antennas Wireless Propag. Lett*., vol. 12, pp. 983-986, 2013.

[11] M. C. Tang, S. Xiao, T. Deng, Duo Wang, J. Guan, B. Wang, and G.-D. Ge, "Compact UWB antenna with multiple band-notches for WiMAX and WLAN," *IEEE Trans. Antennas Propag*., vol. 59, pp. 1372-1376, 2011.

[12] Q.-X Chu, C.-X. Mao, and H. Zhu, "A compact notched band UWB slot antenna with sharp selectivity and controllable bandwidth," *IEEE Trans. Antennas Propag*., vol. 61, pp. 3961-3966, 2013.

[13] C.-C. Lin, P. Jin, and R. W. Ziolkowski, "Single, dual and tri-band-notched ultrawideband (UWB) antenna using capacitively loaded loop (CLL) resonators," *IEEE Trans. Antennas Propag*., vol. 60, pp. 102-109, 2012.

[14] J. R. Kelly, P. S. Hall, and P. Gardner, "Band-notched UWB antenna incorporating a microstrip open-loop resonator," *IEEE Trans. Antennas Propag*., vol. 59, pp. 3045-3048, 2011.

[15] Y. Sung, "Triple band-notched UWB planar monopole antenna using a modified H-shaped resonator," *IEEE Trans. Antennas Propag*., vol. 61, pp. 953-957, 2013.

[16] D. Jiang, Y. Xu, R. Xu, and W. Lin, "Compact dual-band-notched UWB planar monopole antenna with modified CSRR," *Electron. Lett*., vol. 48, pp. 1250-1251, 2012.

[17]Z. Esmati and M. Moosazadeh, "Dual-band notched ultra-wideband antenna by using step-by-step design inside conductor-backed plane," *Microwave Opt. Technol. Lett*., vol. 55, pp. 1069-1074, 2013.
[18]M. Moosazadeh, A. M. Abbosh, and Z. Esmati, "Design of compact planar ultrawideband antenna with dual-notched bands using slotted square patch and pi-shaped conductor-backed plane," *IET Microw. Antennas Propag*., vol. 6, pp. 290-294, 2012.
[19]S. J. Wu, C. H. Kang, K. H. Chen, and J. H. Tarng, "Study of an ultrawideband monopole antenna with a band-notched open-looped resonator," *IEEE Trans. Antennas Propag*., vol. 58, pp. 1890-1897, 2010.
[20]X.-J. Liao, H.-C. Yang, N. Han, and Y. Li, "UWB antenna with dual narrow band notches for lower and upper WLAN bands," *Electron. Lett*., vol. 46, pp. 1593-1594, 2010.
[21]T. D. Nquyen, D. H. Lee, and H. C. Park, "Design and analysis of compact printed triple band-notched UWB antenna," *IEEE Antennas Wireless Propag. Lett*., vol. 10, pp. 403-406, 2011.
[22]Ansoft High Frequency Structure Simulations (HFSS), Ver. 13, Ansoft Corporation, 2010.
[23]S. Saario, D. V. Thiel, J. W. Lu, and S. G. O'Keefe, "An assessment of cable radiating effects on mobile communications antenna measurements," *Proc. IEEE Int. Symp. Antennas and Propagation*, pp. 550-553, 1997.
[24]H. Arai, *Measurement of Mobile Antenna Systems* (Artech House, 2001).
[25]C. Icheln, J. Krogerus, and P.Vainikainen, "Use of balun chokes in small antenna radiation measurements," *IEEE Trans. Instrum. Meas*., vol. 53, pp. 498-506, 2004.

Zahra Esmati was born in 1987 in Oroumieh, Iran. She received her B.Sc. degree in Electrical Engineering from Azad University, Urmia Branch. From 2015, she is working towards the M.Sc. degree at the University of Western Sydney (UWS). Her research interests include analysis and design of microstrip antennas, monopole antenna, ultra-wideband (UWB) and small antennas for wireless communications, antenna array, array feed networks, and their antenna applications. She is the author or co-author of several refereed journal articles.

Mahdi Moosazadeh was born in 1980 in Oroumieh, Iran. He received his B.Sc. degree in Electrical Engineering from Azad University, Urmia Branch and M.Sc. degree in Electrical Engineering from Science and Research Branch, Tehran Branch. From 2010 until 2012, he was a Teaching Assistant with the Department of Electrical Engineering, Islamic Azad University, Urmia Branch, Iran. From 2013, he is working towards the Ph.D. degree at the University of Western Sydney (UWS). His research interests include analysis and design of microstrip antennas monopole antenna, microwave structures, microwave imaging applications, and electromagnetic theory. He is the author or co-author of several refereed journal articles.

Time-Reversal Through-Wall Microwave Imaging in Rich Scattering Environment Based on Target Initial Reflection Method

Amin B. Gorji and Bijan Zakeri

Department of Electrical and Computer Engineering
Babol Noshirvani University of Technology, Babol, Iran
amin.gorji@stu.nit.ac.ir, zakeri@nit.ac.ir

Abstract ─ In recent years, time reversal (TR) methods have been widely employed in microwave imaging (MI) applications due to their efficient functionality in heterogeneous media. One of the applications turning into a great interest is through-wall microwave imaging (TWMI). In this paper, classic TR method is applied to detect and localize a target obscured by a brick wall inside a rich scattering environment using numerically generated data. Regarding this, it is shown when the signals acquired by a set of receivers are time reversed and backpropagated to the background media, finding an optimum time frame which the constituted image represents a true location of the target becomes infeasible. Indeed, based on target distance and increasing multiple scattering in the media the previously-used maximum E-field method and entropy-based methods fail to select the optimum time frame. As a result, an improved procedure named target initial reflection method (TIRM) is proposed. Even in the case of rich scattering environment, the results show this method prevails over the incapabilities of the former methods.

Index Terms ─ Finite-difference time-domain (FDTD), optimum focusing, rich scattering environment, target initial reflection method (TIRM), through-wall microwave imaging, time reversal (TR).

I. INTRODUCTION

In the area of microwave imaging (MI), the great interest on detection and localization of objects through walls and obstacles has been emerging in recent years. This phenomenon basically arises from various unique civilian and military applications, including non-destructive evaluations, earthquake search and rescue missions, hostage operations or hostile threat assessment situations [1]. In fact, a through-wall microwave imaging (TWMI) system would be capable of collecting information of the total media consisting of target(s) and wall(s), performing a comprehensive process on it, and then identify and localize the target. The way of how to process the collected data in order to get the best performance of the system has opened a gate to the advent and development of various techniques in the last decade. Encouraging results have been obtained with backscattering algorithms [2], synthetic-aperture-radar (SAR) [3], polarimetric-based techniques [4], tomographic approach [5], and high-speed imaging algorithm known as Envelope [6].

However, among the processing algorithms, time reversal (TR) methods have shown that would exploit ultrawideband (UWB) signals and the concept of multipath components in the intervening media to ameliorate the detection capabilities [7]. Originally, TR has been utilized in acoustics [8], but later on has been introduced in electromagnetics and more research has been carried out on subsurface object imaging [9], wireless communication systems [10], bio-malignant tissue detection in early stage breast cancer [11]-[13], and most recently through-wall imaging of the obscured targets [14]-[17].

In TR method, a source radiates a signal to be propagated through a media including the target. The waves are then reflected and the corresponding data are recorded by an array of receivers. By extracting the target responses from the data, reversing them in time and synthetically propagating them back from their respective reception points, an image of the scene is constituted at each time frame, consequently by utilizing an appropriate approach to take an optimum time frame, detection and localization of the target becomes possible. Furthermore, in TWMI applications, TR entails to detect targets through materials including plywood, drywall, solid/hollow brick and concrete, which their relative high permittivity or inhomogeneous structure may result in further burden for selecting the optimum time frame.

In this paper, we embark on solving the problem of finding an optimum time frame which represents a true image of the target. In this regard, maximum electric-field (E-field) method [14] and entropy-based methods [11], [12], [15], [16] have been recently employed in both TWMI and breast cancer detection scenarios. These methods may guarantee maximum amplitude or a tightly focused image corresponding to the detected location of

Submitted On: January 1, 2014
Accepted On: May 10, 2015

the target. However, we show there are situations based on target distance and rich scattering environment in which the preceding methods fail to image the true location of the target. As a result, an alternative improved method, based on initial reflection from the target, which is robust to the effect of these parameters and prevails over previous methods is proposed.

The rest of the paper is organized as follows: in Section II a general description and fundamental theories of TR method for inverse scattering problem is presented. In Section III, the geometry of TWMI problems along with the specifications of computational setup which is carried out numerically using finite-difference time-domain (FDTD) [18] is introduced. In Section IV, the methods of finding an optimum time frame together with the proposed method are fully addressed. The results regarding the performance of the methods to successfully localize the target are completely demonstrated in Sections V. Finally, in Section VI, a summary of the present work and the future contributions is drawn.

II. TR METHOD

A. TR overview

Time reversal (TR) technique is an imaging method based on the invariance of Maxwell's equations under time reversal, which in electromagnetics is known as the principle of reciprocity. In general, the procedure for detection and localization of the scatterer (target) based on TR consists of three main steps shown in Fig. 1.

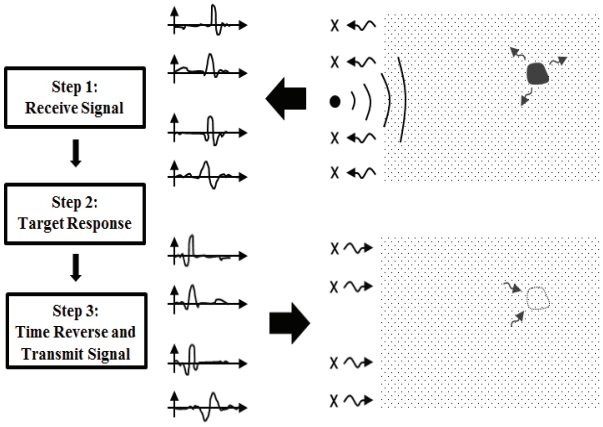

Fig. 1. General scheme of TR method. A source radiates a signal and the scatterer reflects a portion of it back to the TRA. The target responses are then reversed in time and backpropagated to the background media, eventually space-time focusing is achieved at the target location.

First, a source radiates a signal to be propagated through an arbitrary media including the targets as well. Then, the reflected fields from the media are recorded by an array of receiving antennas which in an ideal situation, should be placed all around the media to capture all the possible directions of the reflected waves. However, unlike this full-aspect configuration [19], in other types of scenarios, it is presumably impossible to entirely surround the media and a limited number of arrays are particularly feasible. This limited-aspect configuration is in prevalent use for the applications including TWMI and subsurface objects imaging. Thereupon, the aim of forward propagation step is to collect the data of the media and process them in order to image and localize the targets. Accordingly, the data can be generated either analytically [7], [20], numerically [11]-[14], or physically via on-site measurement [21], in which the first two suffices when one deals with the development of imaging algorithms in the way that spending time and energy on practical measurements is almost cumbersome.

Next, the target response must be extracted from the recorded signal at each array receiver. Since the recorded signal of the media consists of background clutter plus target, assuming that the background is stationary, its solo signature with no target in present can be calculated and collected at each receiver. Now let's assign E_T and E_B as the total and background reflected signals, respectively. Then for each receiver, the target (scattered) response E_S is obtained as:

$$E_S = E_T - E_B . \tag{1}$$

This method of extracting the target response is called background subtraction method. In fact, extracting the target response is the basis of all TR processing methods including Classic TR [11], [12], DORT [9], [22], MUSIC [23] and TRAIC [24]. In scenarios in which E_B cannot be obtained separately, the target response is directly extracted from the total response by applying a time-window on the total signal [9] or matched-filter analysis [25]. However, these methods will surely yield more mathematical efforts. Additionally, in moving target scenarios, the information about E_B may not be required and corresponding target response can be achieved using the total response subtraction of two successive moving target runs. This method is called differential TR and is fully addressed in [26].

In the final step, based on TR processing method used in the previous step, imaging and localization of the target become possible. By time-reversing (phase conjugating in frequency domain) the target responses at each array receiver and synthetically propagating them back to the background media (no target), the wave focuses on the location of target, approximately recreating an image of it. It is obvious this step is performed computationally either analytically by using Green functionals named point spread functions (PSF) [27] or numerically including FDTD [11]-[14], TLM [28], and Ray-Tracing methods [29]. Despite this, unlike the imaging applications, physical back propagation of

the waves may be applied in applications involving actual retransmission of signals such as destruction of kidney stones with ultrasonic waves [30].

B. TR theory of inverse scattering problem

General fundamental theories of TR method can be addressed as following. Suppose a source located at r_s which emits a time domain pulse $P(t)$, and an array of K receivers each located at r_k as in Fig. 2. The fields incident on the target area at r' is then given by:

$$\begin{aligned} E_F(r',t) &= P(t) * G_F(r_s, r', t) \\ &= \int P(\tau) G_F(r_s, r', t-\tau) d\tau \ , \end{aligned} \tag{2}$$

where $G_F(r_s,r,t)$ is the Green's function between any representative point in the media (background+traget) and the radiating point in forward-propagation step. Noting that physical interaction of antennas are not considered and the asterisks * represents time-domain convolution. Here, for the sake of conciseness we are considering scalar two-dimensional form of the fields and Green's functions. Extension to the vector case is also straightforward in principle, but may be complicated to be expressed in general form.

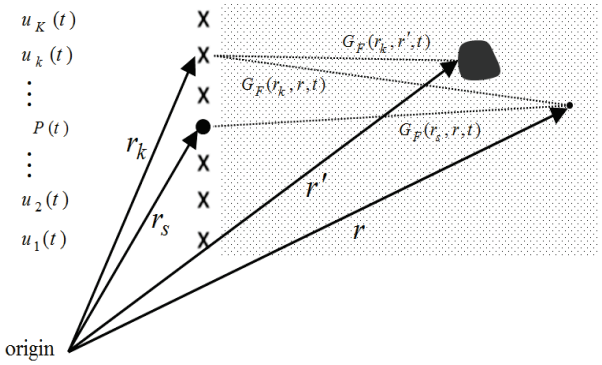

(a)

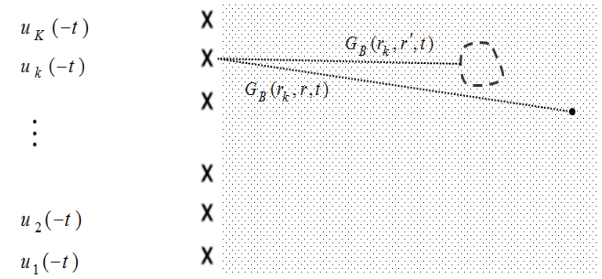

(b)

Fig. 2. TR theory of inverse scattering problem. The source is placed at the center of TRA and the corresponding Green's function between TRA and any point in the media is specified: (a) forward-propagation, and (b) back-propagation.

In continue, the fields are scattered by the target, ignoring multiple interactions between the target and the background media, which is analogous to first order scattering model (Born approximation) [31], the field observed at k^{th} receiver is then obtained as in equation (3). Considering the higher orders of scattering models including second order model and full multiple scattering interactions using Foldy-Lax equations are also investigated in [32]:

$$u_k(t) = \int_{\text{on target}} B(r') E(r',t) * G_F(r', r_k, t) ds' \ , \tag{3}$$

where $B(r')$ is the scattering coefficient of each point on the target area. In fact $B(r')$ represents the conversion of incident fields $E(r',t)$ into equivalent currents that re-radiate as the secondary sources.

Reducing the integral in equation (3) using a high-frequency asymptotic approximation, which is a case for well-resolved point like scatterer, $u_k(t)$ is simplified to:

$$u_k(t) = \hat{B}(r') P(t) * G_F(r_s, r', t) * G_F(r', r_k, t) \ . \tag{4}$$

It is notable that $\hat{B}(r')$ accounts for all terms introduced by the asymptotic approximation, and thus, can be inferred as the average scattering coefficient of the target.

To perform TR process, the scattered fields recorded at each array are time-reversed and back-propagated from their respective positions. The field observed at each point r in the imaging domain is obtained by:

$$E_B(r,t) = \sum_{k=1}^{K} u_k(-t) * G_B(r_k, r, t) \ , \tag{5}$$

where $G_B(r_k,r,t)$ is the Green's function between any representative point in the background-only media and the k^{th} receiver in back-propagation step. Equation (5) is solely enough for one to perform an imaging and localization process using the collected raw data of $u_k(t)$ (actually without knowing about the terms appeared in (4)), and a precise estimation of G_B. The way to estimate G_B, either analytically or numerically is the main core of TR method, particularly for the scenarios in which no exact knowledge about the background media is available [16].

Now, we proceed our discussion to analytically investigate and show how a constructive interference will happen in the imaging domain where $E_B(r,t)$ will respond to the target location. Let's expand equation (5) using equation (4) to obtain equation (6) as:

$$\begin{aligned} E_B(r,t) &= \sum_{k=1}^{K} u_k(-t) * G_B(r_k, r, t) \\ &= \sum_{k=1}^{K} \hat{B}(r') P(-t) * G_F(r_s, r', -t) \\ &\quad * G_F(r', r_k, -t) * G_B(r_k, r, t) \ , \end{aligned} \tag{6}$$

because of reciprocity,

$$G_F(r,r_k,t)=G_F(r_k,r,t). \quad (7)$$

According to Fig. 2, it is interpreted that the only point in which $G_F(r_k,r,t)$ is equivalent to $G_B(r_k,r,t)$ is the location of the formerly existing target, which means for $r=r'$. So,

$$G_F(r_k,r',t)=G_B(r_k,r',t). \quad (8)$$

Using equations (7)-(8) and rewriting equation (6) for $r=r'$, $E_B(r',t)$ is obtained as:

$$E_B(r',t)=\sum_{k=1}^{K}\hat{B}(r')P(-t)*G_F(r_s,r',-t) *G_B(r_k,r',-t)*G_B(r_k,r',t). \quad (9)$$

Based on equation (9), $G_B(r_k,r',-t)*G_B(r_k,r',t)$ is indeed representing a matched-filter with a maximum at $t=0$. As a result, maximum of $E_B(r,t)$ happens for spatial-temporal location of $r=r'$ and $t=0$ (optimum time frame) which in fact the location of the target.

Further discussion about the interpretation of $t=0$ is given in section IV, where we are dealing in more details with the optimum time methods to focus the waves on the true location of the target.

III. GEOMETRY AND COMPUTATIONAL SETUP

A. Geometry of rich scattering environment

The geometries of rich scattering environment for TWMI problem considered in this work are shown in Fig 3. A standard commercial solid brick cell with ε_r=4.8 and σ=0.001 S/m [33] is used to construct a wall with 10 cm thickness at the front and inner partitions with 5 cm thickness behind it. A linear array with aperture size of a=90 cm consisting of 16 isolated z-directed infinitesimal electric dipoles with equidistant separation of 6 cm are placed 20 cm in front of the wall to act as the receiving probes. These probes are also in use as the transmitter in synthetically backpropagation step of TR imaging algorithm. A z-directed electric dipole is also placed at the center of the array line as the monostatic transceiver to cylindrically radiate the excitation signal toward the scene in TM_z mode. More information regarding TE_z and full polarimetric polarization can also be found in [34]. A cylindrical disk scatterer with diameter D=6 cm and distance L away from the array with ε_r=47 is introduced as the target in near distance for L/a<1 (Fig. 3 (a)) and far distance for L/a>1 (Fig. 3 (b)). The locations of the target are shown in Table 1.

Table 1: Target locations for TWMI problem

Target Location (x,y)	(70,40)	(160,85)
Distance Ratio L/a	(near) < 1	(far) > 1

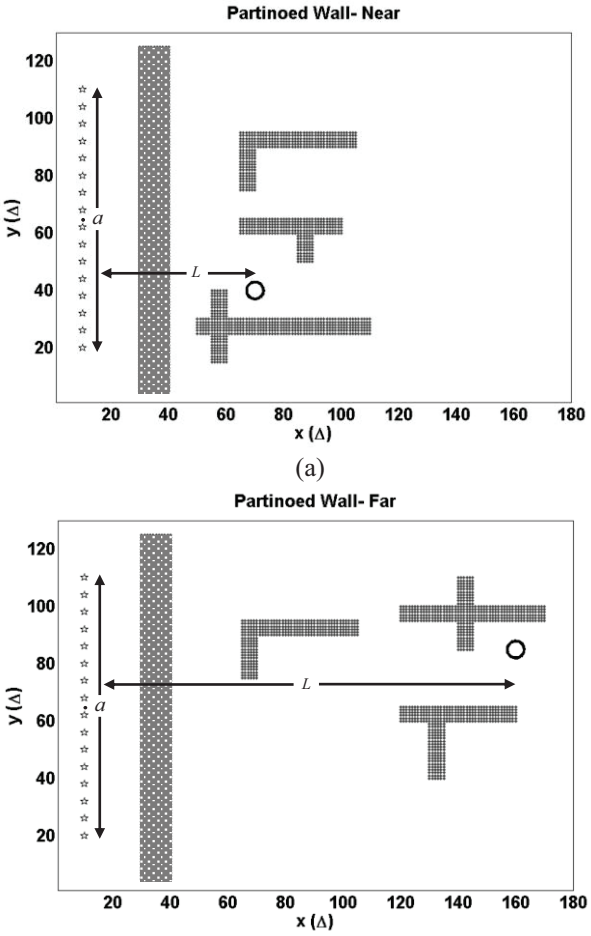

Fig. 3. Geometry of rich scattering environment for TWMI problem. The source (dot) and TRA (stars) are shown. The aperture size and target distance are also denoted by a and L, respectively. The target is located at: (a) near distance, and (b) far distance.

B. FDTD computational setup

Both forward-propagation and back-propagation steps of TR method are carried out numerically using two-dimensional finite-difference-time-domain (FDTD) method. Taking into account the standard FDTD notation, the update equations of back-propagation step for TM_z case take the following form as in equations (10)-(12).

$$H_x^{n'+\frac{1}{2}}(i,j+\tfrac{1}{2})=\left(\frac{1-\frac{\sigma(i,j)\Delta t}{2\mu(i,j)}}{1+\frac{\sigma(i,j)\Delta t}{2\mu(i,j)}}\right)H_x^{n'-\frac{1}{2}}(i,j+\tfrac{1}{2})+ \left(\frac{\frac{\Delta t}{\mu(i,j)}}{1+\frac{\sigma(i,j)\Delta t}{2\mu(i,j)}}\right)\left(-\frac{E_z^{n'}(i,j+1)-E_z^{n'}(i,j)}{\Delta y}\right), \quad (10)$$

$$H_y^{n'+\frac{1}{2}}(\mathrm{i}+\tfrac{1}{2},\mathrm{j}) = \left(\frac{1-\frac{\sigma(\mathrm{i},\mathrm{j})\Delta t}{2\mu(\mathrm{i},\mathrm{j})}}{1+\frac{\sigma(\mathrm{i},\mathrm{j})\Delta t}{2\mu(\mathrm{i},\mathrm{j})}}\right) H_y^{n'-\frac{1}{2}}(\mathrm{i}+\tfrac{1}{2},\mathrm{j}) + \left(\frac{\frac{\Delta t}{\mu(\mathrm{i},\mathrm{j})}}{1+\frac{\sigma(\mathrm{i},\mathrm{j})\Delta t}{2\mu(\mathrm{i},\mathrm{j})}}\right)\left(\frac{E_z^{n'}(\mathrm{i}+1,\mathrm{j}) - E_z^{n'}(\mathrm{i},\mathrm{j})}{\Delta x}\right), \quad (11)$$

$$E_z^{n'+1}(\mathrm{i},\mathrm{j}) = \left(\frac{1-\frac{\sigma(\mathrm{i},\mathrm{j})\Delta t}{2\varepsilon(\mathrm{i},\mathrm{j})}}{1+\frac{\sigma(\mathrm{i},\mathrm{j})\Delta t}{2\varepsilon(\mathrm{i},\mathrm{j})}}\right) E_z^{n'}(\mathrm{i},\mathrm{j}) + \left(\frac{\frac{\Delta t}{\varepsilon(\mathrm{i},\mathrm{j})}}{1+\frac{\sigma(\mathrm{i},\mathrm{j})\Delta t}{2\varepsilon(\mathrm{i},\mathrm{j})}}\right)\left(\frac{H_y^{n'+\frac{1}{2}}(\mathrm{i}+\frac{1}{2},\mathrm{j}) - H_y^{n'+\frac{1}{2}}(\mathrm{i}-\frac{1}{2},\mathrm{j})}{\Delta x} - \frac{H_x^{n'+\frac{1}{2}}(\mathrm{i},\mathrm{j}+\frac{1}{2}) - H_x^{n'+\frac{1}{2}}(\mathrm{i},\mathrm{j}-\frac{1}{2})}{\Delta y}\right), \quad (12)$$

where n′ is the time step corresponding to backpropagation step. The 2D computational domain is gridded into dimensions of X×Y=180×130 cm, with a uniform spatial discretization of Δx=Δy=Δs and a time step of Δt (the stability Courant Factor S_c=c*Δt/Δs is chosen to be 0.5). The value of Δs is so assigned to create at least 10 nodes per λ_m, where λ_m denotes the wavelength corresponding to the maximum frequency content of the excitation signal. The maximum runtime is also set to maxtime=600Δt for near distance target and maxtime=1200Δt for far distance target which are sufficiently enough for the incident wave to travel from the source to the right end of the domain in a round-trip. The boundary condition is also a convolutional perfectly matched layer (CPML) formulated with recursive-convolution technique to provide reflectionless truncation of the computation domain. The thickness of CPML is set to 5Δs at all four sides of the boundaries.

It is also worth noting that in medium with high losses or dispersion, the performance of TR imaging based on standard FDTD may become degraded due to double attenuation in forward and back propagation steps. To dispel this problem, a modification on FDTD update equations may be performed at back-propagation step in order to compensate for losses or dispersion caused by the background media [11], [35].

C. Excitation signal

In general, various constraints and specifications including particular electrical characteristics of the media, signal penetration through wall materials, target dimensions, and also portability of the setup will determine the best operating frequency range for microwave penetrating radar (MPR) systems. Practically such systems operate in the range of 0.5-10 GHz [36] and a minimum system bandwidth of nearly to 30% with respect to the center frequency is essential for providing sufficient resolution for target detection [4]. In this work, a UWB Modulated Gaussian pulse is considered as the excitation sources by:

$$P(t) = e^{\left(\frac{t-t_s}{t_p}\right)^2}.\sin\left(2\pi f_p(t-t_s)\right), \quad (13)$$

where t_p and t_s are temporal width and temporal shift, respectively, which specify the spectrum bandwidth of $P(t)$ and f_p is the center frequency. These parameters are then assigned as f_p=1.95 GHz, t_p=0.35 ns and t_s=2*t_p which stimulate the target in Mie (resonance) scattering mode [37]. The excitation pulse and its frequency spectrum are also depicted in Fig. 4.

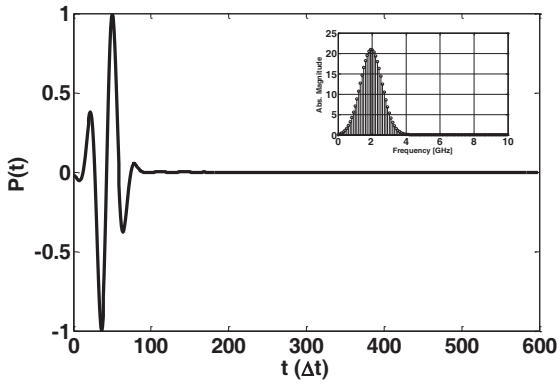

Fig. 4. Modulated Gaussian excitation signal source and its frequency spectrum for f_p = 1.95 GHz, t_p = 0.35 ns, and t_s = 2*t_p.

IV. OPTIMUM TIME FRAME METHODS

After exciting the source and collecting the data of the reflected signals, we obtain target responses by using background subtraction methods. The target responses are then time reversed and backpropagated to the background media consisting of the front wall and inner partitions with no prior information of the target location. Accordingly, the computationally backpropagated fields constitute an image of the scene at each frame of the time. Next, we embark on solving a problem of finding an optimum time frame which represents an image of the scene with true focusing on target location.

A. Maximum E-field method

As reported by Zheng, et al. [14], in this method the maximum electric field amplitude of the imaging domain at each time frame is found and then plotted along the time axis. The optimum time frame is then selected as a time which corresponds to the maximum of this plot, as:

$$t_{opt}^{\text{Zheng}} = \left\{t' : E_{\max}(t') > E_{\max}(t),\ t_0 < t < t_1 \ \ \&\ \ t \neq t'\right\}. \quad (14)$$

B. Entropy-based methods

In an ideal full-aspect configuration, the behavior of backpropagated waves on target location is such that it first converges toward the target and a time after that it diverges from it. In order to find a time frame which is

corresponding to the convergence-divergence instant, a minimum entropy criterion will be defined as in (16) and (17) reported by Cresp, et al. [15] and Kosmas, et al. [11], respectively:

$$p_{ij}^{n} = \frac{E_n{}^2(i,j)}{\sum\sum_{i,j} E_n{}^2(i,j)}, \tag{15}$$

$$\overset{\text{Cresp}}{ENT}(n) = \frac{-\sum\sum p_{ij}^{n} \ln p_{ij}^{n}}{\max(p_{ij}^{n})}, \tag{16}$$

$$\overset{\text{Kosmas}}{ENT}(n) = \frac{\left[\sum\sum_{i,j} E_n{}^2(i,j)\right]^2}{\sum\sum_{i,j} E_n{}^4(i,j)}, \tag{17}$$

where n represents the time frame, (i,j) the grid cell coordinates and the summation is over the entire imaging domain. The defined entropy is calculated at each time frame and a time instant when it becomes minimized is selected as an optimum time frame. Unlike the previous method, minimum entropy method guarantees a tightly focused image rather than maximum field amplitude at the focusing point.

C. Target initial reflection method (TIRM)

In this work, we examine the functionality and efficiency of the above focusing methods and investigate the situations in which they may fail to image the true location of the target. As a result, an alternative optimum time focusing method which is valid for all situations and prevails over the shortcomings of other methods must be utilized. In this part we are attempting to characterize this proposed method, named target initial reflection method (TI-RM), which is primarily based on ray-tracing method.

Let's postulate the geometry of a wall and a target which is placed in an arbitrary location in free space as shown in Fig. 5. Now, we follow the transmitted wave starting at the source point, propagating into the scene, possessing interactions with the wall and the target, and then reflecting back to the receiving arrays. In addition, we are interested to monitor the target response waveforms of three particular receivers; the source receiver, which corresponds to a receiver at the source point (R_S), the nearest receiver to the target (R_N), and the farthest receiver away from the target (R_F). The source is excited and after a delay of t_d it reaches to the corresponded peak value. In its path toward the target, it travels the route A_1B_1, B_1C_1 and C_1D, where D is the point which the transmitted wavefront is incident on the target. The target scatters the fields and a portion of them are received by the arrays. For the source receiver R_S, the scattered wave travels DC_1, C_1B_1 and B_1A_1, likewise the wave travels DC_2, C_2B_2 and B_2A_2 to reach to nearest receiver R_N, and DC_3, C_3B_3 and B_3A_3 to reach to farthest receiver R_F. The detailed waveforms monitored by each of these three receivers are shown in Fig. 6.

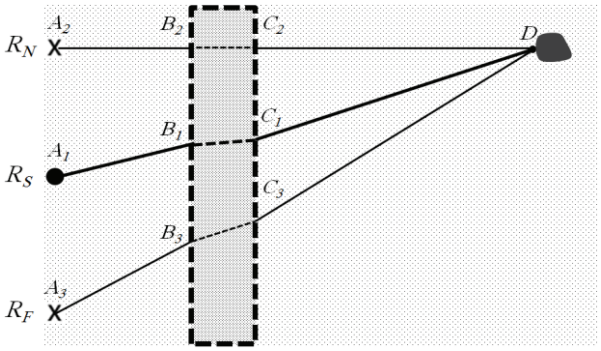

Fig. 5. Detailed route path of forward and back propagated waveforms for source receiver (R_S), nearest receiver (R_N), and farthest receiver (R_F).

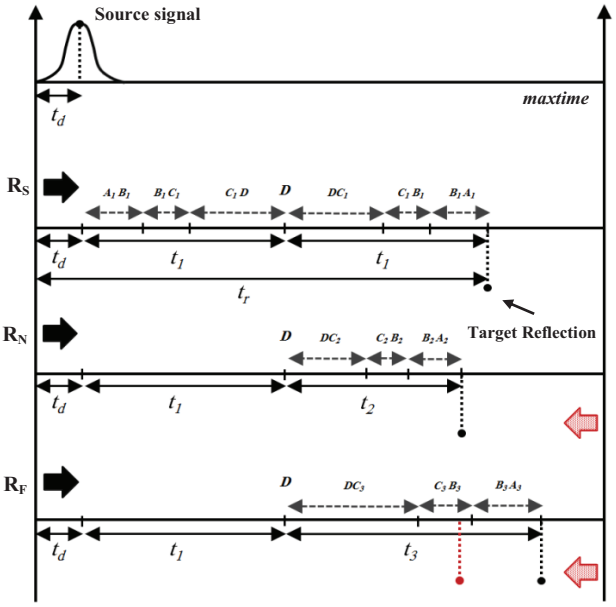

Fig. 6. Signal waveforms monitored by each of source receiver (R_S), nearest receiver (R_N), and farthest receiver (R_F). Time reversing and backpropagating the waveform is analogous to start propagation from the right end of the axis.

The received fields are then time-reversed and back-propagated, which is analogous to start the propagation from the right end of each waveform (maxtime) and move toward the left (Fig. 6). According to the depicted waveforms, the first antenna starting backpropagation process is the farthest one, it travels along the path toward the target up until the time the nearest antenna as the last antenna starts backpropagation. Based on Fig. 6, it is derived that the two waveforms will simultaneously

reach the target location D if they both travel only the remained time amount of t_2, which is the stacked time for the scattered waveform to travel from the target D to the nearest receiver at A_2. As a result, these two waveforms together with the waveform from the rest of the arrays will arrive at the same time to point D and their amplitudes are constructively added to each other to construct a contrasted image of the location of he target. More detailed route path of backpropagated waveforms are shown in Fig. 5.

In other words, the optimum time frame is a time instant in which the nearest receiver R_N is powered on and then continues traveling for t_2 sec. To formulize the optimum time, we may write:

$$t_{opt} = \underbrace{\left(\text{maxtime-}(t_d + t_1 + t_2)\right)}_{R_N \text{ is powered on}} + t_2 \qquad (18)$$

$$= \text{maxtime} - (t_d + t_1) \ ,$$

where t_1 is the stacked time for the source waveform to travel from starting point A_1 to target D or vice versa. According to the waveform of the source receiver,

$$t_r = t_d + 2t_1 \longrightarrow t_1 = \frac{t_r - t_d}{2}, \qquad (19)$$

where t_r is the time when the initial reflection from the target arrives to the source receiver. As a result by knowing the maxtime along with t_d and t_r, substituting equation (19) in equation (18), the optimum time frame t_{opt} could be readily derived as:

$$t_{opt} = \text{maxtime} - \frac{t_r + t_d}{2} \ . \qquad (20)$$

The optimum time frame based on TIRM guarantees well that the back-propagated waves of the entire receivers will simultaneously focus on a desired location which represents the target location. In the next section, it is investigated that this method yields to accurate results even in the case of rich scattering environment.

V. TARGET LOCALIZATION AND RESULTS

In this section, we are going through the localization of target for the geometries showed in Fig. 3 and apply focusing methods introduced in Section IV to select the optimum time frame for target location. Figure 7 shows the corresponding curves for each of focusing methods. Plots of Fig. 7 (a) and Fig. 7 (b) pertain to near and far distance ratios of the target, respectively. The optimum time frame derived by TIRM is determined by a vertical dashed line in each case. All the curves are plotted starting from 200Δt which is an instant the backpropagated waves pass the wall, up to the corresponding maximum runtime. The curves are also normalized with respect to their maximum value in order to become possible to be compared with each other. As it can be seen, in general plots of maximum E-field method have an increasing manner as it reaches to the maximum and then starts to descend. The entropy-based methods may also face inconsistent manner in the case of rich scattering environment rather than a monotonically decreasing manner, which is observed in the case of free space background [38]. Table 2 shows the optimum time frame concluded from the above curves for each method. The difference (in terms of Δt) between each method with respect to TIRM is also cited in the parentheses.

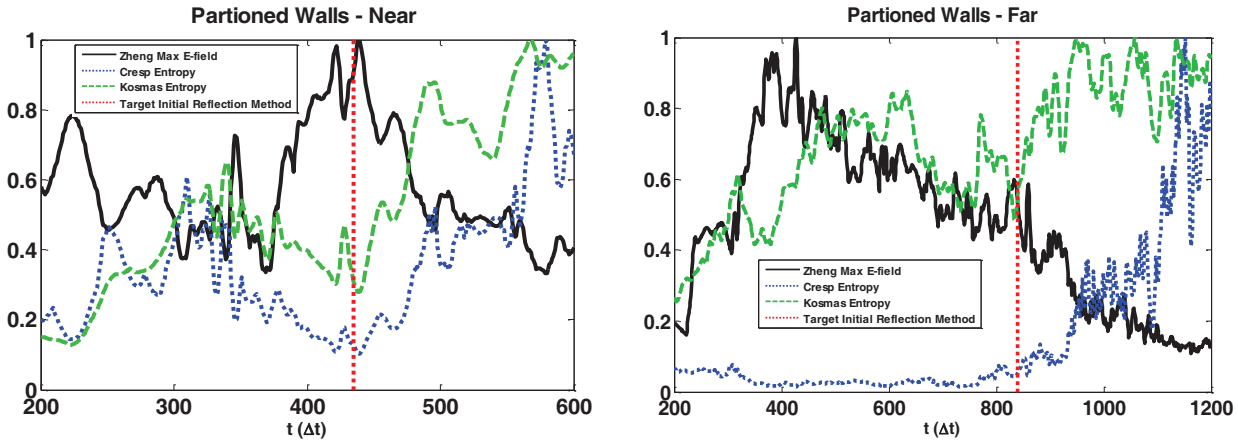

Fig. 7. Curves of optimum time frame for Zheng maximum E-field method, Cresp entropy-based method Eq. (16), Kosmas entropy-based method Eq. (17), and Target Initial Reflection Method (TIRM). (a) Near distance target, and (b) far distance target.

Table 2: Optimum time frame concluded from each method

	Near Distance	Far Distance
Zheng max E-field	439 (4)	427 (413)
Cresp entropy	439 (4)	733 (107)
Kosmas entropy	222 (213)	200 (640)
TIRM	435	840

Next, the images of spatial refocusing constituted by each method are demonstrated in Fig. 8 and Fig. 9 regarding near distance and far distance target location, respectively. The focused wave features a red spot and the true location of the target is drawn as a small circle. For near distance target (Fig. 8), it is clear from the images that the accurate focusing is almost achieved for all the methods including maximum E-field method, entropy-based methods, and TIRM. However entropy-based method of equation (17) yields an amount of displacement which is observed in the case of rich scattering environment. On the other hand, when target is located at far distance (Fig. 9), for all methods except TIRM, focusing is achieved with considerable amount of displacement to left from the true location of the target which leads to an inaccurate estimation about the existence of the target at its true location. It can be seen that no spot representing the target is even constituted for maximum E-field method and entropy-based method of equation (17).

More quantitative comparison of the images are depicted in Fig. 10, where for each method, the difference between the estimated location of the target and the true location is calculated and represented on account of target diameter D. In addition, the same results corresponded to free space case is also derived to further compare the effect of rich scattering environment on the performance of TR optimum time frame methods.

It is evident from Fig. 10, that when multiple scattering in the medium increases, for near distance target the performance of entropy-based method of equation (17) is degraded. All other methods including maximum E-field method, entropy-based method of equation (16), and TIRM are improved and they could estimate the target with less than 50 percent (0.5ΔD) displacement error. This improvement is in accordance with the concept of TR method that more scattering in the medium increases the spatial-temporal resolution of the focused waves. On the other hand, for far distance target the performance of all former optimum time frame methods are substantially degraded for both free space and rich scattering environment. However, the only method estimating the location of the target as accurate as possible is TIRM with still approximately less than 50 percent (0.5ΔD) displacement error which is quite appreciable. In general, we can conclude that TIRM prevails over all other methods without being totally dependent on the target near/far locations and free space or rich scattering background.

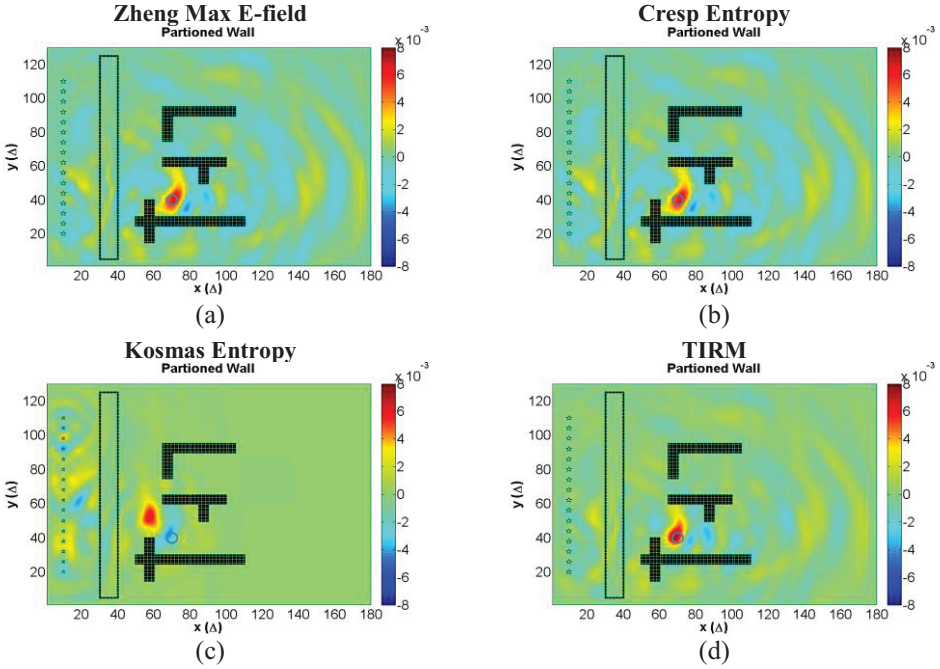

Fig. 8. The images constituted by TR method for target located at near distance. (a) Zheng Maximum E-field Method, (b) Cresp Entropy-based Methods Eq. (16), (c) Kosmas Entropy-based Methods Eq. (17), (d) TIRM. It is seen true focusing is achieved for almost of them. However, Kosmas Entropy-based method faces an amount of displacement to left with respect to the target.

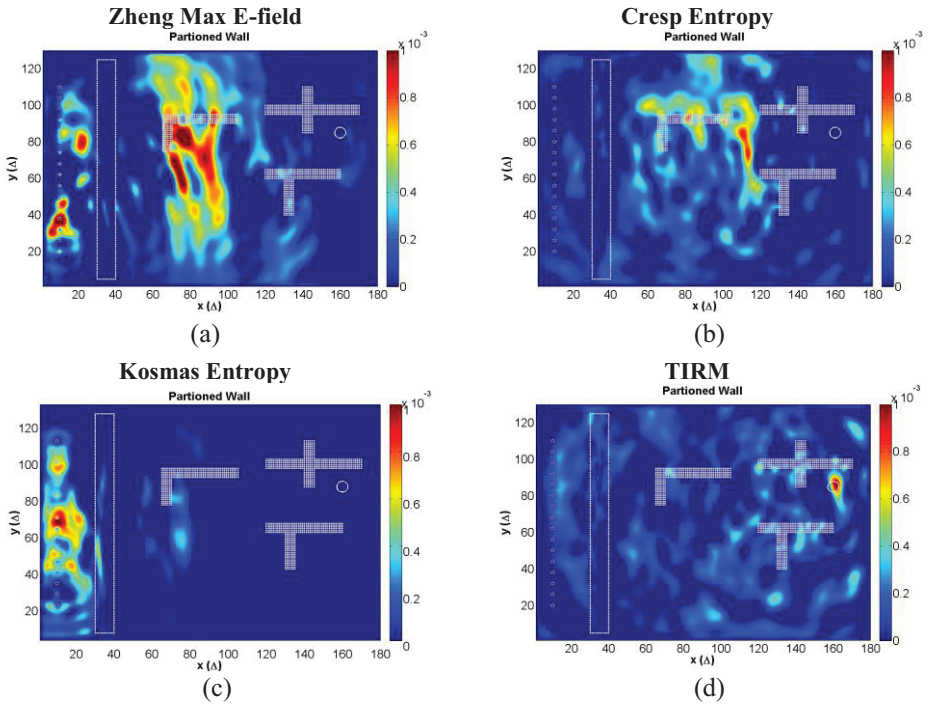

Fig. 9. The images constituted by TR method for target located at far distance: (a) Zheng maximum E-field method, (b) Cresp entropy-based methods Eq. (16), (c) Kosmas entropy-based methods Eq. (17), and (d) TIRM. It is seen only TIRM leads to a true estimation of the target location.

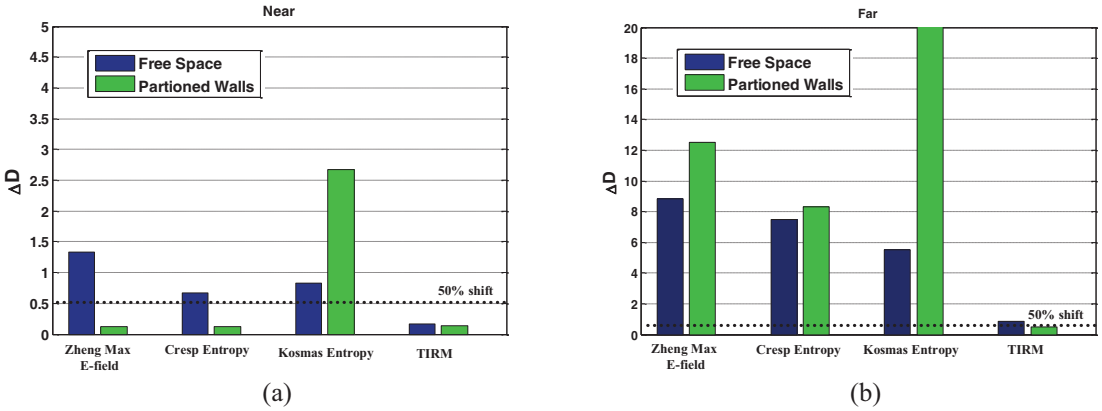

Fig. 10. Difference between estimated and true location of the target for maximum E-field method, entropy-based methods Eq. (16) and Eq. (17), and TIRM. Both free space and rich scattering environment are investigated for: (a) near distance target, and (b) far distance target.

VI. CONCLUSION

In this paper, TR method was employed to detect and localize a target for through-wall microwave imaging (TWMI) problem in a rich scattering environment. Regarding this, the data were generated numerically using FDTD method for both forward and back propagation steps. In order to find the optimum time frame which represents an image of true target location, maximum E-field method, entropy-based methods, and the proposed Target Initial Reflection Method (TIRM) were introduced. The target was placed in two general locations defined as near and far distance. The results showed when the target is located at near distance the performance of almost all methods improved in rich scattering environment compared to free space. However, for far distance in both free space and rich scattering environment, all methods except TIRM significantly failed to accurately estimate the target location. In general, TIRM prevailed over all other methods without being totally dependent on the target

near/far locations and free space or rich scattering background.

Last but not least, future works may include investigating the performance of TR imaging technique and optimum time frame methods with respect to target scattering mode and frequency contents of the excitation signal. In addition, employing this discussion to be gone through for the media of much heterogeneity including biological and under-the-ground imaging applications are of great interest.

REFERENCES

[1] M. G. Amin and F. Ahmad, *Through-the-Wall Radar Imaging: Theory and Applications*, Villanova Univ., Villanova, PA, Sep. 27, 2012.

[2] R. Zetik, S. Crabbe, J. Krajnak, P. Peyerl, J. Sachs, and R. Thoma, "Detection and localization of person behind obstacles using M-sequence through-the-wall radar," in *Proc. SPIE*, vol. 6201, 2006.

[3] X. Liu, H. Leung, and G. Lampropoulos, "Effect of wall parameters on ultra-wideband synthetic aperture through-the-wall radar imaging," *IEEE Trans. Aerosp. Electron. Syst.*, vol. 48, no. 4, pp. 3435-3449, Oct. 2012.

[4] K. M. Yemelyanov, N. Engheta, A. Hoorfar, and J. A. McVay, "Adaptive polarization contrast techniques for through-wall microwave imaging applications," *IEEE Trans. Geosci. Remote Sens.*, vol. 47, no. 5, pp. 1362-1374, May 2009.

[5] F. Soldovieri, R. Solimene, and G. Prisco, "A multiarray tomographic approach for through-wall imaging," *IEEE Trans. Geosci. Remote Sens*., vol. 46, no. 4, pp. 1192-1199, Apr. 2008.

[6] S. Kidera, T. Sakamoto, and T. Sato, "High-resolution 3-D imaging algorithm with an envelope of modified spheres for UWB through-the-wall radars," *IEEE Trans. Antennas Propag*., vol. 57, no. 11, pp. 3521-3529, Nov. 2009.

[7] A. Ishimaru, S. Jaruwatanadilok, and Y. Kuga, "Time reversal effects in random scattering media on superresolution, shower curtain effects, and backscattering enhancement," *Radio Sci*., vol. 42, 2007.

[8] M. Fink, D. Cassereau, A. Derode, C. Prada, P. Roux, M. Tanter, J. Thomas, and F. Wu, "Time-reversed acoustics," *Rep. Prog. Phys*., vol. 63, pp. 1933-1995, 2000.

[9] G. Micolau, M. Saillard, and P. Borderies, "DORT method as applied to ultrawideband signals for detection of buried objects," *IEEE Trans. Geosci. Remote Sens*., vol. 41, no. 8, pp. 1813-1820, Aug. 2003.

[10] H. T. Nguyen, J. B. Andersen, G. F. Pedersen, P. Kyritsi, and P. C. F. Eggers, "Time reversal in wireless communications: a measurement-based investigation," *IEEE Trans. Wireless Commun*., vol. 5, no. 8, pp. 2242-2252, Aug. 2006.

[11] P. Kosmas and C. M. Rappaport, "Time reversal with the FDTD method for microwave breast cancer detection," *IEEE Trans. Microw. Theory Techn*., vol. 53, no. 7, pp. 2317-2323, Jul. 2005.

[12] P. Kosmas and C. M. Rappaport, "FDTD-based time reversal for microwave breast cancer detection: localization in three dimensions," *IEEE Trans. Microw. Theory Techn.*, vol. 54, no. 4, pp. 1921-1927, Apr. 2006.

[13] Y. Chen, E. Gunawan, K. S. Loon, S. Wang, C. B. Soh, and T. C. Putti, "Time-reversal ultrawideband breast imaging: pulse design criteria considering multiple tumors with unknown tissue properties," *IEEE Trans. Antennas Propag*., vol. 56, no. 9, pp. 3073-3077, Sep. 2008.

[14] W. Zheng, Z. Zhao, and Z. Nie, "Application of TRM in the UWB through wall radar," *PIER*, vol. 87, pp. 279-296, 2008.

[15] A. Cresp, I. Aliferis, M. J. Yedlin, Ch. Pichot, and J. Y. Dauvignac, "Investigation of time-reversal processing for surface-penetrating radar detection in a multiple-target configuration," in *Proc. 5th European Radar Conference*, Amsterdam, The Netherland, Oct. 2008.

[16] L. Li, W. Zhang, and F. Li, "A novel autofocusing approach for real-time through-wall imaging under unknown wall characteristics," *IEEE Trans. Geosci. Remote Sens.*, vol. 48, no. 1, pp. 423-431, Jan. 2010.

[17] W. Zhang, A. Hoorfar, and L. Li, "Through-the-wall target localization with time reversal MUSIC method," *PIER*, vol. 106, pp. 75-89, 2010.

[18] A. Taflove and S. C. Hagness, *Computational Electrodynamics: The Finite-Difference Time-Domain Method*, 3rd ed., Boston, MA: Artech House, 2005.

[19] J. P. Stang, "A 3D active microwave imaging system for breast cancer screening," *Ph.D. Dissertation*, Dept. of Elec. Eng., Duke Univ., Durham, NC, 2008.

[20] T. Chan, S. Jaruwatanadilok, Y. Kuga, and A. Ishimaru, "Numerical study of the time-reversal effects on super-resolution in random scattering media and comparison with an analytical model," *Waves in Random and Complex Media*, vol. 18, no. 4, pp. 627-639, Nov. 2008.

[21] D. Liu, S. Vasudevan, J. Krolik, G. Bal, and L. Carin, "Electromagnetic time-reversal source localization in changing media: experiment and analysis," *IEEE Trans. Antennas Propag*., vol. 55, no. 2, pp. 344-354, Feb. 2007.

[22] M. Yavuz and F. L. Teixeira, "Full time-domain DORT for ultrawideband electromagnetic fields in dispersive, random inhomogeneous media," *IEEE*

Trans. Antennas Propag., vol. 54, no. 8, pp. 2305-2315, Aug. 2006.

[23] A. J. Devaney, "Time reversal imaging of obscured targets from multistatic data," *IEEE Trans. Antennas Propag*., vol. 53, no. 5, pp. 1600-1610, May 2005.

[24] J. F. Moura and Y. Jin, "Time reversal imaging by adaptive interference canceling," *IEEE Trans. Signal Process.*, vol. 56, no. 1, pp. 233-247, Jan. 2006.

[25] P. Kosmas and C. M. Rappaport, "A matched-filter FDTD-based time reversal approach for microwave breast cancer detection," *IEEE Trans. Antennas Propag*., vol. 54, no. 4, pp. 1257-1264, Apr. 2006.

[26] N. Maaref, P. Millot, X. Ferrieres, C.Pichot, and O. Picon, "Electromagnetic imaging method based on time reversal processing applied to through-the-wall target localization," *PIER*, vol. 1, pp. 59-67, 2008.

[27] D. Liu, J. Krolik, and L. Carin, "Electromagnetic target detection in uncertain media: time-reversal and minimum-variance algorithms," *IEEE Trans. Geosci. Remote Sens.*, vol. 45, no. 4, pp. 934-944, Apr. 2007.

[28] I. Scott, "Developments in time-reversal of electromagnetic fields using the transmission-line modeling method," *Ph.D. Dissertation*, School of Elec. and Electron. Eng., Univ. of Nottingham, Nottingham, UK, 2009.

[29] D. Liu, G. Kang, L. Li, Y. Chen, S. Vasudevan, W. Joines, Q. H. Liu, J. Krolik, and L. Carin, "Electromagnetic time-reversal imaging of a target in a cluttered environment," *IEEE Trans. Antennas Propag*., vol. 53, no. 9, pp. 3058-3066, Sep. 2005.

[30] G. Montaldo, P. Roux, A. Derode, C. Negreira, and M. Fink, "Ultrasonic shock wave generator using 1-bit time-reversal in a dispersive medium: application to lithotripsy," *Appl. Phys. Lett*., vol. 80, pp. 897-899, 2002.

[31] E. Marengo and F. K. Gruber, "Single-snapshot signal subspace methods for active target location: part II: born-approximable case," *Proc. 2nd IASTED Int. Conf. on Antennas, Radar, and Wave Propag.*, Banff, Alberta, Canada, Jul. 19-21, 2005.

[32] A. Devaney, E. Marengo, and F. Gruber, "Time-reversal-based imaging and inverse scattering of multiply scattering point targets," *J. Acoust. Soc. Amer*., vol. 118, pp. 3129-3138, 2005.

[33] C. Thajudeen, A. Hoorfar, and F. Ahmad, "Measured complex permittivity of walls with different hydration levels and the effect on power estimation of TWRI target returns," *PIER*, vol. 30, pp. 177-199, 2011.

[34] M. Yavuz and F. L. Teixeira, "A numerical study of time-reversed UWB electromagnetic waves in continuous random media," *IEEE Antennas Wireless Propag. Lett.*, vol. 4, pp. 43-46, 2005.

[35] M. Yavuz and F. L. Teixeira, "Frequency dispersion compensation in time reversal techniques for UWB electromagnetic waves," *IEEE Geosci. Remote Sens. Lett.*, vol. 2, no. 2, pp. 233-237, Apr. 2005.

[36] J. D. Taylor, *Ultrawideband Radar: Applications and Design*, CRC Press, 2012.

[37] A. B. Gorji, "Scattering of complex media by using numerical methods in electromagnetics," *M.Sc. Thesis*, Dept. of Elec. Eng., Babol Noshirvani Univ. of Tech., Babol, Iran, 2013.

[38] A. B. Gorji and B. Zakeri, "An improved time-reversal-based target localization for through-wall microwave imaging," *Journal of Electrical and Computer Engineering Innovations (JECEI)*, vol. 1, no. 2, pp. 89-97, 2013.

Amin B. Gorji was born in Cardiff, UK, in 1989. He received the B.Sc. and M.Sc. degrees in Electrical Engineering from Babol Noshirvani University of Technology, Babol, Iran, in 2011 and 2013, respectively. Since 2014, he has been pursuing his Ph.D. in the Department of Electrical and Computer Engineering, Iowa State University, US.

In 2010 to 2014, he has been an Assistant and Researcher with the Antenna and Microwave Laboratory, Babol Noshirvani University of Technology, and starting from 2014 he joined the Center for Non-Destructive Evaluation (CNDE) and Electromagnetic Materials Design and Characterization (EMDC) group of Iowa State University.

His scientific fields of interest include microwave imaging based on time-reversal techniques, Ground-Penetrating Radar (GPR) imaging methods, and microwave non-destructive evaluations.

Bijan Zakeri was born in Babol, Iran, in 1974. He received the M.Sc. and Ph.D. degrees in Electromagnetics Engineering from Amirkabir "Polytechnic" University of Technology, Tehran, Iran, in 1999 and 2007, respectively.

Since 2010, he is an Assistant Professor with Babol Noshirvani University of Technology, Babol, Iran. He is currently the head of Department of Communication and the Director of Antenna and Microwave Laboratory at Babol

Noshirvani University of Technology. He is also a Member of Iranian Association of Information and Communication Technology.

His current research activities are in the fields of computational electromagnetics, microwave imaging, inverse scattering, radar microwave subsystems design, UWB antenna, and Polin-SAR remote sensing.

Fast Orthonormal Propagator Direction-Finding Algorithm Based on Fourth-Order Cumulants

Heping Shi, Wen Leng, Anguo Wang, Hua Chen, and Yuchu Ji

School of Electronic Information Engineering
Tianjin University, Tianjin 300072, China
shiheping@tju.edu.cn, lengwen@tju.edu.cn, agwang@tju.edu.cn, dkchenhua@tju.edu.cn, jiyuchu@126.com

Abstract ─ In this paper, a low complexity approach called modified fourth-order cumulants orthonormal propagator method (MFOC-OPM) is proposed for direction-of-arrival (DOA) estimation of incident narrowband signals impinging on a uniform linear array (ULA). In the proposed algorithm, the modified fourth-order cumulants (MFOC) matrix is achieved via removing the redundant information encompassed in the primary fourth-order cumulants (FOC) matrix, and then the direction-of-arrivals (DOAs) estimation of source signals can be resolved by exploiting the orthonormal propagator method (OPM). Without any spectrum-peak searching and eigenvalue decomposition (EVD) of the MFOC matrix, the theoretical analysis coupled with simulation results show that in comparison with the MFOC-MUSIC algorithm, the resultant algorithm can reduce computational complexity significantly, as well as yield good estimation performance in both spatially-white noise and spatially-color noise environments.

Index Terms ─ Direction-of-arrival (DOA), fourth-order cumulants (FOC), orthonormal propagator method (OPM), spatially-color noise, spatially-white noise.

I. INTRODUCTION

Over the past two decades, the issue of finding the direction-of-arrival (DOA) of source signals has received considerable attention in array signal processing fields such as radar, sonar, underwater acoustics, radio astronomy, speaker localization, mobile communication systems and wireless communication systems [1-2]. The classical high-resolution subspace algorithms for direction-of-arrivals (DOAs) estimation, such as multiple signal classification (MUSIC) [3-4] and estimation of signal parameters via rotation invariance techniques (ESPRIT) [5-6] algorithms, have provided satisfactory performance. Because these subspace-based algorithms break through the limitation of the Rayleigh, the super resolution DOAs estimation of the radiation sources can be achieved [7-8]. However, the aforementioned algorithms are not only sensitive to the noise, but also require a priori information of the noise. In addition, these algorithms employ either the eigenvalue decomposition (EVD) or singular value decomposition (SVD) to obtain the signal subspace and the noise subspace. Therefore, the computational complexity of these subspace-based algorithms is high especially when the number of sensors and snapshots is relatively large. This indicates that these conventional high-resolution algorithms might not be useful when the low-computational cost and highly real-time data process are required.

To alleviate aforesaid drawbacks, various useful algorithms have been proposed. Fortunately, the fourth-order cumulants (FOC) are asymptotically insensitive to Gaussian noise. Therefore, FOC have been shown to be a promising substitute for second-order statistic (SOS) in solving DOA estimation, since it is not necessary to know or to estimate the noise covariance as long as the noise is normally distributed [9-10], which is a reasonable assumption in practical situations. In order to reduce computational complexity, the propagator method (PM) in [11-12] and its improved algorithm called orthonormal propagator method (OPM) [13] are presented. The OPM executes a linear operator instead of EVD or SVD to obtain the signal subspace and the noise subspace, which can decrease the computational complexity effectively. Moreover, the OPM can obtain the same estimation performance as the high-resolution subspace-based algorithms but more efficient in computation in medium and high signal-to-noise ratio (SNR) conditions. An OPM-like (FOC-OPM) algorithm [14], based on FOC, is proposed to achieve good estimation performance. However, the computational complexity of this method is high since a great number of redundant information is contained in the FOC matrix. In [15], the authors considered the redundancy among the FOC matrix through analyzing the effective array aperture, which can increase the computational complexity greatly. Moreover, due to the finite sampling snapshots, there exists an estimation error between the FOC statistical matrix of the array received signal and its ideal matrix, thus the capacity of DOA estimation degrades.

Submitted On: April 3, 2013
Accepted On: December 10, 2014

In this paper, a novel MFOC-OPM algorithm is presented. The emphasis of this paper is on the investigation of the computational load. In the presented algorithm, the reduced-rank FOC matrix is obtained by removing the redundant information encompassed in the primary FOC matrix. Meanwhile, the effective extended aperture of the virtual array keeps unchanged for improving estimation performance. Then the DOAs estimation of source signals can be estimated by using the OPM to reduce computational complexity. Compared with the MFOC-MUSIC method in [16], the proposed algorithm not only has the advantages of good performance but also the reduction of computation.

The rest of the paper is organized as follows. The signal model is briefly introduced in Section II. The proposed algorithm is discussed in detail in Section III. In Section IV, simulation results are presented to verify the effectiveness of the proposed algorithm. Finally, some concluding remarks are made in Section V.

For the purpose of description, the following notations are used. Boldface italic lower/upper case letters denote vectors/matrices. $(\cdot)^*$, $(\cdot)^T$ and $(\cdot)^H$ stand for the conjugation, transpose and conjugate transpose of a vector/matrix, respectively. The notation E(x), *cum*(x) and $\otimes$ separately denote the expectation operator, the cumulants, and the Kronecker product, respectively.

II. SIGNAL MODEL

Consider M narrowband far-field plane wave sources $s_l(t)$, (l=1,…,M) impinging on a uniform linear array (ULA) with N identical omni-directional sensors, where the inter-element spacing is half of the wavelength. Assume that the source signals are stationary and mutually independent. The noise is the additive white/color Gaussian one, and statistically independent of the sources. Let the first sensor of the ULA be the reference, and then the observed data received by the kth sensor can be expressed as:

$$x_k(t)=\sum_{i=1}^{M}a_k(\theta_i)s_i(t)+n_k(t),\quad k=1,\cdots,N, \tag{1}$$

where $s_l(t)$ is the ith source, $n_k(t)$ is the Gaussian noise at the kth sensor and $\alpha_k(\theta_i)$ is the response of kth sensor corresponding to the ith source;

$$a_k(\theta_i)=\exp(j2\pi(d/\lambda)k\sin\theta_i), \tag{2}$$

where λ is the central wavelength, d is the spacing between two adjacent sensors. Thus, one column vector, which contains all the observed data received by N sensors, can be achieved:

$$\begin{aligned}\begin{bmatrix}x_1(t)\\x_2(t)\\\vdots\\x_N(t)\end{bmatrix}&=\begin{bmatrix}1&1&\cdots&1\\\exp(j\alpha_1)&\exp(j\alpha_2)&\cdots&\exp(j\alpha_M)\\\vdots&\vdots&\ddots&\vdots\\\exp(j(N-1)\alpha_1)&\exp(j(N-1)\alpha_2)&\cdots&\exp(j(N-1)\alpha_M)\end{bmatrix}\begin{bmatrix}s_1(t)\\s_2(t)\\\vdots\\s_M(t)\end{bmatrix}+\begin{bmatrix}n_1(t)\\n_2(t)\\\vdots\\n_N(t)\end{bmatrix}\\&=\begin{bmatrix}\boldsymbol{a}(\alpha_1)&\boldsymbol{a}(\alpha_2)&\cdots&\boldsymbol{a}(\alpha_M)\end{bmatrix}\begin{bmatrix}s_1(t)\\s_2(t)\\\vdots\\s_M(t)\end{bmatrix}+\begin{bmatrix}n_1(t)\\n_2(t)\\\vdots\\n_N(t)\end{bmatrix},\end{aligned} \tag{3}$$

where α_i=exp($2\pi(d/\lambda)sin\theta_i$). Therefore, the matrix form of (3) can be modeled as:

$$\boldsymbol{X}(t)=\boldsymbol{A}\boldsymbol{S}(t)+\boldsymbol{N}(t), \tag{4}$$

where $\boldsymbol{X}(t)=[x_1(t),\ldots,x_N(t)]^T$ is the $N\times1$ array output vector, $\boldsymbol{S}(t)=[s_1(t),\ldots,s_M(t)]^T$ is the $M\times1$ source vector, $\boldsymbol{A}=[\boldsymbol{a}(\theta_1),\ldots,\boldsymbol{a}(\theta_M)]$ is the $N\times M$ array manifold matrix and $\boldsymbol{N}(t)=[n_1(t),\ldots,n_N(t)]^T$ denotes the $N\times1$ complex Gaussian noise vector.

Assume that the source signals are zero-mean stationary random process, the FOC can be defined as:

$$\begin{aligned}cum(k_1,k_2,k_3^*,k_4^*)=&E(x_{k_1}(t)x_{k_2}(t)x_{k_3}^*(t)x_{k_4}^*(t))-\\&E(x_{k_1}(t)x_{k_3}^*(t))E(x_{k_2}(t)x_{k_4}^*(t))-\\&E(x_{k_1}(t)x_{k_4}^*(t))E(x_{k_2}(t)x_{k_3}^*(t))-\\&E[x_{k_1}(t)x_{k_2}(t)]E[x_{k_3}^*(t)x_{k_4}^*(t)]\\&k_1,k_2,k_3,k_4\in[1,\cdots,N],\end{aligned} \tag{5}$$

where $x_{k_m}(m=1,2,3,4)$ is the stochastic process. Apparently, $cum(k_1,k_2,k_3^*,k_4^*)$ has N^4 values with the change of k_1,k_2,k_3,k_4. For simplicity, equation (5) can be collected in matrix form, which is denoted by cumulants matrix $\boldsymbol{C}_4$. Therefore, the N^4 values can be stored in the $N^2\times N^2$ matrix $\boldsymbol{C}_4$, and $cum(k_1,k_2,k_3^*,k_4^*)$ appears as the [$(k_1$-1)$N+k_2$]th row and [$(k_3$-1)$N+k_4$]th column of $\boldsymbol{C}_4$;

$$\begin{aligned}&\boldsymbol{C}_4[(k_1-1)N+k_2,(k_3-1)N+k_4]\\&=cum(k_1,k_2,k_3^*,k_4^*)\\&=cum(\sum_{l=1}^{M}\boldsymbol{a}_l(k_1)s_l(t),\sum_{l=1}^{M}\boldsymbol{a}_l(k_2)s_l(t),\sum_{l=1}^{M}\boldsymbol{a}_l(k_3^*)s_l(t),\\&\quad\sum_{l=1}^{M}\boldsymbol{a}_l(k_4^*)s_l(t))+cum(n_{k_1}(t),n_{k_2}(t),n_{k_3^*}(t),n_{k_4^*}(t))\\&=cum(\sum_{l=1}^{M}\boldsymbol{a}_l(k_1)s_l(t),\sum_{l=1}^{M}\boldsymbol{a}_l(k_2)s_l(t),\sum_{l=1}^{M}\boldsymbol{a}_l(k_3^*)s_l(t),\\&\quad\sum_{l=1}^{M}\boldsymbol{a}_l(k_4^*)s_l(t))\\&=\sum_{l=1}^{M}\sum_{m=1}^{M}\sum_{i=1}^{M}\sum_{j=1}^{M}\boldsymbol{a}_l(k_1)\boldsymbol{a}_m(k_2)\boldsymbol{a}_i(k_3^*)\boldsymbol{a}_j(k_4^*)\\&\quad cum(s_l(t)s_m(t)s_i(t)s_j(t))\\&=\sum_{l=1}^{M}\boldsymbol{a}_l(k_1)\boldsymbol{a}_l(k_2)\boldsymbol{a}_l(k_3^*)\boldsymbol{a}_l(k_4^*)\\&\quad cum(s_l(t)s_l(t)s_l(t)s_l(t))\\&=\boldsymbol{B}\boldsymbol{C}_s\boldsymbol{B}^H,\end{aligned} \tag{6}$$

where $\boldsymbol{B}$ and $\boldsymbol{C}_s$ represent the extended array manifold and the FOC matrix of incident source signals, respectively. $\boldsymbol{B}=\boldsymbol{A}\otimes\boldsymbol{A}$, and each column of $\boldsymbol{B}$ is $\boldsymbol{b}(\theta)=\boldsymbol{a}(\theta)\otimes\boldsymbol{a}(\theta)$. It is obvious that $\boldsymbol{b}(\theta)$ is a $N^2\times1$ vector, which means that the array aperture of ULA is extended. That is, the number of resolved source signals is no less than that of sensors.

III. THE PROPOSED ALGORITHM

A. The effective array aperture extended

As proven in [17], an array of N arbitrary identical omni-directional sensors can be extended to at most of

N^2-N+1. Especially, the number of virtual elements is 2N-1 for ULA according to [17]. In order to discuss the effective aperture of ULA, three real elements (N=3) are considered, and $\boldsymbol{b}(\theta)$ can be expressed in detail as follows:

$$\begin{aligned}\boldsymbol{b}(\theta) &= \boldsymbol{a}(\theta) \otimes \boldsymbol{a}(\theta) \\ &= [1, z, z^2]^T \otimes [1, z, z^2]^T \\ &= [1, z, z^2, z, z^2, z^3, z^2, z^3, z^4]^T,\end{aligned} \tag{7}$$

where $z=exp(j2\pi(d/\lambda)sin\theta)$ and $\boldsymbol{a}(\theta)=[1, z, z^2]$. Equation (7) shows that there is a lot of redundancy in expanded steering vector $\boldsymbol{b}(\theta)$. That is, only from 1th to Nth and all kNth (k=2,...,N) items of the $\boldsymbol{b}(\theta)$ are valid, while others are redundant ones. In order to eliminate these repetitive elements, a (2N-1)×(2N-1) matrix $\boldsymbol{R}_4$ is firstly defined. Next, the 1th to Nth and all kNth (k=2,...,N) rows of $\boldsymbol{C}_4$ are taken out in sequence, and then store these rows in the 1th to (2N-1)th row of the new matrix $\boldsymbol{R}_4$. The same operation is performed on the 1th to Nth and all kNth (k=2,...,N) columns of $\boldsymbol{C}_4$ to obtain the 1th to (2N-1)th columns of $\boldsymbol{R}_4$. Similar to equation (6), $\boldsymbol{R}_4$ can be expressed as:

$$\begin{aligned}\boldsymbol{R}_4 &= \sum_{l=1}^{M}\sum_{m=1}^{M}\sum_{i=1}^{M}\sum_{j=1}^{M} \boldsymbol{d}_l(k_1)\boldsymbol{d}_m(k_2)\boldsymbol{d}_i(k_3^*)\boldsymbol{d}_j(k_4^*) \\ &\quad cum(s_l(t)s_m(t)s_i(t)s_j(t)) \\ &= \sum_{l=1}^{M} \boldsymbol{d}_l(k_1)\boldsymbol{d}_l(k_2)\boldsymbol{d}_l(k_3^*)\boldsymbol{d}_l(k_4^*) \\ &\quad cum(s_l(t)s_l(t)s_l(t)s_l(t)) \\ &= \boldsymbol{D}\boldsymbol{C}_s\boldsymbol{D}^H,\end{aligned} \tag{8}$$

where $\boldsymbol{D}$ denotes the extended array manifold without redundancy, and each column of $\boldsymbol{D}$ has the form of $\boldsymbol{d}(\theta)=[1,z,...,z^{2N-2}]^T$. Therefore, the reduced-dimension $\boldsymbol{R}_4$ not only contains all of the information about the original matrix $\boldsymbol{C}_4$, but also keeps the extended array aperture unchanged.

B. The MFOC-OPM algorithm

In practical applications, the actual $\boldsymbol{C}_4$ cannot be achieved. Therefore, we have to estimate $\hat{\boldsymbol{C}}_4$ from the received data by array measurements. Instead, we utilize the estimated value $\hat{\boldsymbol{R}}_4$ in place of $\boldsymbol{R}_4$, and then the DOAs estimation can be achieved by performing OPM on the $\hat{\boldsymbol{R}}_4$. Under the assumption of the independent sources, since $\boldsymbol{D}$ is a Vandermonde matrix as long as θ_i comes from M different directions, the matrix $\boldsymbol{D}$ is column full rank. That is, only M rows of the matrix $\boldsymbol{D}$ are linearly independent, and the remaining rows of matrix $\boldsymbol{D}$ can be expressed as a linear combination of the M rows. Without loss of generality, assume that the first M rows of matrix $\boldsymbol{D}$ are linear independent, and then the matrix $\boldsymbol{D}$ can be partitioned as follows:

$$\boldsymbol{D} = \begin{bmatrix}\boldsymbol{D}_1 \\ \boldsymbol{D}_2\end{bmatrix}, \tag{9}$$

where the dimension of $\boldsymbol{D}_1$ and $\boldsymbol{D}_2$ are M×M and (2N-1-M)×M, respectively. The propagator matrix $\boldsymbol{P}$, which is a unique linear operator, can be written as:

$$\boldsymbol{P}^{\mathrm{H}}\boldsymbol{D}_1 = \boldsymbol{D}_2. \tag{10}$$

Defining:

$$\boldsymbol{Q}^{\mathrm{H}} = [\boldsymbol{P}^{\mathrm{H}} \quad -\boldsymbol{I}_{2N-1-M}]. \tag{11}$$

According to (9) and (11):

$$\boldsymbol{Q}^{\mathrm{H}}\boldsymbol{D} = [\boldsymbol{P}^{\mathrm{H}} \quad -\boldsymbol{I}_{2N-1-M}]\begin{bmatrix}\boldsymbol{D}_1 \\ \boldsymbol{D}_2\end{bmatrix} = \boldsymbol{0}_{(2N-1-M)\times M}, \tag{12}$$

where $\boldsymbol{I}_{(2N\text{-}1\text{-}M)}$ is a (2N-1-M)×(2N-1-M) identity matrix. The equation (12) shows that the columns of $\boldsymbol{Q}$ are orthogonal to the extended steering vectors $\boldsymbol{d}(\theta)$ and the subspace of the $\boldsymbol{d}(\theta)$ is equal to the signal subspace. According to the orthogonal principle between the signal subspace and the noise subspace, the subspace of $\boldsymbol{Q}$ is equivalent to the noise subspace.

Now, the spatial spectrum of the PM algorithm is defined as:

$$p(\theta) = \frac{1}{\boldsymbol{d}^{\mathrm{H}}(\theta)\boldsymbol{Q}\boldsymbol{Q}^{\mathrm{H}}\boldsymbol{d}(\theta)}. \tag{13}$$

The key problem of the PM is how to estimate the propagator matrix $\boldsymbol{P}$ from the array manifold matrix. However, in real environments, the array manifold matrix is usually unknown. Obviously, it is known from equation (8) that the matrix $\boldsymbol{D}$ is included in the $\boldsymbol{R}_4$. Therefore, the propagator matrix $\boldsymbol{P}$ can be estimated by substituting $\boldsymbol{R}_4$ for $\boldsymbol{D}$. In order to improve the estimation accuracy, the reduced-dimension $\hat{\boldsymbol{R}}_4$ is partitioned into two submatrices:

$$\hat{\boldsymbol{R}}_4 = \begin{bmatrix}\hat{\boldsymbol{R}}_{41} \\ \hat{\boldsymbol{R}}_{42}\end{bmatrix}, \tag{14}$$

where the dimension of $\hat{\boldsymbol{R}}_{41}$ and $\hat{\boldsymbol{R}}_{42}$ are M×(2N-1) and (2N-1-M)×(2N-1), respectively, and then the estimated propagator matrix $\hat{\boldsymbol{P}}$ can be obtained by minimizing the cost function $\xi(\hat{\boldsymbol{P}})$:

$$\xi(\hat{\boldsymbol{P}}) = \left\| \hat{\boldsymbol{R}}_{42} - \hat{\boldsymbol{P}}^{\mathrm{H}}\hat{\boldsymbol{R}}_{41} \right\|_F^2, \tag{15}$$

where $\|\cdot\|_F$ indicates the Frobenius norm, and then the optimal solution $\hat{\boldsymbol{P}}$ is given by:

$$\hat{\boldsymbol{P}} = (\hat{\boldsymbol{R}}_{41}\hat{\boldsymbol{R}}_{41}^{\mathrm{H}})^{-1}\hat{\boldsymbol{R}}_{41}\hat{\boldsymbol{R}}_{42}^{\mathrm{H}}. \tag{16}$$

Then,

$$\hat{\boldsymbol{Q}}^{\mathrm{H}} = [\hat{\boldsymbol{P}}^{\mathrm{H}} \quad -\boldsymbol{I}_{2N-1-M}]. \tag{17}$$

The difference between PM and MUSIC algorithm is that the columns of $\hat{\boldsymbol{Q}}$ are not orthogonal. In order to introduce the orthogonalization, the orthonormalized matrix $\hat{\boldsymbol{Q}}_0$ is obtained as follows:

$$\hat{\boldsymbol{Q}}_0 = \hat{\boldsymbol{Q}}(\hat{\boldsymbol{Q}}^{\mathrm{H}}\hat{\boldsymbol{Q}})^{-1/2}. \quad (18)$$

Till now, the implementation of the proposed algorithm with finite array data can be summarized as follows:

Step 1 Estimate $\hat{\boldsymbol{C}}_4$ from the received data by (6).

Step 2 Obtain the reduced-dimension matrix $\hat{\boldsymbol{R}}_4$ by removing the redundant items of the expanded matrix $\hat{\boldsymbol{C}}_4$ according to (8).

Step 3 Achieve the linear operator $\hat{\boldsymbol{P}}$ according to (15) and (16), and then calculate the orthonormalized matrix $\hat{\boldsymbol{Q}}_0$ based on (18).

Step 4 Estimate the DOAs of source signals with the help of the following spatial spectrum $\hat{p}_0(\theta)$.

$$\hat{p}_0(\theta) = \frac{1}{\boldsymbol{d}^{\mathrm{H}}(\theta)\hat{\boldsymbol{Q}}_0\hat{\boldsymbol{Q}}_0{}^{\mathrm{H}}\boldsymbol{d}(\theta)}. \quad (19)$$

C. Complexity analysis

Regarding the computational complexity, we only consider the major part, which involves in cumulant matrix construction, the linear operation, EVD implementation and one-dimensional (1-D) spectrum-peak searching. The computational complexity of proposed algorithm is analyzed in comparison with the MFOC-MUSIC algorithm [14]. For MFOC-MUSIC algorithm, the major computations involved are to calculate the $N^2\times N^2$ cumulant matrix $\boldsymbol{C}_4$, to perform EVD of the reduced-dimension $(2N\text{-}1)\times(2N\text{-}1)$ cumulant matrix $\boldsymbol{R}_4$ and to perform 1-D spectrum-peak searching. Therefore, the computational complexity of the MFOC-MUSIC algorithm is $O((9N^4L)+(4/3)(2N\text{-}1)^3+(180/\Delta\theta)(2N\text{-}1)^2)$, where L and $\Delta\theta$ denote the number of snapshots and the scanning interval, respectively. For proposed MFOC-OPM algorithm, the major computational complexity is to form one $N^2\times N^2$ cumulant matrix $\boldsymbol{C}_4$ and perform the linear operator on the reduced-dimension $(2N\text{-}1)\times(2N\text{-}1)$ cumulant matrix $\boldsymbol{R}_4$, since it doesn't require EVD and spectrum-peak searching. Therefore, the computational complexity of the proposed algorithm is $O((9N^4L)+(M(2N\text{-}1)^2))$. From the analysis above, it is obvious that the proposed algorithm has lower computational cost than the MFOC-MUSIC algorithm, especially when the number of sensors and snapshots increases.

IV. SIMULATION RESULTS

In this section, simulation results are provided to validate the effectiveness of the proposed algorithm both in spatially-white noise and spatially-color noise environments, respectively. A three-element ULA (N=3) with $\lambda/2$ spacing is employed. Consider three mutually independent far-field source signals (M=3) coming from {-20°, 20°, 45°}. The noise is assumed to be spatial white or color complex Gaussian, and the SNR is defined relative to each source signal. The mentioned algorithms are carried out by 500 independent Monte-Carlo trials. Two performance indices, called normalized probability of success (NPS) and average estimate variance (AEV), are defined to evaluate the performance of the two algorithms:

$$\mathrm{AEV} = \frac{\sum_{i=1}^{M}\mathrm{var}\,\hat{\theta}_i}{M},\ i=1,\cdots M \quad (20)$$

$$\mathrm{NPS} = \frac{\Upsilon_{suc}}{\mathrm{T}_{total}} \quad (21)$$

where $\hat{\theta}_i$ is the estimate of real θ_i. The Υ_{suc} and T_{total} denote the times of success and Monte-Carlo trial, respectively. Furthermore, a successful experiment is that satisfies $\max(|\hat{\theta}_i-\theta_i|)<\varepsilon$, and ε equals 0.8 and 1.6 for comparison versus SNR and snapshot, respectively.

Experiment 1: AEV and NPS versus SNR

In the first experiment, we examine the performance of the proposed algorithm against SNR. The number of snapshots L is 2000, and the SNR is varied from 5 to 25 dB. Figures 1 and 2 show the AEV of the DOAs estimation against input SNR in both spatially-white noise and spatially-color noise environments, respectively. It can be observed from Figs. 1 and 2 that the MFOC-OPM provides almost the same performance as the MFOC-MUSIC algorithm at low SNR. Figure 3 displays the NPS of the DOAs estimation against the SNR. Similar to Figs. 1 and 2, Fig. 3 achieves a similar performance to the MFOC-MUSIC algorithm even if at low SNR. Moreover, as the SNR increases, the performance curves of each figure tend to become consistent. Although the MFOC-OPM performs quite like MFOC-MUSIC algorithm at low, medium and high SNR, the computational complexity of the proposed method is significantly lower than that of the MFOC-MUSIC algorithm. The reason is that the proposed algorithm doesn't require EVD and spectrum-peak searching.

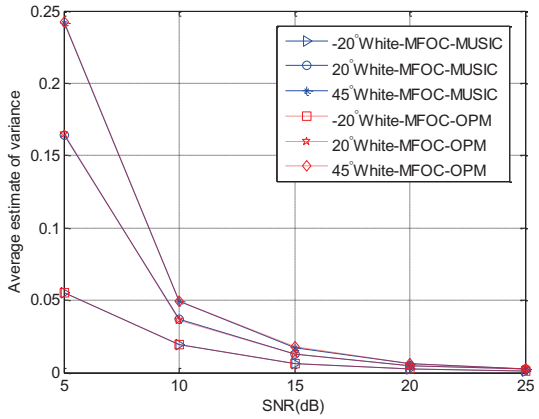

Fig. 1. AEV comparisons versus SNR in white situation.

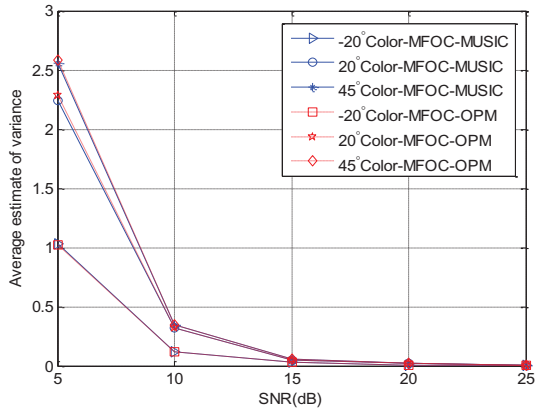

Fig. 2. AEV comparisons versus SNR in color situation.

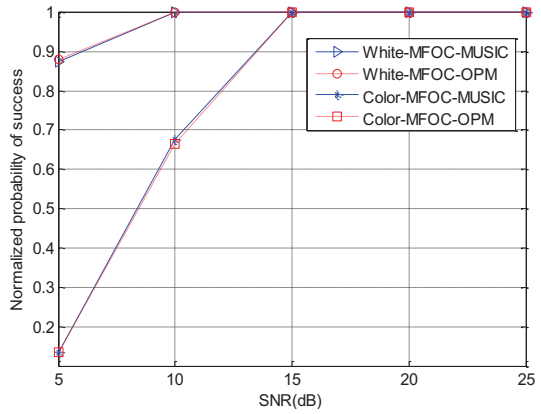

Fig. 3. NPS comparisons versus SNR.

Experiment 2: AEV and NPS versus snapshots

In the second experiment, we consider the same scenario as the first one at different number of snapshots. When the SNR is set to be 10 dB, the performance curves of AEV and NPS versus the number of snapshots in both spatially-white noise, and spatially-color noise environments are plotted in Figs. 4, 5 and 6, respectively. It can be seen from Figs. 4, 5 and 6 that the performance of the MFOC-OPM is approximately identical to that of the MFOC-MUSIC algorithm at low SNR. Furthermore, due to the small snapshots case, the curves of the two algorithms display sharp fluctuation as the number of snapshots is varied from 400 to 800. Moreover, Figs. 4, 5 and 6 illustrate the performance of the two algorithms under the white noise situation is better than that of the color noise situation. As the snapshots increases, the performance curves of each figure tend to become stabilized. Therefore, we can come to a conclusion that the estimated performance of the MFOC-OPM and MFOC-MUSIC algorithms becomes optimal when the snapshots number goes to infinity. However, as the analysis given in section III.C, the complexity of the MFOC-OPM is obviously smaller than that of the MFOC-MUSIC algorithm, and the convergence speed of the MFOC-OPM is much faster than that of the MFOC-MUSIC algorithm due to without using EVD and spectrum-peak searching. The merit of the proposed algorithm lies in the simple and efficient implementation in comparison to the MFOC-MUSIC algorithm.

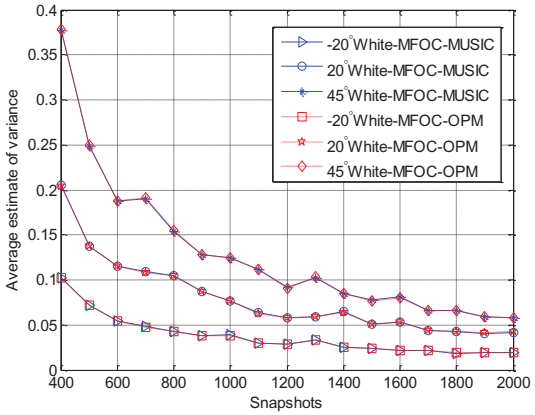

Fig. 4. AEV comparisons versus snapshots in white situation.

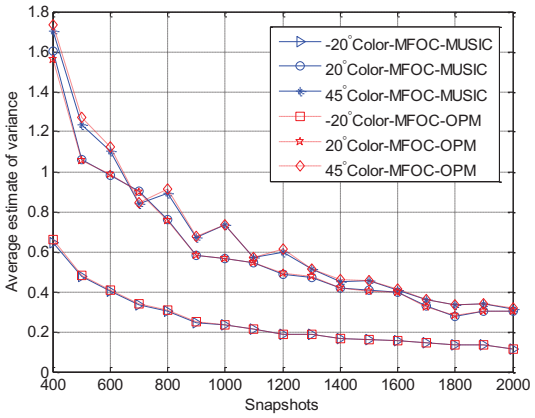

Fig. 5. AEV comparisons versus snapshots in color situation.

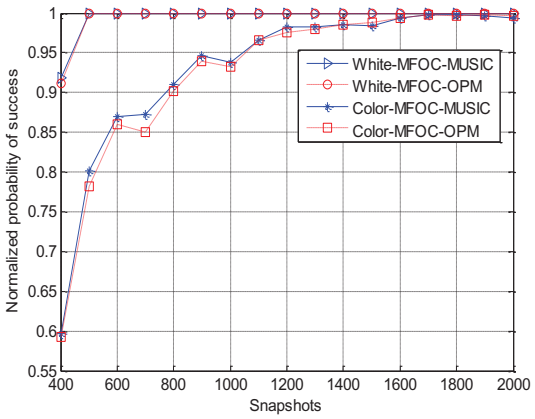

Fig. 6. NPS comparisons versus snapshots.

Experiment 3: Computational complexity versus number of sensors and snapshots

In the last experiment, the computational burden required by the proposed algorithm is compared with the MFOC-MUSIC algorithm. The number of the source signals is set to be M=3. For MFOC-MUSIC algorithm, the scanning interval is defined as $\Delta\theta$=0.01. Figure 7 shows the computational complexity of the two algorithms as a function of the number of sensors (from N=3 to N=10) when the number of snapshots is L=50. Figure 8 shows the computational complexity of the two algorithms as a function of the number of snapshots (from L=100 to L=1000) when the number of sensors is N=3. Figures 7 and 8 clearly show that the proposed algorithm achieves less computational load than MFOC-MUSIC algorithm as the number of sensors and snapshots increases, respectively. This is consistent with the theoretical analysis given in Section III.C.

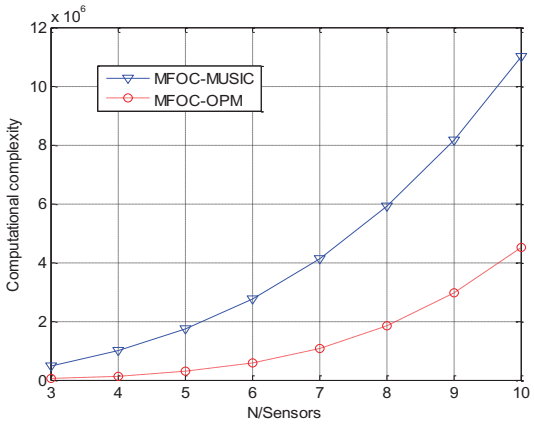

Fig. 7. Computational complexity comparison versus the number of sensors.

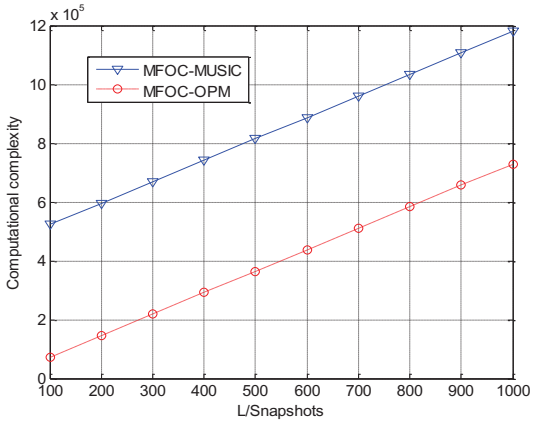

Fig. 8. Computational complexity comparison versus the number of snapshots.

V. CONCLUSION

In this paper, a low complexity DOA estimation algorithm called the MFOC-OPM has been proposed. In the proposed algorithm, the extended effective array aperture can resolve the number of sources more than or equal to that of the array elements, and the proposed algorithm can almost perform like MFOC-MUSIC algorithm especially in low SNR and small number of snapshots. Moreover, the proposed algorithm has the advantage of reduced computational load due to the fact that it doesn't require EVD and spectrum-peak to obtain its signal subspace and noise subspace. Therefore, such an advantage is highly desirable for practical applications when the low-computational cost and highly real-time data process are required. Simulation results demonstrate the effectiveness of the proposed algorithm both in spatially-white noise and in spatially-color noise environments.

ACKNOWLEDGMENT

This work was supported partially by the National Natural Science Foundation of China (no. 61002010) and the project of the State Key Laboratory of Millimeter Waves (no. K201314).

REFERENCES

[1] H. Krim and M. Viberg, "Two decades of array signal processing research: the parametric approach," *IEEE Signal Processing Magazine*, vol. 13, no. 4, pp. 67-94, Jul. 1996.

[2] I. Bekkerman and J. Tabrikian, "Target detection and localization using MIMO radars and sonars," *IEEE Trans. Signal Process.*, vol. 54, no. 10, pp. 3873-3883, 2006.

[3] R. O. Schmidt, "Multiple emitter location and signal parameter estimation," *IEEE Trans. Antennas and Propagation*, vol. 34, no. 3, pp. 276-280, Mar. 1986.

[4] E. M. Al-Ardi, R. M. Shubair, and M. E. Al-Mualla, "Direction of arrival estimation in a multipath environment: an overview and a new contribution," *Applied Computational Electromagnetics Society Journal*, vol. 21, no. 3, pp. 226-239, Nov. 2006.

[5] R. Roy and T. Kailath, "ESPRIT-estimation of signal parameters via rotational invariance techniques," *IEEE Trans. Acoust. Speech Signal Process*, vol. 37, no. 7, pp. 984-995, Jul. 1989.

[6] C. Qian, L. Huang, and H. C. So, "Computationally efficient ESPRIT algorithm for direction-of-arrival estimation based on Nyström method," *Signal Process.*, vol. 94, no. 1, pp. 74-80, 2014.

[7] M. L. McCloud and L. L. Scharf, "A new subspace

identification algorithm for high resolution DOA estimation," *IEEE Trans. Antennas Propag.*, vol. 10, no. 50, pp. 1382-1390, 2002.

[8] H. Changuel, A. Changuel, and A. Gharsallah, "A new method for estimating the direction-of-arrival waves by an iterative subspace-based method," *Applied Computational Electromagnetics Society Journal*, vol. 25, no. 5, pp. 476-485, May 2010.

[9] W. J. Zeng, X. L. Li, and X. D. Zhang, "Direction -of-arrival estimation based on the joint diagonalization structure of multiple fourth-order cumulant matrices," *IEEE Signal Processing Letters*, vol. 16, no. 3, pp. 164-167, 2009.

[10] B. Porat and B. Friedlander, "Direction finding algorithms based on high-order statistics," *IEEE Trans. Signal Process.*, vol. 39, no. 1, pp. 2016-2025, 1991.

[11] J. Munier and G. Y. Delisle, "Spatial analysis using new properties of the cross-spectral matrix," *IEEE Trans. on Signal Processing*, vol. 39, no. 3, pp. 746-749, 1991.

[12] A. Li and S. Wang, "Propagator method for DOA estimation using fourth-order cumulant," *Wireless Communications, Networking and Mobile Computing (WiCOM), 2011 7th International Conference on*, Wuhan, China, pp. 1-4, 2011.

[13] S. Marcos, A. Marsal, and M. Benidir, "The propagator method for source bearing estimation," *Signal Processing*, vol. 42, no. 2, pp. 121-138, 1995.

[14] P. Palanisamy and N. Rao, "Direction of arrival estimation based on fourth-order cumulant using propagator method," *Progress In Electromagnetics Research B*, vol. 18, pp. 83-99, 2009.

[15] P. Chevalier, L. Albera, A. Ferreol, and P. Comon, "On the virtual array concept for the fourth-order array processing," *IEEE Trans. Signal Process.*, vol. 53, no. 4, pp. 1254-1271, 2005.

[16] J. H. Tang, X. C. Si, and P. Chu, "Improved MUSIC algorithm based on fourth-order cumulants," *Systems Engineering and Electronics*, vol. 32, no. 2, pp. 256-259, 2010.

[17] P. Chevalier and A. Ferreol, "On the virtual array concept for the fourth-order direction finding problem," *IEEE Transactions on Signal Processing*, vol. 47, no. 9, pp. 2592-2595, 1999.

Heping Shi received the B.S. and M.S. degrees from Tianjin University of Technology and Education, China, in 2009 and 2012, respecttively. He is now a Ph.D. candidate at Tianjin University. His research interest is in the area of direction-of-arrival (DOA) and array signal processing.

Wen Leng received the B.S. degree and M.S. degrees from Northwestern Polytechnical University and Tianjin University in 1989 and 1992, respectively. He is currently a Lecturer in Tianjin University. His current research interests include Wireless data transmission, smart antenna, array signal processing, etc.

Anguo Wang received the Ph.D. degree from Tianjin University, China, in 2001. He is currently a Professor of Electronic Information Engineering with Tianjin University. He has co-authored over 80 scientific papers. His current research interests include communication system, smart antenna, microwave circuit, etc.

Hua Chen received the B.S. and the M.S. degree from Tianjin University, China, in 2010 and 2013, respecttively. He is now a Ph.D. candidate at Tianjin University. His research interests include image processing and direction-of-arrival (DOA).

Yuchu Ji received the B.S. and M.S. degrees from China University of Mining & Technology, Xuzhou, China, in 2008 and 2011, respectively. He is currently a Lecturer in Civil Aviation University of China. His research interests include cooperation communication and space time coding techniques.

Wideband Hexagonal Fractal Antenna on Epoxy Reinforced Woven Glass Material

M. A. Dorostkar [1], R. Azim [2], M. T. Islam [1], and Z. H. Firouzeh [3]

[1] Department of Electrical, Electronic & Systems Engineering
Universiti Kebangsaan Malaysia, 43600 UKM Bangi, Malaysia

[2] Depatment of Physics
University of Chittagong, Chittagong 4331, Bangladesh
rezaulazim@yahoo.com

[3] Department of Electrical & Computer Engineering
Isfahan University of Technology, Isfahan, Iran

***Abstract*—** In this paper a novel hexagonal-circular Fractal antenna is proposed for wideband applications. The proposed antenna is made of iterations of a circular slot inside a hexagonal metallic patch with a transmission line and is fabricated on low cost epoxy matrix reinforced woven glass material. Measurement shows that with a dimension of $0.36\lambda_0 \times 0.36\lambda_0 \times 0.0071\lambda_0$ (where λ_0 is the lower edge frequency of the operating band), the proposed antenna achieves a wide impedance bandwidth ranging from 1.34 GHz to 3.44 GHz (88%). The proposed antenna also achieves high gain and exhibits a stable radiation pattern which makes it suitable for many wireless communications such as DCS-1800, PCS-1900, IMT-2000/UMTS, ISM (including WLAN), Wi-Fi and Bluetooth.

***Index Terms* —** DCS, Epoxy material, Fractal geometry, ISM, wideband, Wi-Fi.

I. INTRODUCTION

Recent developments in wireless communication have heightened the need for wideband antennas with compact size and low cost. An antenna is considered as a wideband antenna if its impendence and pattern do not change significantly over about an octave or more. Several methods and approaches have been reported for designing antennas with wide and ultra-wide operating band in which the periodic structure is one of the most common methods [1-3]. Periodic geometry has been studied using the fundamental concept of Fractal structure for the last few decades. Self-similarity and space filling are two common properties for designing of Fractal antennas. Self-similarity leads to multiband while the space filling causes the long electrical length. If the antenna dimensions are smaller than a quarter of wavelength, it cannot be an efficient design because of decreasing of radiation resistances [1-5].

Most studies in the field of Fractal antenna have focused on Koch, Sierpinski and Hilbert, Cantor, Minkowski and Fractal tree shapes in recent years. The Koch monopole antenna is designed by iterating the initial triangle pulse [6]. The Log periodic Fractal Koch antenna for UHF band application is proposed in [7]. Koch like sided Sierpinski Gasket multi-Fractal dipole antenna is one of the most important Fractal antennas based on the triangle shape and is suitable for multi-band application [8]. In designing of the antenna proposed in [9], the Sierpinski Fractal shape is perturbed and two iteration stages had been introduced to achieve dual band centered at 915 MHz and 1.575 GHz.To yield multiband behavior, the antenna proposed in [10] considered two Fractal stages of the Sierpinski Gasket as base shape. With an overall size of 60×80 mm, the proposed antenna achieved dual operating bands centered at 898 MHz and 2.44 GHz. By taking the planar Sierpinki prefractal as a reference shape, the antenna proposed in [11] achieved a multiband behavior

Submitted On: July 11, 2013
Accepted On: September 7, 2014

with a dimension of 80×80 mm. In [12], a modified Fractal slot antenna was presented for DCS, WiMAX and IMT applications. By applying Minkowski Fractal concept, the reported antenna achieved dual operating band of 1.71-1.88 GHz and 3.2-5.5 GHz. Despite having fairly compact dimensions (38.54×75.2 mm), this antenna requires a complex structure to create and control dual operating band. The CPW-fed slot antenna proposed in [13] is based on hexagonal Fractal geometry and only applicable for the UWB frequency band. However, the realized gain of this antenna is quite low. In [14], the hexagonal shape is obtained by three iterations with arranging dipole configuration that is large in physical size. By using side-fed feeding configuration to the hexagonal geometry, the antenna proposed in [15] achieved an impedance bandwidth of 2.5 GHz (1.1-3.6 GHz). However, the reported antenna does not possess a physical compact profile having a dimension of 150×150 mm. To achieve an operating band ranging from 1.9-2.4 GHz, two parallel slots were incorporated into the patch of a microstrip antenna proposed in [16]. However, the designed antenna is not suitable for portable mobile devices due to its large volumetric size of 140×210×10 mm. Tapering the radiating patch or ground plane shape and use of lossy substrates have also been reported in achieving wide and ultra-wide band frequency response [17-18]. Despite of wide and ultra-wide operating band, none of these reported Fractal antennas deal with hexagonal circular geometry which could be a new arena in the designing of Fractal antenna.

In this paper, a novel wideband Fractal antenna based on hexagonal-circular geometry is proposed and designed on epoxy matrix reinforced woven glass material. The iterations of a circular slot inside a hexagonal metallic patch fed by a transmission line help to achieve wide impedance bandwidth ranging from 1.34 to 3.44 GHz. The achieved high gain and stable radiation patterns makes the proposed suitable for being used in various wireless applications such as DCS-1800 (1710-1880 MHz), PCS-1900 (1850-1990 MHz), IMT-2000/UMTS (1885-2200 MHz), ISM (2400-2483 MHz), Wi-Fi (2400 MHz) and Bluetooth (2400-2500 MHz). Compared to the antennas reported in [11-12, 15-16], the proposed antenna is compact, simple and easy to fabricate.

II. ANTENNA DESIGN

The proposed antenna designed on substrate material consists of an epoxy matrix reinforced woven glass. The fiber glass in the composition is 60% while the epoxy resin contributes 40% of the composition. This composition of epoxy resin and fiber glass varies in thickness and is direction dependent. One of the attractive properties of polymer resin composite is that they can be shaped and reshaped repeatedly without losing their material properties [19]. Due to ease of fabrication, design flexibility, low manufacturing cost and market availability, the epoxy matrix reinforced woven glass material has become popular in the designing of microstrip patch antenna.

The design of the proposed antenna is based on a hexagonal geometry. In the proposed shape, the initial shape is a subtraction of hexagonal shape with a length of $(R_1+d_1/(\sqrt{3/2})$ and circle with radius R_1, where d_1 is the thickness between hexagonal and circle, and is as shown in Fig. 1 (a). The existence of edges leads to losses of energies, so the internal geometry has been changed to circular. The next shape is the subtraction of hexagonal with a length of $(R_2+d_2)/(\sqrt{3/2})$ and circle with radius R_2, while it rotates by 30^0. This process is continued to seven steps, and in every step the shapes are rotated 30^0. The shape can rotate clockwise or counterclockwise due to the symmetrical nature of the proposed shape. If the proposed shape is chosen to rotate in a clockwise (counterclockwise), the other shapes should be rotated clockwise (counterclockwise). For limiting 3*D* modulator error, the next iterations are constructed so that it introduces interference between the main patch and next iteration. The metallic concentration between the iterations (hexagonal and circle) is about 0.1mm. The configuration is the iterations of a circular slot inside a hexagonal metallic patch. Figure 1 shows the shapes and relations based on their distances from the center and design procedure of proposed Fractal structured geometry.

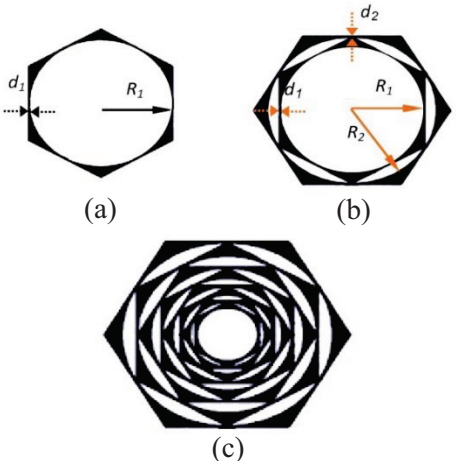

Fig. 1. Design procedure of the proposed Fractal geometry: (a) base shape, (b) first iteration, and (c) final shape.

The variation of return loss for various iterations is shown in Fig. 2. It is seen that the antenna with higher iteration exhibits better impedance bandwidth. It is also observed that the base shape with iteration (Itr) 0 has a narrow bandwidth which permits to continue the iterations up to seven to obtain a wider operating bandwidth.

Five parameters are considered for the design of hexagonal geometry including R_i (length of hexagonal and circular), d_i (difference between the lengths of hexagonal and circle), L_T (length of transmission line), L_G (side length of ground plane), and W_T (width of the transmission line) that their relations are based on the following equations:

$$R_{i+1} = \frac{R_i + d_i}{\sqrt{\frac{3}{2}}} i = 1, 2, 3, \ldots\ldots N, \quad (1)$$

and the vertical gap between the ground plane and the radiating element is:

$$h = L_T - L_G. \quad (2)$$

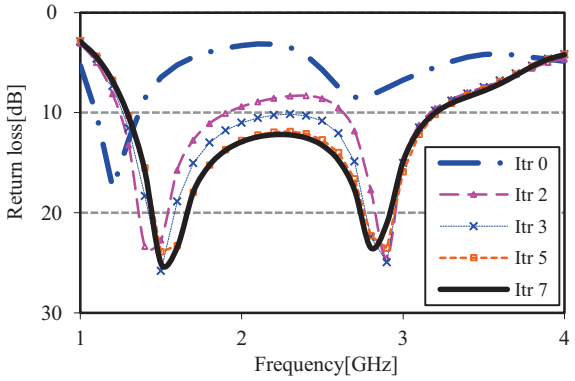

Fig. 2. Return loss curves for various iterations.

The configuration of the proposed antenna is shown in Fig. 3. The hexagonal Fractal patch is printed on one side of a 1.6-mm thick epoxy woven glass material of relative permittivity 4.6, while the partial ground plane with side length L_G is printed on the other side. The hexagonal patch with side length R_{16} is fed by a transmission line. The length and width of the transmission line are fixed at L_T and W_T respectively to achieve 50Ω characteristic impedance. An SMA is connected to the transmission line. The overall electrical dimension of the proposed antenna is $0.36\lambda_0 \times 0.36\lambda_0 \times 0.0071\lambda_0$ (where λ_0 is the lower edge of the operating band), which is smaller than the antenna proposed in [11, 16] for DCS, PCS, IMT/UMTS, and ISM applications.

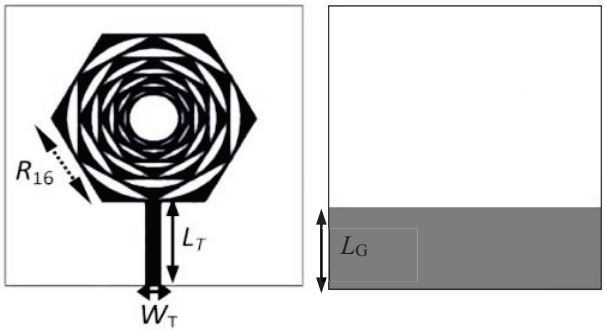

Fig. 3. Configuration of the proposed antenna: (a) top view (left side), and (b) bottom view (right side).

III. ANTENNA SPECIFICATIONS

The dimension of the perimeter of a hexagonal is equal 1 (D = 1) and hexagonal area is called $S_{hexagonal}$ with dimension of 2 (D = 2), so the dimensions of the proposed shape are between 1 and 2 ($1<D<2$). Due to existing of two types of shapes (hexagonal and circular), the dimension of the proposed geometry is not able to be figured out only by one scale factor. In the first step, the equivalent hexagonal shape with circular shape can be calculated according to the relation (4). Then the dimension of the new proposed Fractal shape can be computed according to the relation (6). $(1.5\sqrt{3})\times(R_1^2-R_n^2)$ is scale factor where R_1 is the length of the first hexagonal and R_n is the length of the equivalent hexagonal with the circle radius of nth iterations.

S_n is the area of the nth iterations that is determined with relation (5). The hexagonal area $S_{hexagonal}$ is defined as:

$$S_{hexagonal} = \frac{3\sqrt{3}}{2} R_1^2. \quad (3)$$

R_n, the length of the corresponding hexagonal with a circle radius of nth iterations can be written as:

$$R_n = \sqrt{\frac{2\pi}{3\sqrt{3}}} \left[R_{n-1} cos\left(\frac{\pi}{6}\right) - d \right], \text{ n=2, 3, 4,..} \quad (4)$$

The area corresponding to the hexagon-circular Fractal area of nth iterations is:

$$S_{hexagonal} - S_n = \frac{3\sqrt{3}}{2} (R_1^2 - R_n^2), \quad (5)$$

$$D = \frac{Log(S_{hexagonal} - S_n)}{Log\{1.5\sqrt{3} \times (R_1^2 - R_n^2)\}}. \quad (6)$$

The first design is done with R_{16} = 27.6 mm and d = 0.5 mm, that d is constant for all the iterations. The dimensions for the proposed geometry to 7 iterations are arranged in Table 1. It can be observed that increasing iterations enhance the dimension, so lead to increasing the electrical length.

Table 1: Dimension of the proposed Fractal geometry for various iterations

Iteration	Base Shape	First	Second	Third
Dimension (mm)	1.0025	1.1389	1.2303	1.3040
Iteration	Fourth	Fifth	Sixth	Seventh
Dimension (mm)	1.3692	1.4302	1.4895	1.5488

IV. PARAMETERIC STUDY

A parametric study is conducted to investigate the effects of the different parameters on the antenna performances. All the parametric studies have been conducted using high frequency simulation software from Ansoft. In the simulation, only the parameter of interest has been changed and the other parameters are kept constant using of the objective function $S_\lambda(f)$ with the strategy of $S_\lambda(f) < -10$, where $S_\lambda(f)$ is function of return loss with specified parameters, λ = {L_T, L_G, W_T, R_{16}, d_i: i =1, 2, ., .8}, of the proposed antenna that has larger bandwidth.

The variation of the return loss with λ parameter is shown in Fig. 4. It is observed that decreasing and increasing of λ from a certain value leads to decrease in the bandwidth. Table 2 summarizes the effects of λ on bandwidth performances with various values.

The variations of the return loss with R_{16} (length of last hexagonal structure) are shown in Fig. 5. It is observed that decreasing and increasing of R_{16} from a certain value leads to decrease in the bandwidth. It can be seen from the Fig. 5, that a value of 27.6 mm for R_{16} can maintain the good impedance bandwidth with better return loss values. The variation of the return loss with L_T (length of transmission line) is depicted in Fig. 6.

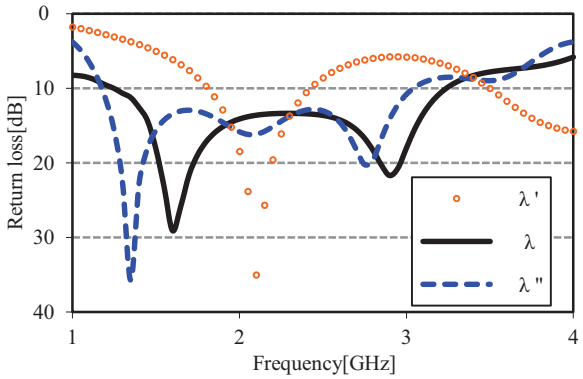

Fig. 4. Effect of λ on return loss characteristics.

Table 2: Variation values for all λ parameters

Parameter(mm)	λ'2	λ2	λ"2
L_T	27	24	20
L_G	26	23	19
W_T	4	3.3	2
R_{16}	30	27.6	20
d_1	0.4	0.47	0.36
d_2	0.67	0.3	0.445
d_3	0.45	0.65	0.4
d_4	0.45	0.35	0.68
d_5	0.42	0.4	0.49
d_6	0.35	0.4	0.32
d_7	0.5	0.44	0.5
d_8	0.42	0.5	0.42

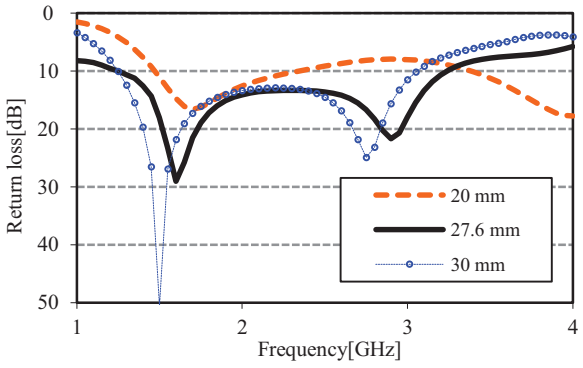

Fig. 5. Effect of R_{16} on return loss characteristics.

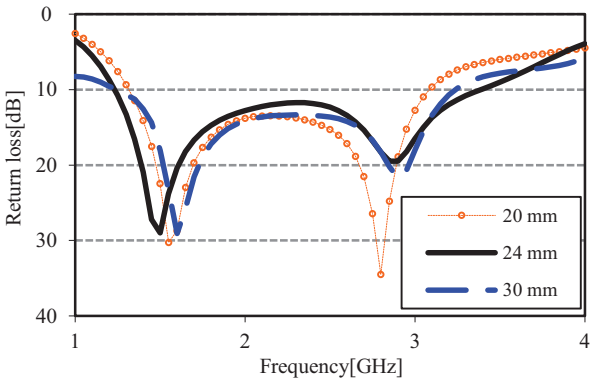

Fig. 6. Effect of L_T on return loss characteristics.

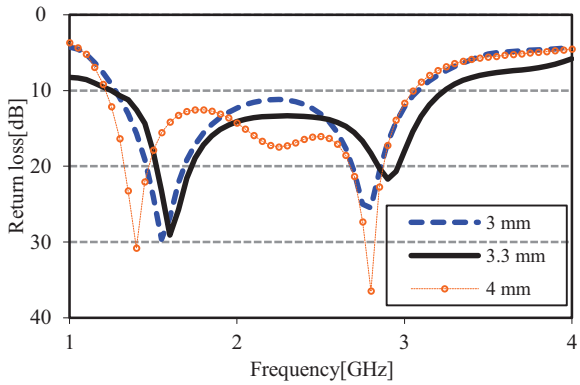

Fig. 7. Effect of W_T on return loss characteristics.

In the simulation of performance analysis of L_T versus frequency, only the value of L_T is varied while the other parameters are kept constant at R_{16} = 27.6 mm, W_T = 3.3 mm, L_G = 23 mm and h = 1 mm. It is seen from the plot that decreasing of L_T leads to decrease in the operating bandwidth, while increasing of L_T leads to increase in operating bandwidth. It is also noted that, decreasing and increasing of L_T from a certain value leads to a mismatch of the input impedance. Based on the observations, it is found that a value of 24 mm is an appropriate choice for L_T in achieving the widest operating bandwidth.

Figure 7 shows the variations of the return loss characteristics with the width of the transmission line, W_T. In optimization, only the value of W_T is varied while the other parameters are kept constant at R_{16} = 27.6 mm, L_T = 24 mm, L_G = 23 mm and h = 1mm. It is seen from the figure that, decreasing and increasing of the W_T leads to decrease the impedance bandwidth. It is also observed that, when W_T decreases and increases from a certain value, the impedance matching becomes poor at higher frequencies resulting in a bandwidth reduction. In this design, a width of 3.3 mm performs with better return loss and input impedances.

The variation of return loss with h parameter (the vertical gap between the ground plane and the radiating element) is shown in Fig. 8. It can be observed that, increasing and decreasing of h from the certain value leads to decrease in the bandwidth. From the plot in Fig. 8, it is clear that a gap of 1mm can maintain the good impedance bandwidth with better return loss values.

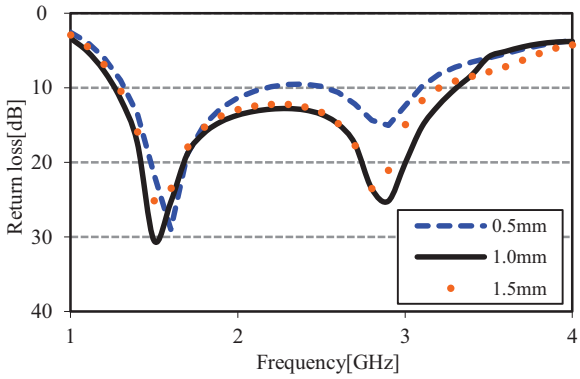

Fig. 8. Effect of h on return loss characteristics.

V. RESULTS AND DISCUSSION

The characteristics of the proposed antenna have been optimized by high frequency simulation software HFSS. A prototype with optimized dimensions tabulated in Table 3 has subsequently been fabricated for experimental verification and shown in Fig. 9. The antenna performances have been measured in an anechoic chamber using far field antenna measurement system and Agilent E8362C Vector Network Analyzer. The experimental setup was calibrated carefully by considering the effect of feeding cable using an Agilent digital calibration kit.

The simulated and measured return losses and VSWR of the proposed antenna are depicted in Fig. 10. It is observed from the plot that the measured impedance bandwidth of the proposed antenna is ranging from 1.34 to 3.44 GHz, which is equivalent 88%. A good agreement between the simulated and

measured results has been observed. The disparity between the measured and simulated results especially at edge frequencies is attributed to manufacturing tolerance and imperfect soldering effect of the SMA connector.

Table 3: Optimized antenna parameters

Parameter	Value (mm)	Parameter	Value (mm)
L_T	30	d_3	0.65
L_G	23	d_4	0.35
W_T	3.3	d_5	0.4
R_{16}	27.6	d_6	0.4
d_1	0.47	d_7	0.44
d_2	0.3	d_8	0.5

Fig. 9. Photograph of the realized Fractal antenna.

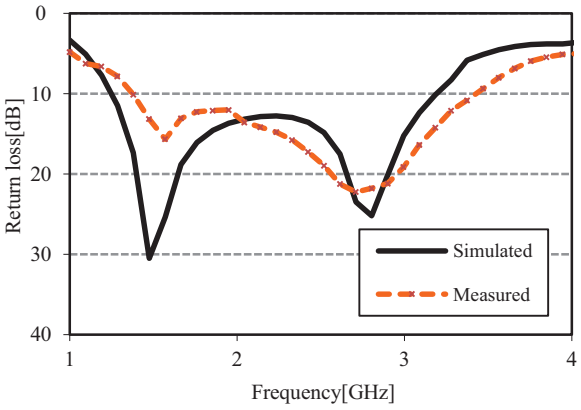

(a)

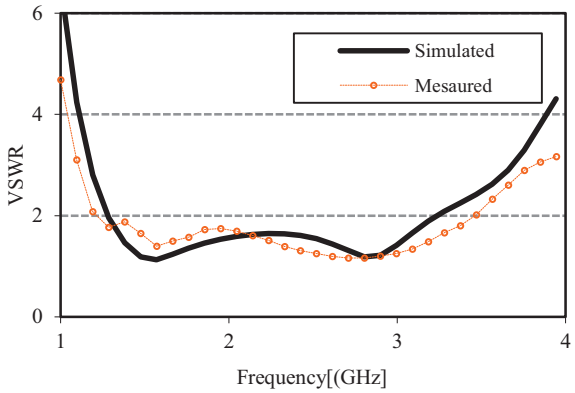

(b)

Fig. 10. Measured: (a) return loss, and (b) VSWR.

The measured phase variation of the input impedance of the proposed antenna is shown in Fig. 11. The phase variation across the entire operating band is reasonably linear, except at around 2.2 GHz. This linear variation in the phase with frequency ensures that all the frequency components of signal have the same delay, leading to same pulse distortion.

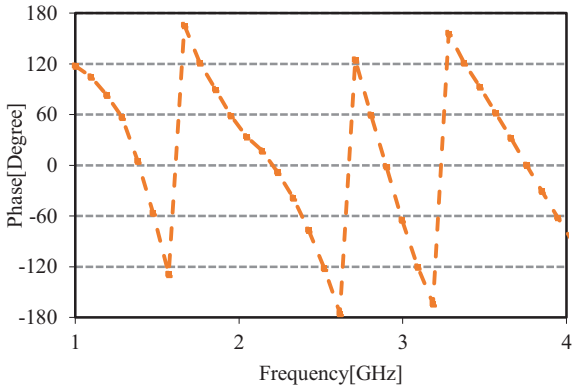

Fig. 11. Measured phase of the proposed antenna.

Figure 12 shows the peak gain and efficiency of the proposed antenna in the frequency range of 1-4 GHz. It can be observed from the figure that the antenna has a good average gain of 4.65 dBi. The maximum peak gain is 6.8 dBi at 1.34 GHz. The plot of radiation efficiency shows that the maximum radiation efficiency of the proposed antenna is 84% at 1.34 GHz and the average efficiency is 75% across the entire operating band.

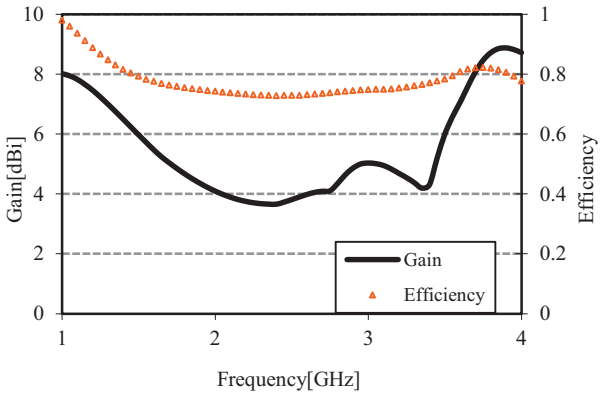

Fig. 12. Peak gain and radiation efficiency.

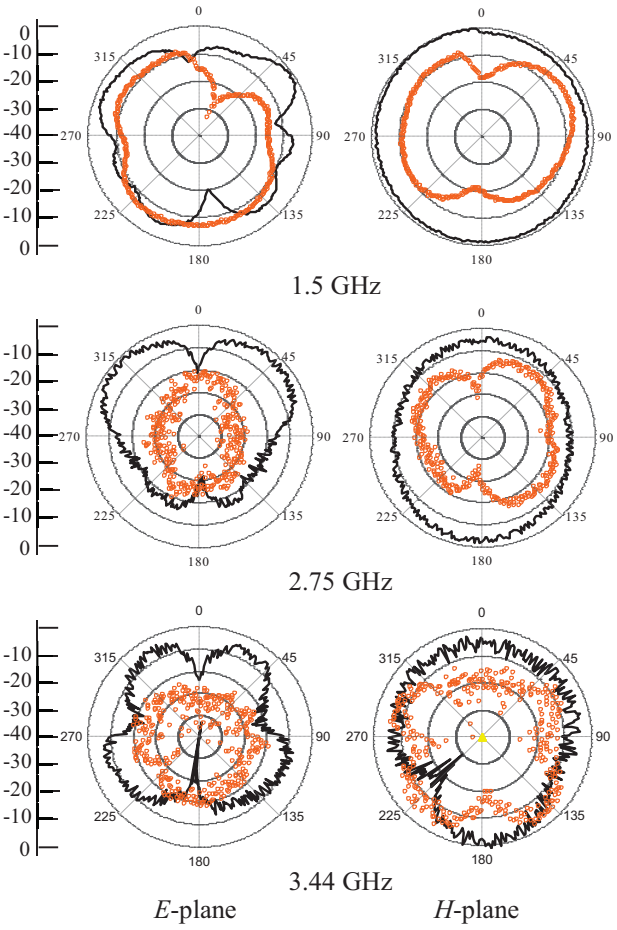

Fig. 13. Measured radiation patterns at different frequencies (black line: co-polarized field, orange line: cross-polarized field).

The measured radiation patterns of the proposed antenna at 1.5 GHz, 2.75 GHz and 3.44 GHz are depicted in Fig. 13. It can be observed from the figure that at low frequency of 1.5 GHz both the *E*-plane and *H*-plane patterns are omnidirectional and *H*-plane pattern is characterized with low cross-polarization level. At higher frequencies of 2.75 GHz and 3.44 GHz, the *E*-plane patterns become donut shape and main beam slightly tilt away from the broad side direction due to higher order harmonic, while *H*-plane patterns almost retains its omni-directionality.

VI. CONCLUSION

A novel wideband hexagonal-circular antenna has been proposed and prototyped for wideband applications. The composition of epoxy resin and fiber glass material has been used for fabrication due to their low manufacturing cost and market availability. A design evolution and a parametric study of the proposed antenna are presented to provide information for designing, optimizing and to understand the fundamental radiation mechanism. The design of the proposed antenna is simple, easy to fabricate, and very suitable to integrate into microwave circuitry due to its planar profile. Experimental results show that the proposed antenna achieved an impedance bandwidth of 2.1GHz.The nearly stable omnidirectional radiation patterns with a flat gain make the proposed antenna suitable for DCS-1800, PCS-1900, IMT-2000/UMTS, ISM, Wi-Fi and Bluetooth applications.

ACKNOWLEGMENT

The authors would like to thank Isfahan Mathematics House (IMH), Iran for helping this research.

REFERENCES

[1] C. A. Balanis, *Antenna Theory: Analysis and Design*, John Wiley & Sons, New York, 2005.

[2] D. H. Werner and S. Ganguly, "An overview of fractal antenna engineering research," *IEEE Antennas Propagat. Mag.*, vol. 45, no. 1, pp. 38-57, 2003.

[3] N. Cohen, "Fractal antenna application in wireless telecommunications," *Electronics Industries Forum of New England*, Boston, USA, pp. 43-49, May 1997.

[4] J. F. Gouyet, *Physics and Fractal Structures*, Springer, Paris, France, 1996.

[5] D. H. Werner, R. L. Haupt, and P. L.Werner, "Fractal antenna engineering: the theory and design of fractal antenna arrays," *IEEE Antennas Propagat.*

Mag., vol. 41, no. 5, pp. 37-58, 1999.

[6] N. A. Saidatul, A. A. H. Azremi, R. B. Ahmad, P. J. Soh, and F. Malek, "Multiband fractal planar inverted F antenna (F-PIFA) for mobile phone application," *Prog. Electromagn. Res. B*, vol. 14, pp. 127-148, 2009.

[7] C. Puente, J. Romeu, R. Pous, J. Ramis, and A. Hijazo, "Small but long Koch fractal monopole," *Electron. Lett.*, vol. 34, no. 1, pp. 9-10,1998.

[8] M. N. A. Karim, M. K. A. Rahim, H. A. Majid, O. Ayop, M. Abu, and F. Zubir, "Log periodic fractal Koch antenna for UHF band applications," *Prog. Electromagn. Res.*, vol. 100, pp. 201-218, 2010.

[9] F. Viani, M. Salucci, F. Robol, G. Oliveri, and A. Massa, "Design of a UHF RFID/GPS fractal antenna for logistics management," *J. Electromagn. Waves Appl.*, vol. 26, pp. 480-492, 2012.

[10] F. Viani, M. Salucci, F. Robol, and A. Massa, "Multiband fractal ZigBee/WLAN antenna for ubiquitous wireless environments," *J. Electromagn. Waves Appl.*, vol. 26, nos. 11-12, pp. 1554-1562, 2012.

[11] L. Lizzi, F. Viani, E. Zeni, and A. Massa, "A DVBH/GSM/UMTS planar antenna for multimode wireless devices," *IEEE Antennas Wireless Propagat. Lett.*, vol. 8, pp. 568-571, 2009.

[12] C. Mahatthanajatuphat, P. Akhharaekthalin, S. Saleekaw, and M. Krairiksh, "A bidirectional multiband antenna with modified fractal slot fed by CPW," *Prog. Electromagn. Res.*, vol. 95, pp. 59-72, 2009.

[13] A. Azari and J. Rowhani, "Ultrawideband fractal microstrip antenna design," *Prog. Electromagn. Res. C*, vol. 2, pp. 7-12, 2008.

[14] P. W. Tang and P. F. Wahid, "Hexagonal fractal multiband antenna," *IEEE Antennas Wireless Propagat. Lett.*, vol. 3, pp. 111-112, 2004.

[15] K. P. Ray and S. Tiwari, "Ultra wideband printed hexagonal monopole antennas," *IET Microw. Antennas Propag.*, vol. 4, no. 4, pp. 437-445, 2010.

[16] F. Yang, X-X. Zhang, X. Ye, and Y. Rahmat-Samii, "Wide-band E-shaped patch antennas for wireless communications," *IEEE Trans. Antennas Propagat.*, vol. 49, no. 7, pp. 1094-1100, 2001.

[17] R. Azim, M. T. Islam, and N. Misran, "Compact tapered shape slot antenna for UWB applications," *IEEE Antennas Wireless Propagat. Lett.*, vol. 10, pp. 1190-1193, 2011.

[18] H. W. Son, "Design of RFID tag antenna for metallic surfaces using lossy substrate," *Electron. Lett.*, vol. 44, no. 12, pp. 711-713, 2008.

[19] I. Yarovsky and E. Evans, "Computer simulation of structure and properties of crosslinked polymers: application to epoxy resins," *Polymer*, vol. 43, no. 3, pp. 963-969, 2002.

A Novel CRLH-CP Antenna with the Capability to be Integrated Inside RF Components for RF Electronic Devices and Embedded Systems

Mohammad Alibakhshi-Kenari [1] and Mohammad Naser-Moghaddasi [2]

[1] Department of Electrical and Communication Engineering
University of Shahid Bahonar, Kerman, 4751677996, Iran
makenari@mtu.edu

[2] Department of Electrical and Communication Engineering
Islamic Azad University, Science and Research Branch, Tehran, Iran

Abstract ─ In this paper, design and manufacturing of a composite right/left-handed carved planar (CRLH-CP) antenna with $\varepsilon-\mu$ constitutive parameters is introduced. The composite right/left-handed transmission line (CRLH-TL) is introduced as a general TL possessing both left-handed (LH) and right-handed (RH) natures. The proposed antenna is constructed of four CRLH unit cells, each of which occupies space of $0.004\lambda_0\times0.01\lambda_0\times0.001\lambda_0$, where λ_0 is free space wavelength at 0.5 GHz. The antenna practical bandwidth is 120%, so that the proposed antenna can be used for frequency band from 0.5 GHz to 2 GHz in measurement. Also, the antenna gains and radiation efficiencies at the operational frequencies f=0.7, 1.5 and 2 GHz are 3.8 dBi and 53%, 4.85 dBi and 68.5%, and 4.3 dBi and 60.2%, respectively. According to the results, the proposed minimized ultra wideband (UWB) antenna is a good candidate to use in the RF electronic devices and embedded systems.

Index Terms ─ Carved Circuit Boards (CCBs), Composite Right/Left-Handed Carved Planar (CRLH-CP) antenna, embedded systems, Metamaterial (MTM), Standard Carved Planar Manufacturing Technique (SCPMT), Ultra Wideband (UWB) RF electronic devices.

I. INTRODUCTION

An antenna is a device that is used to transfer guided electromagnetic waves (signals) to radiating waves in an unbounded medium, usually free space and vice versa (i.e., in either the transmitting or receiving mode of operation). Antennas are frequency-dependent devices. Each antenna is designed for a certain frequency band. Beyond the operating band, the antenna rejects the signal. Therefore, we might look at the antenna as a band-pass filter and a transducer. Antennas are an essential part in telecommunication systems; therefore, understanding their principles is important. There are many different antenna types. The isotropic point source radiator, one of the basic theoretical radiators, is useful because it can be considered a reference to other antennas. The isotropic point source radiator radiates equally in all directions in free space. Physically, such an isotropic point source cannot exist. Most antennas' gains are measured with reference to an isotropic radiator and are rated in decibels with respect to an isotropic radiator (dBi).

The multitude of potential techniques proposed over the years to size reduction of the microstrip antennas are mainly based on the reactive loading of a patch antenna with suitably designed slots, shorting posts and lumped elements. These solutions, however, do not usually allow obtaining the drastic reduction of the antenna dimensions needed for the aforementioned applications [9-10-11]. Another possibility to the patch size reduction is

Submitted On: September 9, 2013
Accepted On: October 11, 2014

employment of the dielectric substrates exhibiting high-values of the permittivity. However, due to the increased excitation of surface waves in the substrate, bandwidth, efficiency, and shape of the radiation pattern of the antenna may be significantly deteriorated [1]. Therefore, the aforementioned standard techniques do not represent sufficient tools to beat the challenge of miniaturized antenna design. Some new approaches, based on the use of artificially engineered materials and metamaterials (MTMs), seem to be more promising in this sense, opening the path to substantial achievements for the purposes of size reduction [12-13-14].

In this paper, we have introduced a novel minimized ultra wideband (UWB) carved planar (CP) antenna based on metamaterial (MTM) CRLH-TLs with high gain and efficiency. Recently, MTMs based transmission lines have been developed and have been shown to exhibit unique features of anti-parallel phase and group velocities $(v_p - v_g)$ and zero propagation constant at a certain frequency at the fundamental operating mode [2-3]. Furthermore, metamaterials exhibit qualitatively new electromagnetic response functions which cannot be found in the nature. These metamaterials have been used to realize the novel planar antennas.

The prefix "meta-" has the Greek origin and is translated as "outside of," that allows to interpret the term "metasubstances" as structures whose effective electromagnetic behavior falls outside of the property limits its forming components. The analysis of publications on various aspects of metamaterials technology allows to classify all variety of artificial environments depending on their effective values of permittivity (ε) and magnetic permeability (μ) according to the classification diagram presented in Fig. 1.

MTM technology may be caused to designing antenna structure with physically small size, whereas, this antenna can cover large frequency bandwidth [5-6].

In this paper, the MTM and carved planar technologies on the carved circuit boards (CCBs) by standard manufacturing techniques for downsizing of the antenna structure are applied. Too, with using of the proper inductive and capacitive elements including rectangular inductors, via holes and Y-formed slots with their regulated dimensions, the good performance parameters such as bandwidth, radiation gains and efficiencies have been achieved. The proposed CRLH-CP antenna have advantages of small physical size and UWB and good radiation properties, planar, low loss, unidirectional radiation patterns, simple of construction, and also presented antenna can be integrated within RF components and embedded circuits.

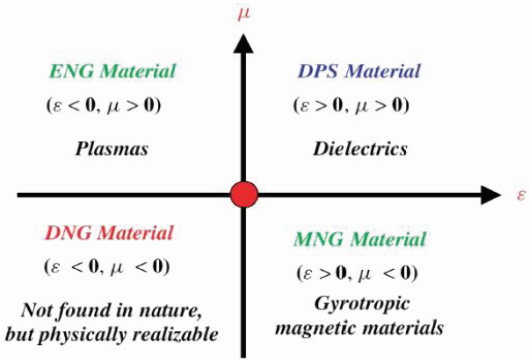

Fig. 1. Classification of physical environments depending on its effective values of permittivity (ε) and magnetic permeability (μ) [4].

The paper is classified as follows. Section II expresses the design procedure of the proposed CRLH-CP antenna. Section III consists of the results. Finally, Section IV concludes the paper.

II. DESIGN PROCEDURE OF THE RECOMMENDED CRLH-CP ANTENNA

The proposed antenna design procedure is based on a simple topology that incorporates the carved planar patches that have been implemented on the carved circuit boards (CCBs) by standard manufacturing techniques, and also rectangular inductors accompanying via holes that are connected to ground plane. This topology makes it possible to combine the antenna with integrated RF electronics. In here, the standard carved planar manufacturing technique (SCPMT) on the radiation patches for production of series capacitances (C_L) have been used, which leads to foot print area reduction. Furthermore, with implement of the minimized Y-formed slots, rectangular inductors with adjusted dimensions

and uniform excitation mechanism, which caused to increase the antenna effective aperture [1], the good performance parameters have been provided. The proposed CRLH-CP antenna is composed of four simplified CRLH unit cells, that each are included of a rectangular radiation patch with one **Y**-shaped slot that is carved on the radiation patch by standard manufacturing technique and a rectangular inductor connected to ground plane through a via hole. The equivalent circuit model of the proposed antenna structure is shown in Fig. 2.

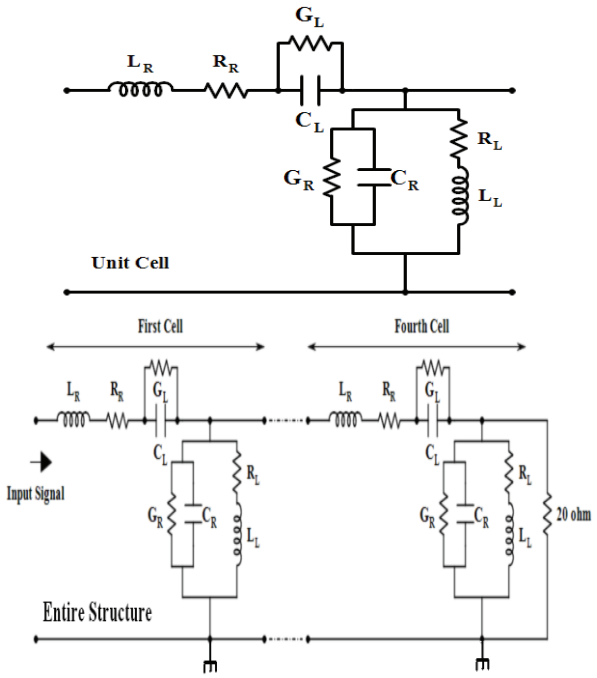

Fig. 2. Equivalent circuit model of the proposed CRLH-CP antenna.

Figure 3 shows the layout structure of the proposed antenna. According to Figs. 2 and 3, in each unit cell, to production of the series left handed capacitance (C_L) and the shunt left handed inductance (L_L) have used a carved **Y**-shape slot and a rectangular inductor that is connected to ground plane through a metallic via hole, respectively. In fact, a purely left/handed TL is not physical and can never be realized because of the parasitic right/handed effects. MTMs with left/handed properties have inevasible right/handed properties, known as composite right/left hand MTMs. Hence, the proposed transmission line structure possesses the right-handed parasitic effects that can be seen as shunt capacitance (C_R) and series inductance (L_R) [15-16]. The shunt capacitance C_R is mostly come from the gap capacitance between the strip and the ground plane, and unavoidable current flows on the patches establishes the series inductance L_R, which indicates that these capacitance and inductance cannot be ignored. The structure losses are modeled by RH and LH resistances and conductance; i.e., R_R, R_L, G_R and G_L. In this antenna structure, the uniform excitation mechanism by implementing of two ports is applied, so that port 1 is excited with input signal and port 2 is matched to a 20 Ohm load impedance of the SMD1206 resistance components, while size of this load is 4.2 mm and is considered into the overall size of antenna structure, and also it is connected to ground plane through a via hole. This point should be noted that, the series capacitances (C_L) and the shunt inductances (L_L) can be adjusted by varying the dimension of **Y**-shape slots and rectangular inductors, respectively. This feature provides another superior capability that can be used to change the performances of the antenna. In this design for reach to the desired performances, the tuned dimensions and the optimized values of the structural components that were obtained of the optimization processes of three 3-D full wave EM simulators, such as Advanced Design System (ADS), High Frequency Structural Simulator (HFSS) and CST Microwave Studio are shown in Fig. 3. Also, the values of these components; i.e., series left handed (LH) capacitances (C_L) and shunt LH inductances (L_L) that were created by implement of the Y-shape slots and the rectangular inductors are equal to 4.9 pF and 6.2 nH, respectively. In additional to C_L and L_L, amounts of the shunt Right Handed (RH) capacitances (C_R) and series RH inductances (L_R), which were created by gap capacitance between strips and ground plane and unavoidable current flows on the patches are equal to 1.6 pF and 1.8 nH, respectively. Also, the losses of the antenna structure that have been modeled by R_R, R_L, G_R and G_L are 2.5 Ω, 2.7 Ω, 1.2 Ʊ and 1.4 Ʊ, respectively.

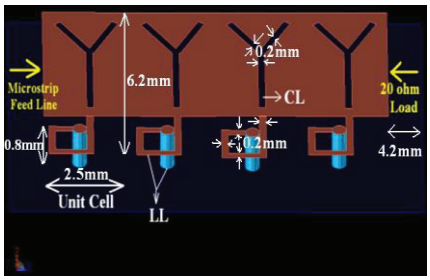

Simulated prototype

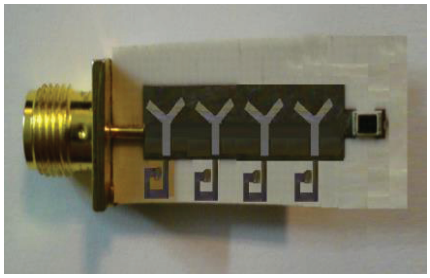

Fabricated prototype

Fig. 3. Configuration of the proposed **Y**-shape CRLH-CP antenna composed of four unit cells.

The CRLH-CP antenna is designed on a Rogers_RO4003 substrate with thickness of h=0.8 mm, dielectric constant of $\varepsilon_r = 3.38$ and tanδ=0.0022. The physical size of the antenna is $0.023\lambda_0 \times 0.01\lambda_0 \times 0.001\lambda_0$, where λ_0 is the free space wavelength at 0.5 GHz; thus, the length, width and height of the antenna are 14.2 mm, 6.2 mm and 0.8 mm, respectively. The recommended antenna has 1.5 GHz measured bandwidth and can be used to frequency band from 0.5 GHz to 2 GHz in measurement for VSWR<1.5, which corresponds to 120% practical bandwidth. In addition, the measured radiation gains and efficiencies of the CRLH-CP antenna at the operational frequencies of f=0.7, 1.5 and 2 GHz are 3.8 dBi and 53%, 4.85 dBi and 68.5%, and 4.3 dBi and 60.2%, respectively. These results express that the proposed CRLH-CP antenna has good radiation properties and ultra wide bandwidth with small size enough to fit on the embedded systems and integration into RF components.

III. RESULTS AND DISCUSSIONS

To validate the design processes, the proposed CRLH-CP antenna was designed by three 3-D full wave EM softwares, they are: Advance Design System (ADS), High Frequency Structure Simulator (HFSS) and CST Microwave Studio and was fabricated on a Rogers_RO4003 substrate with dielectric constant of 3.38, 0.8 mm thickness and tanδ=0.0022. The physical length, width and height of the antenna are $0.023\lambda_0$, $0.01\lambda_0$ and $0.001\lambda_0$, in terms of free space wavelength at 0.5 GHz. Figure 4 shows the reflection coefficients (S_{11}<-10 dB parameters) of the proposed antenna. The antenna bandwidth (S_{11}<-10 dB) achieved from the measurement, ADS, HFSS and CST Microwave Studio simulators are 1.5 GHz and 120% from 0.5 GHz to 2 GHz, 1.68 GHz and 135% from 0.4 GHz to 2.08 GHz, 1.57 GHz and 125% from 0.47 GHz to 2.04 GHz, and 1.65 GHz and 129% from 0.45 GHz to 2.1 GHz, respectively.

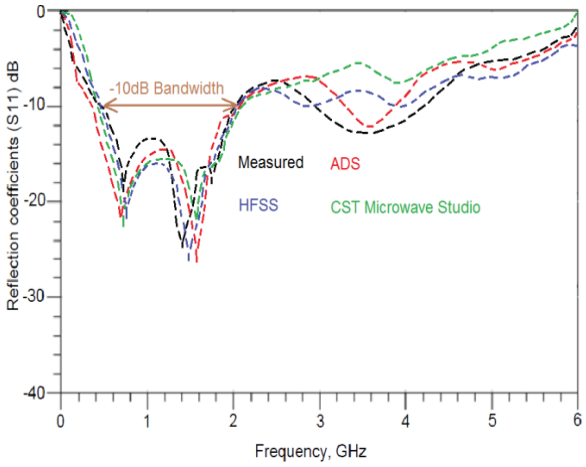

Fig. 4. Reflection coefficients (S_{11}<-10 dB parameters) of the antenna.

The radiation gains patterns of the proposed antenna at the operating frequencies of f=0.7, 1.5 and 2 GHz are plotted in Fig. 5. As is clear from this figure, the radiation patterns have unidirectional specifications. The radiation gains and efficiencies provided from the measurement, ADS, HFSS and CST Microwave Studio at 0.7 GHz are 3.8 dBi and 53%, 3.9 dBi and 57.1%, and 3.95 dBi and 56%, and 3.85 dBi and 55%; at 1.5 GHz are 4.85 dBi and 68.5%, 4.92 dBi and 70%, 4.96 dBi and 71.2%, and 4.9 dBi and 69%; at 2 GHz are 4.3 dBi and 60.2%, 4.35 dBi and 63%, 4.4 dBi and 62.8%, and 4.42 dBi and 64%, respectively.

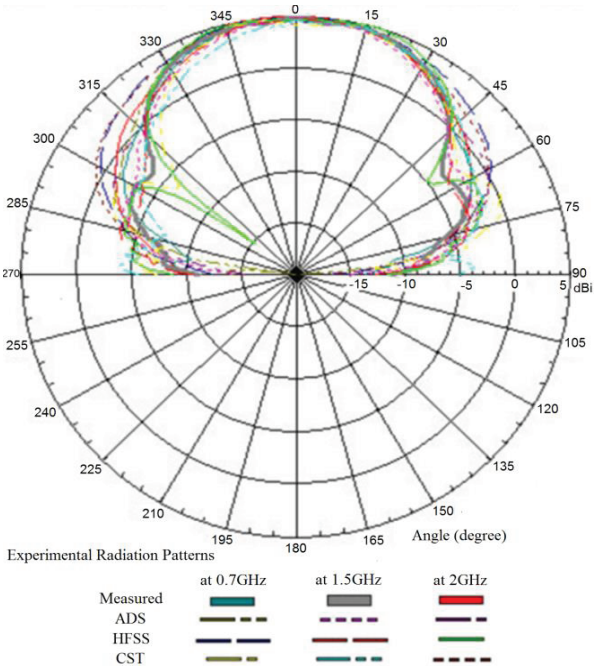

Fig. 5. Experimental radiation gains patterns of the suggested CRLH-CP antenna.

To validate the design and fabrication procedures, the proposed CRLH-CP antenna was compared with several conventional antennas and their specifications were summarized in Table 1.

Table 1: Characteristics of some of the conventional antennas in comparison to the proposed PPMTM antenna

Table 1-1: Dimensions

[5]	50.8×25.2×1 mm^3 & $0.404\lambda_0\times0.2\lambda_0\times0.007\lambda_0$ at 2.39 GHz
[6]	12×12×3.33 mm^3 & $0.093\lambda_0\times0.093\lambda_0\times0.026\lambda_0$ at 2.34 GHz
[7]	60×5×5 mm^3 & $0.164\lambda_0\times0.013\lambda_0\times0.013\lambda_0$ at 0.82 GHz
[8]	20×25×0.8 mm^3 & $0.23\lambda_0\times0.287\lambda_0\times0.009\lambda_0$ at 3.45 GHz
PROPOSED	14.2×6.2×0.8 mm^3 & $0.023\lambda_0\times0.01\lambda_0\times0.001\lambda_0$ at 0.5 GHz

Table 1-2: Bandwidths

[5]	2.39-2.87 GHz & 18.25%
[6]	2.34-2.54 GHz & 8.2%
[7]	0.82-2.48 GHz & 100.6%
[8]	3.45-3.75 GHz & 8.33%
PROPOSED	Measured: 0.5-2 GHz & 120%
	ADS: 0.4-2.08 GHz & 135%
	HFSS: 0.47-2.04 GHz & 125%
	CST: 0.45-2.1 GHz & 129%

Table 1-3: Gains in dBi (for proposed antenna at 0.7, 1.5 and 2 GHz, respectively, in each of four cases)

[5]	2.2	
[6]	1	
[7]	0.4	
[8]	2	
PROPOSED	Measured	3.8-4.85-4.3
	ADS	3.9-4.92-4.35
	HFSS	3.95-4.96-4.4
	CST	3.85-4.9-4.42

It should be noted that, the simulation processes were performed on the infinite GND, but due to size limitations and requirements for design of the small structure to fit on the RF electronic devices and embedded systems, the fabrication procedures have been performed on the finite GND. Hence, the simulation and measurements results have slightly differences.

IV. CONCLUSION

A novel composite right/left-handed carved planar (CRLH-CP) antenna with minimized size, ultra wide bandwidth and good radiation properties has been presented and fabricated. In the design procedure, for producing series capacitances with smaller amounts, the Y-form slots with minimized sizes have been implemented on the carved circuit boards (CCBs) by the standard manufacturing techniques (SMTs); also, to obtain the good performance parameters, the suitable inductive elements such as rectangular inductors with regulated dimensions were designed, and for the uniform excitation mechanism by applying two ports for increase of the antenna, effective aperture have been used, so that these ways have caused to provide a UWB minimized antenna with

appropriate radiation characteristics. The physical dimension of the proposed CRLH-CP antenna is $0.023\lambda_0$ by $0.01\lambda_0$ by $0.001\lambda_0$, in terms of free space wavelengths at 0.5 GHz, which corresponds to overall size of $14.2\times6.2\times0.8$ mm^3. As well as, this antenna has 120% practical bandwidth from 0.5 GHz to 2 GHz with maximum of 4.85 dBi radiation gain and 68.5% efficiency that occur at 1.5 GHz. According to the results, the carved planar (CP) UWB minimized antenna based on MTM CRLH-TL is sufficiently small for integration into RF components for use in the UWB RF electronic devices and embedded systems.

REFERENCES

[1] W. L. Stutzman, "Antenna theory and design," Second Edition, *J. Wiley &Sons*, 1997.

[2] R. W. Ziolkowski and A. D. Kipple, "Application of double negative materials to increase the power radiated by electrically small antennas," *IEEE Trans. Antennas Propag*., vol. 51, no. 10, pp. 2626-2640, October 2003.

[3] G. V. Eleftheriades, A. Grbic, and M. Antoniades, "Negative-refractive-index transmission-line metamaterials and enabling electromagnetic applications," *In Proc. IEEE Antennas and Propagation Int. Symp*., pp. 1399-1402, June 2004.

[4] N. Engheta and R. W. Ziolkowski, "Metamaterials: physics and engineering explorations," *Wiley-IEEE Press*, 414 p., 2006.

[5] C. J. Lee, M. Achour, and A. Gummal la, "Compact metamaterial high isolation MIMO antenna subsystem," *2008 Asia Pacific Microwave Conference*, pp. 1-4, December 2008.

[6] C. J. Lee, K. M. H. Leong, and T. Itoh, "Broadband small antenna for portable wireless application," *International Workshop on Antenna Technology: Small Antennas and Novel Metamaterials, iWAT* 2008, pp. 10-13, March 4-6, 2008.

[7] Y. Li, Z. Zhang, J. Zheng, and Z. Feng, "Compact heptaband reconfigurable loop antenna for mobile handset," *IEEE Antennas and Wireless Propagation Letters*, vol. 10, pp. 1162-1165, 2011.

[8] C. C. Yu, M. H. Huang, L. K. Lin, and Y. T. Chang, "A compact antenna based on MTM for WiMAX," *Asia-Pacific Microwave Conference, (APMC)*, Macau-China, December 16-20, 2008.

[9] H. A. Wheeler, "Fundamental limitations of small antennas," *Proc. IRE*, vol. 35, pp. 1479-1484, December 1947.

[10] C. Caloz and T. Itoh, "Electromagnetic metamaterials transmission line theory and microwave applications," *New Jersey: John Wiley & Sons, Inc*., 2006.

[11] R. Porath, "Theory of miniaturized shorting-post microstrip antennas," *IEEE Trans. Antennas Propag*., vol. 48, no. 1, pp. 41-47, January 2000.

[12] S. Jahani, J. Rashed-Mohassel, and M. Shahabadi, "Miniaturization of circular patch antennas using MNG metamaterials," *IEEE Antennas and Wireless Propagation Letters*, vol. 9, 2010.

[13] C. Wang, B. J. Hu, and X. Y. Zhang, "Compact triband patch antenna with large scale of frequency ration using CRLH-TL structures," *IEEE Antennas and Wireless Propagation Letters*, vol. 9, 2010.

[14] F. Bilotti, A. Alu, and L. Vegni, "Design of miniaturized metamaterial patch sntennas with μ-negative loading," *IEEE Transaction on Antennas and Propagation*, vol. 56, no. 6, June 2008.

[15] M. Alibakhshi Kenari, "Introducing the new wide band small plate antennas with engraved voids to form new geometries based on CRLH MTM-TLs for wireless applications," *International Journal of Microwave and Wireless Technologies*, page 1, DOI:http://dx.doi.org/10.1017/S1759078714000099, March 2014.

[16] M. Alibakhshi Kenari, "Printed planar patch antennas based on metamaterial," *International Journal of Electronics Letters*, pp. 37-42, http://dx.doi.org/10.1080/21681724.2013.874042, January 2014.

Mohammad Alibakhshi-Kenari was born February 24, 1988 in Iran, Mazandaran, Freidounkenar. He received the B.S. and M.S. degrees in the Electrical Engineering field of Telecommunication from the Islamic Azad University, Najafabad Branch at Esfahan, Iran in February 2010 and the Islamic Republic of Iran, Shahid Bahonar University of Kerman in February 2013, respectively. His researches interests include microwave and millimeter wave circuits, radars, antennas and wave propagation, composite right/left-handed transmission lines (CRLH-TLs), metamaterial (MTM) applications, integrated RF technologies, embedded systems, electromagnetic waves applications and wireless telecommunication systems.

He is now "Editor-in-Chief" with Journal Club for

Electronic and Communication Engineering (JCECE) and also works as a Reviewer in the several ISI journals such as Elsevier, Taylor & Francis, Wiley, ACES, and etc. A-Kenari has served as a Member of the Technical Program Committee (M-TPC) of some of the international conferences such as APACE 2014, APPEIC 2014, MobiWIS 2014, ICEPIT 2014, CICN 2014, ADVCIT 2014, DPNoC 2015, MobiApps 2015 and etc. So far, he has been published several papers. Master Thesis of A-Kenari entitled "Designing and Fabricating the Ultra Compact and UWB Antennas based on Metmaterial Transmission Lines with Application in Wireless Radio Transceivers" was approved and granted by Iran Telecommunication Research Center (ITRC) in December 2012 with grant number of 6987/500/T.

Mohammad Naser-Moghadasi was born in Saveh, Iran, in 1959. He received the B.Sc. degree in Communication Eng. in 1985 from the Leeds Metropolitan University (formerly Leeds Polytechnic), UK. Between 1985 and 1987, he worked as an RF Design Engineer for the Gigatech Company in Newcastle Upon Tyne, UK. From 1987 to 1989, he was awarded a full scholarship by the Leeds Educational Authority to pursue an M.Phil. studying in CAD of Microwave circuits. He received his Ph.D. in 1993, from the University of Bradford, UK. He was offered then a two years Post Doc. to pursue research on Microwave cooking of materials at the University of Nottingham, UK. From 1995, Naser-Moghadasi joined Islamic Azad University, Science and Research Branch, Iran, where he currently is Head of Postgraduate Studies and also Member of Central Commission for Scientific Literacy and Art Societies. His main areas of interest in research are Microstrip antenna, Microwave passive and active circuits, RF MEMS.

Naser-Moghadasi is Member of the Institution of Engineering and Technology, MIET, and the Institute of Electronics, Information and Communication Engineers (IEICE). He has so far published over 140 papers in different journals and conferences.

Physics-Based Modeling of Power Converter Drive System for Evaluation of Electromagnetic Compatibility

M. R. Barzegaran, A. Nejadpak, Student ACES, and O. A. Mohammed, Fellow ACES

Energy Systems Research Laboratory, ECE Department
Florida International University, Miami, FL. 33174, USA
mohammed@fiu.edu

Abstract ─ In this paper, detailed physics-based modeling of a power converter drive is proposed. The 3D finite element (FE) modeling of a power inverter was developed and analyzed. An approach in physical modeling of the switching activity of the inverter in FE is proposed. In addition, the solver was modified and implemented for analyzing nonlinear materials in time-harmonic cases to achieve faster computation. The frequency response analysis was also implemented in simulation and measurements at various locations from the source. The numerical simulation provided the exact field solution at any given distance and defined the correlation between the electromagnetic fields generated by each of these components. The importance of this work is to facilitate the ability to evaluate the stray electromagnetic field levels used for evaluating EMC compliance at the design stage. In addition, the recognition of a failure condition inside each component of the system by observing the fields is another important contribution of this work. The optimum operation of the system components for lower EMI and optimum design of related shielding for EMC evaluation studies are added benefit of this work.

Index Terms ─ FE analysis, low frequency EMC analysis, power electronics drives.

I. INTRODUCTION

With the increased development and utilization of power electronic drives, the evaluation of low frequency stray electromagnetic fields (DC to hundreds of kHz) in these devices becomes necessary. Power electronic drives have an electric system of significant power consisting of power converters, electric motors and electric loads. This is in addition to all connecting wires and cables which are usually located in close proximity within the systems. For example, in electric vehicles as an important application of power electronic drives, it is a common practice to place the battery stack as far as possible from the bodywork to reduce the risk of battery damage. This arrangement implies placing them just under the seats of the vehicle. It follows that during acceleration or deep regenerative braking, there might be currents in the hundreds of amperes circulating a few centimeters away from the passengers [1]. In addition to the effect of the stray field into the environment, when harmonic current of low order is emitted into a network, the voltage is distorted reducing the voltage quality. The level of voltage distortion is dependent on the network strength. Similarly, high frequency current harmonics may cause the voltage harmonics in the network. As a harmonics effect, the current harmonics may cause overheating of, e.g., neutral conductors and capacitors in three-phase systems. Also, the voltage harmonics may upset the electronics, e.g., due to multiple zero crossings; therefore, the loading capability of induction machines may be reduced [2].

The equivalent circuit modeling of power electronic drives is not applicable for studying the radiated emission in the three dimensional areas around the drive. Therefore, the physics based modeling is proposed in this paper to evaluate the stray field in the three dimensional space around the devices. In addition, the material properties of the devices and shape representation were investigated in this modeling process. On the other hand, time-varying electric and magnetic fields generate MMFs and EMFs that can sustain the fields that compromise the flux. Also, the currents and voltages in electric power systems are time-varying, which causes stray electromagnetic fields. Therefore, there is a need to model the EMI generated by these systems to develop designs meeting EMC standards.

Several studies were performed in the area of radiated low frequency electromagnetic field (EMF) analysis of power electronic devices [3]-[8]. In [3], some general principles on how to allocate responsibilities between the power grid and connected equipment were investigated with the aim to achieve electromagnetic compatibility in electric power systems. It was shown, in this paper, that in medium and high voltage systems, in absence of comprehensive equipment emission and immunity standards, it is

Submitted On: September 22, 2013
Accepted On: September 24, 2014

suggested that the grid responsible party provides relevant data such as on voltage dips to the party responsible for connecting equipment to the grid. Some studies have dealt with the impact of stray EMFs on the environment including humans and the operation of devices [4]. This test is implemented from very low frequencies 5 Hz to medium frequencies 300 kHz. Both magnetic and electric fields are tested using gauss meters and electric field meters. On the other side, other studies were conducted to implement attenuators and shielding of the conducted and field bound EMI [5], [6]. Akagi, *et al*., focuses on a line EMI filter and its combination with a motor EMI filter, along with their effects on attenuation of conducted emission voltage. Furthermore, the effectiveness of an EMI filter configuration when the filter is applied to the motor was discussed [5]. In [6], EMI noises generated in the power converter and diffused on the surface of conductors are targeted to be controlled. Consequently, a new approach based on distributed constant circuit theory along with multilayer power printed circuit technology was used.

For developing a model, the equivalent source representation as well as the physics based modeling were studied. Aouine, *et al*., designed high and low frequency models of the converter for magnetic near field by using modeling switching parts by circular magnetic dipoles [7]. Moreover, the physics based modeling of the power electronic drives in low frequency EMF was studied in [8]-[11]. In [8], the optimum equivalent source modeling along with the physics based modeling of an AC motor was analyzed. The idea of loops was enhanced based on optimization methods. In addition to the implementation of the physics based modeling to machines, this type of modeling was also utilized for the power converter switches for the study of the conducted EMI [11]. Since the conducted EMI mostly exist on printed circuit boards (PCB), the FE model of the PCB was studied. Also, the optimization of EMI performance was accomplished in terms of component placement on the PCB [11].

There is a need to have a physics based model, with all details, for the various system components to include the physical effects of stray fields such as superposition and shielding. However, this model has some issues such as the problem of fast switching of the IGBTs and nonlinear commutation curves. Hence, in this paper, the three dimensional full finite element modeling of a typical power electronic drive at low frequency is analyzed. The identified issues with the proposed resolutions are explained. The frequency response analysis of the power converter drive was implemented in the simulation as well as in the experimental setup in two cases of setup, one with an AC load and the other with an induction motor, as a dynamic load. The results of these two cases were compared and their application in EMC study was discussed.

II. STRAY LOW FREQUENCY FIELD CALCULATION

Assuming an electric component as consisting of a series of a large number of infinitesimally short conducting elements, each of such elements is so short that the current may be considered uniform over its length. The field of the entire component may be obtained by integrating the fields from all these differential elements, with the proper magnitude and phases taken into account. It is proposed to review the radiation properties of such a differential element, named as a short dipole for low frequency propagation.

A short dipole, also called a Hertzian dipole, is a thin, linear conductor whose length l is very short compared with the wavelength λ, l should not exceed λ/50 which is not an issue for low frequency analysis. The wire which is oriented along the z-direction as shown in Fig. 1, carries a sinusoidally varying current $i(t) = I_0 \cos\omega t$, where I_0 is the current amplitude.

Based on the Biot-Savart law and Ampere's law for time-varing volume current, the retarded magnetic potential in phasor domain is:

$$\mathbf{A} = \frac{\mu}{4\pi}\int_v \frac{\mathbf{J}e^{-jkR}}{R}dv, \tag{1}$$

where J is the current density distribution through volume v observed at the p point with the R distance and

$$k = \frac{\omega}{\upsilon_p}, \tag{2}$$

is the wavenumber of the propagation medium and υ_p is the velocity of propagation in the medium between the charge distribution and observation point [12].

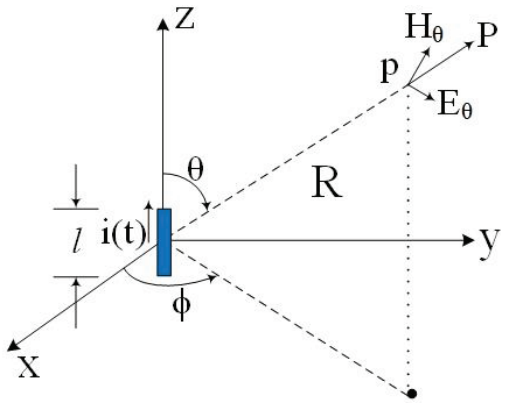

Fig. 1. The electric dipole antenna (the Hertzian dipole).

The time-variant currents and the potential in (1) will lead to an inconstant field with Maxwell equation. The reason is that the time-variant fields give rise to wave propagation. According to which the effect of the source current at a given value of time is felt at a distance R from the origin after a time delay of R/υ_p. Conversely, the effect seen at a distance R from the origin at time t is due to the current existing at the origin at an earlier time ($t- R/\upsilon_p$). Thus, for the time-varying current element $I_0\, dl\, \cos\omega t\, a_z$ situated at the origin, the magnetic vector potential is given by:

$$\mathbf{A} = \frac{\mu I_0\, dl}{4\pi R}\cos(\omega t - \beta R)\mathbf{a}_z\,, \tag{3}$$

where β is R/υ_p, the phase constant. The magnetic field **H** due to the Hertzian dipole is given by:

$$\mathbf{H} = \frac{I_0\, dl \sin\theta}{4\pi}\left[\frac{\cos(\omega t - \beta R)}{R^2} - \frac{\beta \sin(\omega t - \beta R)}{R}\right]\mathbf{a}_\phi . \tag{4}$$

Equation (4) represents the radiated magnetic field due to the Hertzian dipole [13]. Using Maxwell's curl equation for **H** with **J** set equal to zero in view of perfect dielectric medium, the radiated electric field due to the Hertzian dipole would be given by:

$$\mathbf{E} = \frac{2I_0\, dl\cos\theta}{4\pi\varepsilon\omega}\left[\frac{\sin(\omega t - \beta R)}{R^3} + \frac{\beta\cos(\omega t - \beta R)}{R^2}\right]\mathbf{a}_R + \frac{I_0\, dl\sin\theta}{4\pi\varepsilon\omega}\left[\frac{\sin(\omega t - \beta R)}{R^3} + \frac{\beta\cos(\omega t - \beta R)}{R^2} - \frac{\beta^2\sin(\omega t - \beta R)}{R}\right]\mathbf{a}_\theta . \tag{5}$$

The stray field of a complex model with thousands of dipoles, such as the proposed drive, needs the calculation of the field of each of these dipoles using equations (4) and (5) as well as a vigorous field calculated by using a numerical technique such as the FE method.

The proposed model was accurately built in FE in which the above equations are calculated by modifying the default equations for obtaining electric and magnetic fields. The conductors are modeled as wires, which are modified from volumetric model into linear model, while their magnetic and electric flux density kept constant [CEFC]. The other components which have effect on radiated fields, are mainly switches and capacitors, which are modelled in 3D, but with some modifications that are explained in the following section.

III. SIMULATION AND MEASUREMENT

The proposed setup consists of an inverter, an induction machine, connecting cables and an AC load. The study was divided into two cases for further investigation. The converter connected to an AC load as the case 1 and converter connected to an induction motor as case 2. Each study was discussed along with its application as follows:

Case 1: Converter connected to the load

The proposed full finite element model for the first case is shown in Fig. 2. This electronic drive consists of an inverter, AC load and the armored connection cable. The details of the devices are identified in Table 1.

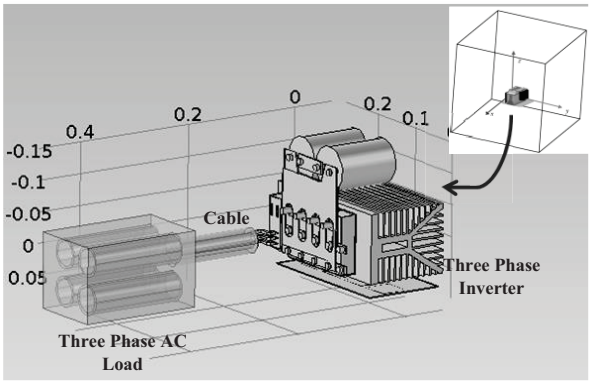

Fig. 2. The prototype of the inverter, load and the connection cable.

Table 1: The details of the components in the tested setup

Component	Characteristics
Inverter	Three-phase, 5.5 kW, Switching frequency: 5-kHz, Switching algorithm: SVM, Length: 30-cm, Width: 30-cm, Height: 25-cm, Nominal voltage: 320-V, Amp: 20-A
Electric load	3-kW AC load
Connection cable	XLPE, Diameters: Cross-sectional area: 1000 mm^2, Thickness of insulation: 2.8 mm, Nominal thickness of pvc sheath: 2.4 mm, Overall diameter: 51 mm, insulated and armored PVC sheathed cable

The schematic of the inverter's circuit is shown in Fig. 3. In this simulation, the IGBT module was operated for a relatively low switching frequency to illustrate the behavior of the circuit. In the PWM inverter of Fig. 3, the duty cycle ratio of the input signal to the IGBT gate drivers is varied using the space vector PWM technique to produce a 60-Hz sinusoidal variation of the RL load current [14].

The operation of the inverter was divided into six sections. During the first $\pi/3(rad)$ of 60-Hz inverter

operation, IGBTs S_{ap}, S_{bn} and S_{cn} are switched on while the others are in the off state. This process changes in a way to track the reference voltage as [14]:

$$V_{ref} = \frac{3}{2}(V_a + \alpha V_b + \alpha^2 V_c), \quad \alpha = e^{j\frac{2\pi}{3}}. \tag{6}$$

The inverter operation during other sequences of the 60-Hz reference sine wave is similar to the aforementioned sequence, except that the opposite phase of the bridge is switched on and off. The sinusoidal variations of the duty cycle ratios for each phase were specified by comparing triangular waveforms to the magnitude of the sinusoidal reference signal. When the value of the reference sine wave is larger than the value of the upper triangle wave, S_{ap} is switched on; otherwise, it must be off. The same procedure goes within the other IGBTs as well. Figure 4 shows the simulated load current for the space vector PWM (SV-PWM) operation.

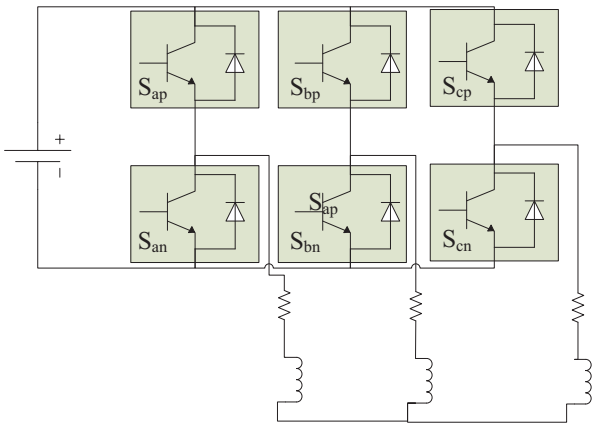

Fig. 3. Schematic of six switch inverter circuit, [17].

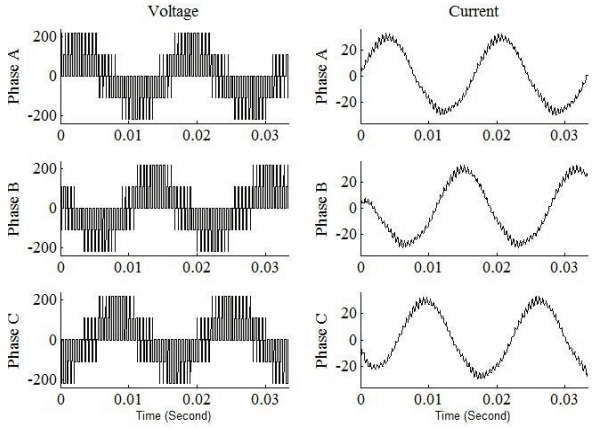

Fig. 4. Line current and voltage in the case of SVPWM.

To model the IGBT switches of the inverter for signature studies, the switches must be considered OFF for a moment of time and then it must be considered ON for the next time instant. This shift occurs based on the switching frequency of the converter. In order to do this in FE simulation, the plate between the load and the positive bus, shown in Fig. 5, is considered a conductive plate for the switch-ON case. Subsequently, this plate is considered a non-conductive plate for the switch-OFF case. This alteration of the conductivity of the plate occurs 5000 times in a second due to the switching frequency (5 kHz).

As mentioned earlier, time-harmonic solution method is being used. Therefore, the transient conditions of the inverter and machines are not considered. The base is on the steady-state condition of a power train. In order to apply this condition in time-harmonic solvers, the model was being captured for the moments of ON and OFF individually and finally the results of the period was accumulated. Since the simulation time would increase dramatically if all time-instants of a time period was considered, hundred time instants are measured.

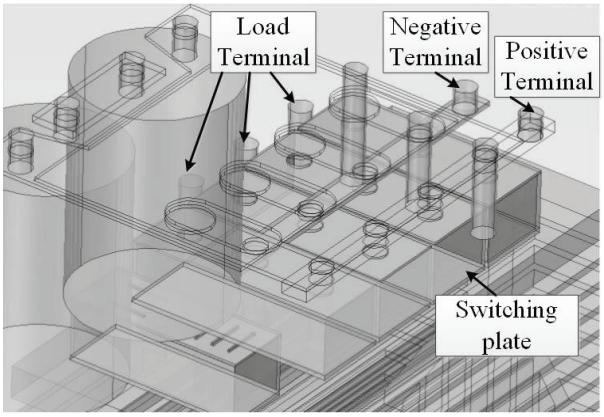

Fig. 5. Physical model of the inverter switches.

The simulation was computed in six hours with about one million elements including face, line and node meshes in the model with six million degrees of freedom. The large number of elements is necessary because of the very small surfaces, edges and lines of the critical part of inverter and cable, as shown in Fig. 6. The details of FE modeling is reflected in [21]-[23]. The simulation was implemented in a fast computer with 192 GB ram and 16 core Intel Xeon 3.47 GHz CPU.

Since there are two cases in this study, it was decided to define two types of results. In case 1, the generated fields of the system on three different surfaces at a distance in space are considered as the result, and in the case 2, the harmonics of the fields and the frequency responses are investigated. Hence, in this case, the generated stray magnetic and electric fields

are obtained in three dimensions at a given distance in both switching circumstances.

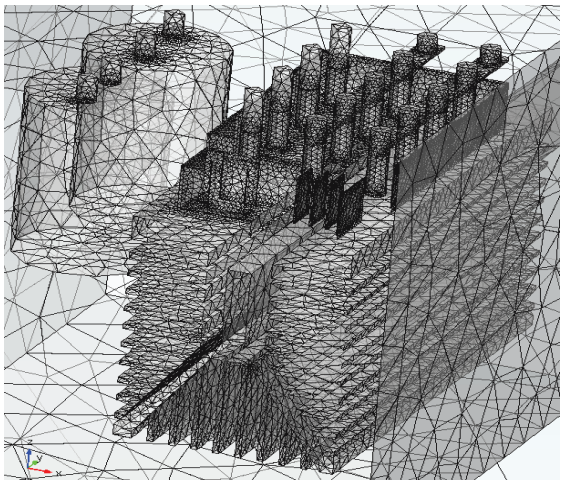

Fig. 6. Mesh pattern of the modeled inverter.

Figures 7 (a) and (b) show that, turning on and off the switches have the effect only on the amplitude of the magnetic field density and the spatial distribution of the stray magnetic field on the slices doesn't change significantly. This is due to the presence of the AC load which is discussed further. On the other hand, the electric field which is shown in Fig. 8, illustrates that when the switches turn on, the electric field in two lateral planes, XY-plane, YZ-plane, increases while the field in the XZ-plane decreases. The increase of the electric field, in these planes, is due to the flow of current in the switches. It is also due to the creation of a current loop and its reduction is because of the superposition which is, suppression in this case. The suppression occurs due to the propagation of fields into the other conductive parts of the devices in vicinity; therefore, the stray field induced from the imposed conductive parts decreases. The reason of the suppression is the inverse direction of the induced field due to Lenz's law [15]. Therefore, the induced stray field is subtracted from the main stray field and the total field decreases as in Fig. 8 (a).

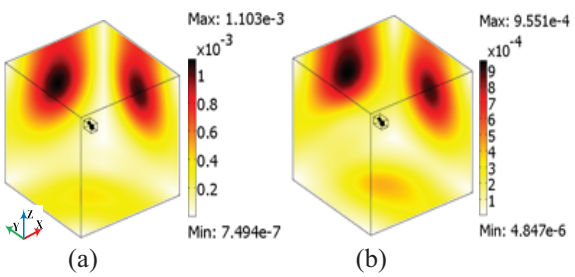

Fig. 7. Stray magnetic field density of the system: (a) IGBT switched on, and (b) IGBT switched off (μT).

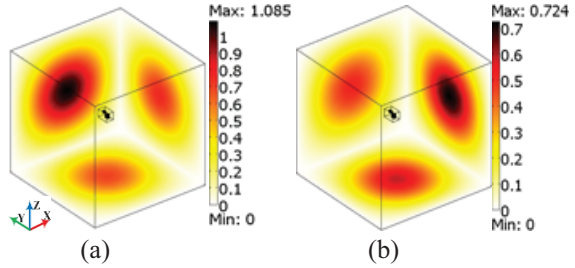

Fig. 8. Stray electric field of the system: (a) IGBT switched on, and (b) IGBT switched off (μV/m).

To recognize which element of the setup has more effect on the total field, the stray magnetic field of each component in this setup were analyzed individually to observe their spectrum and compare it with the overall fields. The results are shown in Figs. 9 (a)-(d). Comparing Fig. 9 (c) with Fig. 9 (a) and Fig. 9 (b), while only the load is switched ON, the stray magnetic field has a higher value in comparison with Fig. 9 (a), (b) and the total field was affected by it (compare Fig. 9 (c) with Fig. 9 (d)). The reason is that the AC load has bigger conductive elements including iron and copper materials compared to the other elements in the setup.

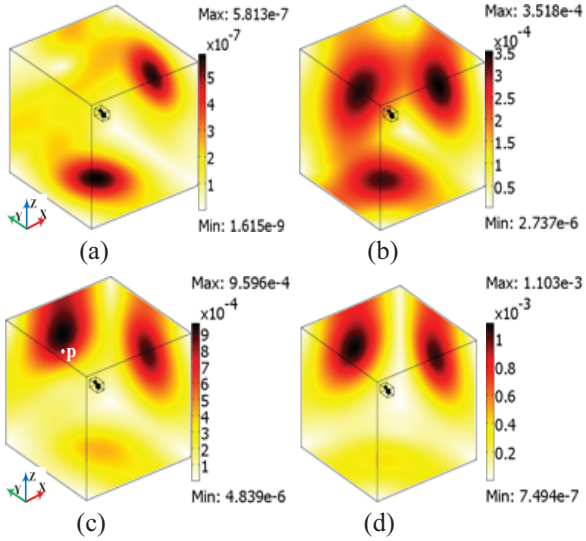

Fig. 9. Stray magnetic field density of the system (μT): (a) only the cable is switched on, (b) only the inverter is switched on, (c) only the load is switched on, and (d) the whole system is switched on.

In order to investigate the effect of superposition, the generated field of a random point (p) of the figures, shown in Fig. 9 (c), can be used. For instance, the values of a point of the three cases (0, 5 m, 0) of Fig. 9, Fig. 9 (a)-Fig. 9 (c), are aggregated. The result is $1.31e^{-3}$ (μT) while the overall maximum point is $1.10e^{-3}$ (μT), as shown in Fig. 9 (d). This can be due to the

dissimilarity of permeabilities and conductivities of the elements of the model. If the resistance of an element is less than another element in the vicinity while there is no shield between them, the EMF will be induced from the component with less conductivity into the one with higher conductivity [16]. As mentioned above, due to Lenz's law, the field radiated from the induced EMF will be the opposite of the main field. Therefore, the overall field will be less than the aggregation of the fields.

Case 2: Converter connected to the motor

In this case, the inverter is connected to an induction motor. The aim of this case is investigating the radiation of the harmonic fields from the inverter while the distance and the speed of the motor change. The parameters of the induction motor are: 5.5-kW, 3-phase, 208-V, PF: 0.85, length: 30-cm, diameter: 25-cm, number of poles: 4. This case was simulated using FE shown in Fig. 10 (a).

The simulation was computed in six hours with 950000 elements and 5.7 million degrees of freedom. Since the case includes very small elements and also nonlinear materials, e.g., the core of the machine, the simulation of the inverter connected to the load or motor may take 8 hours or more for only one time instant.

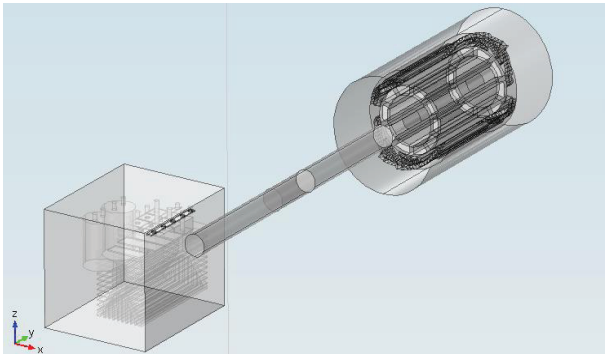

(a)

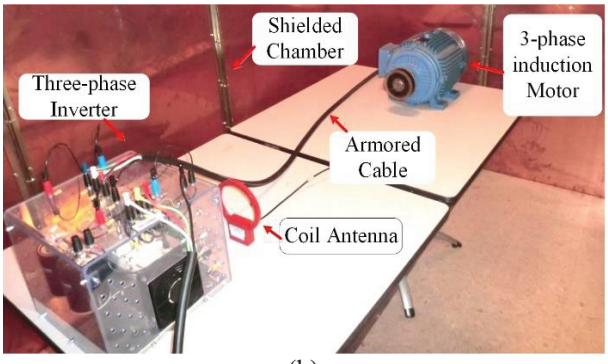

(b)

Fig. 10. The scheme of the setup of case 2: (a) FE simulation, and (b) measurement.

Generally, linear or non-linear solvers are being used in the FE simulations. In this case, since there are several materials with nonlinear characteristics, the linear solver cannot be used. On the other hand, using nonlinear material rises the simulation time dramatically. Hence, a modification in choosing the solver and the associated iterative technique was employed. Instead of having linear or curved commutation curve, the ramp of the curve in several zones was calculated (μ_{r1}, μ_{r2} …) and used instead of the commutation curve in this part, as shown in Table 2. The benefit of this modification is that the magnetic flux density of a component changes in a very small period due to the steady state condition of the system. For example, the magnetic flux density of the stator core of the induction motor is about 1.5-2 T in power frequency analysis, 50-60 Hz. For higher frequencies, it goes down to under 1 T. Therefore in this case, a specific zone of the permeability can be chosen for this component. Similarly, the permeability of the other components of the system can be chosen based on the working frequency. Therefore, having the idle parts of the commutation curves of the elements would be avoided and the simulation time decreases. This algorithm can be defined in the material properties part of the FE simulation.

Table 2: Commutation curve of some material used in the simulation

Material	Flux Density (T)	Permeability (μ)
Steel (μ_{r1})	0-1.2	1.2×10^{-3}
Steel (μ_{r2})	1.2-1.5	1.5×10^{-4}
Steel (μ_{r2})	1.5-1.8	4.2×10^{-5}
Iron	0.2-0.6	1.3×10^{-4}

In addition to the modification in defining the material properties, some modification needs to be performed for the solver to have a flexible solution. Hence, as the iterative solver, the fast generalized minimal residual technique, GMRES, with the Krylov's method as the pre-conditioner was used. The fast GMRES is a variant of the GMRES method with flexible preconditioning that enables the use of a different pre-conditioner at each step of the Arnoldi process. The Krylov subspace is a linear subspace which enables multi-preconditioning [17]. In particular, a few steps of GMRES can be used as a pre-conditioner for fast GMRES. The flexibility of this solution method is beneficial for the problem with nonlinear material characteristics such as the motor's core. Therefore, the simulation time decreases from about 8-9 hours to about 20 minutes. More explanation is given in [18].

In addition to the simulation, the experimental setup was implemented in a chamber which isolates the setup from the outside environment, shown in Fig. 10 (b). The experiment was implemented based on the

MIL-STD-462D [19]. The coil antenna and the real-time spectrum analyzer, which is used in the measurement, are specifically for low frequency analysis with high precision. The frequency range of the utilized coil antenna is between 20-Hz–500-kHz. The winding of the antenna is 36 turns of 7-41 litz wire shielded with 10 Ohms resistance and 340-μH inductance. The antenna and the setup were located based on the standards (MIL-461-STD [20], MIL-462-STD). The spectrum analyzer also covers 1-Hz-3–GHz with ±0.5 dB absolute amplitude accuracy to 3-GHz. The coil antenna was located at 10 cm away from the inverter to obtain the stray magnetic field. The fields were transferred to an EMI receiver, real-time spectrum analyzer, with a cable of 50-Ω impedance.

The magnetic field intensity (H-field) generated from the setup in simulation is shown in Fig. 11. The H-field at 5-kHz frequency is shown on a slice at 10 cm away from the setup, the same as experimental setup. As illustrated in this figure, the amplitude of the stray field around the inverter box is higher than other places. The reason is that the switching frequency of the inverter is 5 kHz, the same as the frequency depicted from the simulation figure. The simulation was implemented at several other frequencies. Only the switching frequency of the inverter which is 5-kHz, is shown here.

The setup was also implemented experimentally. The frequency response from DC to 20-kHz was obtained and shown in Fig. 12.

The unit of the simulation result is μA/m, while the unit of the experimental results is dBμA/m. The μA/m can be converted to dBμA/m by using eq. (7). Using this equation, the peak of the stray magnetic field at 5-kHz at the given distance is -4.37 dBμA/m experimentally, would be 0.61 μA/m which is very close to the value in simulation, see Fig. 11;

$$1\,\mu A/m = 10^{\frac{dB\mu A/m}{20}}. \quad (7)$$

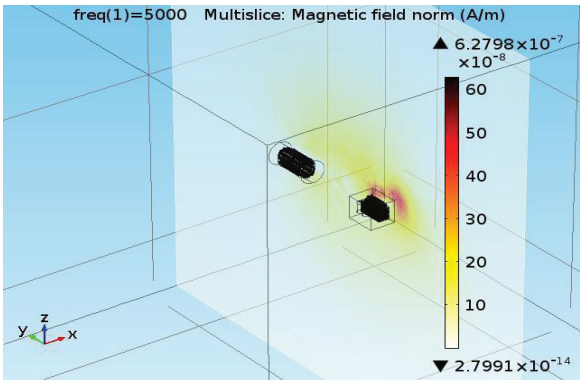

Fig. 11. Stray magnetic field intensity of the setup case 2 at 5 kHz simulated in FE (μA/m).

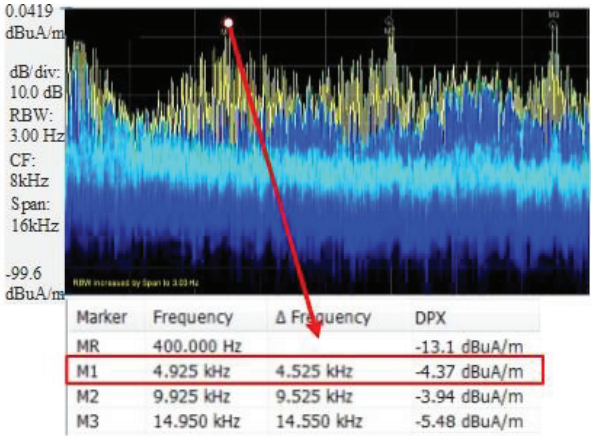

Fig. 12. Measured frequency response of the stray magnetic field intensity of the setup case 2 from DC to 20 kHz (dBμA/m).

IV. APPLICATIONS OF THE FREQUENCY RESPONSE ANALYSIS OF THE STRAY FIELD

Following the experimental verification of the simulation results, related applications such as monitoring of components for the diagnosis of failures and shielding were investigated:

As shown in Fig. 12, the first peak located at very low frequency is generated from the induction motor, since the motor is working at the power frequency, 60 Hz. As the working frequencies of the components in the system are different, the behavior of each component can be investigated individually. This can be a very useful hint in monitoring the conditions as well as detecting the faults of the motor and the inverter. For example in case 2, Fig. 12, if a failure occurs in the motor, the peak at the power frequency and the related higher harmonic orders will shift along the frequency band or the amplitudes would change. Similarly, failures to the inverter may cause the same type of changes in switching frequency and the related higher harmonic orders. Note that, the peaks at 10-kHz and 15-kHz in Fig. 12 are due to the second and the third harmonics of the inverter. The frequency responses in between the harmonics are noises and sub-harmonics.

As another application of this case, the shielding in the vicinity of the switch, 5 cm, was tested. Figure 13 shows the frequency response of the stray H-field with and without the shield between the switches and the antenna by means of simulation and measurement. Using a steel shield, Steel 1018, as an example in this test, it can be seen that the noises, sub-harmonics between the main harmonic orders, decrease dramatically. The experimental results show a wider band of frequency, DC–20 kHz, as shown in Fig. 14 to illustrate the effect of shielding on the other harmonic

orders.

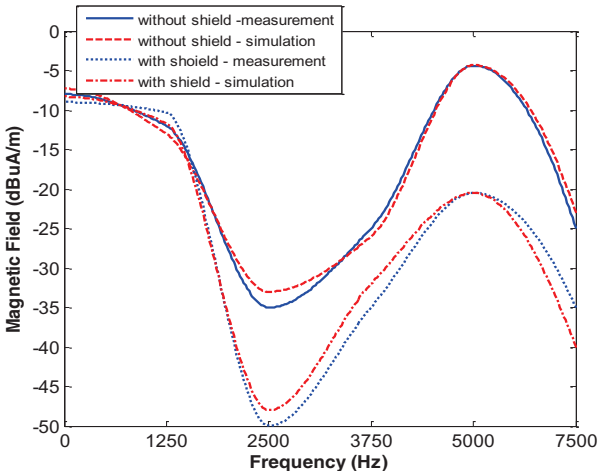

Fig. 13. Stray H-field of the case2 from DC-7.5 kHz (dBμA/m) at 5 cm from the inverter with and without shield by simulation and measurement.

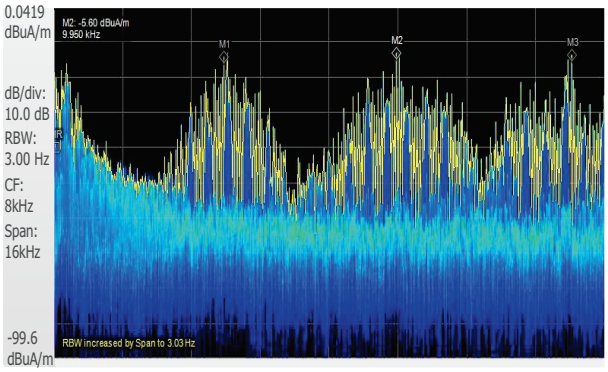

(a) Without shield

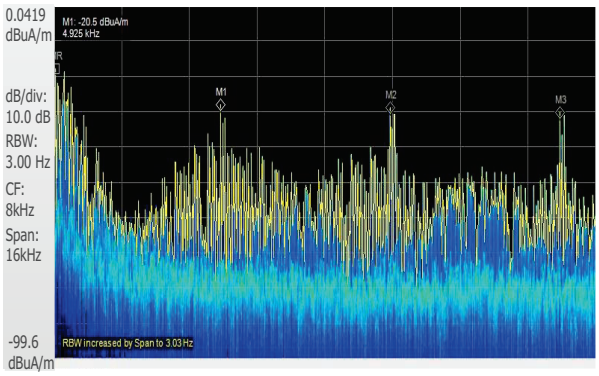

(b) With shield

Fig. 14. Stray H-field of the case 2 from DC-20 kHz (dBμA/m) at 5 cm away from the inverter: (a) without shield, and (b) with shield.

Consequently, considering this test, the main harmonics and the related sub-harmonics can help in selecting a shield with proper characteristics including the permittivity and permeability. Comparing the curves of Fig. 13, the simulation result is similar to the experimental one. Hence, the proposed shield can be studied and optimized using the physics based simulation. The permittivity, permeability, conductivity and other physical characteristics of the shield can be altered and optimized for the best electromagnetic compliance or any other purposes using simulation and experimental design.

V. CONCLUSION

In this paper, 3D full finite element modeling for the radiated EMI study of a typical power electronic drive was implemented. The physical approach for applying the switching activity was utilized. In order to have the detailed simulation of the model and simultaneously consider the non-linearity of commutation curve in the frequency analysis, the fast GMRES methods with proper pre-conditioners were used as the solution method which increases the simulation speed. The measurement was also applied for verification of the numerical results as well as for investigating the stray fields under different operating conditions. The results show that the FE model has a good accuracy for evaluating the stray fields. Two cases of using the inverter in the system were studied and their applications were explained. The results show that the frequency response of the field can be used for assessing shielding arrangements as well as for monitoring the conditions of the drive.

ACKNOWLEDGEMENTS

Part of this work was supported by a grant from the Office of Naval Research.

REFERENCES

[1] M. Halgamuge, C. D. Abeyrathne, and P. Mendis, "Measurement and analysis of electromagnetic fields from trams, trains, and hybrid cars," *Radiation Protection Dosimetry*, vol. 141, no. 3, pp. 255-268, 2010.

[2] M. Olofsson, "Low frequency EMC and power quality," *In Compliance Mag*., pp. 34-41, Apr. 2012.

[3] M. Olofsson and U. Grape, "Framework for electromagnetic compatibility in electric power systems," *VIII International Symposium and Exhibition on Electromagnetic Compatibility and Electromagnetic Ecology*, St. Petersburg, Russia, June 16-19, 2009.

[4] Electromagnetic Health Organization, "EMF test of 2007 Toyota Prius hybrid," *Electromagn. Health*, 2008.

[5] H. Akagi and T. Shimizu, "Attenuation of conducted EMI emissions from an inverter-driven

motor," *IEEE Transactions on Power Electronics*, vol. 23, pp. 282-290, 2008.
[6] N. Mutoh, J. Nakashima, and M. Kanesaki, "Multilayer power printed structures suitable for controlling EMI noises generated in power converters," *IEEE Transactions on Industrial Electronics*, vol. 50, no. 6, pp. 1085-1094, Dec. 2003.
[7] O. Aouine, C. Labarre, and F. Costa, "Measurement and modeling of the magnetic near field radiated by a buck chopper," *IEEE Transactions on Electromagnetic Compatibility*, vol. 50, no. 2, pp. 445-449, May 2008.
[8] M. R. Barzegaran and O. A. Mohammed, "3-D FE wire modeling and analysis of electromagnetic signatures from electric power drive components and systems," *IEEE Transactions on Magnetics*, vol. 49, no. 5, pp. 1937,1940, May 2013.
[9] G. Ala, M. C. Di Piazza, G. Tine, F. Viola, and G. Vitale, "Numerical simulation of radiated EMI in 42V electrical automotive architectures," *IEEE Transactions on Magnetics*, vol. 42, no. 4, pp. 879-882, Apr. 2006.
[10] Z. Cheng, H. Takahashi, B. Forghani, L. Liu, Y. Fan, T. Liu, J. Zhang, and X. Wang, "3-D finite element modeling and validation of power frequency multi-shielding effect," *IEEE Transactions on Magnetics*, vol. 48, pp. 243-246, Feb. 2012.
[11] A. Nejadpak and O. A. Mohammed, "Physics-based modeling of power converters from finite element electromagnetic field computations," *IEEE Transactions on Magnetics*, vol. 49, no. 1, pp. 567-576, Jan. 2013.
[12] F. T. Ulaby, *Fundamental of Applied Electromagnetics*, 5th Edition, Prentice Hall, pp. 321-324, 2006.
[13] N. N. Rao, *Elements of Engineering Electromagnetics*, 6th Edition, Prentice Hall, pp. 637, 2004.
[14] A. Nejadpak, B. Mirafzal, O. Mohammed, and L. Wei, "Effects of different switching algorithms on the thermal behavior of IGBT modules under pulse-load conditions," *IECON 2010-36th Annual Conference on IEEE Industrial Electronics Society*, vol., no., pp. 451-456, Nov. 7-10, 2010.
[15] D. C. Giancoli, *Physics: Principles with Applications*, Pearson Education, pp. 624, 2005.
[16] C. R. Paul, *Inductance: Loop and Partial*, Wiley-IEEE Press, pp. 195, 2011.
[17] W. E. Arnoldi, "The principle of minimized iterations in the solution of the matrix eigenvalue problem," *Quarterly of Applied Mathematics*, vol. 9, pp. 17-29, 1951.
[18] J. Stoer and R. Bulirsch, *Introduction to Numerical Analysis*, 3rd Edition, Springer, New York, 2002.
[19] MIL-STD-462D, *Measurement of Electromagnetic Interference Characteristics*, Aug. 20, 1999.
[20] MIL-STD-461F, *Requirements for the Control of Electromagnetic Interference Characteristics of Subsystems and Equipment*, pp. 91-98, Dec. 10, 2007.
[21] M. R. Barzegaran, A. Nejadpak, and O. A. Mohammed, "Evaluation of high frequency electromagnetic behavior of planar inductor designs for resonant circuits in switching power converters," *Applied Computational Electromagnetic Society (ACES) Journal*, vol. 26, no. 9, pp. 737-748, Sep. 2011.
[22] G. L. Skibinski, R. J. Kerkman, and D. Schlegel, "EMI emissions of modern PWM AC drives," *IEEE Industrial Application Magazine*, vol. 5, no. 6, pp. 47-80, 1999.
[23] O. Martins, S. Guedon, and Y. Marechal, "A new methodology for early stage magnetic modeling and simulation of complex electronic systems," *IEEE Transaction on Magnetics*, vol. 48, no. 2, pp. 319-322, 2012.

Mohammadreza Barzegaran (S'10) obtained his B.Sc. and M.Sc. degrees in Power Engineering from University of Mazandaran, Iran in 2007 and 2010 respectively. He defended his Ph.D. degree in the Department of Electrical and Computer Engineering, Florida International University, Florida, USA. He is now Assistant Professor at Lamar University. His research interests include studying electromagnetic compatibility in power components, life assessment of electrical power components, fault detection in electrical machines, and also computer-aid simulation of power components. He has many published papers in journals and conferences.

Arash Nejadpak received his B.S. degree in Electrical Engineering and his M.S. degree in Power Electronics and Electric Machines from Sharif University of Technology, Tehran, Iran, in 2007 and 2009, respectively. Currently, he is working towards the Ph.D. degree in Electrical Engineering at the Florida International University, Miami. His current research interests include intelligent control of PM machines and

development of physics-based models and design optimization of power electronic conversion systems. He has many published papers in international journals and conferences.

Osama A. Mohammed (S'79, M'83, SM'84, F'94): is a Professor of Electrical and Computer Engineering and the Director of the Energy Systems Research Laboratory at Florida International University. He received his M.S. and Ph.D. degrees in Electrical Engineering from Virginia Polytechnic Institute and State University. He published numerous journal articles over the past 30 years in areas relating to power systems, electric machines and drives, computational electromagnetics and in design optimization of electromagnetic devices, artificial intelligence applications to energy systems. He authored and co-authored more than 350 technical papers in the archival literature. He has conducted research work for government and research laboratories in shipboard power conversion systems and integrated motor drives. He is also interested in the application communication and wide area networks for the distributed control of smart power grids. He has been successful in obtaining a number of research contracts and grants from industries and Federal government agencies for projects related to these areas. Mohammed also published several book chapters including: Chapter 8 on Direct Current Machinery in the Standard Handbook for Electrical Engineers, 15th Edition, McGraw-Hill, 2007 and a book Chapter entitled "Optimal Design of Magnetostatic Devices: the Genetic Algorithm Approach and System Optimization Strategies," in the book entitled: Electromagnetic Optimization by Genetic Algorithms, John Wiley & Sons, 1999.

Mohammed is a Fellow of IEEE and is the recipient of the IEEE PES 2010 Cyril Veinott Electromechanical Energy Conversion Award. Mohammed is also a Fellow of the Applied Computational Electromagnetic Society. He is Editor of IEEE Transactions on Energy Conversion, IEEE Transactions on Magnetics, IEEE Transactions on Smart Grid and COMPEL. Mohammed was the past President of the Applied Computational Electromagnetic Society (ACES). He received many awards for excellence in research, teaching and service to the profession and has delivered numerous invited lectures at scientific organizations around the world.

Mohammed has been the general chair of several international conferences including; ACES 2006, IEEE-CEFC 2006, IEEE-IEMDC 2009, IEEE-ISAP 1996 and COMPUMAG-1993. He has also chaired technical programs for other major international conferences including; IEEE-CEFC 2010, IEEE-CEFC-2000 and the 2004 IEEE Nanoscale Devices and System Integration. Mohammed also organized and taught many short courses on power systems, Electromagnetics and intelligent systems in the U.S.A and abroad. Mohammed has served ACES in various capacities for many years. He also serves IEEE in various boards, committees and working groups at the national and international levels.

A Three-Conductor Transmission Line Model for MOS Transistors

F. Daneshmandian, A. Abdipour, and R. Mirzavand

Electrical Engineering Department, Institute of Communications Technology and Applied Electromagnetics
Micro/mm-wave & Wireless Comm. Research Lab, Amirkabir University of Technology, Tehran, 15914, Iran
f.daneshmandian@yahoo.com, abdipour@aut.ac.ir, rmirzavand@aut.ac.ir

Abstract ─ An accurate high frequency small signal model for MOS transistors is presented. In the proposed model, by considering the layout of the MOS transistor, it is considered as a three-conductor transmission line. Then, a set of current-voltage equations are derived for the structure using the transmission line theory. These coupled equations are solved by the Finite-Difference Time-Domain (FDTD) technique in a marching-in-time process. To verify the model, the scattering parameters of a 0.13 μm transistor are extracted from the time domain results over the 1–100 GHz frequency band and compared with the results obtained from the available models and commercial simulator. The suggested model can be useful in design of various types of high frequency integrated circuits.

Index Terms ─ CMOS technology, distributed analysis, FDTD method, MOSFET model, transmission line model.

I. INTRODUCTION

The increasing demand of implementing low cost monolithic microwave integrated circuits leads to significant advancement in CMOS technology [1,2]. On the other hand, by increasing the operating frequencies, the modeling issue in such high-density integrated circuits becomes more imperative. For accurate device modeling an electromagnetic interaction must be taken into account, especially when the device dimension is on the order of the wavelength [3]. In such cases, distributed modeling approach can be used to consider the wave propagation effect along the MOS transistors. Distributed analysis method is based on the transmission line model of the transistors.

Distributed modeling of field effect transistors in the case of GaAs MESFET was previously studied [4,5]. In these studies the transistor is considered as a multi-conductor active transmission line. Also, transmission line modeling of transistor in the case of MOS transistor was formerly investigated [6-9], but in all these reports only the distributed effect of gate electrode of the MOS transistor are considered. In this paper, the approach used for MESFET transistor modeling is utilized for distributed modeling of MOS transistor based on three coupled transmission lines in CMOS technology, so the more accurate model for MOSFETs are achieved compared to the earlier models. In this approach, the transistor width is divided into a discrete number of segments and then by considering the proper equivalent circuit for each segment, the required equations for analysis of the transistor can be obtained. In other words, the transmission line theory is applied to each segment of transistor to obtain the wave equations in the MOS transistor structure [10-12]. To solve the attained system of active multi-conductor transmission line differential equations, a suitable method must be chosen. Since the time domain analytical solution doesn't exist for these equations, the finite-difference time-domain (FDTD) method, as a powerful and versatile numerical method is utilized for solving them [13-15]. The parasitic capacitances and inductances of the MOSFET model are numerically computed by solving the two-dimensional electrostatic field problem in the cross section of each transmission lines. By considering the layout of Fig. 1 and proposing that three electrodes of the transistor are placed on the 600 um silicon substrate, per unit-length capacitances and inductances in the MOSFET model are achieved by using finite difference method. Using these values in distributed model, results of proposed approach, Cadence SpectreRF simulator, lumped model, and an analytical approach which is based on the gate electrode distribution [9] are compared. It is shown that at low frequencies, the results of various models are the same while at higher frequencies, difference between them increases. It is expected that the distributed analysis describes the MOSFET behavior more accurate because of considering the wave propagation.

II. DISTRIBUTED SMALL SIGNAL FOR MOSFETS

The width of a MOSFET becomes in the order of wavelength at high frequencies and wave propagation along its electrodes must be considered. To investigate this distributed effect, a MOS transistor can be modeled as three coupled transmission lines on a silicon

Submitted On: November 29, 2013
Accepted On: May 10, 2015

substrate while assuming the magnitude of longitudinal electromagnetic field is negligible with respect to the transverse one. Therefore, the device electrodes can be considered in just the dominant quasi-TEM mode. For numerical simulation, transistor's electrodes must be divided into some segments in propagation direction while considering active and passive equivalent circuit for each part, as shown in Fig. 2. The active part describes the small signal behavior of intrinsic device, and the passive part indicates electromagnetic interaction between electrodes. All parameters in the active and passive parts are per unit-length values. In the limiting case of $\Delta z \to 0$, using Kirchhoff's circuit laws in the circuit of Fig. 2 for drain, gate, and source currents and voltages, i.e., I_d, V_d, I_g, V_g, and I_s, V_s, respectively, we have [4,5]:

$$\frac{\partial I_d}{\partial z}+\frac{\partial (C_1V_d-C_{12}V_g-C_{13}V_s)}{\partial t}+G_{ds}(V_d-V_s) +G_mV_g'=0, \tag{1}$$

$$\frac{\partial V_d}{\partial z}+R_dI_d+\frac{\partial (L_dV_d+M_{dg}V_g+M_{ds}V_s)}{\partial t}=0, \tag{2}$$

$$\frac{\partial I_g}{\partial z}+\frac{\partial (C_2V_g-C_{23}V_g+C_{gs}V_g'-C_{12}V_d)}{\partial t}=0, \tag{3}$$

$$\frac{\partial V_g}{\partial z}+R_gI_g+\frac{\partial (L_gV_d+M_{dg}V_g+M_{gs}V_s)}{\partial t}=0, \tag{4}$$

$$\frac{\partial I_s}{\partial z}+\frac{\partial (C_3V_s-C_{13}V_d-C_{23}V_g)}{\partial t}-C_{gs}V_g' -G_{ds}(V_d-V_s)-G_mV_g'=0, \tag{5}$$

$$\frac{\partial V_s}{\partial z}+R_sI_s+\frac{\partial (L_sV_d+M_{ds}V_g+M_{gs}V)}{\partial t}=0. \tag{6}$$

Using V_g' as the voltage on C_{gs}, another equation can be written as:

$$V_g'+V_s+R_iC_{gs}\frac{\partial V_g'}{\partial t}-V_g=0, \tag{7}$$

where

$$\begin{aligned} C_1&=C_{dp}+C_{ds}+C_{dsp}+C_{dg}+C_{dgp},\\ C_2&=C_{gp}+C_{gsp}+C_{dg}+C_{dgp},\\ C_3&=C_{sp}+C_{ds}+C_{dsp}+C_{gsp},\\ C_{12}&=C_{dg}+C_{dgp},C_{13}=C_{ds}+C_{dsp},C_{23}=C_{gsp}. \end{aligned} \tag{8}$$

Equations (1)-(6) can simplify to matrix form of:

$$\frac{\partial \mathbf{V}}{\partial z}+L\frac{\partial \mathbf{I}}{\partial t}+R\mathbf{I}=0, \tag{9}$$

$$\frac{\partial \mathbf{I}'}{\partial z}+C\frac{\partial \mathbf{V}'}{\partial t}+G\mathbf{V}'=0, \tag{10}$$

with the following definitions:

$$\begin{aligned} \mathbf{V}(z,t)&=\left[V_d,V_g,V_s\right]^T(z,t),\\ \mathbf{I}(z,t)&=\left[I_d,I_g,I_s\right]^T(z,t),\\ \mathbf{V}'(z,t)&=\left[V_d,V_g,V_s,V_g'\right]^T(z,t),\\ \mathbf{I}'(z,t)&=\left[I_d,I_g,I_s,0\right]^T(z,t), \end{aligned} \tag{11}$$

$$C=\begin{pmatrix} C_1 & -C_{12} & -C_{13} & 0\\ -C_{12} & C_2 & -C_{23} & C_{gs}\\ -C_{13} & -C_{23} & C_3 & -C_{gs}\\ 0 & 0 & 0 & R_iC_{gs}\end{pmatrix}, \tag{12}$$

$$G=\begin{pmatrix} G_{ds} & 0 & -G_{ds} & G_m\\ 0 & 0 & 0 & 0\\ -G_{ds} & 0 & G_{ds} & -G_m\\ G_m & -1 & -1 & 1\end{pmatrix},$$

$$L=\begin{pmatrix} L_d & M_{dg} & M_{ds}\\ M_{dg} & L_g & M_{ds}\\ M_{ds} & M_{gs} & L_s\end{pmatrix}, R=\begin{pmatrix} R_d & 0 & 0\\ 0 & R_g & 0\\ 0 & 0 & R_s\end{pmatrix}. \tag{13}$$

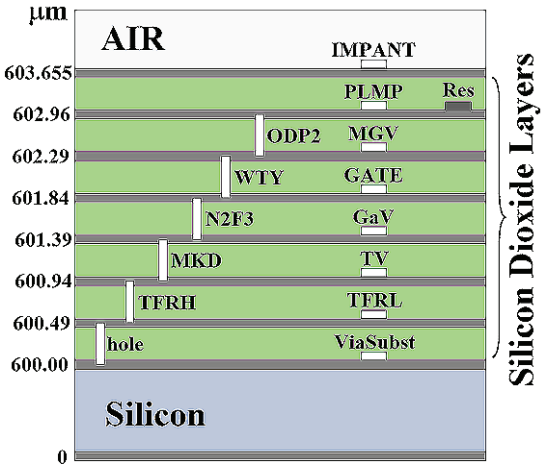

Fig. 1. The layout of a 130 nm CMOS technology.

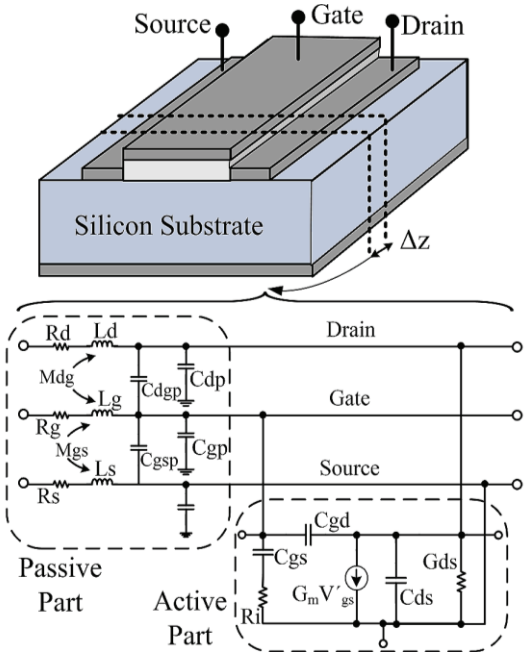

Fig. 2. A MOSFET and its partial equivalent model.

In order to apply the FDTD method to above equations of the MOSFET, total length and simulation time are divided into *Nz* and *Nt* sections with length of Δz and Δt, respectively. Adjacent voltage and current points are separated by half of Δz and half of Δt, as illustrated in Fig. 3. Then, applying FDTD to (9) and (10) leads to:

$$\frac{\mathbf{V}_{k+1}^{n+1}-\mathbf{V}_{k}^{n+1}}{\Delta z}+L\frac{\mathbf{I}_{k}^{n+3/2}-\mathbf{I}_{k}^{n+1/2}}{\Delta t} +R\frac{\mathbf{I}_{k}^{n+3/2}+\mathbf{I}_{k}^{n+1/2}}{2}=0, \tag{14}$$

$$\frac{\mathbf{I}_{k}^{\prime n+1/2}-\mathbf{I}_{k-1}^{\prime n+1/2}}{\Delta z}+C\frac{\mathbf{V}_{k}^{\prime n+1}-\mathbf{V}_{k}^{\prime n}}{\Delta t} +G\frac{\mathbf{V}_{k}^{\prime n+1}+\mathbf{V}_{k}^{\prime n}}{2}=0, \tag{15}$$

where

$$\begin{aligned}\mathbf{V}_{j}^{i}&=\mathbf{V}((i-1)\Delta z, j\Delta t),\\ \mathbf{V}_{j}^{\prime i}&=\mathbf{V}'((i-1)\Delta z, j\Delta t),\\ \mathbf{I}_{j}^{i}&=\mathbf{I}((i-1/2)\Delta z, j\Delta t),\\ \mathbf{I}_{j}^{\prime i}&=\mathbf{I}'((i-1/2)\Delta z, j\Delta t).\end{aligned} \tag{16}$$

Solving (14) and (15) gives the required recursion relations for computing voltages and currents in each interior point on the transistor electrodes as:

$$I_{k}^{\prime n+3/2}=\left(\frac{L}{\Delta t}+\frac{R}{2}\right)^{-1}\left\{\left(\frac{L}{\Delta t}-\frac{R}{2}\right)I_{k}^{\prime n+1/2} -\frac{V_{k+1}^{\prime n+1}-V_{k}^{\prime n+1}}{\Delta z}\right\};k=1,2,...,N_Z, \tag{17}$$

$$V_{k}^{\prime n+1}=\left(\frac{C}{\Delta t}+\frac{G}{2}\right)^{-1}\left\{\left(\frac{C}{\Delta t}-\frac{G}{2}\right)V_{k}^{\prime n} -\frac{I_{k}^{\prime n+1/2}-I_{k-1}^{\prime n+1/2}}{\Delta z}\right\};k=2,3,...,N_Z. \tag{18}$$

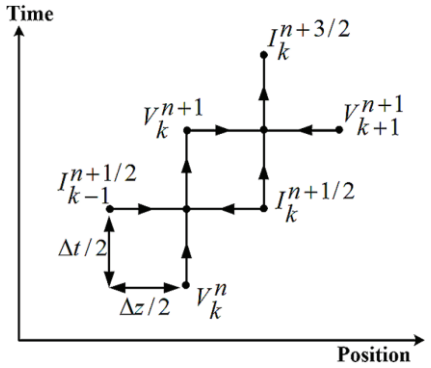

Fig. 3. The current and voltage solution points in space and time for the FDTD analysis.

Equations (18) and (17) are calculated in order with marching manner to obtain voltage and current along the electrodes. To find the boundary conditions, voltage and current at the beginning of transistor can be written using (18) and circuit of Fig. 4 (a) as:

$$V_{1}^{\prime n+1}=\left(\frac{C}{\Delta t}+\frac{G}{2}\right)^{-1} \cdot\left\{\left(\frac{C}{\Delta t}-\frac{G}{2}\right)V_{1}^{\prime n}-\frac{I_{1}^{\prime n+1/2}-I_{0}^{\prime n+1/2}}{\Delta z/2}\right\}, \tag{19}$$

$$I_{0}^{\prime}=\frac{V_{in}^{\prime n}+V_{in}^{\prime n+1}-V_{1}^{\prime n}-V_{1}^{\prime n+1}}{2R_S^{\prime}}, \tag{20}$$

$$V_{in}^{'}=\begin{pmatrix}V_{ind}\\ V_{ing}\\ V_{ins}\\ 0\end{pmatrix}, G_s^{'}=\frac{1}{R_s^{'}}\begin{pmatrix}G_{sd}&0&0&0\\ 0&G_{sg}&0&0\\ 0&0&G_{ss}&0\\ 0&0&0&0\end{pmatrix}. \tag{21}$$

Then, equations (19) and (20) give a boundary value as:

$$V_{1}^{\prime n+1}=\left(\frac{C}{\Delta t}+\frac{G}{2}+\frac{1}{R_S^{\prime}\Delta z}\right)^{-1} \cdot\left\{\begin{array}{l}\left(\frac{C}{\Delta t}-\frac{G}{2}-\frac{1}{R_S^{\prime}\Delta z}\right)V_{1}^{\prime n}\\ -\frac{2}{\Delta z}(I_{1}^{\prime n+1/2}-\frac{V_{in}^{\prime n}-V_{in}^{\prime n+1}}{2R_S^{\prime}})\end{array}\right\}. \tag{22}$$

Similarly, from (18) and Fig. 4 (b) we have:

$$V_{Nz+1}^{\prime n+1}=\left(\frac{C}{\Delta t}+\frac{G}{2}\right)^{-1} \cdot\left\{\left(\frac{C}{\Delta t}-\frac{G}{2}\right)V_{Nz+1}^{\prime n}-\frac{I_{Nz+1}^{\prime n+1/2}-I_{Nz}^{\prime n+1/2}}{\Delta z/2}\right\}, \tag{23}$$

$$I_{Nz+1}^{\prime}=\frac{V_{Nz+1}^{\prime n}+V_{Nz+1}^{\prime n+1}}{2R_L^{\prime}}, \tag{24}$$

$$G_L^{'}=\frac{1}{R_L^{'}}\begin{pmatrix}G_{Ld}&0&0&0\\ 0&G_{Lg}&0&0\\ 0&0&G_{Ls}&0\\ 0&0&0&0\end{pmatrix}, \tag{25}$$

which give another boundary value as:

$$V_{Nz+1}^{\prime n+1}=\left(\frac{C}{\Delta t}+\frac{G}{2}+\frac{1}{R_L^{\prime}\Delta z}\right)^{-1} \left\{\left(\frac{C}{\Delta t}-\frac{G}{2}-\frac{1}{R_L^{\prime}\Delta z}\right)V_{Nz+1}^{\prime n}+\frac{2}{\Delta z}(I_{Nz}^{\prime n+1/2})\right\}. \tag{26}$$

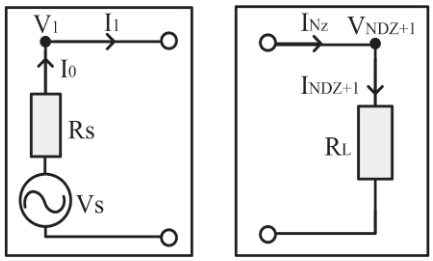

(a) Source (b) Load

Fig. 4. Discretization at source and load terminals.

Now, we can start with an initially relaxed line having zero voltage and current values and find the voltages by equations (22), (18), and (26). It must be noted that to have a stable numerical solution, the space and time steps must satisfy the Courant condition [16]:

$$\Delta t \le \Delta z / v, \tag{27}$$

where v is the maximum velocity of wave propagation along the electrodes of transistor.

In this modeling approach the intrinsic parameters of MOS transistor including g_m, C_{gs}, C_{ds}, C_{gd}, R_i, and G_{ds} are computed based on the accurate physical based model of the MOSFET, BSIM3v3. In this model, the drain-source current in all regions is expressed as follows:

$$I_{ds} = \frac{I_{ds0}(V_{dseff})}{1+\frac{R_{ds} I_{ds0}(V_{dseff})}{V_{dseff}}}(1+\frac{V_{ds}-V_{dseff}}{V_A}) \cdot(1+\frac{V_{ds}-V_{dseff}}{V_{ASCBE}}). \tag{28}$$

By using the drain-source current, the transistor conductance G_m can be obtained as:

$$G_m = \left.\frac{\partial I_{ds}}{\partial V_{gs}}\right|_{V_{ds}=Const.} \tag{29}$$

Also, all capacitances are derived from the charges to ensure charge conservation as:

$$C_{ij} = \frac{\partial Q_i}{\partial V_j}; \; i, j = g, d, s, b, \tag{30}$$

where the terminal charges Q_g, Q_b, Q_s, and Q_d are the charges associated with the gate, bulk, source, and drain terminals, respectively. The details of this model containing other equations and the parameters description are given in [17].

III. RESULTS AND DISCUSSION

In order to analyze the MOS transistor based on the discussed approach, a one finger MOSFET with gate dimension of 0.13×10 μm is proposed. A schematic of the proposed transistor and its relevant boundary condition is shown in Fig. 5. As shown, the beginning of gate electrode is connected to the source voltage V_S and resistance R_S, and the end of drain electrode is connected to a load R_L. In this example, both R_S and R_L are considered to be 50 ohm. Furthermore, the end of gate electrode and the beginning of drain electrode are open, while both sides of the source electrode are grounded.

The per-unit-length parameters of the intrinsic MOSFET are obtained at the V_{gs}=1.2 V and V_{ds}=1.2 V bias point, using the BSIM3v3 model and applying scaling technique. The per-unit-length capacitance and inductance matrixes of the passive part of the transistor are numerically determined by solving the two-dimensional electrostatic field problem in the cross section of each transmission lines based on the layout of Fig. 1. The per-unit-length resistances of the passive part of the MOSFET are achieved by considering the skin effect of the transistor electrodes [18]. The achieved parameters are listed in Table 1. The transistor is simulated by applying a small signal input voltage with amplitude of 0.05 V to achieve the voltages and currents of all points of the electrodes at different frequencies.

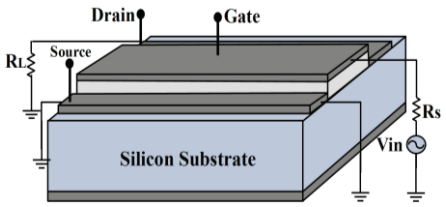

Fig. 5. Schematic of simulated MOSFET.

Table 1: The per-unit-length parameters of the passive part in the distributed MOSFET model

Element	The Per-Unit-Length Values
L_d	1.919 μH/m
L_s	1.919 μH/m
L_g	1.95 μH/m
M_{gd}	1.54 μH/m
M_{gs}	1.54 μH/m
M_{ds}	1.407 μH/m
R_d	600 kΩ/m
R_s	600 kΩ/m
R_g	740 kΩ/m
C_{gp}	136.75 pF/m
C_{dp}	110.5 pF/m
C_{sp}	110.5 pF/m
C_{gdp}	63.07 pF/m
C_{gsp}	63.07 pF/m
C_{dsp}	29.65 pF/m

The scattering parameters of the transistor are extracted from the time domain results at 1-100 GHz frequency band and compared with those of obtained by the analytical approach based on gate electrode distribution in [9], lumped model of the MOS transistor, and also simulator. Figure 6 and Fig. 7 show the magnitude and the phase of scattering parameters of the transistor, respectively. It seems that the results of distributed analysis based on three-conductor, one-conductor and lumped models are in close agreement at low frequencies. But, by increasing the frequency, the difference between the results becomes larger. Especially at higher frequencies, the result of our distributed model is closer to the Cadence SpectreRF simulator result. Due to the fact that at high frequencies the transistor dimensions become comparable with the wavelength, difference between various modeling

approaches becomes more obvious. In such cases, the distributed analysis of the transistor based on three-conductor transmission line can describe the behavior of the device at high frequencies more accurate than others. As the further work, to achieve more precise results, one can develop the discussed approach based on the nonlinear model of an intrinsic MOSFET and also used this model for distributed analysis and design of integrated circuits, so a monolithic analysis of the circuit can be realized.

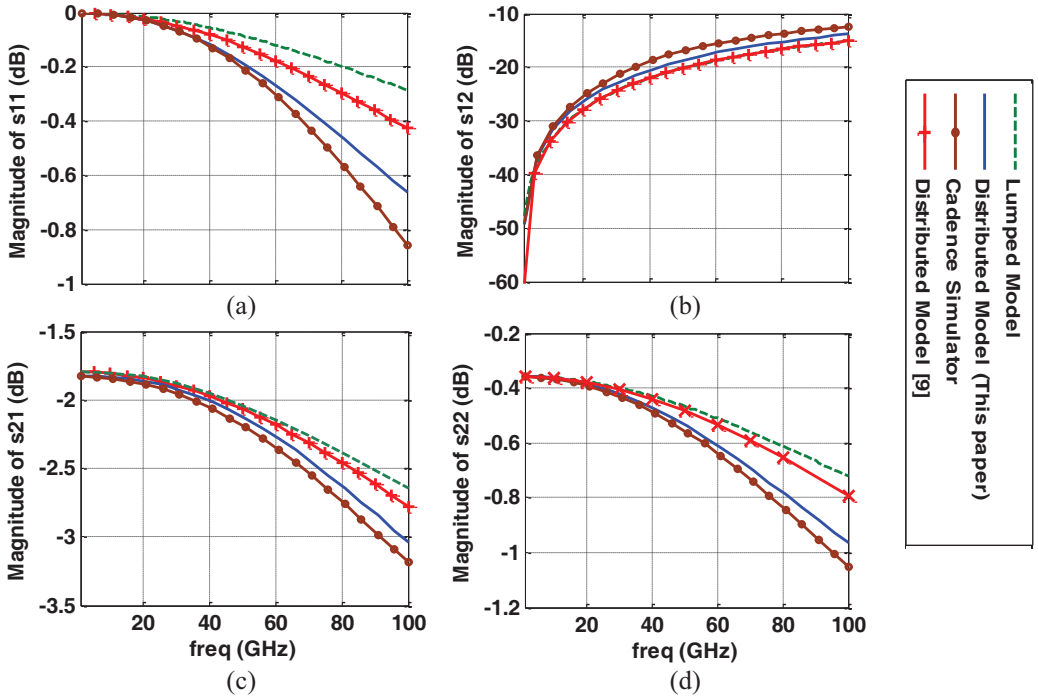

Fig. 6. The magnitude of scattering parameters of the MOS transistor: (a) S_{11}, (b) S_{12}, (c) S_{21}, and (d) S_{22}.

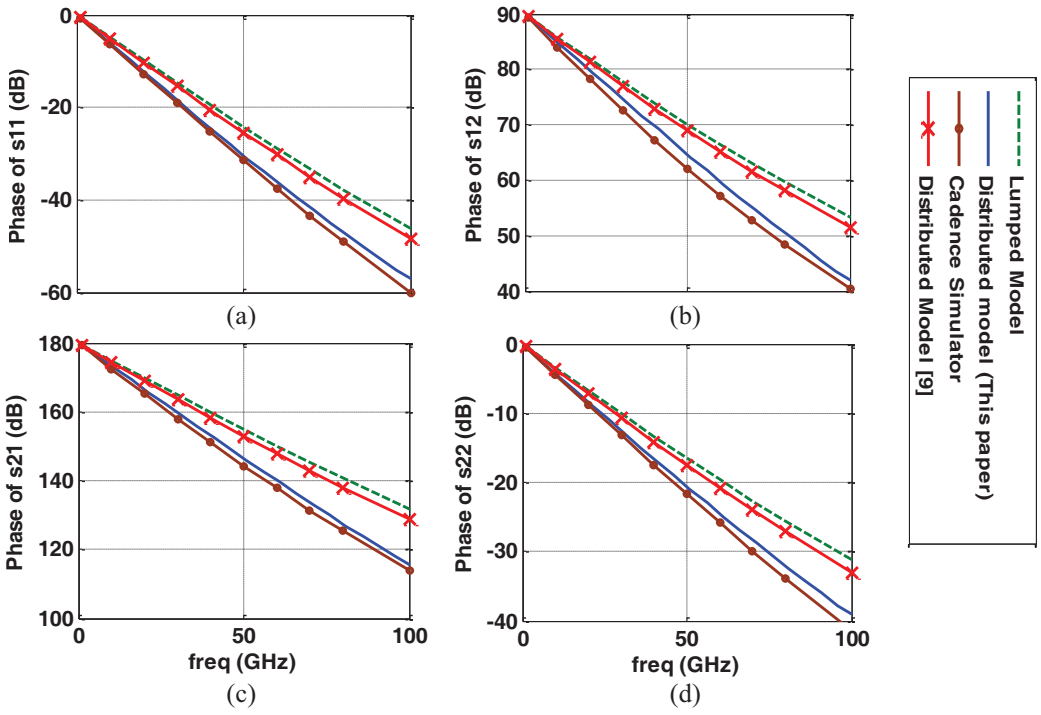

Fig. 7. The phase of scattering parameters of the MOS transistor: (a) S_{11}, (b) S_{12}, (c) S_{21}, and (d) S_{22}.

IV. CONCLUSION

A small signal model for high frequency MOSFETs based on three coupled transmission lines structure is investigated. The relevant differential equations of that structure are derived and solved using the FDTD method. By applying the proposed approach to a 0.13 μm MOS transistor, the small signal parameters are obtained from the time domain results at 1–100 GHz frequency band and compared with the conventional models. Results of the proposed distributed model show a close agreement with other models at low frequencies. But for the higher frequencies the differences become significant and the obtained result of proposed method is closer to the commercial simulator. Therefore, the three-conductor transmission line modeling of MOS transistors is more precise than other conventional approaches.

REFERENCES

[1] H. Y. Li, L. W. Yi, H. Sanming, J. Shi, J. Minkyu, and K. H. Teo, "On the impact of through-silicon-via-induced stress on 65-nm CMOS devices," *IEEE Electron. Device Letters*, vol. 34, pp. 18-20, Jan. 2013.

[2] Z.-Y. Cui, J.-W. Park, C.-S. Lee, and N.-S. Kim, "Integration of CMOS logic circuits with lateral power MOSFET," *2013 4th International Conference on Intelligent Systems Modelling & Simulation (ISMS)*, pp. 615-618, Jan. 2013.

[3] S. M. S. Imtiaz and S. M. El-Ghazali, "Global modeling of millimeter-wave circuits: electromagnetic simulation of amplifiers," *IEEE Trans. Microwave Theory Tech.*, vol. 45, pp. 2208-2216, Dec. 1997.

[4] K. Afrooz, A. Abdipour, A. Tavakoli, and M. Movahhedi, "Nonlinear and fully distributed field effect transistor modelling procedure using time-domain method," *IET Microw. Antennas Propag*., vol. 2, no. 8, pp. 886-897, 2008.

[5] K. Afrooz, A. Abdipour, A. Tavakoli, and M. Movahhedi, "FDTD analysis of small signal model for GaAs MESFETs based on three line structure," *Asia-Pacific Microwave Conference APMC*, pp. 1-4, 2007.

[6] R. P. Jindal, "Noise associated with distributed resistance of MOSFET gate structure in integrated circuits," *IEEE Trans. Electron. Devices*, vol. 31, pp. 1505-1509, Oct. 1984.

[7] B. Razavi, R.-H. Yan, and K. F. Lee, "Impact of distributed gate resistance on the performance of MOS devices," *IEEE Trans. Circuits Systems I*, vol. 41, pp. 750-754, Nov. 1994.

[8] E. Abou-Allam and T. Manku, "A small signal MOSFET model for radio frequency IC applications," *IEEE Trans. Computer-Aided Design*, vol. 16, pp. 437-447, May 1997.

[9] E. Abou-Allam and T. Manku, "An improved transmission-line model for MOS transistors," *IEEE Transaction on Circuits and Systems*, vol. 46, pp. 1380-1387, May 1999.

[10] B. Z. Wang, X. H. Wang, and J. S. Hong, "On the generalized transmission-line theory," *Journal of Electromagnetic Waves and Applications*, vol. 19, no. 3, 413-425, 2005.

[11] C. J. Lin and C. C. Chiu, "A novel model extraction algorithm for reconstruction of coupled transmission lines in high speed digital system," *Journal of Electromagnetic Waves and Applications*, vol. 19, no. 12, 1595-1609, 2005.

[12] C. C. Huang, "Analysis of multiconductor transmission lines with nonlinear terminations in frequency domain," *Journal of Electromagnetic Waves and Applications*, vol. 19, no. 3, 413-425, 2005.

[13] A. Taflove, *Computational Electrodynamics the Finite-Difference Time-Domain Method*, Artech House, Norwood, MA, 1996.

[14] C. R. Paul, "Incorporation of terminal constraints in the FDTD analysis of transmission lines," *IEEE Trans. Electromagnetic Compatibility*, vol. 36, 85-91, 1994.

[15] A. Orlandi and C. R. Paul, "FDTD analysis of lossy, multiconductor transmission lines terminated in arbitrary loads," *IEEE Trans. Electromagnetic Compatibility*, vol. 38, 388-399, 1996.

[16] A. J. Roden, C. R. Paul, W. T. Smith, and D. S. Gedney, "Finite-difference, time-domain analysis of lossy transmission lines," *IEEE Trans. Electromagnetic Compatibility*, vol. 38, pp. 15-24, 1996.

[17] C. Yuhua, et al., *BSIM3v3 Manual: Final Version*, University of California, Berkeley, 1996.

[18] D. Jager, "Slow wave propagation along variable schottky contact microstrip line," *IEEE Tran. Microwave Theory Tech*., vol. 24, pp. 566-573, 1976.

Farzaneh Daneshmandian was born in Tehran, Iran, in 1989. She achieved her B.Sc. degree in Electrical Engineering in 2011 and M.Sc. degree in Communication in 2013 from Amirkabir University of Technology, Tehran, Iran. Her research areas include EM modeling of active devices and circuits, RF/ microwave and mm-wave MMIC circuit design, and nonlinear modeling of active devices. She is currently a Ph.D. student at Amirkabir University of Technology.

Abdolali Abdipour was born in Alashtar, Iran, in 1966. He received his B.Sc. degree in Electrical Engineering from Tehran University, Tehran, Iran, in 1989, his M.Sc. degree in Electronics from Limoges University, Limoges, France, in 1992, and his Ph.D. degree in Electronic Engineering from Paris XI University, Paris, France, in 1996. He is currently a Professor with the Electrical Engineering Department, Amirkabir University of Technology (Tehran Polytechnic), Tehran, Iran. He has authored four books in Persian and authored or co-authored over 300 papers in refereed journals and local and international conferences. His research areas include wireless communication systems, RF/ microwave/millimeter-wave circuit and system design, electromagnetic modeling of active devices and circuits, high-frequency electronics (signal and noise), and nonlinear modeling. Currently, he is Director of the Institute of Communications Tech. and Applied Electromagnetics, Amirkabir University of Technology, Tehran, Iran.

Rashid Mirzavand was born in Boroujen, Iran, in 1983. He received the B.Sc. degree from Isfahan University of Technology, Isfahan, Iran, in 2004, M.Sc. and Ph.D. degrees from Amirkabir University of Technology, Tehran, Iran, in 2007 and 2011, all in Electrical Engineering. In 2009, he joined the Centre for Analysis, Scientific Computing and Applications, Eindhoven University of Technology, Eindhoven, The Netherlands, as a visiting Ph.D. student. Since 2011, he's been a Research Assistant Professor with the Institute of Communications Tech. and Applied Electromagnetics, Amirkabir University of Technology, Tehran, Iran. He is the recipient of the Alberta Innovates Technology Futures (AITF) Post-Doctoral Fellowship and is currently a Research Associate with the Intelligent Wireless Technology Laboratory, University of Alberta, Edmonton, Canada. His research interests are in the areas of intelligent integrated sensors and antennas, microwave & mm-wave circuits and wireless systems, and computational electromagnetic.

Hybrid Method Combining DGTD and TDIE for Wire Antenna-Dielectric Interaction

S. P. Gao [1,3], Y. L. Lu [2], and Q. S. Cao [3]

[1] Department of Electronics & Photonics
Institute of High Performance Computing, 1 Fusionopolis Way, #16-16 Connexis, 138632, Singapore
gaosp@ihpc.a-star.edu.sg

[2] School of Electrical & Electrical Engineering
Nanyang Technological University, 50 Nanyang Avenue, 639798, Singapore
eylu@ntu.edu.sg

[3] College of Electronic and Information Engineering
Nanjing University of Aeronautics and Astronautics, Nanjing, 210016, People's Republic of China
qunsheng@nuaa.edu.cn

Abstract ─ This paper presents a hybrid method that effectively combines two versatile numerical methods - the discontinuous Galerkin time domain (DGTD) method and the time domain integration method (TDIE). The hybrid method is highly applicable to coupling problems involving arbitrarily-shaped thin-wires and dielectric structures with inhomogeneous lossy materials. The original problem can be divided into two sub-regions which are analyzed using the DGTD and the TDIE methods, respectively, and their solutions are exchanged via the interface of the sub-regions by using Huygens' equivalence principle. To improve the efficiency of the hybrid method, a revised Courant–Friedrichs–Lewy (CFL) factor for the DGTD method is proposed, which could effectively reduce computation time. To validate the hybrid method and the revised CFL factor, several numerical examples are presented, proving the proposed method a promising scheme.

Index Terms ─ Electromagnetic coupling, hybrid solution methods, numerical analysis, time-domain analysis, wire antennas.

I. INTRODUCTION

Such electromagnetic problems as arbitrarily oriented thin-wire antennas coupled with nearby inhomogeneous dielectric scatterers are widely encountered in wireless applications [1]. In order to predict the electromagnetic radiation and/or interaction accurately and efficiently, many numerical methods have been used. Finite difference time-domain (FDTD) method has the advantage of simple implementation, but has staircase errors when dealing with complex geometries [2]. Finite element (FE) method can mitigate staircase errors by employing unstructured grids, but it becomes resource-consuming when dealing with electrically small thin-wire structures. Method of moment (MoM) is good at resolving the radiation of thin-wire structure located in free space, but has difficulties to deal with inhomogeneous dielectric objects.

Therefore, a single method is often unable to deal with abovementioned problems effectively. Hybrid methods combining two or more different techniques with the desirable features have been developed to analyze complicated electromagnetic problems. Bretones proposed the TDIE/FDTD method [3] and the FDTD/FETD/TDIE method [4], both of which employ TDIE to handle the thin-wire radiation problems, meanwhile the inhomogeneous objects are analyzed by FDTD in [3] and FETD in [4]. However, as mentioned, the FDTD method suffers from staircase error and the FETD method is computational inefficiency. The discontinuous Gakerkin time-domain (DGTD) method [5,6], which combines the geometrical versatility of FE method with the explicit time-stepping of finite-volume time-domain (FVTD) method [7], has advantages of handling arbitrarily shaped curved objects than FDTD method, and is computationally more efficient than FETD method. DGTD method exceeds FDTD method in accuracy and FETD method in efficiency, thus a very suitable method to replace FDTD and/or FETD in dealing with the abovementioned problems.

The hybrid method bringing together the DGTD and the TDIE methods was preliminarily proposed and studied in [8]. In this paper, we first present the study to improve the efficiency of this method by revising the Courant–Friedrichs–Lewy (CFL) factor of the DGTD

Submitted On: October 26, 2013
Accepted On: May 10, 2015

method and then apply the improved method to two coupling problems with thin-wire antennas and arbitrarily-shaped inhomogeneous dielectric scatters. The presented hybrid DGTD-TDIE method integrates the desirable capabilities of the individual methods for solving different parts of the problem for which they are more suitable. It has the advantages of accuracy, efficiency, and simplicity for analyzing more complicated realistic problems than its hybrid counterparts.

II. DESCRIPTION OF THE HYBRID METHOD

A. Hybrid configuration

Figure 1 shows the configuration of the hybrid DGTD-TDIE method for a generic wire antenna-dielectric interaction problem. Based on Huygens' equivalence principle, the original computational domain can be divided into two sub-regions: i) the source region R^{IE} containing thin-wire antennas, which is calculated by using the TDIE method, and ii) the scatterer region R^{DG} containing dielectric scatters modeled with unstructured elements and analyzed by the DGTD method. R^{DG} includes R^{IE} with the absence of the antenna, thus for the DGTD method, R^{IE} is the scattered field region (SFR) and the rest of R^{DG} is the total field region (TFR). For truncation of the computational domain, the perfectly matched layer (PML) is employed around R^{DG}. The interface S exchanges the solutions between TDIE and DGTD methods. Equivalent surface sources of the antenna radiation on S can be injected in the DGTD simulation as the illumination and the scattering of the dielectric will then be acquired inside S to excite the antenna in the TDIE calculation.

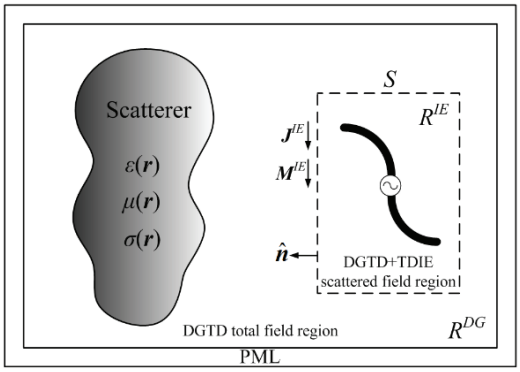

Fig. 1. Hybrid DGTD-TDIE method configuration for the wire antenna-dielectric interaction.

B. TDIE for wire antenna radiation

As the wire-antenna can be considered as a thin-wire structure shown in Fig. 2. $\boldsymbol{r}$ and $\boldsymbol{r}'$ are the field point on the surface and the source point on the axis $C(s')$, respectively; $\boldsymbol{R}=\boldsymbol{r}-\boldsymbol{r}'$. $s\equiv s(\boldsymbol{r})$ axis the coordinates on the surface and $s'\equiv s(\boldsymbol{r}')$ on the axis; $\hat{\boldsymbol{s}}$ and $\hat{\boldsymbol{s}}'$ are the tangential unit vectors at positions $\boldsymbol{r}=s$ and $\boldsymbol{r}'=s'$.

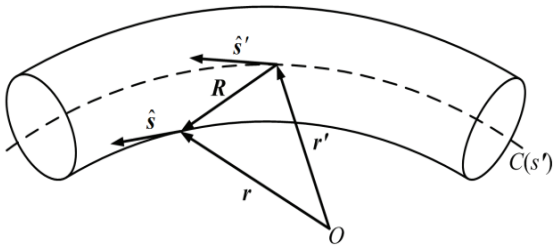

Fig. 2. Geometry of a thin-wire structure.

In region R^{IE}, the wire antenna is analyzed by solving the electric field integral equations (EFIE) using the TDIE method. The derivation of EFIE of thin-wire structures is started by imposing the boundary condition:

$$\hat{\boldsymbol{s}}\cdot\left[\boldsymbol{E}^s(s,t)+\boldsymbol{E}^i(s,t)\right]=0, \tag{1}$$

where $\boldsymbol{E}^i$ and $\boldsymbol{E}^s$ are the incident and the scattered field, respectively. $\boldsymbol{E}^s$ can be expanded using the vector and scalar potential function as:

$$\hat{\boldsymbol{s}}\cdot\boldsymbol{E}^s(s,t)= -\frac{\hat{\boldsymbol{s}}}{4\pi\varepsilon_0}\int_{C(s')}\left[\frac{\hat{\boldsymbol{s}}'}{c^2R}\frac{\partial I(s',t')}{\partial t'}+\frac{\hat{\boldsymbol{R}}}{cR}\frac{\partial I(s',t')}{\partial s'}-\frac{\hat{\boldsymbol{R}}}{R^2}q(s',t')\right]ds', \tag{2}$$

where c is the velocity of light in the media of the wire, $t'=t-R/c$ is the retarded time, and $I(s',t')$ and $q(s',t')$ are the current and charge per unit length at s' of the axis. Substituting (2) into (1), eliminating $q(s',t')$ using the equation of current continuity, and considering the possible impressed field $\boldsymbol{E}^{DG}$ from scatterer in R^{DG}, the EFIE can be obtained in (3):

$$\hat{\boldsymbol{s}}\cdot\left[\boldsymbol{E}^i(s,t)+\boldsymbol{E}^{DG}(s,t)\right]=\frac{\hat{\boldsymbol{s}}}{4\pi\varepsilon_0}\int_{C(s')}\left[\begin{array}{l}\dfrac{\hat{\boldsymbol{s}}'}{c^2R}\dfrac{\partial I(s',t')}{\partial t'}\\ +\dfrac{\hat{\boldsymbol{R}}}{cR}\dfrac{\partial I(s',t')}{\partial s'}\\ -\dfrac{\hat{\boldsymbol{R}}}{R^2}\displaystyle\int_{-\infty}^{t'}\frac{\partial}{\partial s'}I(s',\tau)d\tau\end{array}\right]ds'. \tag{3}$$

If the antenna is divided into N_s wire segments and the time domain into N_t pieces, then the current distribution per unit length at location $\boldsymbol{r}'=s'$ and $t=t'$ can be expressed by (4):

$$I(s',t')=\sum_{i=1}^{N_s}\sum_{l=1}^{N_t}\beta_i^l T_l(t')f_i(s'), \tag{4}$$

where β_i^l are the expansion coefficients, $T_l(t)$ the 3rd order time basis functions and $f_i(s)$ the wire basis functions.

After substituting (4) into (3) and testing it with Dirac function in time domain and $f_i(s)$ in spatial domain, the recursive form of EFIE can be derived in (5):

$$\sum_{j=1}^{N_s} Z_{i,j}^0 \beta_j^n = \frac{V(t_n)}{\Delta s_i} - \sum_{l=1}^{n-1}\sum_{j=1}^{N_s} Z_{i,j}^l \beta_j^{n-l} + \hat{\boldsymbol{s}} \cdot \boldsymbol{E}^{DG}(s_i, t_n), \quad (5)$$

where $V(t_n)$ is the feeding voltage at s_i, Δs_i the length of segment i, and $Z_{i,j}^l$ the element of the impedance matrix expressed by (6):

$$Z_{i,j}^l = \frac{\hat{\boldsymbol{s}}}{4\pi\varepsilon_0} \cdot \int_{C(s)}\int_{C(s')} \left[\begin{array}{l} \dfrac{\hat{\boldsymbol{s}}'}{c^2 R} f(s_i) f(s_j') T'(l\Delta t - R/c) \\ + \dfrac{\hat{\boldsymbol{R}}}{cR} f(s_i) f'(s_j') T(l\Delta t - R/c) \\ - \dfrac{\hat{\boldsymbol{R}}}{R^2} f(s_i) f'(s_j') \displaystyle\int_{-\infty}^{l\Delta t - R/c} T(\tau) d\tau \end{array} \right] ds'ds. \quad (6)$$

Provided $Z_{i,j}^{n-1}$ and $\boldsymbol{E}^{DG}$ at the previous time step t_{n-1} are known, β_j^n at the current time step t_n can be easily obtained by solving (5).

C. DGTD for dielectric scattering

DGTD families have various types of methods which all hold the capability of accurately modeling complicated geometries and media compositions. For simple implementation, we adopt the nodal high-order DGTD method [4] to handle the dielectric scattering in R^{DG}. To introduce the method in a simple way, the Maxwell curl equations for source-free linear isotropic homogeneous lossless non-dispersive media is first used:

$$\begin{aligned} \varepsilon \partial_t \boldsymbol{E}(\boldsymbol{r},t) - \nabla \times \boldsymbol{H}(\boldsymbol{r},t) &= 0, \\ \mu \partial_t \boldsymbol{H}(\boldsymbol{r},t) + \nabla \times \boldsymbol{E}(\boldsymbol{r},t) &= 0. \end{aligned} \quad (7)$$

R^{DG} is discretized by K non-overlapped elements. Assuming the space and time dependencies of the fields can be separated, then fields can be expanded in each element Ω^k with basis functions Φ_q^k:

$$\boldsymbol{\Psi}^k(\boldsymbol{r},t) = \sum_{i=1}^{N_p} \boldsymbol{\Psi}_i^k(t) \cdot \Phi_i(\boldsymbol{r}), \quad \boldsymbol{\Psi} = \{\boldsymbol{E}, \boldsymbol{H}\}, \quad (8)$$

where N_p is the number of the expansion and $\boldsymbol{\Psi}_i^k$ is an N_p-vector of expansion coefficients. Test (7) in element Ω^k with the same basis functions Φ_j, we can get:

$$\begin{aligned} &\int_{\Omega^k} (\varepsilon \partial_t \boldsymbol{E}^k \Phi_j - \Phi_j \nabla \times \boldsymbol{H}^k) dv = 0, \\ &\int_{\Omega^k} (\mu \partial_t \boldsymbol{H}^k \Phi_j + \Phi_j \nabla \times \boldsymbol{E}^k) dv = 0, \quad j = 1 \ldots N_p. \end{aligned} \quad (9)$$

After one manipulation of the curl term in (9), we substitute a so-called numerical flux ($\hat{\boldsymbol{n}}^k \times \boldsymbol{E}^{k*}$ and $\hat{\boldsymbol{n}}^k \times \boldsymbol{H}^{k*}$) into the surface integral and then manipulate back as:

$$\begin{aligned} \int_{\Omega^k} (\varepsilon \partial_t \boldsymbol{E}^k \Phi_j - \Phi_j \nabla \times \boldsymbol{H}^k) dv &= -\iint_{\partial\Omega^k} \left[\hat{\boldsymbol{n}}^k \times (\boldsymbol{H}^k - \boldsymbol{H}^{k*}) \right] \Phi_j ds, \\ \int_{\Omega^k} (\mu \partial_t \boldsymbol{H}^k \Phi_j + \Phi_j \nabla \times \boldsymbol{E}^k) dv &= \iint_{\partial\Omega^k} \left[\hat{\boldsymbol{n}}^k \times (\boldsymbol{E}^k - \boldsymbol{E}^{k*}) \right] \Phi_j ds. \end{aligned} \quad (10)$$

The numerical flux can exchange the solutions between adjacent elements. Here, the upwind flux (11) is employed here for its robustness:

$$\begin{aligned} \hat{\boldsymbol{n}}^k \times \boldsymbol{E}^{k*} &= \hat{\boldsymbol{n}}^k \times \frac{(Y^k \boldsymbol{E}^k - \hat{\boldsymbol{n}}^k \times \boldsymbol{H}^k) + (Y^{k+} \boldsymbol{E}^{k+} + \hat{\boldsymbol{n}}^k \times \boldsymbol{H}^{k+})}{Y^k + Y^{k+}}, \\ \hat{\boldsymbol{n}}^k \times \boldsymbol{H}^{k*} &= \hat{\boldsymbol{n}}^k \times \frac{(Z^k \boldsymbol{H}^k - \hat{\boldsymbol{n}}^k \times \boldsymbol{E}^k) + (Z^{k+} \boldsymbol{H}^{k+} + \hat{\boldsymbol{n}}^k \times \boldsymbol{E}^{k+})}{Z^k + Z^{k+}}. \end{aligned} \quad (11)$$

The superscript "+" denotes the quantity of the neighbor element. $Z^k = (Y^k)^{-1}$ is the local impedance/conductance.

Finally, the semi-discrete DGTD formulation (12) can be obtained by substituting (8) and (11) into (10):

$$\begin{aligned} &\varepsilon^k \mathbf{M}^k \partial_t \boldsymbol{E}^k = \\ &\mathbf{S}^k \times \boldsymbol{H}^k - \mathbf{F}^k \left(\frac{\hat{\boldsymbol{n}}^k \times \left[Z^{k+} (\boldsymbol{H}^k - \boldsymbol{H}^{k+}) - \hat{\boldsymbol{n}}^k \times (\boldsymbol{E}^k - \boldsymbol{E}^{k+}) \right]}{Z^k + Z^{k+}} \right), \\ &-\mu^k \mathbf{M}^k \partial_t \boldsymbol{H}^k = \\ &\mathbf{S}^k \times \boldsymbol{E}^k - \mathbf{F}^k \left(\frac{\hat{\boldsymbol{n}}^k \times \left[Y^{k+} (\boldsymbol{E}^k - \boldsymbol{E}^{k+}) + \hat{\boldsymbol{n}}^k \times (\boldsymbol{H}^k - \boldsymbol{H}^{k+}) \right]}{Y^k + Y^{k+}} \right). \end{aligned} \quad (12)$$

The mass matrix $\mathbf{M}^k$, the stiffness matrices $\mathbf{S}^k$, and the face mass matrix $\mathbf{F}^k$, with respect to the element contour $\partial\Omega_k$ are defined in (13):

$$\begin{aligned} (\mathbf{M}^k)_{ij} &= \int_{\Omega^k} \Phi_i(\boldsymbol{r}) \cdot \Phi_j(\boldsymbol{r}) dv, \\ (\mathbf{S}_m^k)_{ij} &= \int_{\Omega^k} \Phi_i(\boldsymbol{r}) \cdot \partial_m \Phi_j(\boldsymbol{r}) dv, \quad m \in \{x, y, z\}, \\ (\mathbf{F}^k)_{ij} &= \int_{\partial\Omega^k} \Phi_i(\boldsymbol{r}) \cdot \Phi_j(\boldsymbol{r}) ds, \quad j \in \{ j \,|\, \boldsymbol{r}_j \in \partial\Omega^k \}. \end{aligned} \quad (13)$$

The 4th-order low-storage Runge-Kutta scheme is used to solve (12).

D. Detailed time-stepping algorithm

Since the DGTD and the TDIE methods used here are explicit and implicit in time domain, Δt^{DG} could be much smaller than Δt^{IE}, viz. $k = \Delta t^{IE} / \Delta t^{DG}$, $k \geq 1$. To synchronize them, a simple scheme of one TDIE calculation followed by k-time DGTD calculations is performed. As long as each method is stable in their time step, the hybrid method is stable.

Detailed procedure at each Δt^{IE} can be summarized into three steps:

Step 1: Since the feeding voltage $V(s)$ and external scattered field $\boldsymbol{E}^{DG}$ are available from the previous calculation, the currents on the thin-wire antenna can be easily obtained by solving the EFIE. These currents lead to the equivalent

sources on Huygens surface S which yields the same radiating fields outside S and null inside. The equivalent sources can be expressed as the electromagnetic fields or the surface currents.

Step 2: The DGTD method is applied in R^{DG} with the antenna removed. After the interpolation of equivalent sources at k different moments in Δt^{IE}, they can be used to excite DGTD calculation. As either equivalent field or current can be used with same results, we here use the former one:

$$\begin{cases} \boldsymbol{\Psi}^{+} \rightarrow (\boldsymbol{\Psi}^{+} - \boldsymbol{\Psi}^{IE}) & in\ SFR \\ \boldsymbol{\Psi}^{+} \rightarrow (\boldsymbol{\Psi}^{+} + \boldsymbol{\Psi}^{IE}) & in\ TFR \end{cases}, \tag{14}$$

after the k-time calculations, the scattered fields $\boldsymbol{E}^{DG}$ acting on the antenna at certain points should be resolved by linear interpolation.

Step3: Provided the scattered fields $\boldsymbol{E}^{DG}$ and the feeding source $V(s)$ at the current time step, the equivalent sources on S at next time step can be easily evaluated. Then, the recursive procedure can be repeated till the end.

However, this time-stepping algorithm will lead to frequent data exchanges in every Δt^{IE} due to the large k. To release the burden, one should make Δt^{DG} as large as possible without exceeding the stability limit. Normally, the CFL factor which composing Δt^{DG} depends on both the spatial order and the size of the mesh. The order-dependent maximum allowed CFL factor could be found by testing different meshes. After subtraction with a certain safe margin, these factors are then fitted into the quadratic polynomial in (15):

$$CFL_{rev}(p) = 1.13 + 0.68p - 0.027p^2, \tag{15}$$

where p is the order of basis functions. This revised CFL factor is larger than the one proposed by Niegemann in [9]. It can directly improve the efficiency of DGTD and then the overall efficiency of the hybrid DGTD-TDIE method. Compared to Niegemann's function of CFL factor, the expected time saving of the revised CFL factor is listed in Table 1.

Table 1: Expected time saving

Order p	Niegemann's Factor	Revised Factor	Expected Time Saving (%)
2	1.296	2.382	45.59
3	1.511	2.927	48.38
4	1.704	3.418	50.15
5	1.875	3.855	51.36
6	2.024	4.238	52.24
7	2.151	4.567	52.90
8	2.256	4.842	53.41

III. NUMERICAL RESULTS

To verify the capability of the proposed hybrid DGTD/TDIE method and the revised CFL factor, a straight thin-wire antenna located in the neighborhood of a perfectly electric conducting (PEC) plane is first presented, as shown in Fig. 3. The antenna is 0.2 m in each arm and 2 mm in radius. It is modeled with 10 segments and excited at its center by a 4-lightmeter width Gaussian pulse voltage source. The distance between the antenna and the PEC plane is 1 m. The PEC plane is of 2m×2m. And R^{DG} is of 5m×5m×5m with the PML, meshed by 6544 tetrahedrons. The comparable numerical results of E_x at point P by using hybrid DGTD-TDIE, TDIE (3600 faces) and DGTD (19687 grids) are also presented in Fig. 3. Great agreement could be observed between the hybrid method and the TDIE method. However, the result of the DGTD method is not as good as the other two, despite the more refined mesh it used. The computation times used by the hybrid method using different CFL factors are compared in Table 2. The 3rd order basis functions are used in the DGTD part of the hybrid method.

Table 2: Comparison of computation time

Finaltime (Lightmeter)	Using Niegemann's Factor	Using Revised Factor	Actual Time Saving (%)
20.0	10m 12s	6m 47s	33.50

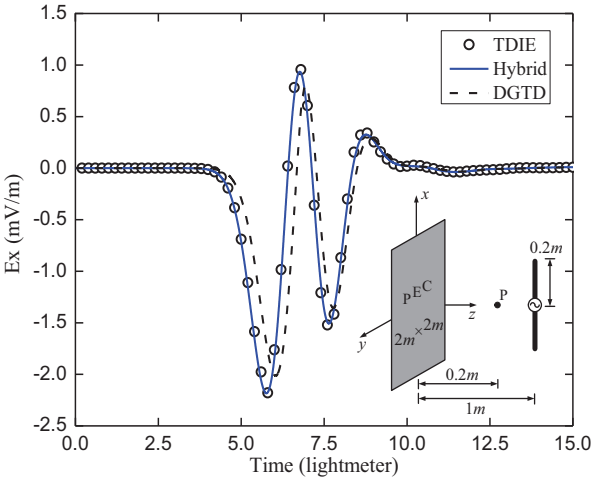

Fig. 3. Amplitude of the x component of the total electric field at point P.

Another example is to verify the capability of the hybrid method to deal with the coupling between thin wire antenna and complex dielectric scatter. A V-shape antenna is placed inside an antenna radome as shown in Fig. 4. The included angle of the wire antenna is 60°. The

radome has the relative permittivity of $\varepsilon_r = 3.3 - j0.02$. The normalized radiation intensity in the E-plane of the wire antenna with or without radome at 9.375 GHz is computed and shown in Fig. 4. From these results, we can obtain the transmittance at the direction of the maximum radiation, which is 0.988. For this geometrically complex and electrically large problem, longer computation time was required as shown in Table 3, where the revised CFL factor successfully reduced the computation times. This case further proves the feasibility of the proposed CFL factor in dealing with complex problem.

Table 3: Comparison of computation time in the presence of dielectric radome

Finaltime (Lightmeter)	Using Niegemann's Factor	Using Revised Factor	Actual Time Saving (%)
30.0	11h 17m	7h 37m	32.49

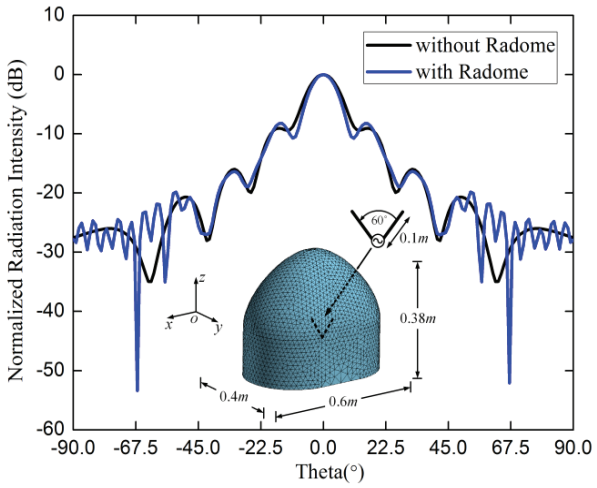

Fig. 4. Normalized radiation intensity at E-plane of the wire antenna with/without radome at 9.375 GHz.

IV. CONCLUSIONS

A hybridization scheme combining DGTD and TDIE methods has been proposed for coupling problems with thin-wire antennas and dielectric scatters. It combines the advantages of the DGTD method in dealing with arbitrary dielectric scatters and the TDIE method in treating arbitrary thin-wire structures. It offers an alternative to the other classic/hybrid method in evaluating transient solution of such problems. In addition, a revised CFL factor of the DGTD method is proposed to improve its computational efficiency and the overall computational efficiency of the hybrid method.

REFERENCES

[1] M. A. Mangoud, R. A. Abd-Alhameed, and P. S. Excell, "Simulation of human interaction with mobile telephones using hybrid techniques over coupled domains," *Microwave Theory and Techniques, IEEE Transactions on*, vol. 48, pp. 2014-2021, 2000.

[2] A. C. Cangellaris and D. B. Wright, "Analysis of the numerical error caused by the stair-stepped approximation of a conducting boundary in FDTD simulations of electromagnetic phenomena," *IEEE Transactions on Antennas and Propagation*, vol. 39, pp. 1518-1525, 1991.

[3] A. Rubio Bretones, R. Mittra, and R. Gómez Martín, "A hybrid technique combining the method of moments in the time domain and FDTD," *IEEE Microwave and Guided Wave Letters*, vol. 8, pp. 281-283, 1998.

[4] A. Monorchio, A. Rubio Bretones, R. Mittra, G. Manara, and R. Gómez Martín, "A hybrid time-domain technique that combines the finite element, finite difference and method of moment techniques to solve complex electromagnetic problems," *IEEE Transactions on Antennas and Propagation*, vol. 52, pp. 2666-2674, 2004.

[5] J. S. Hesthaven and T. Warburton, "Nodal high-order methods on unstructured grids, I. time-domain solution of Maxwell's equations," *Journal of Computational Physics*, vol. 181, pp. 186-221, 2002.

[6] S. D. Gedney, C. Luo, J. A. Roden, R. D. Crawford, B. Guernsey, J. A. Miller, T. Kramer, and E. W. Lucas, "The discontinuous Galerkin finite-element time-domain method solution of Maxwell's equations," *Applied Computational Electromagnetics Society Journal*, vol. 24, pp. 129-142, 2009.

[7] R. J. LeVeque, *Finite Volume Methods for Hyperbolic Problems*, Cambridge University Press, 2002.

[8] S. P. Gao, Q. S. Cao, J. Ding, M. Zhu, and Y. L. Lu, "A hybrid DGTD-TDIE method for solving complex electromagnetic problems," *Journal of Electromagnetic Waves and Applications*, vol. 27, pp. 1017-1027, May 2013.

[9] J. Niegemann and K. Busch, "Time-stepping and convergence characteristics of the discontinuous Galerkin time-domain approach for the Maxwell equations," in *AIP Conference Proceedings*, p. 22, 2009.

Band-Notched Small Slot Antenna Based on Time-Domain Reflectometry Modeling for UWB Applications

N. Mikaeilvand [1], M. Ojaroudi [2], and N. Ghadimi [2]

[1] Department of Mathematics
Ardabil Branch, Islamic Azad University, Ardabil, Iran

[2] Young Researchers and Elite Club
Ardabil Branch, Islamic Azad University, Ardabil, Iran

Abstract ─ A design of a compact band-notched slot antenna by using defected structures with time domain designing method for UWB applications is presented. By cutting two modified meander line slots in the ground plane, a new resonance at the higher frequencies is excited, and hence, much wider impedance bandwidth can be produced that provides an ultra-wideband (UWB) frequency range. To generate a band-notched characteristic, we use the step-impedance resonator (SIR) slot at feed-line which contains a rectangular slot with a W-shaped strip protruded inside the slot. The proposed antenna can operate from 3.07 to 12.91 GHz with frequency band-notched function in 5.12-5.96 GHz to avoid interference from WLAN systems. To verify the validation of the proposed antenna, the equivalent circuit based on time domain reflectometry (TDR) analysis is presented. The proposed antenna exhibits almost omni-directional radiation patterns in UWB frequency range. The designed antenna has a small size of 20×20 mm^2.

Index Terms ─ Defected transmission line, microstrip slot antenna, time-domain modeling.

I. INTRODUCTION

Commercial UWB systems require small low-cost antennas with omni-directional radiation patterns and large bandwidth [1]. It is a well-known fact that planar slot antennas present really appealing physical features, such as simple structure, small size and low cost. Due to all these interesting characteristics, planar slots are extremely attractive to be used in emerging UWB applications and growing research activity is being focused on them [2]-[3], and automatic design methods have been developed to achieve the optimum planar shape [4]-[6]. The wide frequency range for UWB systems between 3.1 to 10.6 GHz will cause interference to the existing wireless communication systems, such as the local area network (WLAN) for IEEE 802.11a which operates in 5.15-5.35 GHz and 5.725-5.825 GHz bands. Therefore, in order to elliminate this unwanted interference, UWB antenna with band notch function is required. Several planar antennas with band notch characteristics have recently been presented. The easiest and most common technique is embedding a narrow slot into the radiating patch of the antenna and change the current flows on it, as used in [7]-[9]. In [7], different shapes of the slots (i.e., square ring and folded trapezoid) are used to obtain the band notch function. On the other hand, another method to avoid this frequency interference is the use of reconfigurable antennas. In [8], RF MEMS are used for notching the WLAN band while in [9], PIN diodes are used for the same reason.

In this paper, a simple method for designing a novel and compact microstrip-fed slot antenna with band-stop performance and time domain reflectometry analysis for UWB applications has been presented. In the presented antenna, based on defected ground structures (DGS) for bandwidth enhancement we use a pair of meander line slots in the ground plane and also based on defected microstrip structures (DMS), to generate a band-stop performance a rectangular slot with a W-shaped strip protruded inside the slot was inserted at feed-line [6]. Unlike other band-notched UWB antennas reported in the literature to date [3-6], this structure has an ordinary square radiating stub configuration. We also report their circuit models based on TDR analysis. The size of the designed antenna is smaller than the UWB antennas with band-notched function reported recently [3]-[9]. Simulated and measured results are presented to validate the usefulness of the proposed antenna structure for UWB applications.

II. ANTENNA DESIGN AND CONFIGURATION

The square slot antenna fed by a 50 Ω microstrip line is shown in Fig. 1, which is printed on a FR4 substrate of width $W_{sub} = 20mm$ and length $L_{sub} = 20mm$, thickness 0.8 mm, permittivity 4.4, and loss tangent 0.018. The proposed antenna is connected to a 50 Ω

Submitted On: December 18, 2013
Accepted On: April 8, 2015

SMA connector for signal transmission. In this structure, by cutting the two meander line slots of suitable at the ground plane, it is found that much enhanced impedance bandwidth can be achieved for the proposed antenna. Regarding defected ground structures, the creating slots in the ground plane provide an additional current path. The DGS applied to a microstrip line causes a resonant character of the structure transmission with a resonant frequency controllable by changing the shape and size of the slot [10]. In addition, the defected microstrip structure (DMS) is playing an important role in the band-stop characteristic of this antenna, because it can adjust the electromagnetic coupling effects between the radiating stub and the ground plane. This phenomenon occurs because, with the use of a defected structure in transmission line distance, additional coupling is introduced between the bottom edge of the square radiating stub and the ground plane [9] and creates a band rejection around 5.12-5.96 GHz.

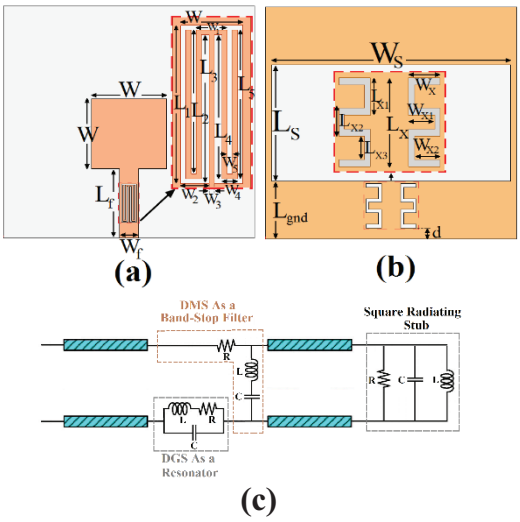

Fig. 1. Geometry of the proposed slot antenna with defected structures: (a) top layer, (b) bottom layer, and (c) the proposed antenna equivalent circuit model.

The final dimensions of the defected structures are as follows: $W_X = 1.25mm$, $L_X = 3.8mm$, $W_{X1} = 1.05mm$, $L_{X1} = 1.6mm$, $W_{X2} = 1mm$, $L_{X2} = 1.2mm$, $L_{X3} = 1mm$, $W = 1.2mm$, $L_1 = 3.3mm$, $W_1 = 0.6mm$, $L_2 = 3mm$, $W_2 = 0.55mm$, $L_3 = 3.1mm$, $W_3 = 0.1mm$, $L_4 = 1.1mm$, $W_4 = 0.3mm$, $L_5 = 1.1mm$, and $W_5 = 0.1mm$.

III. DEFECTED TRANSMISSION LINE

A. Defected structures (DGS and DMS) and its equivalent circuit models

Recently, the defected ground plane structures (DGS) and defected microstrip structure (DMS) have been proposed for suppression of spurious response in the microstrip structures [11]-[12]. The proposed DGS and DMS with their equivalent circuit models are shown in Figs. 2 and 3, respectively. These defected structure on the ground plane and feed-line will perturb the incident and return current and induce a voltage difference on the ground plane and microstrip feed-line. These two effects can be modeled as a parallel LC circuit [12]. The resistance in equivalent circuits represents the loss of the slot and slit, which is small in general [13].

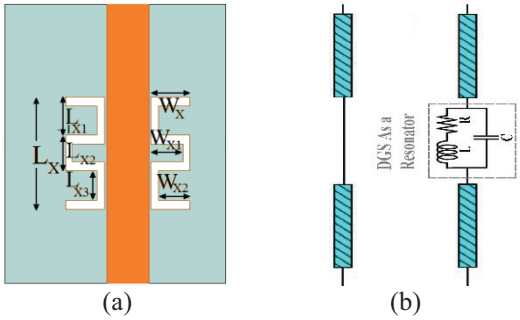

Fig. 2. (a) Geometry of the proposed defected ground structure (DGS), and (b) equivalent circuit model.

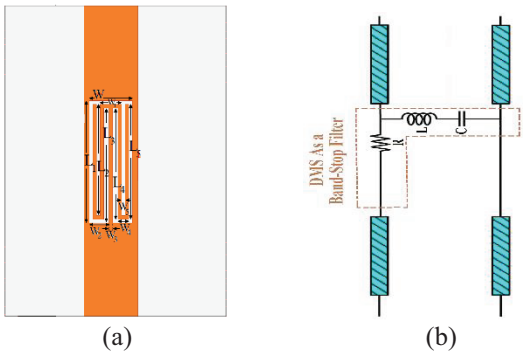

Fig. 3. (a) Geometry of the proposed defected microstrip structure (DMS), and (b) equivalent circuit model.

B. Time domain reflectometry analysis

In this section, the proposed defected structures with mentioned design parameters were simulated, and the TDR results of the input impedance for them in equivalent circuit and full-wave analysis cases are presented and discussed. The simulated full-wave TDR results are obtained using the Ansoft simulation software high-frequency structure simulator (HFSS) [14].

In order to calculate of the TDR results for the proposed equivalent circuits, the impedance of these circuits in Laplace domain can be represented as (1) and (2):

$$Z_{DGS} = \frac{Ls + R}{LCs^2 + RCs + 1}, \quad (1)$$

$$Z_{DMS} = \frac{LCs^2 + RCs + 1}{Cs}. \quad (2)$$

Assume that the characteristic impedance of the microstrip line is Z_0, we can write the reflection coefficient through defected structures as (3) which is observed at the source end, i.e., Port 1:

$$\Gamma_Z(s) = \frac{Z(s)}{Z(s) + 2Z_0}, \quad (3)$$

where *Z(s)* is defected structures impedance as shown in (1) and (2), and Z_0 is equal to 50 Ω. Therefore, the reflected waveform for the proposed DGS and DMs can be written as:

$$\Gamma_{DGS}(s) = \frac{Ls + R}{2Z_0 LCs^2 + (2Z_0 RC + L)s + R + 2Z_0}, \quad (4)$$

$$\Gamma_{DMS}(s) = \frac{LCs^2 + RCs + 1}{LCs^2 + (R + 2Z_0)Cs + 1}. \quad (5)$$

A step voltage source with rise time τ_r and amplitude V_0, can be expressed as [13]:

$$V_{in}(s) = \frac{V_0}{2\tau_r}\frac{1}{s^2}\left(1 - e^{-\tau_r S}\right). \quad (6)$$

Therefore, the reflected waveform in Laplace domain can be written as:

$$V_{TDR}(s) = V_{in}(s).\Gamma_{DGS,DMS}(s). \quad (7)$$

In TDR measurements, the impedance follows from:

$$Z_{TDR} = Z_0 \times \left(V_{in}(t) + V_{TDR}(t)\right) / \left(V_{in}(t) - V_{TDR}(t)\right), \quad (8)$$

where Z_0 is the characteristic impedance of the transmission line at the terminal.

Figures 4 and 5 show the simulated reflection waveforms observed at port 1 of the defected structures, as shown in Fig. 2 and Fig. 3, and with a 50 Ω termination on port 2. The excitation source is a step wave with amplitude 1 Volt and rise time of 30 psec. The corresponding result predicted by the equivalent circuit model is also shown in these figures. As shown in Figs. 4 and 5, TDR curves have started with impedance just under 50 Ω. At impedance discontinuities, part of the input signal is reflected. These reflections, after traveling back, reach terminal Port 1 and are observed there [15]. We computed the values of the L, R and C of the proposed equivalent circuits, by fitting the TDR curves of equivalent circuit (RLC circuit) with the TDR curves of DGS/DMS, by proposing two equivalent circuit models we can try to tune the parameters of the circuit elements in the models so that time domain response from theoretical analysis match. The optimal dimensions of the equivalent circuit models parameters are specified in Table 1.

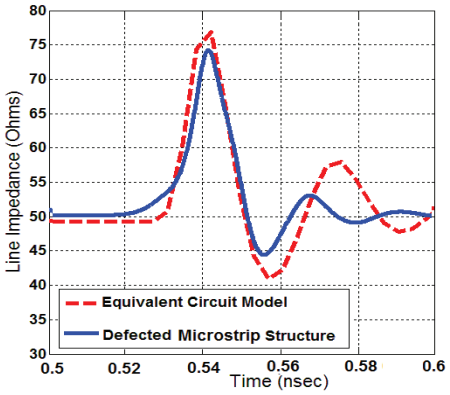

Fig. 4. The reflected waveforms simulated by HFSS and predicted by equivalent circuit model, and the proposed defected microstrip structure shown in Fig. 2.

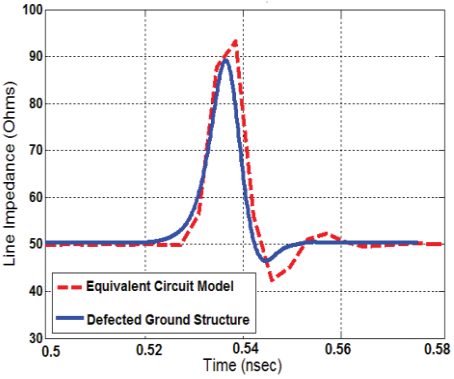

Fig. 5. The reflected waveforms simulated by HFSS and predicted by equivalent circuit model, and the proposed defected ground structure shown in Fig. 3.

Table 1: Equivalent circuit model parameters

Element	DMS	DGS
L	2.8 (nH)	1.6 (nH)
C	6.1 (pF)	17.75 (pF)
R	0.532 (Ω)	0.73 (Ω)

.

IV. RESULTS AND DISCUSSIONS

The planar slot antenna with various design parameters were constructed, and the numerical and experimental results of the input impedance and radiation characteristics are presented and discussed. The parameters of this proposed antenna are studied by changing one parameter at a time and fixing the others.

Figure 6 shows the structure of the various antennas used for simulation studies. Return loss characteristics for ordinary square slot antenna (Fig. 6 (a)), with two modified W-shaped slots with variable dimensions on the ground plane (Fig. 6 (b)), and with two modified

meander line slots with variable dimensions on the ground plane and a protruded W-shaped strip inside rectangular slot on the feed-line (Fig. 6 (c)), are compared in Fig. 7. As shown in Fig. 7, it is observed that the upper frequency bandwidth is affected by using the modified meander line slots in the ground plane and notched frequency bandwidth is sensitive to the protruded W-shaped strip inside rectangular slot on the feed-line.

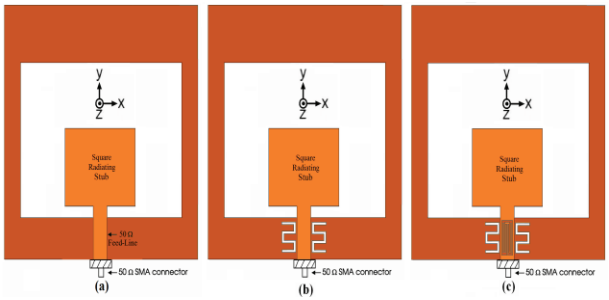

Fig. 6. (a) The ordinary square slot antenna, (b) the square antenna with two modified W-shaped slots on the ground plane (DGS), and (c) the square antenna with two modified meander line slots on the ground plane and a protruded W-shaped strip inside rectangular slot on the feed-line (DGS and DMS).

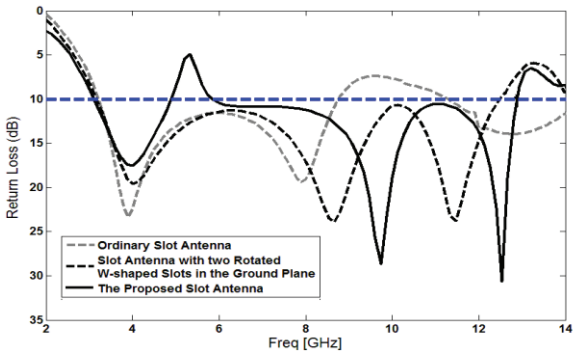

Fig. 7. Simulated return loss characteristics for antennas shown in Fig. 6.

As shown in Fig. 7, in the proposed antenna configuration, the ordinary square slot can provide the fundamental and next higher resonant radiation band at 4.12 and 8.18 GHz, respectively, in the absence of these defected structures. The upper frequency bandwidth is significantly affected by using the meander line slots on the ground plane. This behavior is mainly due to the change of surface current path by the dimensions of meander line slots at third resonance frequency (12.65 GHz), as shown in Fig. 8 (a). In addition, by inserting the protruded W-shaped strip inside rectangular slot with variable dimensions on the feed-line, a band notched function is created [6]. Figure 8 (b) presents the simulated current distributions on the radiating stub and feed-line at the notched frequency (5.5 GHz). As shown in Fig. 8 (b), at the notched frequency the current flows are more dominant around of the protruded W-shaped strip inside rectangular slot at feed-line.

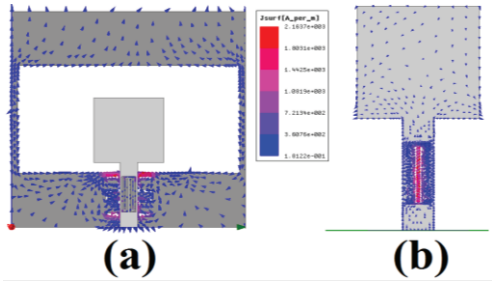

Fig. 8. Simulated surface current distributions plane for the proposed slot antenna: (a) on the ground at the third resonance frequency (12.65 GHz), and (b) on the radiating stub at notch frequency (5.5 GHz).

In order to increase the upper frequency bandwidth, two meander-line slots are inserted in the ground plane of the proposed antenna, as displayed in Fig. 1. To investigate the effects of meander-line slots size on the proposed antenna, the simulated return curves with different values of meander-line slots lengths are plotted in Fig. 9. It is found that by inserting the meander line slots with suitable dimensions in the ground plane additional resonance is excited, and hence, much wider impedance bandwidth with multi-resonance characteristics can be produced, especially at the higher frequencies.

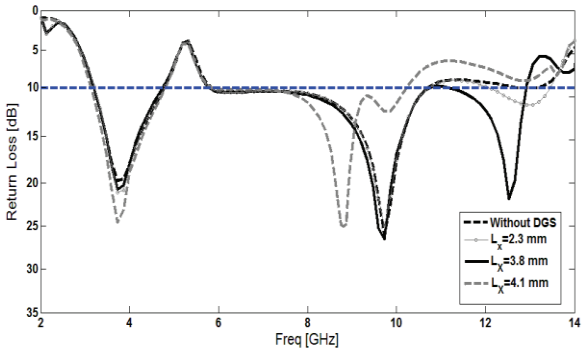

Fig. 9. Simulated return loss characteristics of the proposed antenna with different values of L_X.

In order to generate band notched performance, a protruded W-shaped strip inside rectangular slot is inserted in the microstrip feed line of the proposed antenna, as displayed in Fig. 1. Four such structures with different sizes are specified in Table 2 as cases 1, 2, 3 and 4.

Table 2: Four cases of proposed antenna with different values of protruded W-shaped strip

Parameter	W (mm)	L_1 (mm)	W_2 (mm)	L_3 (mm)
Case I	1	2.8	0.5	2.5
Case II	1.2	3.3	0.55	3.1
Case III	1.4	3.3	0.6	3.3
Case IV	1.25	3.8	0.65	3.6

Figure 10 shows the effects of protruded W-shaped strip with different values on VSWR characteristics. From these results, we can conclude that the notch frequency is controllable by changing the protruded W-shaped strip length.

The proposed antenna with optimal design, as shown in Fig. 11, was built and tested. Figure 12 shows the measured and simulated return loss characteristics of the proposed antenna. The fabricated antenna has the frequency band of 3.06 to over 14.27 GHz. As shown in Fig. 12, there exists a discrepancy between measured data and the simulated results. This discrepancy is mostly due to a number of parameters, such as the fabricated antenna dimensions as well as the thickness and dielectric constant of the substrate on which the antenna is fabricated, the wide range of simulation frequencies.

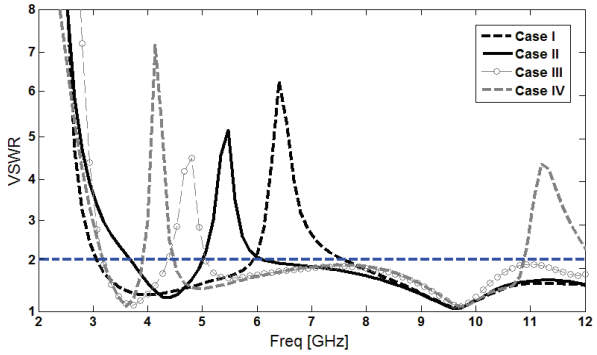

Fig. 10. Simulated VSWR characteristics for the proposed antenna with four cases 1, 2, 3 and 4 as shown in Table 2.

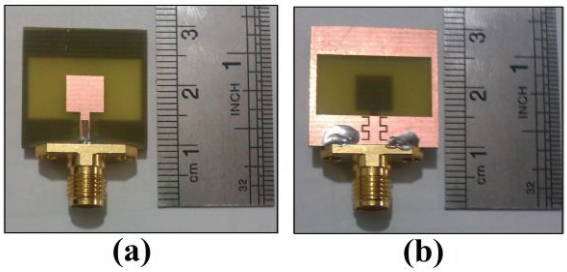

Fig. 11. Photograph of the realized printed square slot antenna.

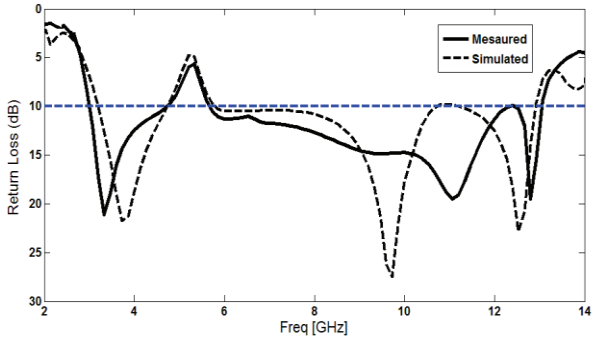

Fig. 12. Measured and simulated return loss for the proposed antenna.

Figure 13 shows the measured radiation patterns including the *H*-plane (*x-z* plane) and *E*-plane (*y-z* plane). The main purpose of the radiation patterns is to demonstrate that the antenna actually radiates over a wide frequency band. It can be seen that the radiation patterns in *x-z* plane are nearly omni-directional for the four frequencies.

Figure 14 shows the measured and simulated maximum gain for the proposed. A two-antenna technique is used to measure the radiation gain in the z axis direction (x-z plane). It can be observed in Fig. 14, that by using defected ground and defected microstrip structures, a sharp decrease of maximum gain in the notched frequency band at 5.5 GHz are shown. Also, as shown in Fig. 14, the measured results agree very well with the simulated results in the desired frequencies.

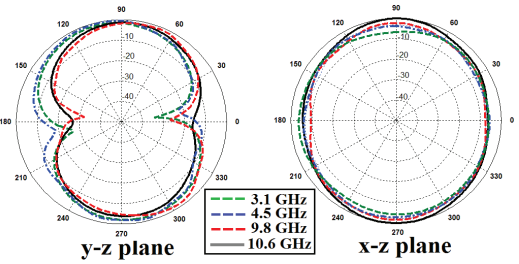

Fig. 13. Measured radiation patterns of the proposed antenna.

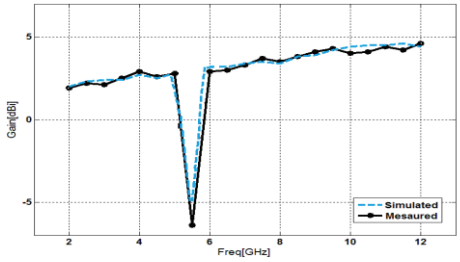

Fig. 14. Measured and simulated maximum gain for the proposed antenna in the z axis direction (x-z plane).

V. CONCLUSION

In this paper, a novel compact printed slot antenna (PSA) with band notched function and a novel time domain method to extract the equivalent RLC of the defected structures has been proposed for UWB applications. The analytic formulations for the equivalent circuit model are obtained based on time-domain reflectometry theory, Laplace transform. The fabricated antenna covers the frequency range for UWB systems between 3.07 to 12.91 GHz with band-notched characteristic around 5.12 to 5.96 GHz to avoid interference from WLAN systems. Experimental results show that the proposed antenna could be a good candidate for UWB application.

REFERENCES

[1] H. Schantz, *The Art and Science of Ultra Wideband Antennas*, Artech House, 2005.

[2] M. Ojaroudi and A. Faramarzi, "Multi-resonance small square slot antenna for ultra-wideband applications," *Microwave and Optical Tech. Letters*, vol. 53, no. 9, Sept. 2011.

[3] A. Dastranj, A. Imani, and M. Naser-Moghaddasi, "Printed wide-slot antenna for wideband applications," *IEEE Transactions on Antenna and Propagations*, vol. 56, no. 10, pp. 3097-3102, Oct. 2008.

[4] M. Ojaroudi, G. Kohneshahri, and J. Noory, "Small modified monopole antenna for UWB application," *IET Microw, Antennas Propag*., vol. 3, no. 5, pp. 863-869, Aug. 2009.

[5] R. Rouhi, C. Ghobadi, J. Nourinia, and M. Ojaroudi, "Ultra-wideband small square monopole antenna with band notched function," *Microwave and Optical Tech. Letters*, vol. 52, no. 8, Aug. 2010.

[6] M. Ojaroudi, H. Ebrahimian, C. Ghobadi, and J. Nourinia, "Small microstrip-fed monopole printed monopole antenna for UWB applications," *Microwave and Optical Tech. Letters*, vol. 52, no. 8, Aug. 2010.

[7] W. J. Lui, C. H. Cheng, Y. Cheng, et al., "Frequency notched ultra wideband microstrip slot antenna with a fractal tuning stub," *Electronic Letters*, no. 41, pp. 294-296, 2005.

[8] S. Nikolaou, N. D. Kingsley, G. E. Ponchak, J. Papapolymerou, and M. M. Tentzeris, "UWB elliptical monopoles with a reconfigurable band notch using MEMS switches actuated without bias lines," *IEEE Transactions on Antenna and Propagation*, vol. 57, no. 8, pp. 2242-2251, Aug. 2009.

[9] A. Valizade, C. Ghobadi, J. Nourinia, and M. Ojaroudi, "A novel design of reconfigurable slot antenna with switchable band notch and multiresonance functions for UWB applications," *IEEE Antennas and Wireless Propagation Letters*, vol. 11, no. 1, pp. 1166-1169, 2012.

[10] H. D. Chen, H. M. Chen, and W. S. Chen, "Planar CPW-fed sleeve monopole antenna for ultra-wideband operation," *IET Microw, Antennas Propag*., vol. 152, no. 6, pp. 491-494, Dec. 2005.

[11] A. B. Abdel-Rahman, A. K. Verma, A. Boutejdar, and A. S. Omar, "Control of bandstop response of hi-lo microstrip low-pass filter using slot in ground plane," *IEEE Trans. Microw. Theory Tech*., vol. 52, no. 3, pp. 1008-1013, Mar. 2004.

[12] C. H. Cheng, C. H. Tsai, and T. L. Wu, "A novel time domain method to extract equivalent circuit model of patterned ground structures," *IEEE Microw. Wireless Compon. Lett*., vol. 17, no. 11, Nov. 2010.

[13] M. Ojaroudi, N. Ojaroudi, and Y. Ebazadeh, "Dual band-notch small square monopole antenna with enhanced bandwidth characteristics for UWB applications," *ACES Journal*, vol. 27, no. 5, pp. 420-426, May 2012.

[14] Ansoft High Frequency Structure Simulation (HFSS), ver. 13, Ansoft Corporation, 2011.

[15] Z. Chen, X. Wu, H. Li, N. Yang, and M. Y. W. Chia, "Considerations for source pulses and antennas in UWB radio systems," *IEEE Trans. Antennas Propag*., vol. 52, no. 7, pp. 1739-1748, Jul. 2004.

Efficient FDTD Implementation of the ADE-Based CN-PML for the Two-Dimensional TMz Waves

Jianxiong Li [1], Haolin Jiang [1], and Naixing Feng [2]

[1] School of Electronics and Information Engineering
Tianjin Polytechnic University, Tianjin, 300387, China
lijianxiong@tjpu.edu.cn, houlinjohn@gmail.com

[2] Institute of Electromagnetics and Acoustics
Xiamen University, Xiamen, 361005, China
fengnaixing@gmail.com

Abstract ─ An efficient, unsplit-field and unconditional stable implementation of the stretched coordinate perfectly matched layer (SC-PML) is proposed for terminating the finite-difference time-domain (FDTD) method. Via incorporating the Crank-Nicolson Douglas-Gunn (CNDG) and the auxiliary differential equation (ADE) methods, respectively, the proposed PML formulations can take advantage of the unconditional stability of the CNDG method which has smaller numerical anisotropy than the existing alternately direction implicit (ADI) method. A numerical test carried out in a 2D free space FDTD domain is provided to validate the proposed CNDG-based PML. It has been shown that the proposed PML can not only overcome the Courant-Friedrich-Levy (CFL) stability constraint, but attenuate the propagating waves efficiently.

Index Terms ─ Auxiliary differential equation (ADE), Crank-Nicolson Douglas-Gunn (CNDG), finite-difference time-domain (FDTD), perfectly matched layer (PML).

I. INTRODUCTION

The finite-difference time-domain (FDTD) method plays an important role in the design and simulation of electromagnetic behaviors [1]. As an explicit numerical method, the Yee's FDTD is conditionally stable, which means that the FDTD time-step is constrained by the Courant-Friedrich-Levy (CFL) limit to maintain stability and makes the FDTD method not very efficient in analyzing electrically small structures [1]. In order to remove the CFL stability constraint on time step and improve computational efficiency, unconditionally stable methods such as the alternating-direction implicit FDTD (ADI-FDTD) scheme and the Crank-Nicolson FDTD (CN-FDTD) scheme have been introduced in [2-6]. As pointed in [5], the ADI's accuracy is inferior to that of CN scheme. The CN-FDTD with Douglas-Gunn (DG) algorithm (denoted as CNDG FDTD method) is developed in [6] to overcome the drawbacks that the CN-FDTD with a huge irreducible matrix is hardly to be solved without approximate algorithms.

In addition, one of the greatest challenges of applying the FDTD method is the development of absorbing boundary conditions (ABCs) which truncate open region problems to simulate the extension of the computational domain to infinity [1]. It has been shown that the perfectly matched layer (PML), introduced by Berenger, is one of the most effective ABCs [7]. The stretched coordinate PML (SC-PML) has the advantage of simple implementation in the corners and edges of the PML regions [8].

To our knowledge, there is only one literature about the formulation of the 2D unconditionally stable PML based on an approximate CN scheme [9]. The method in [9] is a split-field PML for 2D TEz waves.

In this paper, an alternative efficient, unconditionally stable and unsplit-field PML, denoted as ADE CNDG-PML, is constructed for 2D TMz waves. The formulation is based upon incorporating the CNDG algorithm and auxiliary differential equation (ADE) method into the PML implementation.

II. FORMULATION

For simplicity, the PML is constructed for 2D TMz waves only for truncating the free space. The frequency-domain modified Maxwell's equations in the SC-PML can be written as:

$$-j\omega H_x = c \cdot S_y^{-1} \frac{\partial E_z}{\partial y}, \tag{1}$$

$$j\omega H_y = c \cdot S_x^{-1} \frac{\partial E_z}{\partial x}, \tag{2}$$

Submitted On: November 6, 2014
Accepted On: April 2, 2015

$$j\omega E_z = c\cdot S_x^{-1}\frac{\partial H_y}{\partial x} - c\cdot S_y^{-1}\frac{\partial H_x}{\partial y}, \tag{3}$$

where c is the free-space wave-propagation velocity, S_η (η=x,y) is the stretched coordinate variables chosen within the PML region as:

$$S_\eta^{-1} = \frac{1}{1+\sigma_\eta/(j\omega\varepsilon_0)} = 1 - \frac{\sigma_\eta/\varepsilon_0}{j\omega+\sigma_\eta/\varepsilon_0}, \tag{4}$$

where σ_η is the conductivity profile along the η direction in the PML region [8], ε_0 is the free-space permittivity.

Using (4) and the inverse Fourier translation, (1)-(3) can be written in the time domain as:

$$-\frac{\partial}{\partial t}H_x = c\cdot\frac{\partial E_z}{\partial y} - g_{xy}, \tag{5}$$

$$\frac{\partial}{\partial t}H_y = c\cdot\frac{\partial E_z}{\partial x} - g_{yx}, \tag{6}$$

$$\frac{\partial}{\partial t}E_z = c\cdot\frac{\partial H_y}{\partial x} - c\cdot\frac{\partial H_x}{\partial y} - f_{zx} + f_{zy}, \tag{7}$$

where f_{zx}, f_{zy}, g_{xy} and g_{yx} are given by:

$$\frac{\partial}{\partial t}f_{zx} + \frac{\sigma_x}{\varepsilon_0}f_{zx} = c\cdot\frac{\sigma_x}{\varepsilon_0}\frac{\partial H_y}{\partial x}, \tag{8}$$

$$\frac{\partial}{\partial t}f_{zy} + \frac{\sigma_y}{\varepsilon_0}f_{zy} = c\cdot\frac{\sigma_y}{\varepsilon_0}\frac{\partial H_x}{\partial y}, \tag{9}$$

$$\frac{\partial}{\partial t}g_{xy} + \frac{\sigma_y}{\varepsilon_0}g_{xy} = c\cdot\frac{\sigma_y}{\varepsilon_0}\frac{\partial E_z}{\partial y}, \tag{10}$$

$$\frac{\partial}{\partial t}g_{yx} + \frac{\sigma_x}{\varepsilon_0}g_{yx} = c\cdot\frac{\sigma_x}{\varepsilon_0}\frac{\partial E_z}{\partial x}. \tag{11}$$

Applying the CN scheme to discretize (5)-(11), we have the following discrete equations as:

$$H_{x_{i,j+1/2}}^{n+1} = H_{x_{i,j+1/2}}^{n} - \chi_y\cdot\Gamma_y(E_{z_{i,j}}^{n}) + \Delta t_h\cdot(g_{xy_{i,j+1/2}}^{n+1} + g_{xy_{i,j+1/2}}^{n}), \tag{12}$$

$$H_{y_{i+1/2,j}}^{n+1} = H_{y_{i+1/2,j}}^{n} + \chi_x\cdot\Gamma_x(E_{z_{i,j}}^{n}) - \Delta t_h\cdot(g_{yx_{i+1/2,j}}^{n+1} + g_{yx_{i+1/2,j}}^{n}), \tag{13}$$

$$E_{z_{i,j}}^{n+1} = E_{z_{i,j}}^{n} + \chi_x\cdot\Gamma_x(H_{y_{i+1/2,j}}^{n}) - \chi_y\cdot\Gamma_y(H_{x_{i,j+1/2}}^{n}) + \Delta t_h\cdot(f_{zy_{i,j}}^{n+1} + f_{zy_{i,j}}^{n}) - \Delta t_h\cdot(f_{zx_{i,j}}^{n+1} + f_{zx_{i,j}}^{n}), \tag{14}$$

$$f_{zx_{i,j}}^{n+1} = r_{0x_i}\cdot f_{zx_{i,j}}^{n} + r_{1x_i}\cdot\Gamma_x(H_{y_{i+1/2,j}}^{n}), \tag{15}$$

$$f_{zy_{i,j}}^{n+1} = r_{0y_j}\cdot f_{zy_{i,j}}^{n} + r_{1y_j}\cdot\Gamma_y(H_{x_{i,j+1/2}}^{n}), \tag{16}$$

$$g_{xy_{i,j+1/2}}^{n+1} = r_{0y_{j+1/2}}\cdot g_{xy_{i,j+1/2}}^{n} + r_{1y_{j+1/2}}\cdot\Gamma_y(E_{z_{i,j}}^{n}), \tag{17}$$

$$g_{yx_{i+1/2,j}}^{n+1} = r_{0x_{i+1/2}}\cdot g_{yx_{i+1/2,j}}^{n} + r_{1x_{i+1/2}}\cdot\Gamma_x(E_{z_{i,j}}^{n}). \tag{18}$$

The operator $\Gamma_\eta[*]$ denotes the difference form obtained by applying the CN method along direction η, for example:

$$\Gamma_y(E_{z_{i,j}}^{n}) = E_{z_{i,j+1}}^{n+1} - E_{z_{i,j}}^{n+1} + E_{z_{i,j+1}}^{n} - E_{z_{i,j}}^{n}. \tag{19}$$

Other operators take similar forms as (19). The corresponding coefficients in (12)-(18) are given by:

$$\Delta t_h = \Delta t/2,\ \chi_\eta = c\Delta t_h/(\Delta\eta),\ q_{\eta_k} = \sigma_{\eta_k}\Delta t_h/\varepsilon_0,$$
$$r_{0\eta_k} = (1-q_{\eta_k})/(1+q_{\eta_k}),$$
$$r_{1\eta_k} = [q_{\eta_k}/(1+q_{\eta_k})]\cdot(c/\Delta\eta),$$

where $\Delta\eta$ (η=x,y) is the space cell size, Δt is the time step, and k (k=i,j) is the inter-number indices of the computational cells.

It is noted that the discrete electric and magnetic field components are coupled, which leads to a huge sparse matrix to be solved expensively. One way to decouple the electric and magnetic fields is to insert (15)-(18) into (12)-(14) respectively, then substitute H_x^{n+1} and H_y^{n+1} into the expression of E_z^{n+1} to eliminate the implicit magnetic field components:

$$\begin{aligned}[1-(D_{2x}+D_{2y})]E_{z_{i,j}}^{n+1} &= [1+(D_{2x}+D_{2y})]E_{z_{i,j}}^{n}\\ &+2(\chi_x-\Delta t_h r_{1x_i})(H_{y_{i+1/2,j}}^{n}-H_{y_{i-1/2,j}}^{n}) - d_{x_i}^{+}g_{yx_{i+1/2,j}}^{n}\\ &-2(\chi_y-\Delta t_h r_{1y_j})(H_{x_{i,j+1/2}}^{n}-H_{x_{i,j-1/2}}^{n}) + d_{x_i}^{-}g_{yx_{i-1/2,j}}^{n}\\ &-d_{y_j}^{+}g_{xy_{i,j+1/2}}^{n} + d_{y_j}^{-}g_{xy_{i,j-1/2}}^{n} - \Delta t_h(1+r_{0x_i})f_{zx_{i,j}}^{n}\\ &+\Delta t_h(1+r_{0y_j})f_{zy_{i,j}}^{n},\end{aligned} \tag{20}$$

where D_{2x} and D_{2y} are defined as follows:

$$D_{2x}E_{z_{i,j}}^{n+1} = c_{x_i}^{+}E_{z_{i+1,j}}^{n+1} - (c_{x_i}^{+}+c_{x_i}^{-})E_{z_{i,j}}^{n+1} + c_{x_i}^{-}E_{z_{i-1,j}}^{n+1}, \tag{21}$$

$$D_{2y}E_{z_{i,j}}^{n+1} = c_{y_j}^{+}E_{z_{i,j+1}}^{n+1} - (c_{y_j}^{+}+c_{y_j}^{-})E_{z_{i,j}}^{n+1} + c_{y_j}^{-}E_{z_{i,j-1}}^{n+1}. \tag{22}$$

The coefficients of (20)-(22) are defined as:

$$c_{\eta_k}^{\pm} = (\chi_\eta - \Delta t_h r_{1\eta_k})(\chi_\eta - \Delta t_h r_{1\eta_{k\pm1/2}}),$$
$$d_{\eta_k}^{\pm} = (\chi_\eta - \Delta t_h r_{1\eta_k})\Delta t_h(1+r_{0\eta_{k\pm1/2}}).$$

Note that (20) leads to a block tri-diagonal matrix, which still requires very expensive matrix solution at each time step. For an efficient solution of E_z^{n+1}, the CNDG method proposed in [6] is introduced. By adding $D_{2x}D_{2y}E_z^{n+1}$ and $D_{2x}D_{2y}E_z^{n}$ to the left-hand-side (LHS) and right-hand-side (RHS) of (20) respectively, it can be factorized into:

$$(1-D_{2x})(1-D_{2y})E_{z_{i,j}}^{n+1} = (1+D_{2x})(1+D_{2y})E_{z_{i,j}}^{n} + \alpha_{i,j}, \tag{23}$$

where $\alpha_{i,j}$ denotes the other terms of the RHS of (20).

Then (23) can be solved with the following two-step update equations:

$$(1-D_{2x})E_{z_{i,j}}^{*} = (1+D_{2x}+2D_{2y})E_{z_{i,j}}^{n} + \alpha_{i,j}, \tag{24}$$

$$(1-D_{2y})E_{z_{i,j}}^{n+1} = E_{z_{i,j}}^{*} - D_{2y}E_{z_{i,j}}^{n} . \quad (25)$$

From (24) and (25), we can see that the updated equation for principal component E_z^{n+1} splits into two-step update equations by introducing an intermediate parameter E_z^*. However, the LHS of (24) and (25) form two tri-diagonal matrixes which can be solved easily. Once E_z^{n+1} is obtained, g_{xy}^{n+1}, g_{yx}^{n+1}, H_x^{n+1}, H_y^{n+1}, f_{zx}^{n+1} and f_{zy}^{n+1} can be updated explicitly.

III. NUMERICAL RESULT

To validate the effectiveness of the proposed formulation, we implemented the PML in a 2D domain. With 1 GHz of the bandwidth, a derivative gauss pulse is placed at the center of a 101×101 uniform mesh domain, which radiates into the free space as an electric-field source. The computational domain discretized with a space cell size of 3 mm in both x and y directions. All sides of the computational domain were terminated by PML [8, 2, 0.001%], as defined in [7].

To evaluate the reflection error of the proposed PML, this ADE CNDG-PML scheme under different CFL numbers (CFLN) are invoked for field computations. The term CFLN is defined as CFLN=$\Delta t/\Delta t_{max}^{FDTD}$, where Δt_{max}^{FDTD} is the maximum stability constraint of the conventional FDTD. For the sake of comparison, the results using the PML based on the conventional FDTD are also obtained. Figure 1 depicts the results obtained by using these two different approaches. The relative reflection error versus time is computed at an observation point in the corner of the computational domain and with one cell away from the interface between the PML and the computational domain using:

$$R_{dB} = 20\log_{10}\left[\frac{\left|E_z(t)-E_{zref}(t)\right|}{\left|E_{zref\,\max}\right|}\right], \quad (26)$$

where $E_z(t)$ represents the electric field computed using the test domain and $E_{zref}(t)$ is a reference solution based on an extended lattice with the size of 600 cells in both x and y directions and terminated by PML [128, 4, 0.0001%]. $E_{zref\max}$ is the maximum amplitude of the reference solution over the full time simulation.

The results are shown in Fig. 1. At early time to about 7 ns, the performance of the proposed PML degrade as the CFLN increasing. However, the maximum relative errors of the conventional SC-PML and the ADE CNDG-PML with different CFLN (CFLN=1, 2, 4) are -66.46 dB, -66.48 dB, -66.56 dB and -64.65 dB, respectively. Then it can be concluded that the proposed PML can almost maintain the same maximum relative error level with different CFLN.

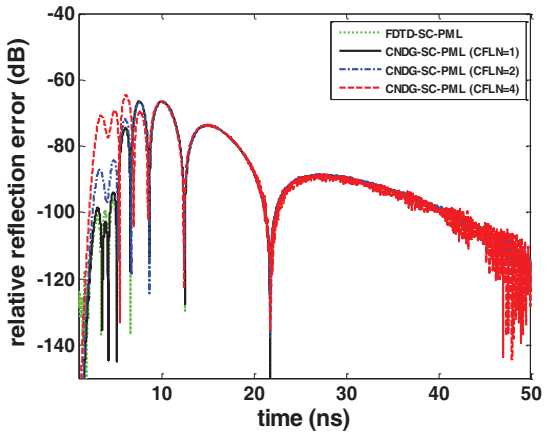

Fig.1. Relative reflection error at observation point in the computational domain terminated by PML [8, 2, 0.001%] for ADE CNDG-PML with various CFLN. The conventional FDTD SC-PML is also included.

IV. CONCLUSION

An efficient algorithm based upon the ADE method is presented in this paper for implementing the SC-PML formulations by making use of a CNDG scheme without the need of splitting the field components. Numerical results demonstrate that the ADE CNDG-PML can be used as a good absorbing boundary condition while the time step is beyond the CFL limit. The simulation time can be reduced by increasing the time step without decreasing of PML performance. Consequently, the computational process uses less time than the conventional SC-PML as the value of CFLN is larger than CFL limit.

ACKNOWLEDGMENT

This work was supported by the National Nature Science Foundation of China (grant 61372011).

REFERENCES

[1] A. Taflove and S. C. Hangess, *Computational Electrodynamics: The Finite-Difference Time-Domain Method*, 3rd ed., Boston, Artech-House, 2005.

[2] T. Namiki, "A new FDTD algorithm based on alternating direction implicit method," *IEEE Trans. Microw. Theory Tech.*, vol. 47, pp. 2003-2007, Oct. 1999.

[3] F. Zheng, Z. Chen, and J. Zhang, "A finite-difference time-domain method without the courant stability condition," *IEEE Microw. Guid. Wave Lett.*, vol. 9, no. 11, pp. 441-443, Nov. 1999.

[4] A. P. Zhao, "A novel implementation for two-

dimensional unconditionally stable FDTD method," *Microw. Opt. Technol. Lett.*, vol. 38, no. 6, pp. 457-462, Aug. 2003.

[5] G. L. Sun and C. W. Trueman, "Approximate Crank-Nicolson schemes for the 2-D finite-difference time-domain method for TEz waves," *IEEE Trans. Antennas Propag.*, vol. 52, no. 11, pp. 2963-2972, Nov. 2004.

[6] G. L. Sun and C. W. Trueman, "Unconditionally stable Crank-Nicolson scheme for solving two-dimensional Maxwell's equations," *Electron. Lett.*, vol. 39, no. 7, pp. 595-597, Apr. 2003.

[7] J. P. Berenger, "A perfectly matched layer for the absorption of electromagnetic waves," *J. Comput. Phys.*, vol. 114, no. 2, pp. 185-200, Oct. 1994.

[8] W. C. Chew and W. H. Weedon, "A 3D perfectly matched medium from modified Maxwell's equations with stretched coordinates," *Microw. Opt. Technol. Lett.*, vol. 7, no. 13, pp. 599-604, Sep. 1994.

[9] H. Lin, P. P. Ding, and G. Wang, "Perfectly matched layer for two-dimensional unconditionally stable FDTD based on approximate Crank-Nicolson scheme," *Microw. Opt. Technol. Lett.*, vol. 49, no. 5, pp. 1178-1182, May 2007.

Jianxiong Li was born in 1969, in Tianjin, China. He received the B.Sc. and M.Sc. degrees in Physics in 1991 and 1994, respectively, and obtained the Ph.D. degree in Communication and Information System in 2007, from Tianjin University, Tianjin, China. His main research interests are in computational electromagnetics, metamaterials, and RFID antenna.

Haolin Jiang was born in 1989, in Chongqin, China. He received the B.Sc. degree in the School of Electronic Engineering in 2012, from Tianjin University of Technology and Education, Tianjin, China. He is currently pursuing the M.Sc. degree in the School of Electronics and Information Engineering, Tianjin Polytechnic University, Tianjin. His current research interests are in computational electromagnetics and metamaterials.

Naixing Feng received the B.S. degree in Electronic Science and Technology and the M.S. degree in Micro-Electronics and Solid-State Electronics from Tianjin Polytechnic University, Tianjin, China, in 2010 and 2013, respectively. He is currently working towards his Ph.D. degree in Radio Physics at Xiamen University, Xiamen. His current research interests include computational electromagnetics and acoustics. He has published over 20 papers in refereed journals and conference proceedings. He has served as a Reviewer of more than 5 journals.

Miniaturized Microstrip Bandpass Filters Using Novel Stub Loaded Resonator

Mohamadreza Salehi and Leila Noori

Department of Electrical and Electronic Engineering
Shiraz University of Technology, Shiraz, Iran
drmohamadreza.salehi@gmail.com, Leila_noori62yahoo.com

Abstract ─ In this paper, a novel structure is proposed to design two compact microstrip bandpass filters operated at 2.39 GHz and 5.73 GHz, which their sizes are 44 mm^2 and 14 mm^2, respectively. Miniaturization, resonance frequency tuning and harmonics attenuation methods are presented. Low insertion losses and wide fractional bandwidths are achieved. The obtained insertion losses and fractional bandwidths of the 2.39 GHz and 5.73 GHz filters are 0.27 dB, 0.19 dB, 46%, and 44%, respectively. Also for both filters, the second and third harmonics are attenuated. The proposed filters are fabricated and measured and there is a good agreement between the simulation and measurement results.

Index Terms ─ Harmonics attenuation, microstrip filter, miniaturization, novel structure.

I. INTRODUCTION

There have been increasing demands for the compact microstrip filters with low insertion loss due to their important role in the modern wireless communication systems [1-5]. But several microstrip bandpass filters with very large size, using different resonators, have been proposed in [6-16]. In [6], a branch line resonator and in [7], a stepped impedance resonator have been used to design microstrip bandpass filters. But they have large insertion losses and small fractional bandwidths. In [8-9], ultra-wide band microstrip bandpass filters have been presented. In [8], a ring resonator and a parallel coupled resonator have been utilized to obtain a wide fractional bandwidth filter, but its insertion loss is large. In [10-14], microstrip band pass filters with small fractional bandwidths and undesired insertion losses have been proposed. To design these filters, inductive-coupled stepped-impedance quarter-wavelength resonators [10], ring resonators [11], rectangular dual spiral resonator [12], and partially coupled resonators [13] have been used. In this paper, two miniaturized microstrip bandpass filters are designed using a novel compact resonator to solve the previous works problems in terms of the large sizes, small fractional bandwidths and the large insertion losses.

II. THEORY AND STRUCTURE

A. Resonator structure

Microstrip stub loaded cells can be used as the compact tuneable resonators. By tuning the widths and lengths of the stubs, the resonance frequency can be tuned without size increase. One of these compact stub loaded tuneable resonators is proposed and shown in Fig. 1. It is a novel U-shape structure, which is loaded by a shunt stub.

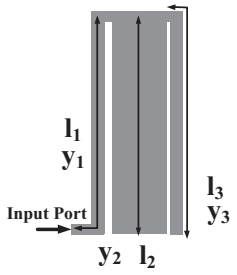

Fig. 1. Proposed resonator.

For even mode analysis, the characteristic admittance, viewed from the open end input port, is achieved as follows:

$$Ye = \frac{(y_{2e} + y_{3e})\, y_{1e}}{y_{2e} + y_{3e} + y_{1e}}. \quad (1)$$

In Equation (1), y_{1e} is the admittance of the structure connected to the input port originated from the structure with length l_1, while y_{2e} comes from the shunt stub loaded inside the U-shape structure and y_{3e} is the equivalent admittance of the open stub with the physical length l_3 (see Fig. 1). According to the transmission line theory, the input admittances of the open-circuited transmission line with the characteristic admittances y_1, y_2 and y_3 are given by [17]:

Submitted On: February 3, 2015
Accepted On: May 10, 2015

$$y_{ie} = j\, y_i \tan(k_i\, f_{oe})$$

$$k_i = (\frac{\pi}{150})\sqrt{\varepsilon_{rei}}\, l_i \qquad for\ \ i = 1,\ 2,\ and\ 3\,, \quad (2.a)$$

where f_{oe} is the even mode resonant frequency (per GHz), ε_{rei} is the effective dielectric constant, and l_i is the physical length (per mm).

The effective dielectric constant can be calculated as follows [17]:

$$\varepsilon_{rei} = \frac{\varepsilon_r + 1}{2} + \frac{\varepsilon_r - 1}{2}\{\frac{1}{\sqrt{(1+12\frac{h}{W_i})}} + 0.04(1+\frac{W_i}{h})^2\}\,. \quad (2.b)$$

In Equation (2.b), i=1, 2 and 3 and h is the thickness of the substrate with a dielectric constant ε_r. Also W_i is the width of the stub with length l_i. From Equation (2.b), the widths have significant effects on the resonator performance.

B. Resonance frequency tuning and miniaturizing method

The resonance condition for the even mode is satisfied when Y_e=0. Therefore, by substituting Equation (2) in Equation (1), the even mode resonance frequencies can be obtained as follows:

$$Y_e = j \times \frac{(y_2 \tan(k_2\, f_{oe2}) + y_3 \tan(k_3\, f_{oe2}))\, y_1 \tan(k_1\, f_{oe1})}{y_2 \tan(k_2\, f_{oe2}) + y_3 \tan(k_3\, f_{oe2}) + y_1 \tan(k_1\, f_{oe1})} = 0\,. \quad (3.a)$$

Therefore, if y_2=y_3, then:

$$f_{oe1} = \frac{m\pi}{k_1} \qquad for \quad m = 1, 2, 3, \ldots, \quad (3.b)$$

$$\tan(k_2\, f_{oe2}) = -\tan(k_3\, f_{oe2})$$

$$so \qquad . \quad (3.c)$$

$$f_{oe2} = \frac{m\,\pi}{k_2 + k_3} \qquad \& \quad m = 1, 2, 3, \ldots$$

If the open stubs with the lengths l_2 and l_3 have the same characteristic admittances, by tuning k_1, k_2, and k_3, the resonance frequency can be adjusted simply. Under this condition (for a defined resonance frequency) if m=1 then k_1, k_2, and k_3 are minimum. Then from (2.a) and (2.b), the lengths and widths of the resonator are minimized. As a result, the resonator size is minimized. Therefore, a compact tuneable resonator is designed, which can be used in the filter structure.

C. Harmonics attenuation method

To design a single-band bandpass filter with attenuated harmonics (for a defined m) a resonance frequency is the desired resonance frequency and another one is an unwanted resonance frequency. The unwanted resonance frequency acts as a harmonic. One method to remove this harmonic is obtained when f_{oe1}=f_{oe2}. Therefore, to remove the harmonic from Equations (3.b) and (3.c):

$$k_1 = k_2 + k_3\,. \quad (4)$$

D. Odd mode analysis

By a similar analysis for odd mode, the characteristic admittance, viewed from the open end input port, Y_O, is:

$$Yo = \frac{(y_{2o} + y_{3o})\, y_{1o}}{y_{2o} + y_{3o} + y_{1o}}\,. \quad (5)$$

In Equation (5), y_{io} (i=1, 2 and 3) are the odd mode admittances of the structures which are described similar to y_{ie}. The input admittances of the open-circuited transmission line with the characteristic admittances y_1, y_2 and y_3 are given by:

$$y_{io} = -\,j\, y_i \cot(k_i\, f_{oo})$$

$$k_i = (\frac{\pi}{150})\sqrt{\varepsilon_{rei}}\, l_i \qquad for\ \ i = 1,\ 2,\ and\ 3\,, \quad (6)$$

where f_{oo} is the odd mode resonant frequency (per GHz). The resonance condition for the odd mode is satisfied when Z_o=1/Y_o=0. Therefore, by substituting Equation (6) in Equation (5), the odd mode resonance frequencies can be obtained as follows:

$$Z_o = -\,j \times \frac{y_1 \cot(k_1\, f_{oo}) + y_2 \cot(k_2\, f_{oo}) + y_3 \cot(k_3\, f_{oo})}{(y_2 \cot(k_2\, f_{oo}) + y_3 \cot(k_3\, f_{oo}))\, y_1 \cot k_1\, f_{oo})} = 0\,. \quad (7.a)$$

A solution for Equation (7.a) is:

$$f_{oo} = \frac{m\pi}{2k_1} = \frac{m\pi}{2k_2} = \frac{m\pi}{2k_3} \qquad for \quad m = 1, 3, 5, 7, \ldots. \quad (7.b)$$

From (2.b) and (7.b):

$$\sqrt{\varepsilon_{re1}}\, l_1 = \sqrt{\varepsilon_{re2}}\, l_2 = \sqrt{\varepsilon_{re3}}\, l_3\,. \quad (7.c)$$

If the lengths and widths l_i and W_i be decreased so that Equation (7.c) be satisfied, then the resonance frequency is obtained and the resonator size is reduced too.

To calculate the resonator dimensions, first a substrate with ε_r=2.2 and h=0.786 mm is chosen. As a result of the presented method, the internal stub must be extensive while the resonator has a minimum size (to tune the resonance frequency with the minimum size of the resonator). Therefore, an appropriate selection of the sizes of the widths is: W_1=W_3=0.1 mm, and W_2=0.7 mm. From Equation (2.b), ε_{re1}=ε_{re3}=1.69 and ε_{re2}=1.84. Whereas the resonance frequency is a presuppose target, from Equations (2.a), (3.b) and (3.c), the length of the stubs have determinate values.

Using the proposed resonator, two compact bandpass filters with symmetric structures are designed to operate at WLANs frequencies. Figure 2 shows the proposed bandpass filter operated at 2.39 GHz. This filter is composed of four stub loaded U-shape

structures. Using the coupled lines, two stub loaded U-shape structures are connected to the other two stub loaded U-shape structures. The stub loaded U-shape structures are similar to the proposed resonator, which can be analyzed in the same method.

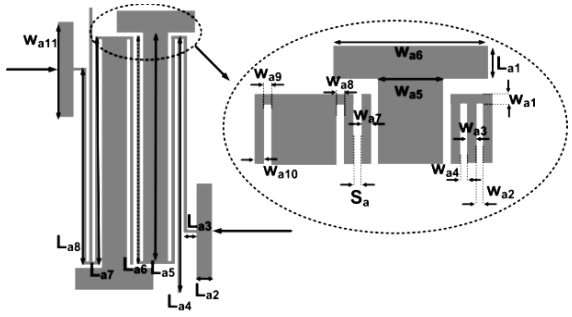

Fig. 2. Proposed 2.39 GHz filter.

As shown in Fig. 3, to design a compact bandpass filter operated at 5.73 GHz, the proposed resonator in Fig. 1 is used. This filter is composed of two resonators, similar to Fig. 1, which connected together using the coupled lines and the taped line feed structures.

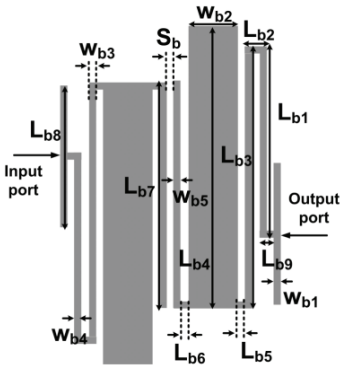

Fig. 3. Proposed 5.73 GHz filter.

The T-shape tapped lines feed structures are added to the input and output ports to improve the insertion loss without size increment. The effect of T-shape tapped line feed structure on the insertion loss (for 2.39 GHz filter) is shown in Fig. 4 (a). In Fig. 4 (a), S_{21} is shown as a function of W_{a11}. As shown in Fig. 4 (a), by increasing W_{a11}, the insertion loss is decreased. S_{21} as a function of the coupled line length is shown in Fig. 4 (b). As shown in Fig. 4 (b), by increasing L_{a6} the resonance frequency is shifted to the left. Also by decreasing L_{a6}, the coupling effect is decreased and as a result the insertion loss is increased. The T-shape cells (with the lengths L_{a5} and L_{a1}) are loaded in the inside of the U-shape structures to control the resonance frequency without size increment. By increasing the wide, the resonance frequency shifts to the left. This is shown in Fig. 4 (c). The coupled lines (in Fig. 3) play an important role to control the insertion loss and resonance frequency. The effect of this parameter is shown in Fig. 4 (d). In Fig. 4 (d), S_{21} is shown as a function of L_{b7}. As shown in Fig. 4 (d), by increasing L_{b7} the resonance frequency is shifted to the left. Also by decreasing L_{b7}, the coupling effect is decreased and as a result the insertion loss is increased. Therefore, by tuning the coupled lines lengths the insertion loss is decreased and the resonance frequency is tuned. To improve the sharpness, S_{21} is changed as a function of L_{b1}. This effect is shown in Fig. 4 (e). As shown in Fig. 4 (e), the frequency response is sharper when L_{b1} is smaller.

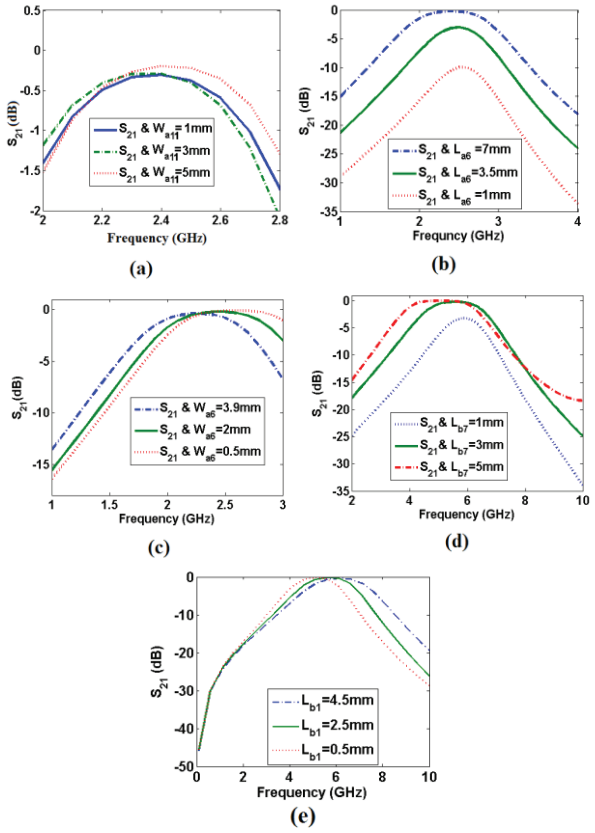

Fig. 4. (a) S_{21} as a function of W_{a11}, (b) S_{21} as a function of L_{a6}, (c) S_{21} as a function of W_{a6}, (d) S_{21} as a function of L_{b7}, and (e) S_{21} as a function of L_{b1}.

III. RESULTS

The proposed filters are simulated using ADS full wave EM simulator and fabricated on a RT Duroid 5880 substrate. They have a dielectric constant of 2.2, 31 mil-thickness and the loss tangent equal to 0.0009.

A. 2.39 GHz filter

The dimensions of the proposed 2.39 GHz filter (Fig. 2) are presented in Table 1.

The frequency response of the 2.39 GHz filter is shown in Fig. 5 (a). The wide-band frequency response of the 2.39 GHz filter is shown in Fig. 5 (b) and the photograph of the fabricated filter is shown in Fig. 5 (c). The insertion loss at 2.39 GHz is better than 0.27 dB, while the return loss is better than -12 dB.

Table 1: Dimensions of the proposed 2.39 GHz filter

L_{a1}	L_{a2}	L_{a3}	L_{a4}	L_{a5}	L_{a6}	L_{a7}
0.7 mm	0.5 mm	0.3 mm	8.1 mm	7.2 mm	7.2 mm	7.2 mm
L_{a8}	W_{a1}	W_{a2}	W_{a3}	W_{a4}	W_{a5}	W_{a6}
6.2 mm	0.1 mm	0.1 mm	0.1 mm	0.1 mm	0.8 mm	2.5 mm
W_{a7}	W_{a8}	W_{a9}	W_{a10}	W_{a11}	S_a	
0.1 mm	0.1 mm	0.1 mm	0.1 mm	3 mm	0.1 mm	

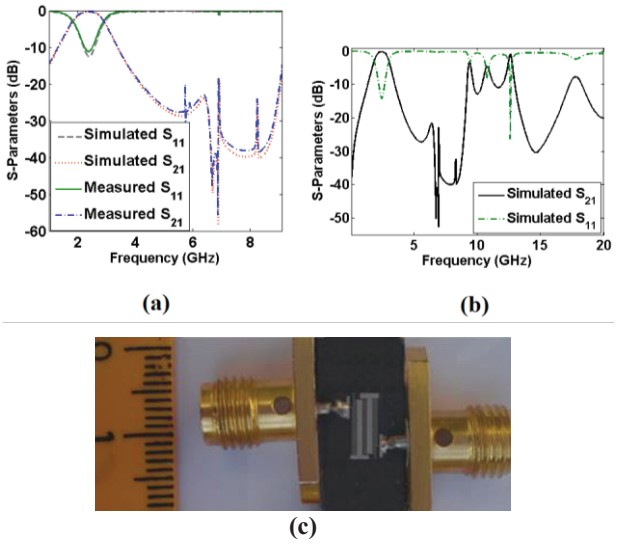

Fig. 5. (a) Frequency response of the proposed 2.39 GHz filter, (b) wide-band frequency response of the 2.39 GHz filter, and (c) photograph of the fabricated 2.39 GHz filter.

The filter size is 9×4.9 mm² (0.09 λ_g × 0.05 λ_g mm²). The obtained fractional bandwidth (FBW) is 46%. This filter has the cut-off frequencies at 1.83 GHz and 2.94 GHz. The harmonics are attenuated from 4.29 GHz up to 9 GH (3.76f_o) with a minimum attenuation above -19 dB.

B. 5.73 GHz filter

The dimensions of the proposed 5.73 GHz filter (Fig. 3) are optimized and presented in Table 2.

The frequency response of the 5.73 GHz filter is shown in Fig. 6 (a). The wide-band frequency response of the 5.73 GHz filter is shown in Fig. 6 (b). The insertion loss at 5.73 GHz is better than 0.19 dB, while the return loss is better than -13 dB. The filter size is 4.8×3.1 mm² (0.11λ_g × 0.07λ_g mm²) and its fractional bandwidth is 43%. It has the cut-off frequencies at 4.48 GHz and 6.99 GHz. The harmonics are attenuated from 9.09 GHz up to 17.28 GHz (3f_o) with a minimum attenuation above -20 dB. The photograph of the fabricated filter is shown in Fig. 6 (c).

Table 2: Dimensions of the proposed 5.73 GHz filter

L_{b1}	L_{b2}	L_{b3}	L_{b4}	L_{b5}	L_{b6}	L_{b7}
2.7 mm	0.3 mm	3.7 Mm	4 mm	0.1 Mm	0.1 mm	3.2 mm
L_{b8}	L_{b9}	W_{b1}	W_{b2}	W_{b4}	W_{b5}	S_b
2 mm	0.2 mm	0.1 mm	0.7 Mm	0.1 mm	0.1 Mm	0.1 mm

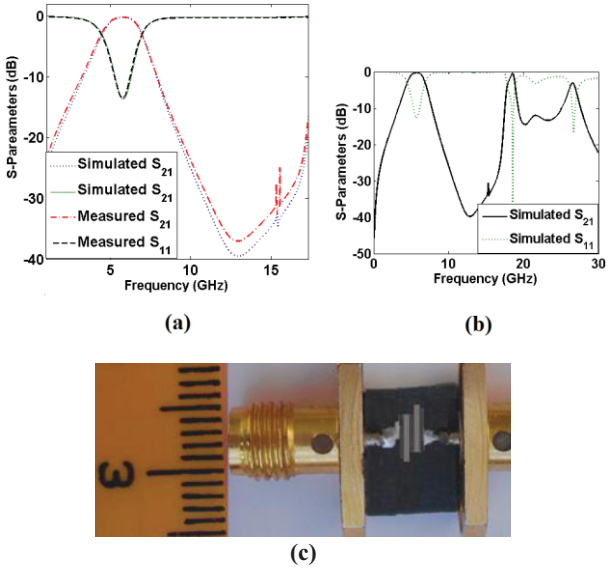

Fig. 6. (a) Frequency response of the proposed 5.73 GHz filter, (b) wide-band frequency response of 5.73 GHz filter, and (c) photograph of the fabricated 5.73 GHz filter.

In comparison with the previous works, the minimum size, good insertion losses and wide fractional bandwidths are obtained. The insertion losses, fractional bandwidths, stopband responses, and the size of the proposed filters are compared with previous works in Table 3. In Table 3, IL, F_O, FBW are the insertion loss, operation frequency and fractional bandwidth respectively. In Table 3, IL, F_O and size are per dB, GHz and mm^2 respectively.

Table 3: Comparison between the previous works and the proposed filters

References	IL	FO	Size	FBW (%)	Stopband Response	Approximated -20 dB Cut-Off Frequencies (GHz)
[6]	2.6	2	149	5.9	-27 dB up to 2.88fo	
[7]	2.5	2	2049	12	-50 dB up to 4 GHz (2fo)	1.6 and 2.4
[8]	2.5	4	177	50	-60 dB up to 7.4 GHz (1.85fo)	2.7 and 5.1
[9]	0.1	4.5	1034	66	---	2.6 and 5.2
[10]	0.85	2.35	220	11.5	---	2 and 2.6
[11]	---	2.05	126	10	---	1.3 and 1.5
[13]	3.8	1	9000	13	-30 dB up to 6.2 GHz (6.2fo)	0.9 and 1.12
[14]	1.8	1.78	488	16.5	-30 dB up to 6.8 GHz (3.8fo)	1.5 and 1.9
[15]	6.4	2.55	225	3.5	-30 dB up to 3.9 GHz (1.5fo)	2.4 and 2.6
Proposed 2.39 GHz BPF	0.27	2.39	44.1	46	-19 dB up to 9 GHz (3.76fo)	0.66 and 4.3
Proposed 5.73 GHz BPF	0.19	5.73	14	43	-20 dB up to 17.28 GHz (3fo)	1.5 and 9.1

IV. CONCLUSIONS

Two miniaturized microstrip bandpass filters (44 mm^2 BPF operated at 2.39 GHz and 14 mm^2 BPF operated at 5.73 GHz) with the good insertion losses and the wide fractional bandwidths are designed and fabricated using a novel resonator. The proposed filters are composed of U-shape structures, which are loaded by the different open stubs. For the 2.39 GHz and 5.73 GHz BPFs, the harmonics are attenuated up to 9 GHz and 17.28 GHz, respectively, where the second and third harmonics are attenuated. The obtained results show that the proposed filters have wider fractional bandwidths, lower insertion losses and minimum sizes in comparison to the previous works.

REFERENCES

[1] M. Hayati, L. Noori, and A. Adinehvand, "Compact dual-band bandpass filter using open loop resonator for multimode WLANs," *IET Electronic Letters*, vol. 48, no. 10, pp. 573-574, 2012.

[2] M. R. Salehi, E. Abiri, and L. Noori, "Design of a microstrip dual-band bandpass filter with compact size and tunable resonance frequency for WLAN application," *International Journal of Electronics Communication and Computer Engineering*, vol. 6, no. 3, pp. 248-251, 2014.

[3] M. Hayati and L Noori, "Compact tunable dual-band bandpass filter using open-loop resonator loaded by step impedances cells for multimode WLANs," *IEICE Electronics Express*, vol. 11, no. 5, pp. 1-6, 2014.

[4] M. Hayati and L Noori, "Compact dual-band bandpass filter using open loop resonator loaded by in-line beeline for wideband applications," *IEICE Electronics Express*, vol. 8, no. 21, pp. 1789-1794, 2011.

[5] M. Hayati and L Noori, "Compact dual-band bandpass filter with ultra-wide stopband using open-loop resonator loaded by T-shape and open stubs," *IEICE Electronics Express*, vol. 8, no. 14, pp. 1168-1173, 2011.

[6] P-H. Deng and J-T. Tsai, "Design of microstrip cross-coupled bandpass filter with multiple independent designable transmission zeros using branch-line resonators," *IEEE Microwave and Wireless Components Letters*, vol. 23, no. 5, pp. 49-251, 2013.

[7] H. Kuan, Y-L. Lin, R-Y. Yang, and Y-C. Chang, "A multilayered parallel coupled microstrip bandpass filter with embedded SIR cells to have a broad upper rejection band," *IEEE Microwave and Wireless Components Letters*, vol. 20, no. 1, pp. 25-27, 2010.

[8] J. Marcotegui, J. Illescas, A. Estevez, and F. Falcone, "Compact ultra wide band microstrip bandpass filter based on multiple-mode resonator and modified complementary split ring resonator," *Scientific World Journal*, 2013.

[9] Z. Zakaria, M. Mutalib, M. Isa, N. Zainuddin, S. Yik, and A. Othman, "Design of microstrip bandpass filter with defected microstrip structure (DMS)," *Australian Journal of Basic and Applied Sciences*, vol. 7, no. 11, pp. 263-269, 2013.

[10] F. Cheng, X. Lin, Y. Jiang, K. Song, and Y. Fan, "Microstrip bandpass filters based on inductive-coupled stepped-impedance quarter-wavelength resonators," *Progress In Electromagnetics Research Letters*, vol. 44, pp. 101-106, 2014.

[11] L. Singh and P. K. Singhal, "Design and comparison of band pass cascade trisection microstrip filter," *The International Journal of Engineering and Science (IJES)*, vol. 2, pp. 104-107, 2013.

[12] D. Bukuru, K. Song, X. Ren, and M. Zhao, "Miniaturized microstrip bandpass filter designed using rectangular dual spiral resonator," *International Journal of Electronics and Communications (AEÜ)*, 2014.

[13] M. Moradian and M. Tayarani**,** "Improving the stopband of microstrip parallel-coupled line bandpass filters using partially coupled resonators," *IET Microwaves, Antennas & Propagation*, vol. 4, no. 7, pp. 906-916, 2009.

[14] Y. C. Li, X. Y. Zhang, and Q. Xue, "Bandpass filter Using Discriminating Coupling for Extended Out-of-band suppression," *IEEE Microwave and Wireless Components Letters*, vol. 20, no. 7, pp. 369-371, 2010.

[15] P. Cheong, T-S. Lv, W-W. Choi, and K-W. Tam, "A compact microstrip square-loop dual-mode balun-bandpass filter with simultaneous spurious response suppression and differential performance improvement," *IEEE Microwave and Wireless Components Letters*, vol. 21, no. 2, pp. 77-79, 2011.

[16] A. Nakhlestani and A. Hakimi, "Wideband microstrip ring resonator bandpass filter with embedded rings," *Microelectronics Journal*, vol. 44, pp. 462-467, 2013.

[17] J-S. Hong and M. J. Lancaster, *Microstrip Filters for RF/Microwave Applications*, New York: Wiley, 2001.

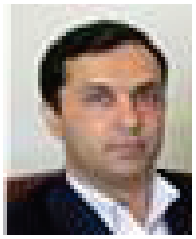

Mohammad Reza Salehi received the B.Sc. degree in Electrical Engineering from Amirkabir University of Technology (Tehran Poly-Technique), Tehran, the M.Sc. degree in Electrical Engineering from Shiraz University, Shiraz, Iran, and the Ph.D. degree at the ENSERG/INPG, France. He has authored and co-authored over 85 journal and conference papers and 7 books.

Leila Noori received her B.Sc. and M.Sc. degrees in Electronic Engineering from Razi University, Kermanshah, Iran in 2005 and 2009 respectively. She currently continues her Ph.D. in Electronic Engineering at the Shiraz University of Technology. Her research interests focus on artificial microstrip coupler, microstrip filter, neural networks and LNAs.